

INFRARED OBSERVATIONS AND STELLAR POPULATIONS MODELING
OF STARBURST GALAXIES

by

Charles William Engelbracht

A Dissertation Submitted to the Faculty of the
DEPARTMENT OF ASTRONOMY
In Partial Fulfillment of the Requirements
For the Degree of
DOCTOR OF PHILOSOPHY
In the Graduate College
THE UNIVERSITY OF ARIZONA

1 9 9 7

INFORMATION TO USERS

This manuscript has been reproduced from the microfilm master. UMI films the text directly from the original or copy submitted. Thus, some thesis and dissertation copies are in typewriter face, while others may be from any type of computer printer.

The quality of this reproduction is dependent upon the quality of the copy submitted. Broken or indistinct print, colored or poor quality illustrations and photographs, print bleedthrough, substandard margins, and improper alignment can adversely affect reproduction.

In the unlikely event that the author did not send UMI a complete manuscript and there are missing pages, these will be noted. Also, if unauthorized copyright material had to be removed, a note will indicate the deletion.

Oversize materials (e.g., maps, drawings, charts) are reproduced by sectioning the original, beginning at the upper left-hand corner and continuing from left to right in equal sections with small overlaps. Each original is also photographed in one exposure and is included in reduced form at the back of the book.

Photographs included in the original manuscript have been reproduced xerographically in this copy. Higher quality 6" x 9" black and white photographic prints are available for any photographs or illustrations appearing in this copy for an additional charge. Contact UMI directly to order.

UMI

**A Bell & Howell Information Company
300 North Zeeb Road, Ann Arbor MI 48106-1346 USA
313/761-4700 800/521-0600**

INFRARED OBSERVATIONS AND STELLAR POPULATIONS MODELING
OF STARBURST GALAXIES

by

Charles William Engelbracht

A Dissertation Submitted to the Faculty of the
DEPARTMENT OF ASTRONOMY
In Partial Fulfillment of the Requirements
For the Degree of
DOCTOR OF PHILOSOPHY
In the Graduate College
THE UNIVERSITY OF ARIZONA

1 9 9 7

UMI Number: 9806804

UMI Microform 9806804
Copyright 1997, by UMI Company. All rights reserved.

**This microform edition is protected against unauthorized
copying under Title 17, United States Code.**

UMI
300 North Zeeb Road
Ann Arbor, MI 48103

THE UNIVERSITY OF ARIZONA @
GRADUATE COLLEGE

As members of the Final Examination Committee, we certify that we have
read the dissertation prepared by Charles William Engelbracht

entitled Infrared Observations and Stellar Populations Modeling
of Starburst Galaxies

and recommend that it be accepted as fulfilling the dissertation
requirement for the Degree of Doctor of Philosophy

Marcia Rieke

Marcia Rieke

May 15, 1997

Date

Robert Kennicutt

Robert Kennicutt

5-15-97

Date

Hans-Walter Rix

Hans Walter Rix

5-15-97

Date

Date

Date

Final approval and acceptance of this dissertation is contingent upon
the candidate's submission of the final copy of the dissertation to the
Graduate College.

I hereby certify that I have read this dissertation prepared under my
direction and recommend that it be accepted as fulfilling the dissertation
requirement.

Marcia J. Rieke

Dissertation Director

Marcia Rieke

August 4, 1997

Date

STATEMENT BY AUTHOR

This dissertation has been submitted in partial fulfillment of requirements for an advanced degree at The University of Arizona and is deposited in the University Library to be made available to borrowers under rules of the Library.

Brief quotations from this dissertation are allowable without special permission, provided that accurate acknowledgment of source is made. Requests for permission for extended quotation from or reproduction of this manuscript in whole or in part may be granted by the head of the major department or the Dean of the Graduate College when in his or her judgment the proposed use of the material is in the interests of scholarship. In all other instances, however, permission must be obtained from the author.

SIGNED: Charles W. Ingalls

ACKNOWLEDGMENTS

This work would not have been possible without the guidance of my thesis advisor, Marcia Rieke. Marcia not only provided me with nifty infrared instrumentation and taught me how to use it but was a great source of wisdom on science, telescopes, instruments, computers, and bicycles. Marcia generously provided me with funding throughout most of my graduate career, which allowed me to concentrate on my work without distraction and also let me know that she was confident that I would produce something useful with the money she was paying me (at least I think that's what it meant...) I am very lucky to have had two advisors for the price of one. George Rieke provided keen insight which dramatically improved this project. His wit and unexpected visits to my office kept me from floundering around too much while trying to get papers done or from wasting too much time juggling (although Chris and Kim managed to sneak me outside every once in awhile—thanks, guys!) He also contributed the discussion on weak-[OI] LINERs in §3.4. I must also thank both George and Marcia for accommodating our disparate tastes in music—Broadway musicals and heavy metal mix poorly, if at all.

I'm happy to thank my other collaborators, Bill Latter and Doug Kelly. Bill taught me how to do narrowband imaging and contributed the narrowband images of NGC 6946. Doug contributed the CLOUDY modeling and much of §3.3.4 and was also a juggling partner in the brief time we overlapped here. I received valuable scientific input from R.C. Kennicutt and H.-W. Rix (who also happened to be on my thesis committee), as well as (in no particular order) J.H. Black, J.H. Bieging, W.G. Tifft, L.M. Shier, C.A. Kulesa, J.H. Lacy, K. Luhman, and R. Mauersberger. The Steward TAC generously provided me with many nights of observing time, and I must also thank the many observers who shared their time with me and allowed me to complete my sample.

Thanks also to my fellow mountain bikers, especially Tim, Chris, Jason, and Craig (who actually didn't bother with the bike, since it just slowed him down...) Together we explored the joys of rocks, cactus, and rattlesnakes while enjoying some fine mountain scenery.

This research has made use of the NASA/IPAC extragalactic database (NED) which is operated by the Jet Propulsion Laboratory, Caltech, under contract with the National Aeronautics and Space Administration. NSO/Kitt Peak FTS data used here were produced by NSF/NOAO. This work was made possible through a Space Grant Fellowship from NASA and through grants AST91-16442 and AST95-29190 from the National Science Foundation.

DEDICATION

This work is dedicated with love to my wife Suzanne, whose steadfast support (while trying to write a thesis of her own), has enabled me to accomplish so much.

TABLE OF CONTENTS

	LIST OF FIGURES	10
	LIST OF TABLES	14
	ABSTRACT	16
1	Introduction	17
1.1	Motivation	17
1.2	Technique	19
2	The Nuclear Starburst in NGC 6946	22
2.1	Introduction	23
2.2	Observations and Data Reduction	24
2.2.1	Imaging	24
2.2.2	Spectroscopy	25
2.3	Discussion	28
2.3.1	Morphology	28
2.3.2	Extinction	29
2.3.3	UV Flux	31
2.3.4	Luminosity	32
2.3.5	He emission lines	34
2.3.6	Supernova Rate	34
2.3.7	Absorption features	36
2.3.8	Mass	37
2.4	Models	42
2.4.1	M 82 models	42
2.4.2	NGC 6946 models	43
2.4.3	Problems with local IMFs	46
2.5	Other results	46
2.5.1	Fe emission	46
2.5.2	Molecular Hydrogen	47
2.6	Conclusions	48

TABLE OF CONTENTS—*Continued*

3	The Nuclear Starburst in NGC 253	70
3.1	Introduction	72
3.2	Observations and Data Reduction	73
3.2.1	Images	73
3.2.2	Near-IR spectra	76
3.2.3	Mid-IR Spectra	78
3.3	Faint emission lines	80
3.3.1	Extinction	81
3.3.2	[Fe II] emission	85
3.3.3	H ₂ emission	87
3.3.4	Temperature of the Hot Stars	90
3.4	Nature of Weak-OI LINERs	93
3.5	Morphology	96
3.5.1	Continuum morphology	96
3.5.2	Emission-line morphology	97
3.6	Other Parameters of the NGC 253 Starburst	98
3.6.1	Mass	98
3.6.2	Luminosity	104
3.6.3	Ionizing Flux	105
3.6.4	Absorption Features	106
3.7	Starburst models	108
3.7.1	Description of Models	108
3.7.2	NGC 253 models	109
3.8	Conclusion	113
4	Exploring the Range of Starburst Properties	141
4.1	Introduction	142
4.2	Observations and Data Reduction	144
4.2.1	Images	144
4.2.2	Near-IR spectra	145

TABLE OF CONTENTS—*Continued*

4.3	Discussion	146
4.3.1	Continuum morphology	146
4.3.2	Emission-line morphology	148
4.3.3	Spectral features	150
4.4	Model constraints	151
4.4.1	Size of starburst region	151
4.4.2	Extinction	153
4.4.3	UV flux	155
4.4.4	Luminosity	156
4.4.5	Mass	158
4.4.6	CO index	161
4.4.7	Supernova rate	161
4.5	Starburst models	162
4.5.1	Description of Models	162
4.5.2	Individual galaxy models	162
4.6	Conclusion	164
5	Filling in the Gaps—A Sequence of Starburst Evolution	203
5.1	Introduction	204
5.2	Observations and Data Reduction	205
5.2.1	Images	205
5.2.2	Near-IR spectra	207
5.3	Model constraints	209
5.3.1	Extinction	210
5.3.2	Luminosity and spectral index constraints	212
5.3.3	Dynamical mass	213
5.3.4	Summary	215
5.4	Models	216
5.5	Discussion of individual galaxies	219
5.6	Conclusion	222

TABLE OF CONTENTS—*Continued*

6	Concluding Remarks	274
6.1	Main results	274
6.2	Future work	276
	References	279

LIST OF FIGURES

2.1	Broadband images of NGC 6946	60
2.2	Narrowband images of NGC 6946	61
2.3	J-band spectrum of NGC 6946	62
2.4	H-band spectrum of NGC 6946	63
2.5	K-band spectrum of NGC 6946	64
2.6	J-H and H-K color maps of the nuclear region of NGC 6946	65
2.7	Velocity gradient plots of infrared lines in NGC 6946	66
2.8	Velocity gradient plots of optical lines in NGC 6946	67
2.9	Position-velocity plots of NGC 6946	68
2.10	Starburst models of NGC 6946	69
3.1	Broadband images of NGC 253	127
3.2	Narrowband images and color maps of NGC 253	128
3.3	Dereddened and deprojected images of NGC 253	129
3.4	High-resolution J-band spectrum of NGC 253	130
3.5	Low-resolution J-band spectrum of NGC 253	131
3.6	High-resolution H-band spectrum of NGC 253	132
3.7	High-resolution K-band spectrum of NGC 253	133
3.8	Low-resolution K-band spectrum of NGC 253	134
3.9	Mid-Infrared spectrum of NGC 253	135
3.10	Plot of [Fe II] line ratios as a function of density	136
3.11	Position-velocity plots of NGC 253	137
3.12	Rotation curves for NGC 253 and NGC 3115	138
3.13	Starburst models of NGC 253	139
3.14	Allowed values in the (mass, age) plane	140
4.1	Broadband images of IC 342	177
4.2	Broadband images of NGC 2146	178
4.3	Broadband images of NGC 3079	179

LIST OF FIGURES—*Continued*

4.4	Broadband images of NGC 7714	180
4.5	$J - H$ and $H - K$ color images of the nuclear region of IC342	181
4.6	Narrowband and color images of NGC 2146	182
4.7	Dereddened and color images of NGC 3079	183
4.8	J-band spectrum of IC342	184
4.9	H-band spectrum of IC342	185
4.10	K-band spectrum of IC342	186
4.11	J-band spectrum of NGC2146.	187
4.12	H-band spectrum of NGC2146.	188
4.13	K-band spectrum of NGC2146.	189
4.14	J-band spectrum of NGC3079.	190
4.15	H-band spectrum of NGC3079.	191
4.16	K-band spectrum of NGC3079.	192
4.17	J-band spectrum of NGC7714.	193
4.18	H-band spectrum of NGC7714.	194
4.19	K-band spectrum of NGC7714.	195
4.20	Position-velocity diagrams of IC 342	196
4.21	Position-velocity diagrams of NGC 2146	197
4.22	Position-velocity diagram of NGC 3079	198
4.23	Position-velocity diagrams NGC 7714	199
4.24	Velocity gradient plots for NGC 2146	200
4.25	Velocity gradient of H_2 along the major axis of NGC 3079	201
4.26	Starburst models using RLRT93's IMF 8.	202
5.1	Broadband images of NGC 520	232
5.2	Broadband images of NGC 520	233
5.3	Broadband images of Maffei 2	234
5.4	Broadband images of NGC 1614	235
5.5	Broadband images of NGC 2782	236
5.6	Broadband images of NGC 3115	237
5.7	Broadband images of NGC 3379	238

LIST OF FIGURES—*Continued*

5.8	Broadband images of NGC 3628	239
5.9	Broadband images of NGC 4102	240
5.10	Broadband images of NGC 4194	241
5.11	Broadband images of NGC 4339	242
5.12	Broadband images of NGC 5590	243
5.13	Broadband images of NGC 5990	244
5.14	Broadband images of NGC 6000	245
5.15	Broadband images of NGC 6240	246
5.16	Broadband images of MKN 331	247
5.17	Color images of NGC 520	248
5.18	Color images of NGC 660	249
5.19	Color images of Maffei 2	250
5.20	Color images of NGC 2782	251
5.21	Color images of NGC 3628	252
5.22	Color images of NGC 6240	253
5.23	J-band spectra of starburst galaxies	254
5.24	H-band spectra of starburst galaxies	255
5.25	K-band spectra of starburst galaxies	256
5.26	J-band composite spectrum	257
5.27	H-band composite spectrum	258
5.28	K-band composite spectrum	259
5.29	Position-velocity plots of NGC 520	260
5.30	Position-velocity plots of NGC 660	261
5.31	Position-velocity plots of NGC 1614	262
5.32	Position-velocity plots of NGC 2782	263
5.33	Position-velocity plots of NGC 3628	264
5.34	Position-velocity plots of NGC 4102	265
5.35	Position-velocity plots of NGC 4194	266
5.36	Position-velocity plots of NGC 6240	267
5.37	Position-velocity plots of MKN 331	268

LIST OF FIGURES—*Continued*

5.38 Velocity gradient plot for NGC 2782	269
5.39 Velocity gradient plot for NGC 3628	270
5.40 Velocity gradient plot for NGC 4102	271
5.41 Velocity gradient plot for NGC 660	272
5.42 Extinction plot	273

LIST OF TABLES

2.1	Aperture Photometry of NGC 6946 at J, H and K	51
2.2	Hydrogen Recombination Line Measurements	52
2.3	[FeII] Emission	53
2.4	He emission line strengths	54
2.5	H ₂ Line Strength Relative to H ₂ (1,0)S(1)	55
2.6	Absorption Features	56
2.7	Line Ratios with Reddening	57
2.8	Velocity gradients of spectral features (km s ⁻¹ /'')	58
2.9	Summary of starburst parameters	59
3.1	NGC 253 Aperture Photometry	117
3.2	Hydrogen Recombination Line Measurements	118
3.3	He Lines	119
3.4	[Fe II] Lines	120
3.5	H ₂ Line Fluxes	121
3.6	H ₂ rotational excitation temperatures	122
3.7	Predicted optical line ratios	123
3.8	Velocity gradients of spectral features	124
3.9	Absorption features	125
3.10	Summary of Starburst Parameters	126
4.1	Galaxy Data	166
4.2	Imaging Observation Log	167
4.3	Spectroscopy Observation Log	168
4.4	IC 342 Photometry	169
4.5	NGC 2146 Photometry	170

LIST OF TABLES—*Continued*

4.6	NGC 3079 Photometry	171
4.7	NGC 7714 Photometry	172
4.8	Hydrogen Recombination Lines	173
4.9	Other Emission Lines	174
4.10	A_V Estimated From Colors and Line Ratios	175
4.11	Starburst parameters	176
5.1	Galaxy Data	224
5.2	Imaging Observing Log	225
5.3	Spectroscopy Observing Log	226
5.4	Aperture Photometry	227
5.5	Strong Emission Line Fluxes	228
5.6	Visual extinction from colors and line ratios	229
5.7	Starburst model constraints	230
5.8	Starburst modeling results	231

ABSTRACT

We present a study of a sample of starburst galaxies. The systems chosen for study range in age and strength. We have obtained high-quality infrared spectroscopy and imaging of 18 starburst galaxies and 4 early-type galaxies as a comparison sample of an old stellar population. The spectra consist of high-resolution data ($R \sim 3000$) in the H ($1.65\mu\text{m}$) and K ($2.2\mu\text{m}$) bands and, in a few cases, the J ($1.25\mu\text{m}$) band; most of the J-band spectra were obtained at a resolution of 800. We obtained broadband images of all the galaxies in the J, H, and K bands, as well as narrowband images of several of the galaxies in the (1,0)S(1) line of H_2 and in $\text{Br}\gamma$.

We use these data and data from the literature to constrain models of the nuclear starbursts for these galaxies. The high sensitivity and resolution of the spectra plus the use of a long slit allows us to derive kinematic properties of the nuclear region in addition to other constraints on the starburst population, such as ionizing flux and CO index. We compare the properties of these galaxies and suggest that a burst of star formation can account for the galaxy properties and that the range of properties observed is derived from a range of burst ages and strengths.

Our high-quality data allow us to examine the properties of the [Fe II] and H_2 emission regions. We measure, for the first time, the density in the [Fe II]-emitting region of a starburst galaxy and find that this density is consistent with the origin of this emission in supernova remnants. We find, in contrast to earlier studies, that fluorescence plays a large role in the H_2 emission of some starburst galaxies.

CHAPTER 1

INTRODUCTION

1.1. Motivation

A significant fraction of nearby galaxies have strong, centrally concentrated infrared sources indicative of rapid star formation in their central few hundred parsecs (Rieke and Lebofsky 1978; Devereux, Becklin, & Scoville 1987). These nuclear starbursts typically do not have enough gas to fuel prodigious star formation for times much longer than 10^7 to 10^8 years, so it is clear that starbursts are phenomena which occur on timescales short relative to the $\sim 10^{10}$ yr age of the universe. What is less clear is whether every galaxy will undergo a starburst phase during its lifetime or if some small fraction of galaxies each account for multiple starburst events.

Starburst events are worthy of study both because they are affected by the evolution and environment of the host galaxy (i.e., they can serve as an indicator of processes which affect the host galaxy) and because they can have a strong effect in turn on the host galaxy and its environment and are therefore a critical

facet of the galaxy formation and evolution process. For example, while it is clear that major mergers of gas-rich galaxies can trigger tremendous bursts of star formation, less dramatic interactions that are perhaps more typical of common galaxy encounters can induce powerful starbursts in one or both of the interacting galaxies. An evolving starburst will quickly generate many supernova explosions as the most massive stars have short lifespans. Along with the prodigious winds these stars generate during their lifetimes, the supernovae deposit large amounts of kinetic energy in the interstellar medium of the galaxy, in many cases driving metal-enriched gas out of the galaxy altogether. This galactic “superwind” can enhance the metallicity of intergalactic gas in addition to affecting the structure and evolution of nearby galaxies. Even once the violent early evolution of a starburst has passed, a large coeval population of stars which may dominate the nuclear properties for hundreds of millions of years will be left behind.

Detailed studies of these nuclear starbursts have concentrated on cases of moderate (e.g., Rieke et al. 1980; Rieke et al. 1993; Krabbe et al. 1994) or high (e.g., Rieke et al. 1985; Goldader et al. 1995; Shier, Rieke, & Rieke 1996) luminosity. It is likely that most of the well studied starbursts are also relatively young, since such systems are the most dramatic and hence will tend to stand out in surveys. An understanding of how these events occur and evolve will require study over the full range of scale and age. Access to a new and highly sensitive infrared spectrometer has allowed us to examine a large number of systems with a range of burst ages and strengths, which will enable us to explore the character and evolution of these systems in unprecedented detail.

This work describes an investigation of the properties of starburst galaxies. We focus on nuclear starbursts occurring in relatively massive galaxies—mostly

large, late-type spirals. Similar investigations have been carried out for a sample of low-mass galaxies, of which the archetype is the well-known starburst M82 (e.g., McLeod et al. 1993; Vanzi & Rieke 1997). To constrain thoroughly the properties of the starbursts, we make use of observational data from the literature over a broad range of wavelengths and have augmented the available data with high-quality infrared observations, both imaging and spectroscopy. These data are used to constrain an evolutionary synthesis model as described in Rieke et al. (1993, hereafter RLRT93). With this model, we can quantitatively account for many properties of these galaxies.

1.2. Technique

These galaxies are typically gas-rich and dusty, rendering optical investigations of the dust-enshrouded nuclei difficult, especially in the edge-on galaxies. We therefore have obtained high-quality imaging and spectroscopy of these galaxies in the near-infrared, since these wavelengths will be less affected by extinction. These data allow us to place constraints on many components of the starburst simultaneously. For example, the continuum radiation at these wavelengths is dominated by cool stars and we can therefore use the NIR luminosity and the absorption features in the spectra as constraints on the cool stellar population. The hot stars make their presence felt through the emission of copious ionizing photons, many of which are absorbed directly by dust but some fraction of which instead ionize a hydrogen atom and can therefore be measured through recombination lines such as the Brackett and Paschen series lines observed in our spectra. These regions of hot stars also excite lines of H_2 and forbidden lines which are observed in the mid-infrared (MIR), most commonly [Ne II] at $12.8\mu\text{m}$. The nonionizing

radiation is largely absorbed by dust and (along with the possibly large fraction of ionizing radiation absorbed directly by dust) reradiated in the far-infrared (FIR), contributing to the large luminosities observed in that part of the spectrum. We can also place constraints on the number of stellar remnants in the starburst region, through lines such as [Fe II] which have been shown to trace regions of shocked gas associated with supernova remnants (e.g. Moorwood & Oliva 1988; Greenhouse et al. (1997); ERRKA97), supplying a constraint on the numbers of massive stars present in the recent past.

In addition to obtaining infrared spectra of exceptional resolution and sensitivity of a large sample of starburst galaxies, a significant advancement made by the present work is the ability to measure the dynamical mass in the nuclear region of these galaxies. The infrared spectra are critical to this exercise since the heavy dust obscuration common to these galaxies biases observations at shorter wavelengths that attempt to measure the kinematics. By measuring the dynamical mass, we can even place constraints on the low-mass stellar population, which contributes little or nothing to the luminosity of a starburst at any wavelength. For some galaxies it is possible to obtain a useful rotation curve (as traced by both emission and absorption lines), while for most of these galaxies our spectra are of sufficient resolution and signal-to-noise to estimate the velocity dispersion of the stellar population. These techniques allow us to place limits on the dynamical mass which can be used to constrain an evolutionary synthesis model.

The advances in observational techniques are coupled with a state-of-the-art evolutionary synthesis code with which we model the stellar population in the starburst. By specifying a star-formation rate and a distribution of stellar masses to form, or *initial mass function* (IMF), the model computes the integrated properties

of the stellar population as a function of time. We compare these predictions with the observations to determine at what time the starburst model can reproduce the observed properties of the galaxy while still remaining within the mass limit.

We begin by studying nearby starburst galaxies (in which we can resolve the starburst region and for which copious observations at other wavelengths can be found in the literature) in great detail to build an accurate picture of individual systems. We then apply our new understanding to a set of galaxies which exhibit a range of properties and provide us with a picture of the evolution of these galaxies. Finally, we examine the larger sample in light of our early investigations to round out our knowledge of this dynamic and energetic galaxy phenomenon.

CHAPTER 2

THE NUCLEAR STARBURST IN NGC 6946

Near-infrared images in both broad and narrow bands plus longslit and aperture spectroscopy at moderate and high resolution have been obtained for NGC 6946. We have used these data and data from the literature to derive a set of observational constraints on the stellar population in the nucleus.

We estimate an ultraviolet flux of 10^{52} ionizing photons per second. A thorough examination of the gas and stellar motions puts a 2σ upper limit on the dynamical mass in the central $8''.5$ (which corresponds to 230 pc at an assumed distance of 5.5 Mpc) of $\sim 3 \times 10^8 M_{\odot}$. A detailed study of broadband colors, emission line ratios and the $10\mu\text{m}$ silicate absorption feature indicate that the extinction to the starburst is high, with $A_V=10.4$ mag. An estimate of the supernova rate from both nonthermal radio emission and $[\text{Fe II}] \lambda=1.644\mu\text{m}$ emission from gas excited in fast shocks agrees well with our models; the current rate of supernova explosions in the nucleus is $\sim 6 \times 10^{-3} \text{ yr}^{-1}$. The bolometric luminosity of the starburst region is

$> 2.2 \times 10^9 L_{\odot}$.

In addition to the diagnostic features we have used here, the infrared spectra show a wealth of stellar features and weaker emission lines, including atomic absorption lines and several H_2 emission lines. We have measured the lines of H_2 and compared the ratios to models to determine the excitation mechanism.

The properties of NGC 6946 have been fitted with a starburst model. We find that the starburst probably had a duration of ~ 20 million years and that the star formation is likely to be biased toward high mass stars compared with that in the local neighborhood.

2.1. Introduction

NGC 6946 is a nearby (~ 5.5 Mpc), nearly face-on spiral galaxy which contains a nuclear starburst of moderate luminosity. This galaxy offers us the opportunity to study starburst activity in a relatively isolated system and at a smaller scale than in the well-studied archetypes M 82 and NGC 253.

This galaxy is particularly suited to detailed study both because of its proximity and because it is a very gas-rich system that has been the target of many observations at other wavelengths, especially in the radio and far-infrared. We make good use of the wealth of other observational data available to derive strong constraints on the starburst in this galaxy.

2.2. Observations and Data Reduction

2.2.1. Imaging

Broadband images of NGC 6946 in the J, H and Ks bands were obtained on 1994 June 21 at the Steward Observatory Bok 2.3m telescope on Kitt Peak with a NICMOS3-based camera. Images of the galaxy were interleaved with blank sky observations and both on- and off-source frames were jittered by several arcseconds on the sky so that bad pixels would be removed in a median combination of the images. Temporally adjacent sky images were subtracted from each galaxy frame and the sky images were median-combined and dark-current-subtracted to make a flat field, which was divided into the object frames. The object frames in each filter were aligned using field stars in the frame for reference and were then median combined to produce images with a total integration time of two to three minutes. The final frames at H and Ks were magnified by small factors (1.011 at H and 1.014 at Ks) so that the scales matched the images taken at J. The frames were aligned to a common center using the many stars in the field for reference. The final frames are presented as greyscale plots in Figure 2.1 at a scale of $0''.62/\text{pixel}$.

The broadband images were calibrated by scaling them to match the flux in a $27''.4$ aperture measured by Aaronson (1977). The image taken through the Ks filter was scaled to match Aaronson's K-band photometry, so we will hereafter refer to this image as the K-band image. Aaronson's apertures are overlaid on the K-band contour map in Figure 2.1. Measurements from this paper are compared to Aaronson's photometry in Table 2.1. The agreement is good except for the largest aperture, in which Aaronson had to correct for a star in the reference beam. We therefore take our photometric errors to be the same as those of Aaronson, i.e., 0.06, 0.05 and 0.03 magnitudes at J, H and K, respectively. The seeing as measured

from the many stars in the field is approximately $1''.2$ FWHM.

The narrowband images were acquired with the same instrumentation and $\sim 0.5\%$ bandwidth filters on 1993 October 27. The filters were tuned by tilting to hydrogen $\text{Br}\gamma$ ($\lambda = 2.1655\mu\text{m}$), H_2 $v = 1 \rightarrow 0$ S(1) ($\lambda = 2.1213\mu\text{m}$), and adjacent continuum (see Latter et al. 1993 for details). Several techniques for continuum subtraction were used, each giving similar results. The narrowband images were magnified by a factor of 0.98 to match the scale of the broadband images and were aligned with the broadband images using the many stars in the field. The central $10''$ of these images is presented as greyscale and contour plots in Figure 2.2.

2.2.2. Spectroscopy

J-band spectroscopy

The J-band spectra were obtained at the MMT (Multiple Mirror Telescope) on 1993 October 2, using GeSpec, a Germanium diode spectrometer. The array consists of two rows of 32 elements each, one for sky and one for the object, corresponding to a spectral coverage of about $0.023\mu\text{m}$ per grating setting at our resolution ($\lambda/\Delta\lambda \sim 800$). The instrument and observing techniques are described in Rix et al. (1990). The data are presented in Figure 2.3. We used five grating settings chosen to include important lines. We used a more nearly complete spectrum of M 82 taken with this instrument (McLeod et al. 1993) to select spectral regions of interest. The spectra were corrected for atmospheric transmission variations using the nearby G3V star HR 7783.

The spectra were initially flux-calibrated by assuming blackbody emission from the standard star; a small adjustment was then made to make the spectrum consistent with our calibrated J-band image (see Table 2.1). The magnitude was

converted to flux density using the zero points of Campins, Rieke, & Lebofsky (1985).

H- and K-band spectroscopy

The H- and K-band spectra were obtained at the Bok telescope on 1993 September 26 with FSpec, a cryogenic longslit near-infrared spectrometer using a NICMOS3 array (Williams et al. 1993). We used both low ($R \sim 700$) and high ($R \sim 2000$ at H and $R \sim 3000$ at K) resolution modes at a position angle of 90° . The slit was two pixels wide, or $2''.34$. We have also obtained additional data at position angles 0° , 30° , 60° (the position angle of the major axis of the galaxy—Rogstad & Shostak 1972), and 120° at the wavelengths of $H_2(1,0)S(1)$ and $Br\gamma$ plus the 1st-overtone CO bands at $2.3\mu\text{m}$. Except for data at the position angle of 0° , the additional measurements were made after an improved array had been installed in FSpec and are of longer integration time and so are of higher signal-to-noise than the other measurements. Figure 2.1 shows a graphical representation of the slit positions and lengths overlaid on the K-band contour map.

The H- and K-band data were reduced using IRAF routines and scripts written specifically for FSpec. From each image a background consisting of the average of the images taken before and after was subtracted. This process removed the sky background as well as the dark current. Dark-current-corrected observations of a blank screen were used to flat-field the data. In the longer galaxy exposures, the background frames were rescaled slightly to improve the removal of airglow lines. The images were shifted and then median-combined to produce a final two-dimensional spectrum. The galaxy spectrum at each grating setting was then

divided by the corresponding spectrum of the F5V star HR 7727 (which had been reduced in a similar manner) to remove the effects of atmospheric absorption.

Since the spectrum of an F5 star is not completely featureless at this wavelength and resolution, the galaxy spectrum was multiplied by a high-resolution solar spectrum obtained by Livingston & Wallace (1991), convolved with a gaussian to the same resolution as the galaxy data and normalized to a flat continuum. This procedure is described in detail by Maiolino et al. (1996). The continuum slope of the standard star was removed from the final galaxy spectrum by multiplying the spectrum by that of a black body at 6200 K.

The segments of corrected galaxy spectrum were wavelength-calibrated using the wavelengths of OH airglow lines tabulated in Oliva & Origlia (1992). For the grating setting centered at $2.35\mu\text{m}$, where the OH features are weak, we obtained a wavelength solution from a Ne-Kr lamp. This solution was confirmed by comparing the regions of overlap with the $2.28\mu\text{m}$ observations and by the wavelengths of the 1st overtone CO bands in the galaxy spectra.

The spectra were flux calibrated from the broadband images, using the absolute calibration of Campins et al. (1985). The spectra are displayed in Figures 2.4 and 2.5, with individual feature measurements in Tables 2.2, 2.3, 2.4, 2.5, and 2.6. The quality of the spectra is evident from the many detected stellar absorptions. These features are narrow; the velocity dispersion in the nucleus of NGC 6946 is very low, as discussed in § 2.3.8. The complicated continuum structure gives rise to some uncertainty in the line measurements. The errors in the emission line measurements were estimated by testing a range of plausible continuum placements. The errors on the narrowband imaging measurements were obtained by assuming that the calibration is good to within 10%.

Optical spectroscopy

Optical spectra of NGC 6946 were obtained on the night of 1996 May 20 at the Bok telescope, using the facility Boller & Chivens spectrograph. Data were obtained at a resolution of ~ 3000 and covered lines of $H\beta$ and $[O\ III](\lambda 5007)$. We obtained two 20-minute exposures at each of three position angles: 30, 60, and 90 degrees east from north. The data were reduced using standard IRAF tasks and were wavelength-calibrated using a He-Ar comparison lamp.

2.3. Discussion

The distance to NGC 6946 is uncertain; estimates from 4 to 11 Mpc are in the literature. For this work we will take the distance to be 5.5 Mpc (Tully 1988), which is a conservative estimate as far as our model predictions are concerned. Adopting a larger distance would increase luminosities and make the inferred starburst more powerful. We also adopt a reference aperture of $8''.5$ (which corresponds to a linear distance of 230 pc at the assumed distance to the galaxy) in which to derive the starburst properties—this aperture contains nearly all the $10\mu\text{m}$ flux (Telesco, Dressel, & Wolstencroft 1993) and most of the $Br\gamma$ flux, as shown by the narrowband images presented here.

2.3.1. Morphology

NGC 6946 is a nearly face-on (inclination 31°) Scd galaxy with a well-defined spiral pattern (Elmegreen, Meloy Elmegreen, & Montenegro 1992). The northern arm is very prominent near the nucleus in both broadband optical and $H\alpha$ images, in CO($1 \rightarrow 0$) (Ishizuki et al. 1990), and in our broadband infrared images. It can be seen from Table 2.1 that the infrared colors grow systematically redder with

decreasing aperture, with $H-K \sim 0.55$ on the nucleus. A map of the $H-K$ color in Figure 2.6 also shows that the red colors extend to the north along the prominent spiral arm. If we assume that these colors result from extinction and hence trace dust and molecular gas, our observations extend the argument of Ishizuki et al. (1990) that the gas flows to the nucleus mainly along this spiral arm. The $J-H$ color map shows similar structure but its morphology is considerably more complex than the $H-K$ image, probably due to patchy dust extinction which shows up at a stronger level at shorter wavelengths.

2.3.2. Extinction

We can estimate the extinction to the stars using our broadband colors and assuming an intrinsic color for the stellar population: the $H-K$ color is typically 0.2 magnitudes throughout the entire Hubble sequence, while a typical $J-H$ color is 0.7 magnitudes (Aaronson 1977). Our starburst models match these colors within a few million years after the burst, so we believe these are appropriate values to apply to NGC 6946. We derive color excesses in an $8''.5$ aperture of $E(H-K)=0.27$ and $E(J-H)=0.32$ from the measurements in Table 2.1. Using the extinction law of Rieke & Lebofsky (1985), a simple foreground screen model for the dust indicates $A_V=3.0$ magnitudes from the $J-H$ color and $A_V=4.3$ magnitudes from the $H-K$ color. A small fraction of that extinction (~ 0.1 magnitudes in the K band) is due to dust in our own galaxy. Throughout this section we will include the galactic extinction in our estimates of the total extinction, regardless of dust geometry.

The extinction derived from the $H-K$ color must be considered an upper limit if there is significant contribution to the K-band emission by hot dust or some other nonstellar source. If dust were filling in the red end of the K band, however, the first overtone CO bands at $\lambda = 2.3\mu\text{m}$ would appear weakened relative to the

second overtone bands around $\lambda = 1.6\mu\text{m}$. Since the relative strengths of the first and second overtone CO bands in NGC 6946 fall well within the scatter of galactic supergiant values (Origlia, Moorwood, & Oliva 1993), emission by dust in the K band must be negligible.

The dust extinction models of Witt, Thronson, & Capuano (1992) include scattering effects and dust distributions mixed with the stars, and hence are more realistic than a foreground screen model. Our J–H and H–K colors most closely match their starburst model, with 10.4 magnitudes of extinction at V. The effective extinctions in the near infrared bands indicated by the Witt et al. model are $A_J = 1.21$, $A_H = 0.75$, and $A_K = 0.48$ magnitudes. As it happens, these are exactly the same values derived from the foreground screen model with $A_V=4.3$ using just the H–K color.

The extinction to the gas can be estimated from the hydrogen and [Fe II] lines, as summarized in Table 2.7. The observed hydrogen recombination ratios agree well with case B ratios reddened by the same amount as the stellar continuum. Br12 ($1.64\mu\text{m}$) was excluded from this comparison because it is blended with the $1.644\mu\text{m}$ [Fe II] line. The [Fe II]($1.257\mu\text{m}$) and [Fe II]($1.644\mu\text{m}$) lines share the same upper level, so their emissivities can be related simply by

$$\frac{j_{ik}}{j_{im}} = \frac{A_{ik}}{A_{im}} \frac{\lambda_{im}}{\lambda_{ik}}. \quad (2.1)$$

Using the transition probabilities of Nussbaumer and Storey (1988), the intrinsic ratio of the $1.644\mu\text{m}$ line to the $1.257\mu\text{m}$ line is 0.74. The observed ratio (where we have corrected the $1.644\mu\text{m}$ flux as described in § 2.5.1) is 1.2, also in satisfactory agreement with the value of 1.0 derived from the continuum reddening estimate.

Since the near-IR extinction is insensitive to the dust geometry (in the models considered here), we will correct the continuum and line emission for a

foreground screen of $A_V=4.3$, using the Rieke & Lebofsky (1985) extinction law and interpolating as necessary to the appropriate wavelengths.

2.3.3. UV Flux

The number of ionizing photons per second, N_{LyC} , and the characteristic temperature of the UV emitting stars are strong functions of the number and spectral types of hot stars. Several emission features in the near- and mid-infrared allow us to estimate these parameters.

From the absence of the fine-structure lines [Ar III](9.0 μm) and [Si IV](10.5 μm) in NGC 6946, Roche et al. (1991) conclude that the temperature of the hottest stars is $\lesssim 35,000$ K. At our assumed distance, they would find $N_{\text{LyC}} \sim 1.5 \times 10^{52} \text{ s}^{-1}$ within a 5.9'' beam, from the strength of the [Ne II] flux and assuming solar metallicity.

We can also derive the ionization rate using the infrared hydrogen recombination line measurements from Table 2.2. The intensity ratios of the near-infrared recombination lines are not very sensitive to temperature and even less so to density, so here we simply use the $T_e = 5000$ K and $N_e = 10^2 \text{ cm}^{-3}$ derived for M 82 by McLeod et al. (1993). Using an extinction-corrected Br γ flux from our narrowband image and an assumed distance of 5.5 Mpc, the recombination line ratio $I(\text{H}\beta)/I(\text{Br}\gamma)=30.3$ from Hummer & Storey (1987) plus a ratio $\alpha_B/\alpha_{\text{H}\beta}^{\text{eff}} = 8.40$, we calculate 8.2×10^{51} ionizing photons per second, in the same 5.9'' beam used by Roche et al.. Given the uncertainties involved, the results seem consistent.

Our measurement of Br γ is about three times fainter than that of Ho, Beck, & Turner (1990). Our data are more extensive, of higher resolution, and have a

larger ratio of signal to noise than theirs. In addition, our spectra and Br γ image were calibrated independently and give consistent results. We therefore take the Br γ flux from our data alone, obtaining 2.9×10^{-14} erg/s/cm² in a 8".5 aperture, with a corresponding N_{LyC} of 1.0×10^{52} s⁻¹. This is consistent with the estimate by Turner & Ho (1983) of 1.2×10^{52} s⁻¹ from radio continuum measurements (after we correct their distance from 7.1 Mpc to 5.5 Mpc).

For our models, we adopt $N_{\text{LyC}} = 1 \times 10^{52}$ s⁻¹. This estimate of N_{LyC} ignores the absorption of potentially ionizing photons by dust, with reradiation as far-infrared photons, not as recombination lines. Our models are therefore conservative in the amount of UV they require.

2.3.4. Luminosity

To estimate the total luminosity of the nuclear starburst, we have proceeded as follows. Engargiola (1991) discusses the far infrared data and derives a luminosity within a 45" beam (and corrected by us to a distance of 5.5 Mpc) of $2.2 \times 10^9 L_{\odot}$ for this spectral component. Using our near-infrared data and the optical measurements of Engargiola (1991; and references therein) we calculate that the optical and near-infrared contribute another $1.2 \times 10^9 L_{\odot}$ to the total in a 45" beam.

To apply these numbers to the central 8".5, we have compared the groundbased Q-band (21 μ m) measure of Lebofsky and Rieke (1979) in a 5".7 beam with the IRAS Band 2 measure in a 45" by 4' beam. The ground based flux has been corrected to 25 μ m using the slope fitted between IRAS Bands 2 and 3 integrated over the entire galaxy. The groundbased measure has also been corrected to an 8".5 beam using the observed aperture dependence at 10 μ m (Rieke 1976). The comparison demonstrates that virtually all the 25 μ m flux in a 45" beam centered

on the nucleus must originate from the central $8''.5$. We therefore derive that the far-infrared luminosity of the nuclear starburst is $2.2 \times 10^9 L_{\odot}$.

To estimate the contribution of the optical and near-infrared light to the total, we must take into account that this radiation is not distributed in the same fashion as the far-infrared flux. Using the aperture dependence of our near-infrared images as a guide, we estimate that the central $8''.5$ of NGC 6946 contains 35% of the optical and near-infrared flux found in a $45''$ beam. Therefore the optical and near-infrared bands must contribute $4 \times 10^8 L_{\odot}$ to the bolometric luminosity in the central $8''.5$. For the starburst population, then, we derive $L_{\text{Bol}} = 2.6 \times 10^9 L_{\odot}$.

To estimate what contribution the preexisting stellar population in the nucleus might make to the observed fluxes, we have compared the K magnitude as a function of aperture in M 31 to the mass in the same aperture. We used the K-band measurements of Aaronson (1977) and the mass determination of Tenjes, Haud, & Einasto (1994). We have assumed that M/L_K is the same in the preexisting nuclear population of NGC 6946 and in the nucleus of M 31 and calculated a K magnitude for the underlying nuclear population in NGC 6946 based on our mass estimate of the old population from § 2.3.8 and setting the total available mass at the 2σ upper limit derived there. Allocating $2.4 \times 10^8 M_{\odot}$ to the old stellar population results in an absolute K magnitude of -17.9 for this component. This is almost exactly the same mass-to-light ratio calculated by Thronson & Greenhouse (1988) for the solar neighborhood. At the adopted distance of 5.5 Mpc, this provides roughly 20% of the broadband K-band flux, so we will subtract this amount from the observed K-band flux when we calculate the target K-band luminosity of the starburst.

The underlying stellar population also contributes no more than 15% to the bolometric luminosity. If we assume a BC_K for a K giant population of ~ 2.7

(Frogel & Whitford 1987), and $M_{\text{Bol}}(\odot) = 4.75$, then the underlying nuclear population has a bolometric luminosity of roughly $4 \times 10^8 L_{\odot}$, so we subtract this amount from L_{Bol} when we determine the target value for the starburst.

If we use our calculated number for the dynamical mass rather than the 2σ upper limit, the contribution of the underlying population to the K-band and bolometric luminosities drops by $2/3$, raising the target values for the starburst but also making a corresponding reduction in the amount of mass available for the stars which generate that luminosity. The requirements for starburst models therefore become significantly more difficult.

2.3.5. He emission lines

We observe two fairly weak He emission lines in the spectra presented here, one at $1.083\mu\text{m}$ and another at $2.058\mu\text{m}$. The fluxes in these lines are presented in Table 2.4. The ratio of He I($\lambda 2.058\mu\text{m}$) to Br γ in NGC 6946 is 0.13 ± 0.06 , which is small compared to the well-studied starburst M 82, where the ratio is 0.43 (our unpublished data). The weakness of the He emission may indicate that the ionizing spectrum in NGC 6946 is very soft, which is consistent with the lack of high-ionization lines in the mid-infrared spectrum of Roche et al. (1991). There are complications in the interpretation of these lines, however (see, e.g., Clegg 1987, Shields 1993), and as they do not offer a strong constraint on our models we will not discuss them further here.

2.3.6. Supernova Rate

There are two independent means by which we can calculate the supernova rate. One is to assume that all the nonthermal radio flux is due to synchrotron emission from relativistic electrons accelerated in fast shocks associated with the supernovae.

Ho et al. (1990) find the nonthermal portion of the 5 GHz flux to be 30 mJy in an $8.5''$ aperture centered on the nucleus. At a distance of 5.5 Mpc, this corresponds to a 5 GHz luminosity of $1.1 \times 10^{20} \text{ W Hz}^{-1}$. Using equation (8) of Condon and Yin (1990), which is based on observations of galactic supernovae, we derive a supernova rate of $3 \times 10^{-3} \text{ yr}^{-1}$ for the nuclear region. We derive essentially the same supernova rate using the relation presented by Huang et al. (1994), which is based on observations of supernovae in M 82.

[Fe II] emission is commonly observed in starburst galaxies (Moorwood & Oliva 1988). The emission is much stronger than is typical of a photoionized region, where the Fe^+ abundance is low. The Fe^+ abundance can be enhanced, however, in regions behind moderately fast ($\gtrsim 50 \text{ km s}^{-1}$) shocks, as grains are destroyed and return Fe to the gas phase. The [Fe II] emission from starburst galaxies has therefore been attributed to shocks associated with supernova remnants.

The [Fe II] $1.644\mu\text{m}$ line is blended with Br12 ($1.641\mu\text{m}$) emission and CO(7,4) absorption. To correct for this effect and derive an estimate of the true flux in the $1.644\mu\text{m}$ line, we have obtained a spectrum of an M3 III star (HR 46), which matches the continuum of NGC 6946 reasonably well, and broadened its spectrum by 45 km s^{-1} (see § 2.3.8). Dividing the galaxy spectrum by the HR 46 spectrum smoothed out the absorptions in the continuum and allowed us to measure accurately the line flux. We estimated the Br12 flux to be about $3.0 \times 10^{-15} \text{ erg/s/cm}^2$ using our Br γ measurement and the intensity ratios of Hummer & Storey (1987) and subtracted that value from the blend. The resulting [Fe II] $1.644\mu\text{m}$ flux was corrected to the $3''$ and $8.5''$ apertures using the observed aperture dependence of the Br γ emission. The measured flux of this line can be found in Table 2.3. At 5.5 Mpc, this corresponds to a luminosity of

$3.3 \pm 0.5 \times 10^{38}$ erg/s/cm² (corrected for extinction.) Assuming that the average [Fe II] luminosity of a supernova remnant (SNR) in NGC 6946 is about equal to the 2×10^{36} erg/s/cm² of a galactic SNR (Moorwood and Oliva 1988) and that the luminous phase of the SNR lasts about 2×10^4 years (Condon and Yin 1990), we derive a supernova rate of $8 \pm 1 \times 10^{-3}$ yr⁻¹. Vanzi et al. (1996) have analyzed the supernova rate and [Fe II] emission in M 82. Their relation would indicate a rate of 5×10^{-3} yr⁻¹ for NGC 6946.

We take the supernova rate to be the average of these results and the uncertainty to be large, i.e., $6 \pm 3 \times 10^{-3}$ yr⁻¹ in the central 8".5. This rate is roughly one-third the Galactic rate but for a region only 200 pc across.

2.3.7. Absorption features

The quality of the infrared spectra permits us to study the wealth of stellar absorption features in NGC 6946. The most prominent absorption features in the spectra presented here are the first overtone CO bands starting at $2.3\mu\text{m}$ and to a lesser extent the second overtone CO bands starting at $1.6\mu\text{m}$. Many atomic features are visible as well, with the strongest absorptions attributed to Si, Mg, and Ca. The equivalent widths of the strongest features are listed in Table 2.6.

The continuum spectrum of NGC 6946 is typical of a massive, evolved star. We can quantify this by comparing the strength of the CO and Si absorptions to the grid of stellar spectra of Origlia et al. (1993), in key features such as Si($1.59\mu\text{m}$), CO(6,3)($1.62\mu\text{m}$), and CO(2,0)($2.29\mu\text{m}$). In particular, while the Si feature at $1.59\mu\text{m}$ remains relatively constant throughout the cool stellar types, late supergiants tend to have very strong CO absorptions. The continuum spectrum of NGC 6946 is most consistent with that of an MIII giant or a K5 supergiant, a

not-unexpected result considering the other evidence (large UV flux, luminosity, and supernova rate) that we are viewing NGC 6946 several million years after a burst of star formation.

Cool stars display a steam feature around $1.9\mu\text{m}$, a very broad absorption which is not immediately evident in our spectra. The strength of this feature is quantified via a H_2O index, which we have determined by comparing the continuum near $2.09\mu\text{m}$ and $2.29\mu\text{m}$ (see Kleinmann & Hall 1985). We obtain a H_2O index of 0.07 magnitudes after converting our spectroscopic index to a photometric index.

Similarly, we can measure a CO index to quantify the strength of the CO absorption. Our spectroscopic index is large, 0.35 magnitudes. By comparison with Kleinmann and Hall (1985), a 0.35 magnitude spectroscopic CO index is equivalent to a 0.21 magnitude photometric CO index, and we assign a photometric uncertainty to this quantity of 0.03 magnitudes. We correct the intrinsic CO index of the starburst population to 0.23 magnitudes by assuming that an old stellar population with a CO index of 0.15 magnitudes (typical of an old stellar population—see Frogel et al. 1978) contributes 20% of the observed K-band flux (see § 2.3.4).

2.3.8. Mass

We now estimate the mass of stars formed in the starburst. Since the starburst in NGC 6946 is confined to the nucleus, we can estimate the dynamical mass present in the nucleus of the galaxy to put an upper limit on the mass participating in the starburst. Both an exponential and a $r^{1/4}$ law profile were fit to the K-band image in a least-squares fashion to determine whether the bulge was more likely to be supported by dispersion or rotation. The bulge was better fit (by an order of

magnitude) by an $r^{1/4}$ law profile than an exponential. The azimuthally-averaged disk profile (where we have made no correction for inclination) was well-fit to an exponential with a scale length of $31''.0$, which is about 830 pc at a distance of 5.5 Mpc, and a central brightness of about 2% of the observed peak brightness.

Stellar motions

Once it was determined that the luminosity profile of the bulge was appropriate to a spherical system, we fit the bulge to a $\eta = 3$ model of Tremaine et al. (1994). The model profile was convolved with $1''.2$ of seeing (determined from stars in the K-band image) and fit to the galaxy profile along with the disk profile determined above. The best-fit model has a scale radius of $4''.3$.

We also carefully checked for signs of rotation in the stellar features. Figure 2.7 shows the velocity offsets of the two strongest CO absorptions as a function of position along the slit for 4 position angles. Table 2.8 summarizes the steepness of the Doppler shift in each feature in km s^{-1} per arcsecond, obtained by fitting a straight line to the points inside a $10''$ radius (if that many were available). We examined both the CO(2,0) and the CO(3,1) features. The quoted error bars represent statistical uncertainties only. An indication of the true uncertainty can be obtained from the graphical representation of the measured points as shown in Figure 2.7. The two different filled markers both represent stellar CO features, so the points should match. We find that the stellar features are consistent with a flat curve at every position angle, with at most a rotation of a few km s^{-1} per arcsecond, while the gas shows strong motions at nearly every position angle (see § 2.3.8).

Even in a heavily obscured region like the nucleus of NGC 6946, the velocity dispersion should be well-represented by the broadening of the stellar CO absorption bands at $2.3\mu\text{m}$. We use this stellar feature to measure the dispersion because the gas may be affected by processes that have nothing to do with the gravitational potential (e.g., shocks, winds). We have measured the broadening of the CO feature in NGC 6946 by cross-correlating the galaxy spectrum with a template star spectrum with a similar CO index, as in Shier et al. (1994). The dispersion we obtain in this fashion is $45 \text{ km s}^{-1} \pm 10 \text{ km s}^{-1}$ in the $2''.4 \times 8''$ aperture over which the spectra were extracted. The error bars indicate statistical errors determined via a Monte Carlo simulation and do not include systematic errors. From numerous tests with a suite of template stars, however, the systematic uncertainties are likely be of similar magnitude to the statistical errors at this dispersion (Shier 1995, private communication), so we simply combine the two errors in quadrature for a total error of 14 km s^{-1} . We derive the same velocity dispersion if we use the measurements along the minor axis of the galaxy (which are of higher signal-to-noise and spectral resolution). These measurements agree with an independent analysis of the data by H.-W. Rix, who obtained 53 km s^{-1} .

The mass estimate was obtained by assuming that the nuclear mass is distributed similarly to the K band light and integrating the model profile we fit over the rectangular aperture of the slit (see Shier et al. (1994)). At a radius of $4''.25$, the enclosed mass in this model is $1.2^{+0.9}_{-0.6} \times 10^8 M_{\odot}$, where the error bars are due to the uncertainty in the velocity dispersion. The mass estimate is insensitive to changes in r_s and η ; the uncertainties are dominated by the uncertainty in the velocity dispersion. The mass estimate scales linearly with the distance to NGC 6946 and with the square of the velocity dispersion.

Gas motions

Since our infrared spectra were not sensitive to the low surface brightness regions outside the galaxy nucleus, we obtained optical spectroscopy to supplement our velocity gradient measurements outside the nuclear region. In Figure 2.8 we plot velocity gradients of $H\beta$ and $[O\ III]$ along three position angles. The velocity curves rise somewhat more steeply in the outer regions of the linear part of the velocity curve ($\sim 3''$ - $8''$ in radius) than the infrared data would indicate, probably due to the smaller pixel scale ($0.8''$ per pixel vs. $1.2''$ per pixel) of the optical spectrograph. The velocity curve flattens in the central $5''$, a behavior not observed in the infrared data. This likely indicates that the optical data are affected by the strong extinction towards the nucleus of NGC 6946, with the higher-velocity gas buried behind obscuring dust.

In Figure 2.9 we present position-velocity maps of H_2 and $Br\gamma$. Points fitted at every pixel along the slit are plotted in Figure 2.7, while the slope of each line in km s^{-1} per arcsecond as determined by a linear fit to the data points within $10''$ radius is listed in Table 2.8. One striking result is that not only are the gas motions not consistent with the flat curves measured for the stellar features, the motions derived from lines of $Br\gamma$ (from ionized gas) and H_2 (from molecular gas) are not even consistent with each other. We interpret this as evidence that the gas in the nuclear region of NGC 6946 is not a good tracer of the gravitation potential but may instead be affected by processes such as infall. In particular, while $Br\gamma$ at position angles of 0° and 120° (these position angles are each 30° from the minor axis of NGC 6946) and H_2 at position angle 120° show no evidence of motion, the H_2 at 0° shows strong motion along the slit. We may be seeing some indication of the gas infall along the spiral arms observed by Ishizuki et al. (1990).

Ratio of dynamical mass to H_2 mass

Some of the mass participating in the starburst must be in the form of molecular gas out of which stars are being made. Ishizuki et al. (1990) estimate that there is $\sim 3 \pm 1.5 \times 10^8 M_\odot$ of H_2 within a $5''.6$ radius of the nucleus of NGC 6946. We correct this value to our $4''.25$ aperture by scaling by the change in disk area. This procedure may tend to underestimate the amount of molecular gas in the nucleus both because the observations show that the CO emission is strongly peaked towards the center and because any gas disk in the center is probably inclined with respect to our line of sight, but the uncertainty in the CO to H_2 conversion probably dominates any error made in this manner. Using the standard conversion, we estimate that there is $1.7 \pm 0.9 \times 10^8 M_\odot$ of molecular gas within a $4''.25$ radius of the nucleus. Although this result suggests that the ratio of molecular gas mass to dynamical mass in our $8''.5$ aperture is very large, it is also likely that the conversion factor from CO to H_2 is smaller than the standard (e.g., Maloney & Black 1988).

Mass budget

As a conservative upper limit to the dynamical mass, we take our 2σ limit of $3 \times 10^8 M_\odot$. We allocate some of this mass to the preexisting nuclear population and some to molecular gas currently in the nucleus as described below, leaving the remainder of the mass available as stars in the burst.

McLeod et al. (1993) make a rough argument that the gas funneling into the nucleus of a galaxy could not exceed half the dynamical mass without triggering the starburst. Bekki (1995) reports smoothed hydrodynamical calculations that

suggest dynamical instabilities and probable triggering of a starburst may occur when the gas exceeds $\sim 20\%$ of the total mass in a strongly perturbed system, so McLeod et al. probably overestimated the portion of material that can take part in the starburst by a factor of ~ 2 . The threshold may be as low as 10% in non-interacting systems (e.g., Wade & Habe 1992). We therefore assume that $\sim 80\%$ of the dynamical mass, or $2.4 \times 10^8 M_{\odot}$, is tied up in old stars in an underlying nuclear population.

The remaining $6 \times 10^7 M_{\odot}$ we allocate to the molecular gas that fueled the starburst; some went into making stars in the burst while the rest remains as the molecular gas measured today. Even given a $N(H_2)/I_{CO}$ conversion factor that is too large by a factor of 5, it is likely that half of this mass is still in the form of molecular gas; that is, no more than $3 \times 10^7 M_{\odot}$ of stars could have formed in the burst. Given that many of the starburst parameters we have derived here are conservative limits, we favor starburst models sufficiently efficient in their use of mass that they fall well below this upper limit.

2.4. Models

We have compiled the relevant observational constraints in Table 2.9. We turn now to modeling the starburst. We make use of the models of Rieke et al. 1993 (RLRT93 hereafter), which we describe briefly below.

2.4.1. M 82 models

RLRT93 modeled the starburst in M 82 using the models of Rieke et al. 1980 with updated stellar tracks and atmospheric parameters. The starburst model uses the grid of stellar evolution tracks of Maeder (1992), which have been assigned

observational parameters based on a combination of atmosphere models and empirical calibration. The starburst models use the evolutionary tracks over a range of stellar masses up to $80 M_{\odot}$ and interpolate between the tracks to reduce oscillations caused by discreteness in the stellar masses. The models form stars over a short gaussian burst (FWHM of 5 million years), with the number of stars in each bin determined by the IMF. The observational parameters are predicted as the stars evolve along theoretical tracks. Further details can be found in RLRT93.

2.4.2. NGC 6946 models

For NGC 6946, the model values of N_{LyC} , L_{Bol} , CO index, and K-band flux are displayed as a function of time in Figure 2.10. Each point along the curves presented has been divided by the observed values for NGC 6946 in Table 2.9, so the target value for each quantity is 1. A fit can be considered good when all curves meet the target value simultaneously. In practice, since some of the observational parameters are uncertain, we choose the point on the plot where the curves come closest to meeting the target values simultaneously.

We have attempted to match the parameters of NGC 6946 with a series of starburst models with different IMF's and SFR's. The results are displayed in Figure 2.10. We have shown results of fits to two different IMF's. The local IMF, represented by IMF 3 of RLRT93, requires a lot of mass ($3.3 \times 10^7 M_{\odot}$) in a single burst (model A) to meet the required K magnitude and N_{LyC} , but the bolometric luminosity predicted by the model is a factor of 1.7 greater than observed. A better fit can be achieved with a double burst, but this requires over $6 \times 10^7 M_{\odot}$ of stars to meet the constraints. Due to the large mass required, we consider these models unlikely to be compatible with the observations.

The IMF found by RLRT93 to fit the M82 observations best (their IMF 8), provides a considerably better fit to the observations. This model is very efficient with mass, so that only $1.1 \times 10^7 M_{\odot}$ are required in a single burst to produce the observed K flux. The single burst model, though, produces too much bolometric luminosity in the region where the other constraints fit, so we have modeled a double burst in panel C. This double burst uses a total of $1.9 \times 10^7 M_{\odot}$, with the bursts separated by 20 million years and the second burst 20% as strong as the first. A reasonable fit is achieved at 32 million years, and here the bolometric luminosity is within 30% of the target value. The supernova rate, which has not been plotted here, is also reasonably consistent with the observations.

The main constraint that excludes models using local IMF's or longer SFR's is the upper limit on the mass. If we lift this constraint and allow the models to use a larger fraction of the dynamical mass, a burst model with an IMF biased towards massive stars is no longer required to fit the observations. For example, the double-burst, local-type IMF model described above is a reasonable fit to the observations, aside from the mass constraint.

Without the mass constraint, we can also fit models with star formation extended over a longer period of time. Models which form stars for tens of millions of years and then turn off can also match the observations, although they require most of the dynamical mass in the nucleus. One such model is shown in panel D. This model formed stars at a rate of $0.56 M_{\odot}$ per year for 1.8×10^8 years using IMF 3. After the star formation shut off, N_{LyC} and L_{Bol} dropped enough to be compatible with the observations. This model consumed $10^8 M_{\odot}$ of stars. Models such as these can reasonably fit the observations (except for the mass constraint), but the star formation rate could not be maintained for more than a 100 million

years or so.

It seems clear that the high rate of star formation in the nucleus of NGC 6946 must be episodic in nature rather than continuous throughout the lifetime of the galaxy. This conclusion is independent of our assumptions about the triggering of a very short burst of star formation, which presumably can only consume a small fraction of the dynamical mass in the nucleus.

If we assume that the nuclear mass is dominated by an old stellar population rather than being largely composed of new stars, our models demonstrate that a short burst of star formation with an IMF biased towards massive stars is required to match the observations of NGC 6946. Our models make use of most or all the mass we believe is available for star formation, and as such they only just meet the target K-band luminosity. Were we to spread the star formation over time, there would never be enough red supergiants (which produce most of the K-band luminosity) at any given time to meet the target luminosity. The nature of the star formation (i.e., the fact that it occurs in a burst) tightly constrains the age of the burst in the following way. The burst produces many massive stars, which produce most of the UV flux and luminosity. As these stars evolve into red supergiants, both the K-band luminosity and CO index of the population increase while the UV flux and total luminosity decrease rapidly. Given the requirement that the UV flux, bolometric luminosity, K-band luminosity, and CO index should all be quite large at the same time, the time since the last significant burst of star formation must be (within 10% or so) 7 million years, independent of which IMF we examine.

2.4.3. Problems with local IMFs

It should be noted that our distance estimate has been conservative—several of the distance estimates to NGC 6946 are close to 10 Mpc. As we noted in § 2.3.8, the mass estimate scales linearly with the distance. The requirements for the starburst model, however, depend on luminosities and hence on the square of the distance. Putting NGC 6946 at 10 Mpc would tighten the constraints and make it even more difficult to fit a local IMF to the observations.

In addition, we have ignored the absorption of Ly α photons by dust, therefore reducing the requirements on the starburst models. The SFR we have chosen also makes the most efficient use of the available mass. The models presented here are therefore highly forgiving in fitting a given IMF. More realistic models would make it more difficult to fit a local IMF to the observations.

2.5. Other results

2.5.1. Fe emission

We have examined our spectra for other [Fe II] emission lines that might be used to constrain the density in the emitting region. The measured fluxes or upper limits of these lines are presented in Table 2.3. Nussbaumer & Storey (1988) calculate that the ratio of [Fe II] 1.257 μ m to [Fe II] 1.533 μ m should be a strong function of density and plot the ratio of 1.533 μ m to 1.257 μ m for a range of densities from 10 cm^{-3} to 10^8 cm^{-3} . We do not directly observe the 1.533 μ m line in our spectra, but we can place an upper limit on it of $\sim 10^{-15}\text{ erg/s/cm}^2$, or an emissivity of about 6% of the 1.257 μ m line. This limit implies a density in the emitting region of $\lesssim 2 \times 10^3\text{ cm}^{-3}$. The complicated continuum structure in the vicinity of the

1.533 μm line makes the upper limit uncertain, so we examine other [Fe II] lines to place additional constraints on the density.

There are many [Fe II] lines in the J band in addition to the 1.257 μm line. We can place upper limits on the 1.321 μm and 1.328 μm lines of 6% of the strength of the 1.257 μm line. We have calculated the ratio 1.328 μm /1.294 μm = 0.61 using the A -values of Nussbaumer & Storey (1988). This implies an upper limit for 1.294 μm /1.257 μm of ~ 0.1 . Using the results of Hudgins, Herter & Joyce (1990), who calculate the density dependence of the 1.294 μm /1.257 μm ratio, this limit implies an upper limit to the density of $\lesssim 4 \times 10^3 \text{ cm}^{-3}$. The strength of the 1.328 μm line is thus consistent with our low density estimate derived from the upper limit on the 1.533 μm line.

Our failure to detect the 1.321 μm line is puzzling. This line comes from the same upper state as the 1.257 μm line, so the ratio of 1.321 μm to 1.257 μm is predicted by the A -values to be 0.26. Our measured upper limit, though, puts the ratio at ~ 0.06 . At this time, we have no explanation for this anomaly unless the line falls in an absorption in the continuum spectrum.

2.5.2. Molecular Hydrogen

In many starburst galaxies, molecular hydrogen appears to be excited collisionally in regions with kinetic temperatures $T_K \gtrsim 1000 \text{ K}$. Such kinetic temperatures are typically associated with moderate velocity shocks, ($V_s \approx 40 - 50 \text{ km s}^{-1}$; Draine & Roberge 1982; Hollenbach & Shull 1977). To investigate the source of the H_2 excitation in NGC 6946, we have compiled a list of observed H_2 line ratios in Table 2.5 and compared them to the models of Black and van Dishoeck (1987). The fluorescent line ratios were taken from their model 14 while the thermal line

ratios were taken from their model S2. The H_2 emission from NGC 6946 is clearly more consistent with the Black & van Dishoeck collisional excitation model; we can place an upper limit of $\sim 15\%$ to any optically thin fluorescent component of the 1-0 S(1) line. If fluorescence plays a significant role, the emitting gas must be at high density as modeled by Sternberg and Dalgarno (1989). The importance of thermal excitation is supported indirectly by the differing velocity pattern we see in the H_2 and $\text{Br}\gamma$ lines, indicating that the UV source and H_2 emission are not closely connected spatially.

2.6. Conclusions

We have used new infrared data and data from the literature to derive a number of properties of the nuclear starburst in NGC 6946. These include N_{LyC} , L_{Bol} , absolute magnitudes in the J, H and K bands, CO index, SNR, and the mass of stars formed in the starburst. The data were compared to starburst models to determine the age of the starburst and to put constraints on the IMF. We have taken into account the properties of a preexisting nuclear population which must underly the starburst. In deriving the starburst parameters, we have tried to be conservative in such a way that it becomes easier for a given IMF to fit the data.

We have compared our NGC 6946 data to starburst models with varying IMF's and single or double bursts of star formation. A burst of star formation converting $4 \times 10^6 M_{\odot}$ into stars occurring 7 million years ago combined with a previous burst of $1.5 \times 10^7 M_{\odot}$ 20 million years before are sufficient to account for the properties of the starburst in the nucleus of NGC 6946 if the IMF is similar to that fit to M 82 by RLRT93. It is difficult to explain the observations with an IMF consistent with the local neighborhood; although the case for an IMF biased

towards high masses is weaker than in the well-studied case of M82, such a bias seems likely for NGC 6946 also.

If the nuclear mass is dominated by an old stellar population, the current SFR is constrained to be a decaying burst because the limited mass available must create enough stars to produce a large K-band luminosity and a SFR with a weak time dependence never produces enough stars at a given time to meet the luminosity requirement. Regardless of the IMF we examined, the age of the burst is determined by the requirement that the starburst model simultaneously produce a large UV flux and bolometric luminosity, both of which weaken rapidly after vigorous star formation ceases, and a large CO index and K-band luminosity, which are initially weak and only become strong after the massive stars evolve into red supergiants.

We have done a detailed kinematic study of the gas and stars in the nucleus of NGC 6946. It seems clear that the processes affecting each component are different. While the stellar component shows no significant rotation and seems to be dominated by dispersion, the gas shows considerable velocity gradients across small regions of the nucleus. In particular, while the molecular gas traced by H_2 emission in our spectra seems to follow the molecular gas traced by CO emission in the radio, the ionized component we observe in $\text{Br}\gamma$ shows kinematics significantly different from both the stars and the molecular gas. We suggest that in a complicated starburst region such as the nucleus of NGC 6946, it may be inappropriate to use gas as a tracer of the gravitational potential.

We have observed several transitions of $[\text{Fe II}]$ and H_2 . The former species appears to be excited in low density regions ($\lesssim 4 \times 10^3 \text{ cm}^{-3}$). The relative H_2 line strengths are inconsistent with excitation via fluorescence at moderate densities.

The emission is consistent with the thermal models of Black & van Dishoeck (1987) or with the high-density, strong UV-field models of Sternberg & Dalgarno (1989). Some of the H_2 appears to be participating in a high velocity flow into or out of the nucleus that is not shared by the ionized component of the gas.

Table 2.1. Aperture Photometry of NGC 6946 at J, H and K

Aperture(")	This Paper			Aaronson 1977		
	$J - H$	$H - K$	m_K	$J - H$	$H - K$	m_K
3	0.86	0.55	10.66
8.5	1.02	0.47	9.44
27.4	0.96	0.39	8.62	0.96	0.39	8.62
41.1	0.92	0.39	8.29	0.94	0.37	8.29
105	0.75	0.46	7.49	0.96	0.34	7.22

Note. — The photometry presented here and the Aaronson (1977) photometry were set equal in the 27".4 aperture

Table 2.2. Hydrogen Recombination Line Measurements

Line	$\lambda(\mu\text{m})$	Flux (erg/s/cm^2)	Beam ($''$)	Source
Pa β	1.282	$3.0 \pm 0.4 \times 10^{-14}$	3.0	spectra
Pa γ	1.094	$1.0 \pm 0.1 \times 10^{-14}$	3.0	spectra
Br α	4.051	$2.3 \pm 0.2 \times 10^{-13}$	7.2	Ho et al.(1990)
Br γ	2.166	$7.9 \pm 0.8 \times 10^{-14}$	7.2	Ho et al.(1990)
Br γ	2.166	$2.9 \pm 0.3 \times 10^{-14}$	8.5	NB image
Br γ	2.166	$2.6 \pm 0.3 \times 10^{-14}$	7.2	NB image
Br γ	2.166	$2.3 \pm 0.2 \times 10^{-14}$	5.9	NB image
Br γ	2.166	$1.3 \pm 0.1 \times 10^{-14}$	3.0	NB image
Br γ	2.166	$1.7 \pm 0.2 \times 10^{-14}$	2.4 \times 8.5	NB image
Br γ	2.166	$1.5 \pm 0.2 \times 10^{-14}$	2.4 \times 8.5(ew)	spectra
Br γ	2.166	$1.8 \pm 0.2 \times 10^{-14}$	2.4 \times 8.5(ns)	spectra
Br10	1.736	$3.4 \pm 1.0 \times 10^{-15}$	2.4 \times 8.5(ew)	spectra
Br11	1.681	$3.7 \pm 1.5 \times 10^{-15}$	2.4 \times 8.5(ew)	spectra
Br13	1.611	$3.4 \pm 1.1 \times 10^{-15}$	2.4 \times 8.5(ew)	spectra

Note. — Br12 was not measured because it is blended with the 1.644 μm [Fe II] line.

Table 2.3. [FeII] Emission

$\lambda(\mu\text{m})$	Flux (erg/s/cm ²)	Beam(")
1.257	$1.7 \pm 0.2 \times 10^{-14}$	3.0
1.321	$< 10^{-15}$	3.0
1.328	$< 10^{-15}$	3.0
1.533	$< 10^{-15}$	2.4×8.5 slit
1.599	?	2.4×8.5 slit ^c
1.644	$2.7 \pm 0.4 \times 10^{-14}$	2.4×8.5 slit ^a
1.644	$2.1 \pm 0.3 \times 10^{-14}$	3.0 ^{a,b}
1.644	$4.6 \pm 0.7 \times 10^{-14}$	8.5 ^{a,b}
1.677	$2.1 \pm 2.0 \times 10^{-15}$	2.4×8.5 slit

^aThe flux in this line has been corrected for stellar absorption and hydrogen emission as described in the text

^bThe corrections to these apertures have been determined by assuming that the [Fe II] emission is distributed similarly to Br γ .

^cThis value is uncertain because the line is completely blended with ¹²CO(5,2).

Table 2.4. He emission line strengths

$\lambda(\mu\text{m})$	Flux (erg/s/cm ²)
1.083	$2.0 \pm 0.3 \times 10^{-14}$
2.058	$2.2 \pm 0.9 \times 10^{-15}$

Table 2.5. H₂ Line Strength Relative to H₂(1,0)S(1)

Transition	$\lambda(\mu\text{m})$	Observed Ratio	Pure Fluorescence	Thermal
(5,3)Q(1)	1.493	<0.08	0.43	1×10^{-4}
(4,2)O(3)	1.510	<0.08	0.42	7×10^{-4}
(6,4)Q(1)	1.601	<0.08	0.33	1×10^{-5}
(5,3)O(3)	1.613	<0.08	0.38	9×10^{-5}
(6,4)O(3)	1.732	<0.08	0.31	1×10^{-5}
(1,0)S(2)	2.033	0.17 ± 0.04	0.50	0.37
(2,1)S(3)	2.073	~ 0.08	0.35	0.08
(1,0)S(1)	2.121	1.00	1.00	1.00
(2,1)S(2)	2.154	<0.08	0.28	0.03
(1,0)S(0)	2.223	0.20	0.46	0.21
(2,1)S(1)	2.247	~ 0.08	0.56	0.08

Note. — H₂(1,0)S(1) flux: $1.2 \pm 0.1 \times 10^{-14}$ erg/s/cm²

Table 2.6. Absorption Features

Species	$\lambda(\mu\text{m})$	$W_\lambda (\text{\AA})$
MgI	1.504	6.0
$^{12}\text{CO}(3,0)$	1.559	4.5
$^{12}\text{CO}(4,1)$	1.578	6.7
FeI	1.583	3.3
SiI	1.590	3.7
$^{12}\text{CO}(6,3)$	1.620	5.5
$^{12}\text{CO}(8,5)$	1.663	3.1
FeI	2.070	1.8
MgI	2.107	1.9
AlI	2.117	1.4
TiI	2.179	2.3
NaI	2.207	8.2
FeI	2.227	4.4
CaI	2.263	4.1
CaI	2.266	3.2
$^{12}\text{CO}(2,0)$	2.296	14.6
$^{12}\text{CO}(3,1)$	2.325	17.0
$^{13}\text{CO}(2,0)$	2.346	13.3
$^{12}\text{CO}(4,2)$	2.352	15.7
$^{13}\text{CO}(3,1)$	2.374	19.5

Table 2.7. Line Ratios with Reddening

Line Ratio	Predicted ^a value	Reddened ^b value	Observed value
$\text{Pa}\beta/\text{Pa}\gamma$	1.86	2.5	3.0 ± 0.5
$\text{Br}\gamma/\text{Pa}\beta$	0.18	0.33	0.4 ± 0.07
$\text{Br}\gamma/\text{Br}10$	3.14	3.7	5.0 ± 1.6
$\text{Br}\gamma/\text{Br}11$	4.42	5.4	4.6 ± 1.9
$\text{Br}\gamma/\text{Br}13$	7.08	9.1	5.0 ± 1.7
$[\text{Fe II}] \frac{\lambda 1.644 \mu\text{m}}{\lambda 1.257 \mu\text{m}}$	0.74	1.0	1.2 ± 0.2

^aFrom Storey & Hummer (1987) for H, assuming $T_e = 5000$ K and $N_e = 100 \text{ cm}^{-3}$; using transition probabilities from Nussbaumer & Storey (1988) for [Fe II].

^bThese line ratios were reddened with the extinction derived in § 2.3.2.

Table 2.8. Velocity gradients of spectral features ($\text{km s}^{-1}/''$)

Feature	PA=0°	PA=30°	PA=60°	PA=90°	PA=120°
Br γ	4.6 ± 2.8	29.8 ± 1.7	21.3 ± 1.0	10.1 ± 1.7	0.4 ± 1.1
H ₂ (1,0)S(1)	20.8 ± 2.5	18.8 ± 0.8	15.2 ± 0.5	9.7 ± 1.3	1.1 ± 0.9
CO(2,0)	...	-1.8 ± 2.7	-1.2 ± 2.0	-0.4 ± 5.3	-9.2 ± 2.2
CO(3,1)	...	-13.8 ± 6.0	-1.3 ± 2.4	-9.0 ± 3.0	-5.0 ± 3.1

Table 2.9. Summary of starburst parameters

Parameter	value
Distance	5.5 Mpc
Mass ^a	$< 6 \times 10^7 M_{\odot}$
L_{BOL}	$2.2 \times 10^9 L_{\odot}$
M_K	< -19.5
$\log N_{LyC}$	> 52
SNR	$6 \pm 3 \times 10^{-3} \text{ yr}^{-1}$
CO	$0.23 \pm .03$

^aThis mass limit includes both molecular gas and stars actually formed in the burst.

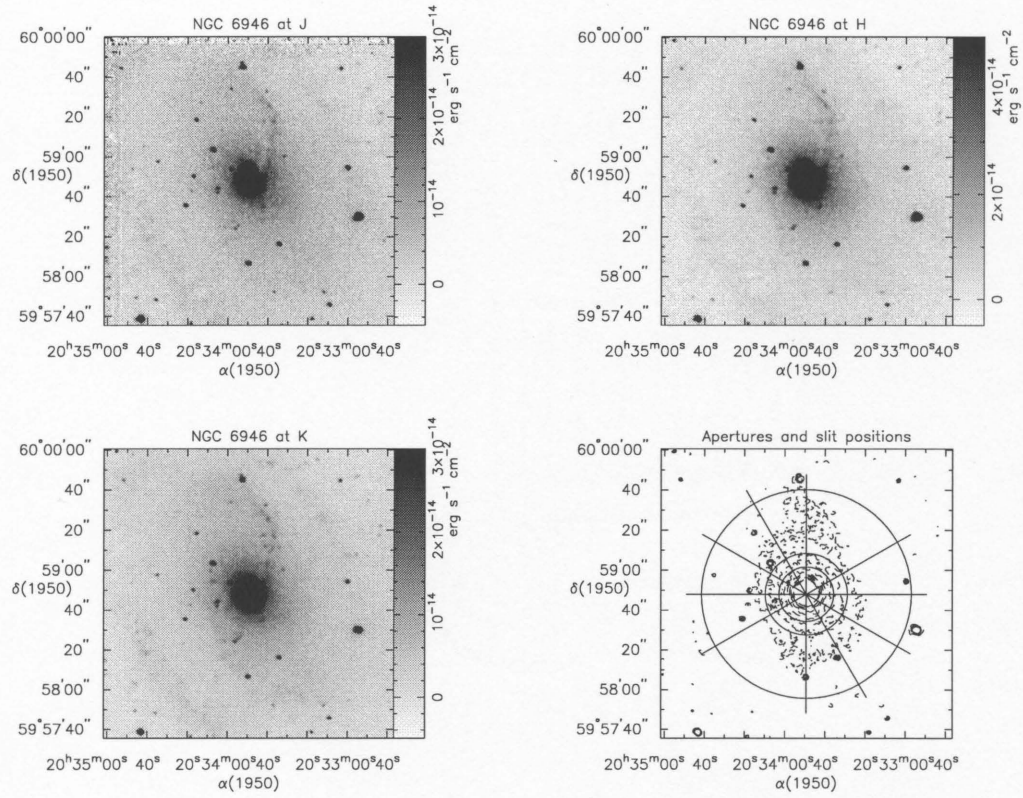


Figure 2.1 Greyscale images of NGC 6946 at J (top left), H (top right), and Ks (bottom left), plus a contour map at Ks (bottom right) overlaid with the slit positions and photometry apertures. The straight lines in the last panel indicate the length and positions of the slit, which was $2''.4$ wide.

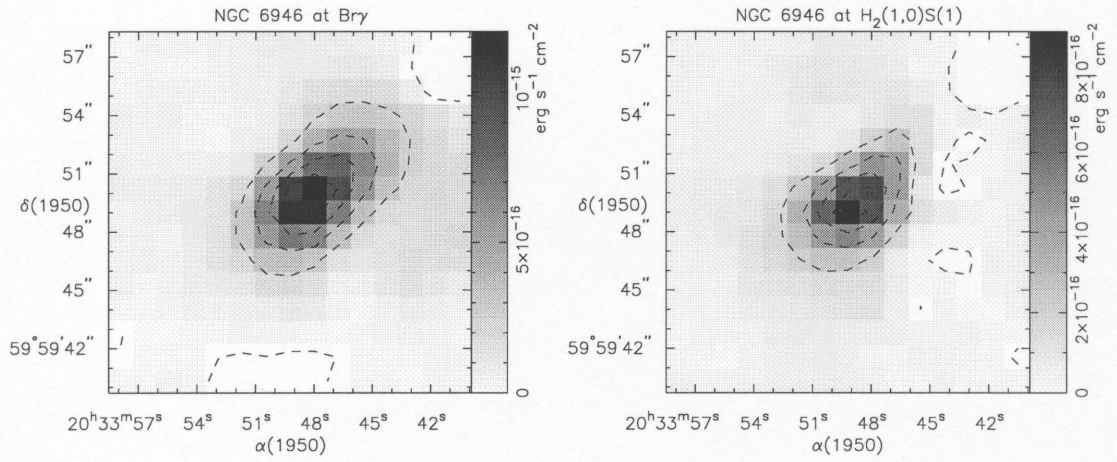


Figure 2.2 Greyscale and contour plots of the central 10'' of NGC 6946 in narrowband filters tuned to H $_2$ (2.121 μ m), displayed on the right, and Br γ (2.166 μ m), displayed on the left.

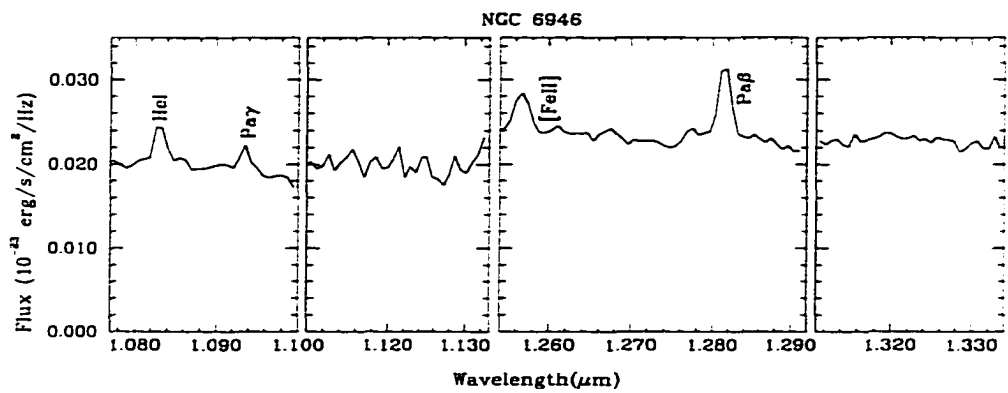


Figure 2.3 Flux-calibrated spectrum of NGC 6946 at J in a 3'' aperture centered on the nucleus.

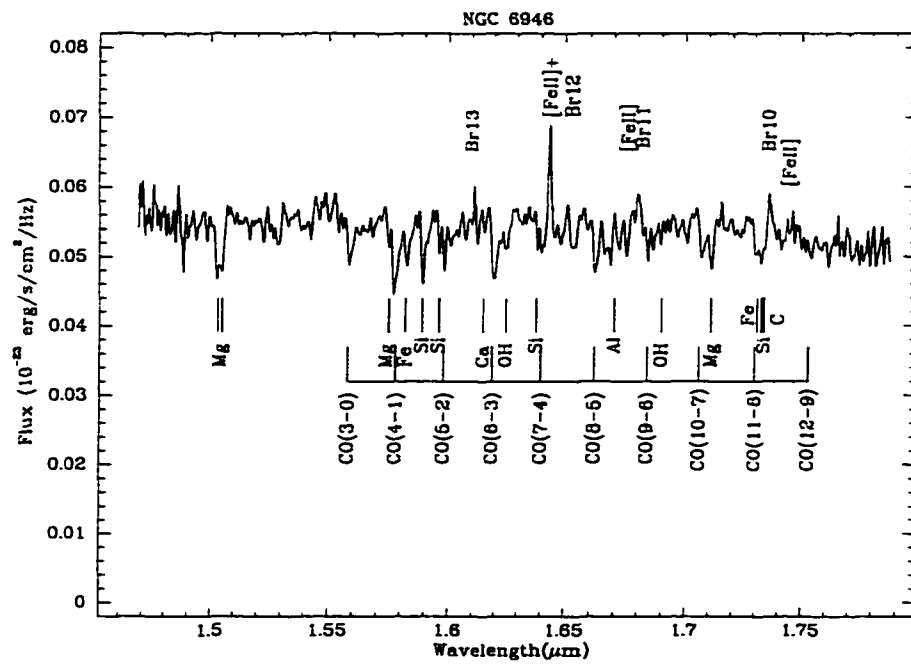


Figure 2.4 Flux-calibrated spectrum of NGC 6946 at H; the slit is oriented E/W, is 2".4 wide, and the spectrum is 12" along the slit.

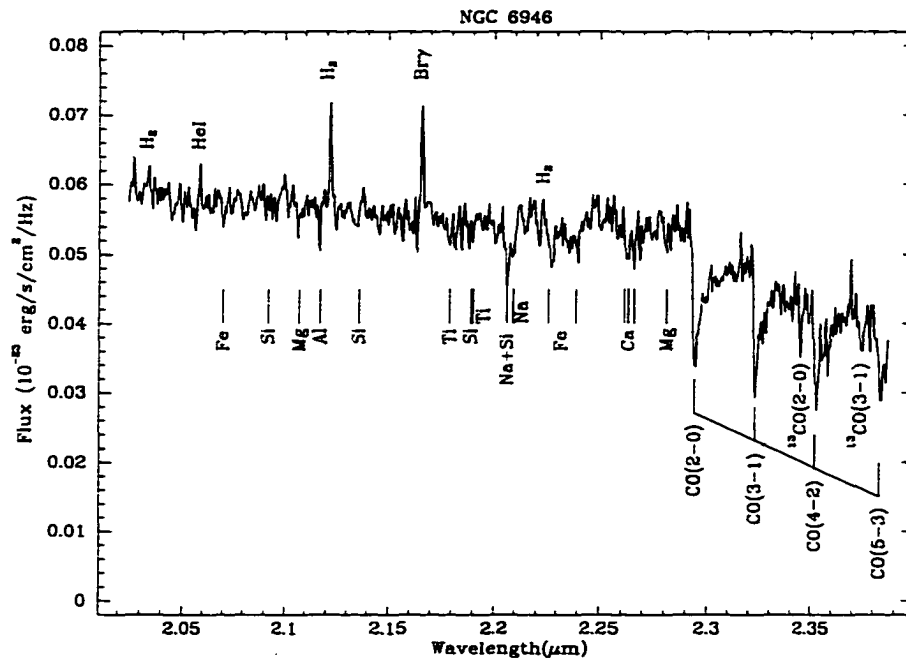


Figure 2.5 Flux-calibrated spectrum of NGC 6946 at K. Details as for the H-band spectrum.

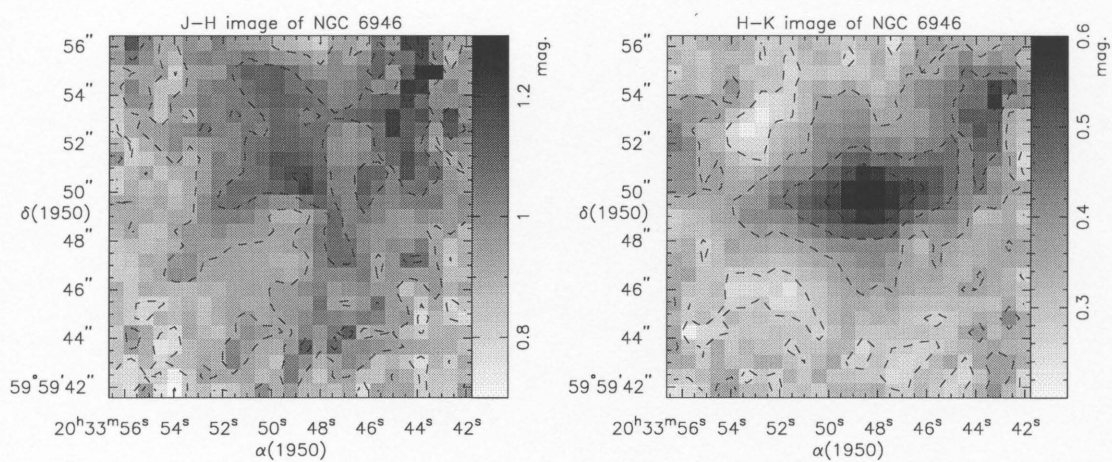


Figure 2.6 J-H and H-K color maps of the nuclear region. J-H is on the left and H-K is on the right. Both images are centered on the K-band emission peak.

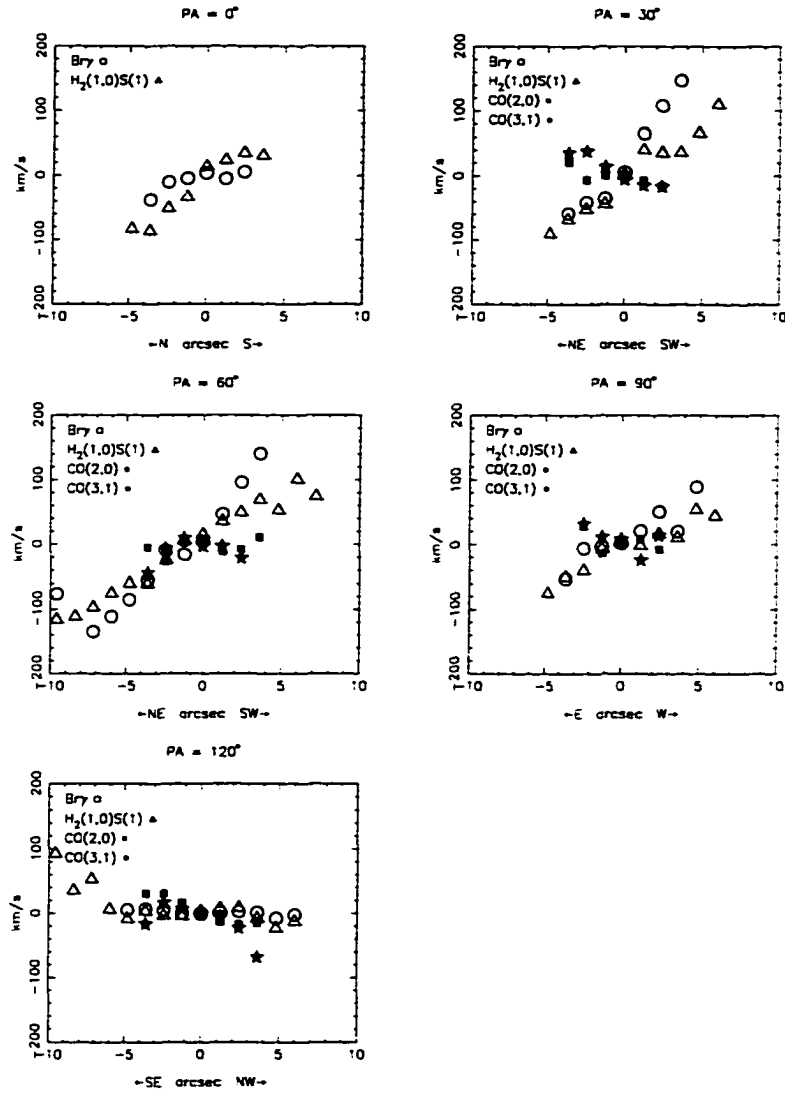


Figure 2.7 Plots of the velocity centroid offsets of stellar CO, Br γ , and H $_2$ at five position angles. The filled points are the stellar features while the open markers trace gaseous features.

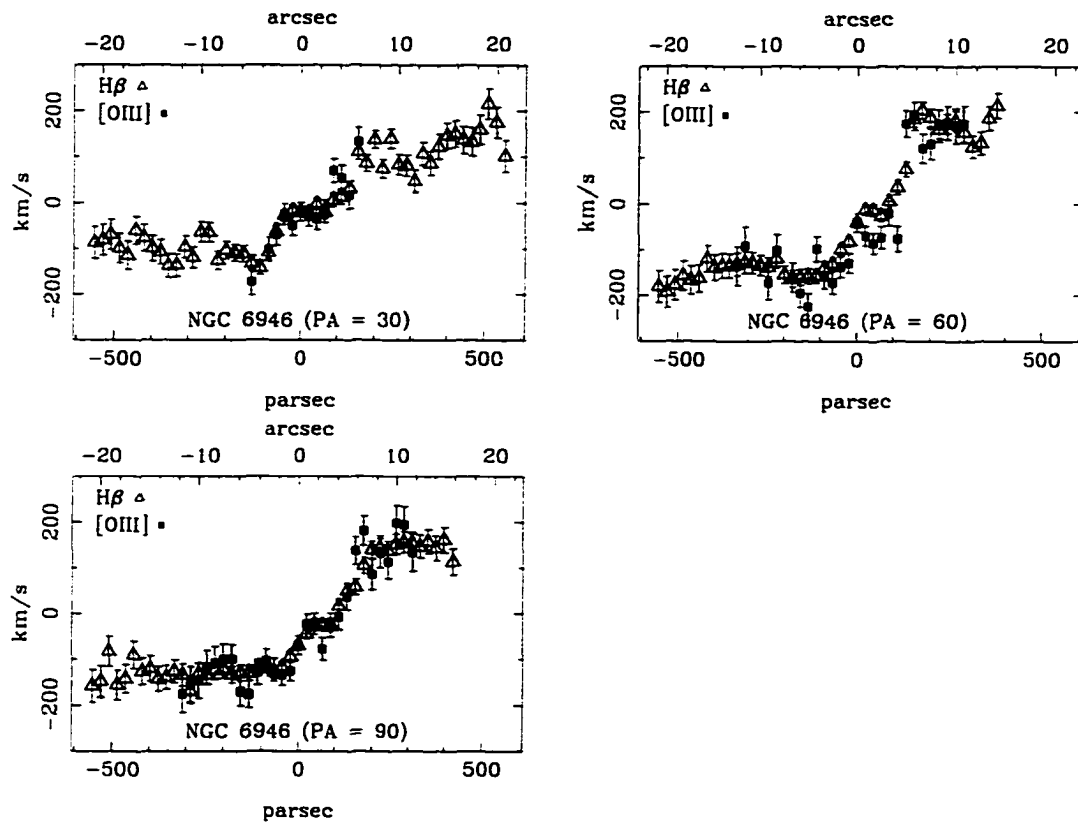


Figure 2.8 Velocity gradient plots of two strong optical emission lines in NGC 6946 at three position angles. The open triangles trace $H\beta$ while the filled squares trace $[O III]$.

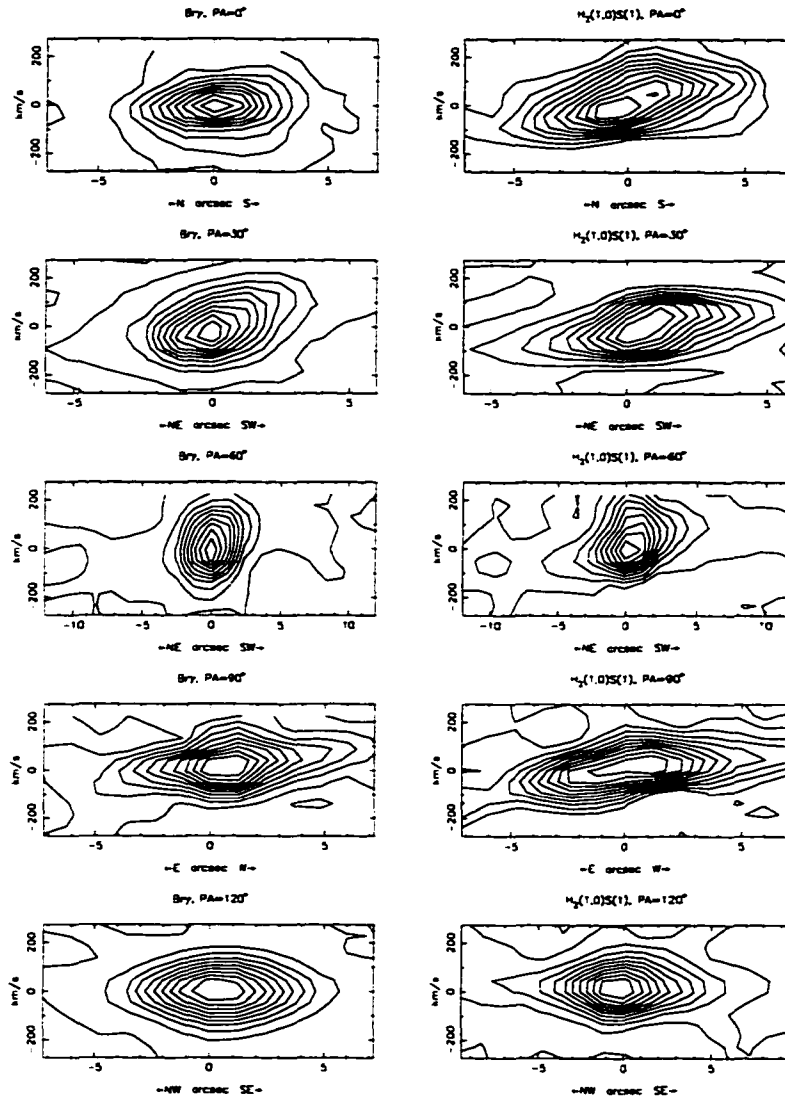


Figure 2.9 Position-velocity plots of two strong emission lines in our longslit spectra of NGC 6946. The spatial axis is centered on the stellar continuum peak while the velocity axis is centered on the intensity peak of the spectral line.

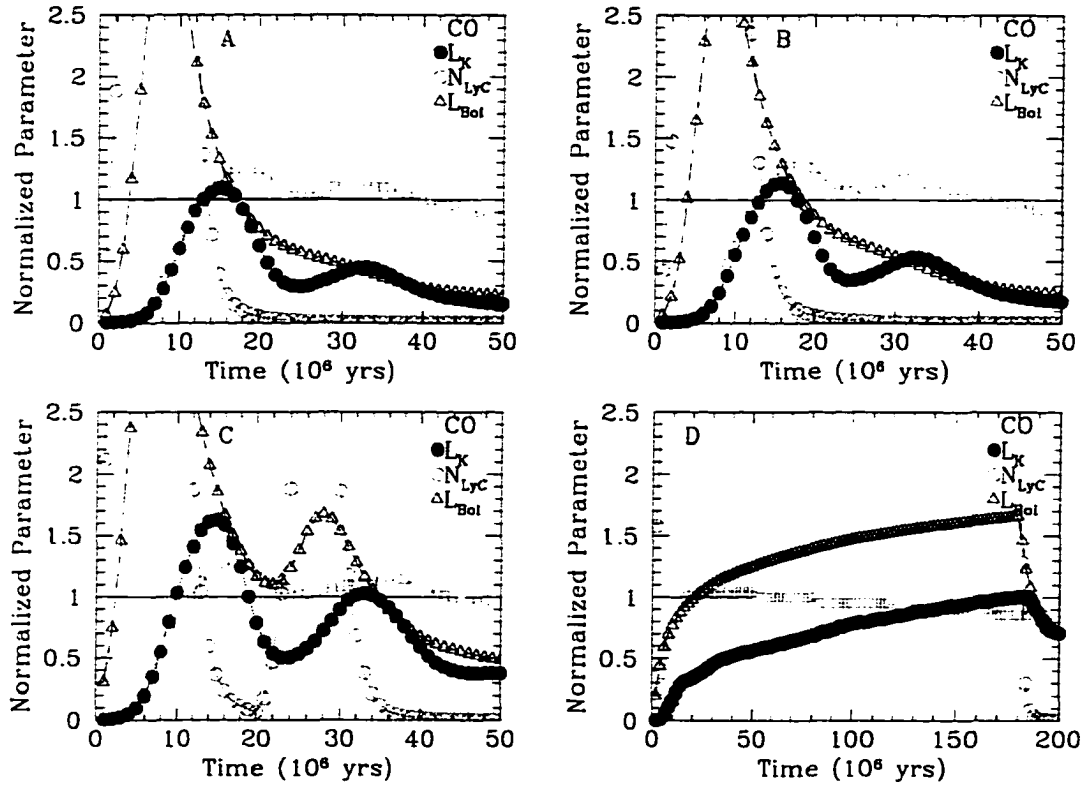


Figure 2.10 Starburst models of NGC 6946 with IMF's and SFR's as described in the text. Models A and B are single-burst models using 3.3 and $1.1 \times 10^7 M_{\odot}$, respectively. Model C uses a double burst with the same IMF as B and a mass in both bursts of $1.9 \times 10^7 M_{\odot}$. Model D forms stars at $0.56 M_{\odot}$ per year until 1.8×10^8 yr, at which time star formation ceases.

CHAPTER 3

THE NUCLEAR STARBURST IN NGC 253

We present high-resolution ($R \sim 3000$), long-slit spectroscopic observations of the nucleus of NGC 253 from $1.25\mu\text{m}$ to $2.43\mu\text{m}$ and at $10\mu\text{m}$, as well as moderate resolution ($R \sim 1200$) spectra which extend our near-infrared spectral coverage to $1.15\mu\text{m}$ and to $2.45\mu\text{m}$. We have also obtained deep broadband imaging of NGC 253 in the J, H, and Ks bands as well as narrowband imaging in Br γ and the (1,0)S(1) line of H₂. We have assembled a composite stellar spectrum and subtracted it from that of NGC 253 to allow us to obtain accurate measurements of faint near-infrared emission lines free from the spectral structure due to stellar absorptions.

We find that both the level of [Fe II] emission and the density in the [Fe II]-emitting region support the origin of this line in supernova remnants. Although the H₂ line ratios suggest superficially that the emission is thermally excited, at the high signal to noise of our spectra we find that roughly two thirds

of the H_2 luminosity is due to UV fluorescence. It is likely that the modest signal to noise near infrared spectra of many other starburst galaxies have failed to detect substantial luminosities in fluorescently excited H_2 . From the mid-infrared fine structure lines of [Ne II] and [S IV], we estimate the temperature of the stars photoionizing the gas in NGC 253 to be $\sim 35500 \pm 1000K$. We also use an upper limit to HeI(1.7)/Br10 to place an independent upper limit on the stellar temperature of $\sim 37,000K$.

The optical line ratios in NGC 253 indicate it is a weak-[OI] LINER and they are fitted well by the hot-star ($T \sim 45,000K$) photoionization models proposed for this type of active galaxy by Filippenko & Terlevich (1992). However, the three independent stellar temperature determinations from our work and that of Carral et al. (1994) are inconsistent with the hot star model. The line ratios can also be fitted by a combination of two components that are consistent with our data. The first, which accounts for the H recombination lines and most of the forbidden optical lines, is a photoionization model for metal rich HII regions, assuming solar metallicity and an effective stellar temperature of $\sim 38,000K$ (Shields & Kennicutt 1995). The second, which accounts for the [OI] and [FeII] emission, is shocks in supernovae occurring at the rate required from our starburst models for NGC 253. These components fit NGC 253 with virtually no adjustment of free parameters. We suggest that many weak-[OI] LINERs can be explained in the same manner, rather than by the presence of a mini-AGN or by very hot stars.

We have used the infrared data to derive extinction-independent estimates of the primary boundary conditions for starburst models of NGC 253: mass, N_{LyC} , maximum stellar temperature, bolometric luminosity, and CO absorption depth. We find that a variety of starburst models can fit these constraints. All

the successful models require a starburst age of 5 to 15 million years. Although local-IMF models can fit, we tend to favor IMFs biased toward high mass stars because their fits are more robust.

We present near-infrared rotation curves of NGC 253 along both the major and minor axes, measured in the strong $\text{Br}\gamma$, $\text{H}_2(1,0)\text{S}(1)$, and $\text{Ne II}(\lambda 12.8\mu\text{m})$ lines. We also present, for the first time, a rotation curve of the nuclear region of NGC 253 derived from a *stellar* feature, the strong first-overtone CO absorptions near $2.3\mu\text{m}$. We present a similar rotation curve for the well-studied galaxy NGC 3115 as an evaluation of our technique.

Our deep images supply a wealth of morphological detail. We have used the information in our $H - K$ color image of the galaxy to produce a dereddened K-band image of the galaxy—i.e., this provides us with images of the galaxy as it would appear in the absence of dust extinction. We have therefore produced the clearest images to date of the strong bar in NGC 253 and a ring with a diameter of over 4kpc. We have also deprojected the dereddened image of this highly-inclined galaxy along the minor axis to produce an image of the galaxy as it would appear if viewed face-on.

3.1. Introduction

NGC 253 has been studied extensively, especially at near-infrared and radio wavelengths (e.g., Rieke et al. (1980), Rieke, Lebofsky, & Walker (1988), Scoville et al. (1985), Mauersberger et al. (1996)). The starburst has a somewhat more moderate luminosity and is contained in a larger galaxy than the other archetypical starburst, M82, and so perhaps serves as a better example of strong star formation in larger, more distant spiral galaxies.

NGC 253 has served as an archetypical starburst galaxy due to its proximity and brightness and hence the possibility of detailed study. This paper continues in this tradition. We have obtained high resolution, high signal to noise near infrared spectra of the starburst and we introduce a technique that allows us to subtract the forest of stellar absorption features so we can study faint emission lines. We combine this information with a very low-noise mid-infrared spectrum. Although NGC 253 is a weak-[OI] LINER, our data demonstrate that the conventional hot star explanation for these galaxies (Filippenko & Terlevich 1992) cannot apply to NGC 253. We show instead that the spectrum can be produced by a combination of photoionization and supernova explosions expected in the starburst. We explore parameters such as the age range of the starburst and the possible initial mass functions (IMFs) to gain some insight to the evolution of the starburst and its relationship to the galaxy as a whole.

3.2. Observations and Data Reduction

3.2.1. Images

Broadband images in the J, H, and Ks bands as well as narrowband images with 0.5% bandwidth filters tuned to Br γ and the (1,0)S(1) line of H $_2$ were obtained at the Steward Observatory 1.5m telescope on 13 and 24 October 1995 using a camera equipped with a NICMOS3 array, while much deeper broadband images were obtained with the same telescope and instrumentation on 24 October 1996. The data were reduced as described in ERRL96.

On 24 October 1996 we obtained 120 individual 10-second frames in each bandpass (J, H, and Ks), alternating between on-galaxy observations and wobbling 5' N to monitor the background. One third of each set of observations were centered

on the nucleus of NGC 253, while one-third each were obtained with the telescope displaced NE and SW along the galaxy plane, such that the nucleus still fell on a corner of the array. Thus, the integration time on the nuclear region (roughly the central $60''$) is a full 600s and falls to 200s in the outer parts of the galaxy (outside the central $4'$).

The deep broadband images were flux-calibrated using the UKIRT faint standard number 2 (Courteau 1994). We present photometry of the nucleus in Table 3.1 in several circular apertures, plus a region the size of our extracted slit aperture (used to calibrate our spectra.) Photometric errors were estimated from the dispersion in multiple measurements of the standard star at different airmasses and are typically 2% in the J and H bands and 4%-5% in the Ks band. The broadband images from 24 October 1995 gave flux values that were systematically 10% - 20% higher. These images suffered from somewhat uncertain background subtraction due to not wobbling the telescope far enough to obtain a background completely free of galaxy emission, so we will only make use of the photometry obtained from our deep images and will not discuss the earlier images further here.

We have calibrated the Ks-band image to K-band magnitudes using the standard-star photometry, and will hereafter refer to this image as the K-band image. We have ignored the small color correction between the Ks and K band, since this correction is smaller than the photometric uncertainty.

The broadband images, as well as a contour map of the Ks-band with our slit positions overlaid on the image, are presented in Figure 3.1. The images have a scale of $0''.9$ per pixel and the coordinate system is plotted assuming that the intensity peak of the infrared images corresponds to the position of NGC 253 quoted in NED (Nasa Extragalactic Database): $\alpha(1950) = 00^h 45^m 05^s.9$, $\delta(1950) = -25^\circ$

33' 40". This position closely matches the position of the K-band peak found by Sams et al. (1994).

The narrow-band images are presented in Figure 3.2. The narrow-band images are the result of ~ 700 s of integration in both the line and continuum bands. In the same figure, we present $J - H$ and $H - K$ color maps of the nuclear region, which show that the galaxy colors become very red on the nucleus.

The deep infrared images we have presented here have allowed us to create very accurate color maps. We will exploit the information contained in the $H - K$ color map to deredden our K-band image. Extinction corrections are discussed more fully in §3.3.1, so here we will confine ourselves to assuming that the intrinsic $H - K$ color of the galaxy is 0.2 (so that $E(H - K) = ((H - K) - 0.2)$ and that colors redder than this value indicate attenuation by dust in a foreground screen. As discussed in §3.3.1 and ERRL96, the K-band extinction derived in this manner is relatively insensitive to the dust geometry.

The $H - K$ color image is converted to a dereddening map as follows, where we have used the Rieke & Lebofsky (1985) extinction law to compute the factor (1.78) to convert $E(H - K)$ to A_K :

$$dered_{image} = 10^{1.78 \times E(H-K)_{image}/2.5}. \quad (3.1)$$

The K-band image was then multiplied by the dereddening image to produce a K-band image of the galaxy free from extinction. This image is presented in Figure 3.3. We also deprojected the dereddened image by stretching it along the minor axis by a factor $1/\cos(i)$, where we have taken $i = 78^\circ$ (Pence 1981). The resulting image is presented in Figure 3.3.

3.2.2. Near-IR spectra

We obtained long-slit spectra of NGC 253 in the J, H, and K bands at a resolution of ~ 3000 with the Steward Observatory 2.3m telescope on 9 December 1994 using FSpec, a near-infrared long-slit spectrometer (Williams et al. 1993). In all cases the slit was centered in the infrared peak of the galaxy with a slit-viewing infrared camera which FSpec uses as a guider. Observing and data-reduction techniques are as described in ERRL96, with the exception that a more precise wavelength calibration was obtained using a set of numerically computed wavelengths for the OH airglow lines (C. Kulesa, private communication); consequently, all near-infrared spectra presented here are calibrated to vacuum wavelengths rather than wavelengths in standard air.

We note that considerable care was taken to correct the spectra for atmospheric transmission. A spectrum of HR 173, a G3V star about 2° away from NGC 253, taken close in time to the galaxy observations, was divided into the galaxy spectrum to remove the effect of atmospheric transmission. This step introduced spurious emission features into the spectrum due to intrinsic absorptions in the standard star. To correct for these features, we multiplied our galaxy spectrum by the high-resolution solar spectrum (smoothed to our instrumental resolution) obtained by Livingston & Wallace (1992). The strength of the features in the solar spectrum was carefully adjusted to match the features observed in the standard star—we used regions of the spectrum relatively free of atmospheric features to make the comparison.

Most of the spectra were obtained with the slit oriented along the major axis of the galaxy, while two key grating settings which cover the (1,0)S(1) line of H_2 , $\text{Br}\gamma$, and the (2,0) and (3,1) CO bands were obtained on 11 October 1995 with

the same telescope and instrument, with the slit oriented along the minor axis to investigate the kinematics of the stars and gas. Observations for a single grating setting typically consist of 5 one-minute exposures on the galaxy, alternated with sky observations of similar duration. The J, H, and K-band spectra are presented in Figures 3.4, 3.6, and 3.7, respectively. Each spectrum is the sum of $2\ 1''.2$ pixels in dispersion and $10\ 1''.2$ pixels along the slit, centered on the intensity peak. We performed an initial flux calibration using HR 173 and compared this calibration to one obtained by measuring the flux in a rectangular region (similar in size to our slit aperture) in our broadband images. The fluxes measured in the rectangular slit apertures are listed in Table 3.1. The flux in the images in each band averaged $\sim 12\%$ higher than in the calibrated spectra, so we adjusted the spectral calibration upward by that amount to make the spectral calibration consistent with our images.

We obtained additional spectra of NGC 253 in the J and K bands at a resolution of 1200 on 19 November 1996 using the same instrument and telescope. The slit was again oriented along the major axis of the galaxy and we extracted a similar aperture from these spectra. The spectra were reduced in a similar fashion to the high-resolution spectra, with the exception that our standard star was HR 232, an A3V, so no corrections were required for intrinsic absorptions in the standard, aside from hydrogen absorptions. We were able to use an A star as our standard because (1) we have already observed the hydrogen emission lines at higher resolution (with a cooler star as a standard) and were not concerned with measuring those lines accurately in these low-resolution spectra, and (2) we were not observing in the H band, where the multiple Brackett absorptions are blended with atmospheric absorptions and are very difficult to correct for. The use of a hotter standard star (in which metal lines are presumably weak or absent)

to correct these spectra allows us to confirm that our correction for the intrinsic absorptions in the standard star used for the high-resolution data was accurate.

The low-resolution spectra, while lacking some of the detail we can observe in the high-resolution spectra, allow us to extend the wavelength coverage of our near-infrared spectroscopy, giving us access to several additional [Fe II] and H₂ lines as well as some unidentified features in the J band. The low-resolution spectra are presented in Figures 3.5 and 3.8. The strong features beyond 2.4 μm not marked as H₂ lines are narrow telluric absorptions which are poorly sampled at our low resolution and which appear as emission features after the spectrum is divided by the standard star.

All measurements taken from the near-infrared spectra are derived from the high-resolution spectra when possible.

3.2.3. Mid-IR Spectra

We obtained spectra of the [S IV] 10.5 μm line in NGC 253 on 16 and 21 October 1989 using the Irshell spectrograph (Lacy et al. 1989) on the NASA Infrared Telescope Facility. The 10" long by 2" wide slit was positioned across the nucleus of the galaxy at PA=61°. Additional spectra were measured with parallel slit positions, one slit width to either side of the nucleus. The 10×64 Si:As array provided 1" sampling along the slit, a spectral dispersion of 15 km s⁻¹ pixel⁻¹, and a spectral resolution of 30 km s⁻¹. The seeing was poor and the weather marginal. The data were taken in chop and nod mode with a 5 Hz chop rate and with nods every 13 seconds. The on-source integration time was 20 minutes. DC sky levels were monitored to identify frames that were contaminated by clouds. A dome-temperature card, chopped against the sky, was used for flat-fielding,

atmospheric correction, and fluxing (Lacy et al. 1989). The data were reduced using a software package developed by Achtermann (1994).

We mapped the [Ne II] 12.8 μm emission from NGC 253 by using Irshell in scanning mode (Lacy & Achtermann 1994). This entailed sweeping the slit back and forth across the galaxy at a rate of 1"/sec while clocking out the array at 80 Hz. Each scan was 22" long. The off-source positions at the ends of the scans were averaged to produce a sky frame. The integration time was 32 seconds per spatial pixel. A set of four such scans were made, stepping 5.4" along the slit between scans. The data were combined to form a 22"×22" by 64 spectral channel data cube. The [Ne II] has a spatial extent of 6" and a velocity width of 150 km s⁻¹ FWHM. The integrated [Ne II] flux is $4.6 \pm 0.1 \times 10^{-11}$ erg/s/cm². A comparison [Ne II] measurement of 3.3×10^{-11} erg/s/cm² can be found in Roche & Aitken (1985).

The [S IV] spectra showed a compact (2"×2") continuum source with only a hint of line emission. The central slit position provided a marginal detection of [S IV] with a flux of 5.5×10^{-14} erg/s/cm². Since the [Ne II] is spread over 6 spatial and 10 spectral pixels, we determined a more conservative upper limit on the [S IV] flux by summing over 6 spatial rows centered on the continuum source and by summing the spectra from the three adjacent slit positions (see Figure 3.9). We then binned by 10 spectral pixels and determined the rms noise of the resulting spectrum. Since only 70% of the flux of a Gaussian lies within 1 σ of line center, we divided the rms by 0.7 to determine our 3 σ upper limit on the [S IV] line strength of 3.0×10^{-13} erg/s/cm².

3.3. Faint emission lines

A difficulty with previous interpretations of near-infrared emission spectra of starburst galaxies is the large number of stellar absorption features. In many cases, especially in the H band, nebular emission features are lost in the structure of the stellar features. To counteract this problem, we have used a library of stellar spectra to model the galaxy continuum. This library includes near-infrared spectra of over 100 stars obtained with the same instrumentation used here (and will be published separately).

As a simple first approach to the problem, we chose likely candidate stars (mostly late-type giants and supergiants), and subtracted each star from the galaxy spectrum. We looked for subtractions which minimized the residual continuum to determine which individual stars best fit the galaxy continuum. The resulting mix of stars is thus not optimized in a population synthesis sense, but instead was empirically chosen to be a good match to the galaxy continuum. We combined the library spectra of the 15 best stars. We redshifted the spectra to the galaxy velocity, broadened them to match the velocity dispersion in the galaxy, and scaled the spectra to match the flux-calibrated spectra presented in Figures 3.6 and 3.7 before subtracting them from the galaxy spectra. The continuum-subtracted spectra of NGC 253 are shown in the lower parts of Figures 3.6 and 3.7. The H-band and K-band flux measurements of emission lines presented in this paper are taken from the continuum-subtracted spectra. The resulting improvement in line detections allows us to address a number of new issues regarding the interstellar medium in NGC 253.

3.3.1. Extinction

In a heavily-obscured region like a starburst nucleus, it is critical to correct the observed fluxes for extinction. In regions of such high obscuration, the visible light is often dominated by a foreground region of the galaxy and not by the nucleus, so conventional optical line ratios are typically less useful indicators of the true extinction than are techniques which utilize data at longer wavelengths.

We first use line ratios from our spectra to determine the extinction. One approach is to use the hydrogen recombination lines and assume that their ratios should reflect case B recombination theory. A foreground screen model with $A_V = 9.2 \pm 0.7$ (where we have used an analytical fit to the Rieke & Lebofsky 1985 extinction law, the Hummer & Storey 1987 recombination line ratios, and have included an 8% uncertainty in the relative flux calibration between filter bands in the line ratio uncertainties) is indicated from the hydrogen recombination lines. This fit roughly agrees with the Br α strength (Beck & Beckwith 1984) indicating that relatively little ionized gas is hidden by extreme optical depths.

The [Fe II] line ratios also allow an estimate of the extinction if we use lines from the same upper level. The ratio of [Fe II](1.257 μ m) to [Fe II](1.644 μ m) should be a constant 1.35 according to the A-values of Nussbaumer & Storey (1988), although this value is subject to some uncertainty in the models. The observed value is 0.68 ± 0.07 (including the uncertainty in the relative flux calibration between the J and H bands), which implies $A_V = 8.42 \pm 1.26$. As shown below, the line measurements imply higher values of A_V than the broad-band measurements, perhaps indicating that the extinction is somewhat higher to the line-emitting regions.

The colors of our broadband images can be useful tracers of extinction.

Aaronson (1977) showed that a typical evolved stellar population has $J - H$ and $H - K$ colors of 0.7 and 0.2, respectively, and our starburst models (Rieke et al. 1993) show that the same is true for a starburst population in the age range of interest here (see §3.7). In general, as long as the population is old enough that some stars have evolved into giants or supergiants, the near-infrared part of the spectrum is dominated by stars of roughly the same temperature and so the colors do not vary much. We can use this fact to our advantage if we assume that colors redder than nominal are purely due to reddening by dust, which is a good assumption if the near-infrared light is dominated by starlight and not by an active nucleus, hot dust, or nebular emission. The spectra presented here suffice to show that the near-infrared continuum is dominated by starlight, as the strength of the absorption features are typical of a population of supergiants and do not indicate the presence of veiling due to a contribution from a featureless continuum.

As shown in Table 3.1, the near-infrared colors in our 15" reference aperture are $J - H = 1.09$ and $H - K = 0.66$, much redder than the nominal colors and implying color excesses of 0.39 and 0.46, respectively. The colors we derive agree well with the values measured by Spinoglio et al. (1995). Forbes et al. (1992) find somewhat redder colors than we do, although our measurements are consistent within the uncertainties. Using an analytical fit to the Rieke & Lebofsky (1985) extinction law and a foreground screen geometry for the dust, $E(J - H) = 0.39$ corresponds to 4.26 ± 0.91 magnitudes of visual extinction while $E(H - K) = 0.46$ implies a much higher value of $A_V = 7.35 \pm 1.33$, where the error bars are derived assuming that the nominal errors on our broadband measurements are $\sim 5\%$, at the high end of our estimate of the statistical uncertainty.

To compare the extinction from broad-band colors to that derived above from

line ratios, we must use the broad-band fluxes measured in the same aperture as our spectrometer slit and at approximately the same wavelengths. To compare our broad-band measurements to the hydrogen recombination lines, we have made extinction estimates from the $J - K$ and $H - K$ colors in the $2.4 \times 12''$ aperture and weighted those values by the uncertainties in the hydrogen recombination line measurements in the J and H bands, respectively. In this way, we derive $A_V = 7.09 \pm 0.73$, which is $\sim 3\sigma$ different from the value derived above from the hydrogen recombination lines. Throughout the rest of this paper, we will adopt the somewhat smaller extinction value predicted by the broadband colors as a conservative lower limit on the extinction.

Although the $H - K$ color and the hydrogen recombination line ratios predict somewhat different values for the extinction, they both predict relatively high values. The $J - H$ color predicts a much smaller value for the extinction. This situation would arise naturally if the dust were mixed with the stars rather than all being in a foreground screen. In the case where stars are mixed with dust, observations made at shorter wavelengths (which tend not to penetrate as far into the dust distribution) will systematically predict smaller values of extinction if a foreground screen is assumed. Conversely, extinction estimates made from longer wavelength observations will predict values closer to the true value. Therefore, the most accurate estimate of the extinction we can make under the assumption of a foreground screen derives from the $H - K$ color. The extinction values in the near-infrared bands implied by a visual extinction derived from our $H - K$ color are $A_J = 2.00 \pm 0.36$, $A_H = 1.33 \pm 0.24$, and $A_K = 0.87 \pm 0.16$.

It is clear that a simple foreground screen model for the dust obscuration is incompatible with the broadband observations. If we instead adopt a more realistic

dust geometry, such as mixing the dust with the stars, we obtain a much better fit to the observed colors. For this purpose, we have made use of the “starburst” dust distribution model of Witt, Thronson, & Capuano (1992), comparing our observed colors to polynomial fits we have made to their model points. This model has a centrally-peaked stellar distribution, the inner third of which is mixed with a sphere of uniformly-distributed dust. The amount of dust in a given model is parameterized by the optical depth to the center of the dust distribution, which we will refer to here in magnitudes as $A_V(\text{cen})$.

The observed colors in the nuclear region of NGC 253 are slightly redder than the most heavily extinguished models presented by Witt et al., so we have used our polynomial fits to extrapolate beyond the values presented in their tables. For our measured values of $E(J - H) = 0.39$ and $E(H - K) = 0.46$, the Witt et al. models imply $A_V(\text{cen})$ of 17.27 ± 6.78 and 19.07 ± 3.32 , respectively—i.e., the near-infrared colors are compatible with the same dust distributions within the uncertainties, unlike the case of the foreground screen model. The extinction values in the near-infrared are $A_J = 1.64 \pm 0.51$, $A_H = 1.24 \pm 0.43$, and $A_K = 0.85 \pm 0.30$ from the $J - H$ color and $A_J = 1.84 \pm 0.32$, $A_H = 1.40 \pm 0.24$, and $A_K = 0.94 \pm 0.16$ from the $H - K$ color.

It is worth noting that although the two dust geometries we have considered here are quite different and imply very different amounts of extinction at V , the extinction values in the near infrared are the same within the uncertainties, regardless of dust geometry. We therefore feel that we can correct our near-infrared fluxes for attenuation by dust with some confidence. We will adopt extinction values that are an average of those derived from the mixed model: $A_K = 0.90 \pm 0.17$, $A_H = 1.32 \pm 0.25$, and $A_J = 1.74 \pm 0.30$.

3.3.2. [Fe II] emission

The high sensitivity and broad wavelength coverage of our near-infrared spectra has allowed us to measure 7 [Fe II] lines. The fluxes in these lines ratioed to ($\lambda 1.644\mu\text{m}$) are listed in Table 3.4. The quality of the spectra allows us to make useful measurements of the electron density in the [Fe II]-emitting region. For this purpose we make use of the models of Bautista & Pradhan (1996), who have performed detailed calculations of the excitation of Fe in several ionization states at various temperatures and densities. From our spectra, we use the ratios $\lambda 1.279\mu\text{m}/\lambda 1.644\mu\text{m}$ and $\lambda 1.533\mu\text{m}/\lambda 1.644\mu\text{m}$ to estimate the density. In the range of interest, the diagnostic ratios we have chosen are essentially independent of temperature. We have plotted the values of these two line ratios as a function of density in Figure 3.10. For each curve, we have marked the range consistent with the observations as a shaded box. The densities indicated by each of the line ratios are consistent with each other and indicate a mean density of $\sim 5000\text{ cm}^{-3}$. This relatively low density for the [Fe II]-emitting region indirectly supports our assumption of a low density for the H_2 -emitting region in the following section.

[Fe II] emission in starbursts is thought to arise predominantly from supernova remnants. In a normal photoionized region, Fe is typically locked up in grains and does not give rise to strong emission. As a supernova shock passes through the ISM, however, the grains are destroyed and Fe is released into the gas phase. However, this origin for [Fe II] has been difficult to prove. For example, Greenhouse et al. (1991) find peaks on bright radio compact sources in the [Fe II] surface brightness in M82. However, these compact sources account for only a small fraction of the total [Fe II] emission. Forbes & Ward (1993) find a correlation between nonthermal 6cm emission and [Fe II]. However, the trend line is offset from that for supernova

remnants. Vanzi & Rieke (1997) explain this offset in terms of the short lifetime for the [Fe II]-emitting stage in a supernova remnant and show that the [Fe II] luminosity in M82 is close to that expected from the observed supernova rate. However, this rate is uncertain by a factor of two, and further uncertainties in their argument arise because of the poor knowledge of the time-integrated [Fe II] output of supernova remnants. Our data add significantly to the arguments favoring a supernova origin for the [Fe II], since the density we derive is in good agreement with that observed in the supernova remnants observed by Oliva, Moorwood, & Danziger (1989).

Vanzi & Rieke (1997) have derived a relation between the [Fe II] luminosity and the supernova rate, based on the observed supernova rate in M 82, which they argue is accurate to within a factor of two. To apply this relation, we correct our observed [Fe II] ($\lambda 1.644\mu\text{m}$) flux (from Table 3.4) to a $15''$ aperture using the ratio of the K-band fluxes in the $15''$ and $2.4 \times 12''$ apertures (this scaling is reasonable because the K-band flux is dominated by cool supergiants which are the immediate precursors to the supernova remnants—see §3.6.4). We also correct for 1.33 magnitudes of extinction. We obtain a total [FeII] flux of 3.8×10^{-12} erg/s/cm², or a luminosity of 2.8×10^{39} erg/s. The Vanzi & Rieke relation then implies a supernova rate of 0.03 per year. If the [Fe II]-emitting phase of each supernova remnant lasts $\sim 10^4$ years, this rate implies that there are currently ~ 300 [Fe II]-emitting supernova remnants in the nucleus of NGC 253.

Ulvestad & Antonucci (1994) estimate a large supernova rate of 0.1 to 0.25 yr⁻¹, based on the number of compact sources currently observed in the nuclear region of NGC 253 and assuming that all of the sources are supernova remnants. Turner & Ho (1985) have shown, however, that some of these sources have flat

spectra and are more likely to be compact HII regions, which would reduce the rate of supernovae required to match the number of compact sources observed. More recent observations by Ulvestad & Atonucci (1997) confirm an upper limit on the supernova rate of 0.3 yr^{-1} . The supernovae have also been modeled by Colina & Pérez-Olea (1992), who estimate a rate of 0.05 yr^{-1} , and by Van Buren & Greenhouse (1994), who find 0.08 yr^{-1} .

The above estimates are all based on modeling supernova counts and hence are to first order distance-independent. The rate can also be estimated from luminosities. For example, if we use the nonthermal radio flux from Turner & Ho (1983) and assume it is entirely due to synchrotron emission from supernova remnants, we can derive a supernova rate of 0.026 yr^{-1} using equation (8) of Condon & Yin (1990). This rate is in close agreement with our estimate using the [Fe II] emission, providing further evidence in support of the supernova origin for the [Fe II]. Both of these estimates are lower than those from supernova counts by a factor of about two. Although this difference is probably within the errors, we note that, if the galaxy is a factor of square root two more distant than the 2.5 Mpc we have assumed, i.e., at 3.5 Mpc (well within the uncertainty in distance), the luminosity- based rates will double and the agreement will be improved.

3.3.3. H_2 emission

The excitation mechanism of H_2 in starburst galaxies is under debate. The strong UV flux typically found in starburst regions should excite a significant amount of H_2 . However, many of these galaxies display strong emission in the (1,0)S(1) line (e.g., Goldader et al. 1996) but not in other H_2 lines, suggesting that collisional processes rather than fluorescent ones dominate (c.f., Black & van Dishoeck 1987).

One reason that UV-excited H_2 is so difficult to detect is that its energy is emitted in a huge number of lines, whereas thermally excited H_2 emits most of its luminosity in just a few lines. In low density gas, fluorescent H_2 emits just 1.6% of its infrared luminosity in the (1,0)S(1) line while thermally excited H_2 emits 9% of its infrared luminosity in the (1,0)S(1) line. Despite the difficulties associated with detecting a number of very weak lines, fluorescent H_2 has been detected recently in some galaxies (Doyon et al. 1994; Kulesa & Black 1997.)

The combination of high resolution and sensitivity, broad spectral coverage, and our technique for subtracting the stellar continuum allow us to measure an unprecedented number of H_2 lines in an extragalactic source. Table 3.5 lists the H_2 lines we have detected, plus upper limits on a few important diagnostic lines. We have also listed a set of line ratios dereddened using the extinction derived in §3.3.1. We compare the observed line ratios to two H_2 models from Black & van Dishoeck (1987)—a UV-excited model (their model 14), plus a collisionally-excited model (their model S2).

We can justify our selection of Black & van Dishoeck's S2 model, which has a temperature of 2000 K, as opposed to their S1 model, which has a temperature of 1000 K, by computing the rotational excitation temperature of the H_2 transitions we observe. We have used the A-values, energy levels, and statistical weights adopted by Ramsay et al. (1993). Our derived temperatures from various line ratios are listed in Table 3.6. The temperature derived from the two strongest lines, (1,0)S(1) and (1,0)S(3), is consistent with 2000 K and not with 1000 K.

A first glance would suggest that the excitation of the H_2 is dominated by collisions, rather than UV pumping. Following the arguments of Kulesa & Black (1997), however, we can show that fluorescent emission plays an important role in

producing the H_2 spectrum of NGC 253. In the table we present a mixed model in which 25% of the flux in the (1,0)S(1) line is due to fluorescence, modifying the other line ratios accordingly. One can see that this model fits the data significantly better, without looking radically different from a pure thermal model. While the (1,0) lines do not change much from the thermal to the mixed model, the contribution from fluorescent H_2 is required to fit the (2,1) lines, which are observed to be much stronger than a pure thermal model would predict.

We measure a flux in the (1,0)S(1) line of 1.2×10^{-13} erg/s/cm² in our $2''.4 \times 12''$ spectroscopic aperture. We correct this value to a $15''$ reference aperture using the narrow-band H_2 image and obtain a flux of 3.5×10^{-13} erg/s/cm². Correcting this value for extinction gives us 8.4×10^{-13} erg/s/cm², or $1.6 \times 10^5 L_\odot$ at a distance of 2.5 Mpc. Using this luminosity, the total H_2 luminosity in the mixed model is $3.8 \times 10^6 L_\odot$ — $1.3 \times 10^6 L_\odot$ from thermal emission and $2.5 \times 10^6 L_\odot$ due to fluorescent emission; that is, nearly two thirds of the total H_2 infrared luminosity is derived from fluorescence. The ability to distinguish between pure thermal and mixed thermal and fluorescent H_2 emission depends on having high-enough sensitivity and resolution to detect faint lines—the H_2 spectrum of NGC 253, observed at lower resolution and sensitivity would likely be interpreted as dominated by thermal processes, even though the total H_2 luminosity is dominated by fluorescence.

Again following Kulesa & Black, we can estimate what portion of the H_2 luminosity might be due to HII regions and what portion might be due to other processes, such as shocks (possibly associated with supernova remnants). Luhman et al. (1994) report global observations of H_2 in Orion, with the result that about $1900 L_\odot$ are due to fluorescent emission while only $40 L_\odot$ are due to thermal emission. From these numbers, we calculate that 1.3×10^3 HII regions similar

to Orion would be required to account for the fluorescent emission we observe in NGC 253. These HII regions would provide $5.3 \times 10^4 L_{\odot}$ of thermal emission, leaving nearly all the thermal emission from NGC 253 unaccounted for. The deficit could be made up by thermal emission from diffuse shocks, either associated with supernova remnants or on larger scales. We next explore the possibility of a supernova origin for the thermal emission.

Graham, Wright, & Longmore (1987) and Burton et al. (1988) derive an H_2 luminosity in the supernova remnant IC 443 of $\sim 70 L_{\odot}$. If we take this to be the average luminosity per supernova remnant in NGC 253, there must be 1.8×10^4 H_2 -emitting supernova remnants in the nucleus of NGC 253. If the supernova rate is as implied from the [Fe II] emission, the average H_2 -emitting lifetime of the supernova remnants must be close to 6×10^5 years. This lifetime is implausibly long, particularly since at this age any supernova remnant in NGC 253 will have expanded and merged with the general hot interstellar medium from other old supernovae. Instead, we suggest that much of the thermal H_2 arises from cloud-cloud collisions, some of which may be powered by mechanical energy released by supernovae and stellar winds.

3.3.4. Temperature of the Hot Stars

We can determine the hardness of the UV radiation field in NGC 253 based on the relative strengths of the mid-infrared fine structure lines. Theoretical line ratios were determined using CLOUDY models by D. Kelly. S^{++} has an ionization potential of 34.8 eV, so the [S IV] $10.5 \mu m$ line is weak in the absence of high mass stars. Neon has a first ionization potential of only 21.6 eV, so the [Ne II] $12.8 \mu m$ line can be excited by less massive stars. In galaxies with active star formation, most of the [S IV] will be excited by stars of $>35 M_{\odot}$. These high mass stars tend

to excite neon to Ne^{++} so most of the $[\text{Ne II}]$ emission is excited by 5–25 M_{\odot} stars. The $[\text{S IV}]/[\text{Ne II}]$ ratio can thus be used as an indicator of the effective temperature and age of a starburst. The main problem with this technique is the strong dependence of the $[\text{S IV}]/[\text{Ne II}]$ ratio on ionization parameter (Kelly et al. 1997). The ratio is also dependent on the relative abundances of sulfur and neon.

We apply an extinction correction of $A_V=14$ mag to the mid-infrared data, based on the $\text{Br}\alpha/\text{Br}\gamma$ data of Rieke et al. (1980). This large extinction only changes the $[\text{S IV}]/[\text{Ne II}]$ color by 0.26 dex (Rieke & Lebofsky 1985) to $\log([\text{S IV}]/[\text{Ne II}]) = -2.7$, or a 3σ upper limit of -1.9 . We compare these values to the single star photoionization models of Kelly et al. (1997) to determine effective temperatures as a function of ionization parameter. The 3σ upper limit of Section 3.2.3 implies upper limits of 36000 K, 38000 K, and 49000 K respectively for $\log U = -1.5$, -2.5 , and -3.5 . The weak detection of $[\text{S IV}]$ on the central slit position implies effective temperatures of 34400 K, 36000 K, and 42300 K for respective $\log U$ values.

We can rule out an ionization parameter of $\log U = -3.5$ based on the large Lyman continuum flux of 10^{53} s^{-1} calculated in Section 3.6.3. From Figure 3.2, we see that all of the $\text{Br}\gamma$ flux comes from within a radius of 7", or 90 pc. From Heckman et al. (1990), we see that the nucleus has an electron density of at least 600 cm^{-3} and probably higher since dust would have hidden the nucleus at 6700 Å. A reasonable upper limit to the density would be 3000 cm^{-3} . These numbers set a lower limit to the ionization parameter of $\log U = -3.0$. The more likely range given the presence of substructure in the nucleus and for an electron density of 600–1000 cm^{-3} would be $-\log U = 2.0$ – 2.5 , and an ionization parameter as large as $\log U = -1.5$ cannot be ruled out.

For the $\log U = -1.5$ and $\log U = -2.5$ cases, we examined a two star model, one

star with $T=T_{eff}$ and the other with $T=40000$ K. We determined how bright the 40000 K star would have to be relative to the T_{eff} star to alter the $[S\ IV]/[Ne\ II]$ ratio by 0.15 dex, or roughly 1σ . For the four cases: $\log U$, $T_{eff} = -1.5$, 34400; -1.5, 36000; -2.5, 36000; -2.5, 38000 we found that the 40000 K star contributed the following percentages of the Lyman continuum photons: 2.5; 7.4; 6.8; 31. These percentages can be combined with the starburst models of Section 3.7 to determine the age of the starburst. As discussed below, the effective temperature is unlikely to be as high as 38000 K, so a conservative upper limit to the contribution of stars hotter than 40000 K is probably 15%.

Another set of constraints can be derived from far infrared fine structure lines. Carral et al. (1994) use these lines to find an effective temperature for the exciting stars of $34,500 \pm 1,000$ K.

Vanzi et al. (1996) suggested that the ratio $HeI(1.7)/Br10$ is particularly useful to constrain the temperature of the hot stars because it is not heavily affected by reddening or electron temperature. Our upper limit for the $1.7\mu m$ HeI line corresponds to an upper limit of $HeI(1.7)/Br10 \leq 0.2$, placing an upper limit of $\sim 37,000$ K on the stellar temperature exciting the ISM.

Thus, three independent means of estimating the temperature of the exciting stars from infrared spectra give consistent results of $T_{eff} \sim 35,000$ K. The $[OIII]/H\beta$ ratio would give a value a few thousand degrees higher than the infrared indicators. However, we show in the following section that a significant portion of the $[OIII]$ may be shock-excited in supernova remnants. Also, at ~ 0.4 solar and higher metallicities, it is expected that $[OIII]/H\beta$ and other optical indicators will overestimate the temperature of the photoionizing field for a variety of reasons, such as an increase in electron temperature due to depletion onto grains or to

photoelectric heating (Shields & Kennicutt 1995). Where it is feasible to measure them, the infrared indicators should give a more reliable result; in particular, values derived from them are virtually independent of electron temperature (Vanzi et al. 1996; Kelly et al. 1997).

3.4. Nature of Weak-OI LINERs

Although the intrinsic $[\text{OII}]/[\text{OIII}]5007$ line ratio is difficult to determine for NGC 253 because of the strong reddening, other, less reddening-dependent diagnostic line ratios indicate it is a transitional HII/weak-OI LINER. Filippenko & Terlevich (1992) use nebular models to demonstrate that this class of galaxy can be excited by hot stars, with $T \geq 45,000$ K. The locus of NGC 253 on the diagnostic plots of Filippenko & Terlevich falls even closer to their theoretical calculations than does the zone they indicate for average weak-OI LINERs. Alternatively, it has been proposed that these LINERs are excited by shocks (e.g., Heckman 1980).

The strong arguments against the effective stellar temperature in NGC 253 being nearly as hot as 45,000 K are difficult to reconcile with the model of Filippenko & Terlevich. In fact, our data are difficult to reconcile with any model based on photoionization from a hard UV spectrum, since the indications of low stellar temperature also argue against a hard UV field from a mini-AGN or other source. Moreover, there are few other traces of a mini-AGN in this galaxy. For example, our measurement of $\text{Br}\gamma$ shows the line to be narrow with no broad wings. On the extinction-free $[\text{OI}]/\text{H}\alpha$ vs. $[\text{Fe II}] 1.64\mu\text{m}/\text{Br}\gamma$ diagnostic diagram, NGC 253 falls near the middle of the starburst locus (Alonso-Herrero et al. 1997). There is no hard x-ray source in the nucleus of the galaxy, and although there is a compact radio source (Turner & Ho 1985), it is of low luminosity.

It seems likely that the LINER characteristics of NGC 253 are produced by a mechanism other than photoionization. We have shown that the [Fe II] emission is likely to be produced in supernova remnants; below we will strengthen this argument by demonstrating that starburst models that fit the other characteristics of NGC 253 predict a supernova rate in reasonably good agreement with that derived under the assumption that the [Fe II] is predominantly from supernova remnants. Alonso-Herrero et al. (1997) demonstrate that NGC 253 falls approximately on the mixing line between HII regions and supernova remnants on the [OI]/H α vs [Fe II]/Br γ diagram. That is, the [OI] strength is also consistent with an origin predominantly in the same supernova remnants that produce the [Fe II], with additional H recombination emission from HII regions.

The influence of supernovae on the observed emission line spectrum of NGC 253 can be determined more quantitatively. We have determined an average supernova emission line spectra by averaging the line strengths (normalized to H α) for 32 supernova remnants measured by Danziger & Leibowitz (1985), Fesen, Blair & Kirshner (1985), and Blair & Kirshner (1985). Similarly, an average ratio of [Fe II] 1.64 μ m/Br γ can be determined for supernovae measured by Oliva, Moorwood & Danziger (1989; 1990). Taking H α /Br γ = 103 from Case B, we find that [OI]/[Fe II] \sim 1.25. Relating these values through the H recombination lines is an essential step because of the differing geometries in the available optical and near infrared spectra. Nonetheless, because of the relatively small amount of infrared data, the derived ratio is somewhat uncertain.

We can predict the optical spectrum from the infrared one with: 1.) the relations derived in the preceding paragraph; 2.) the total [Fe II] flux of 3.8×10^{-12} erg/s/cm² derived in Section 3.2; 3.) the total Br γ flux of

2.14×10^{-12} erg/s/cm² derived in Section 5.4; 4.) case B ratios for the H recombination lines; and 5.) standard nebular calculations for the relative strengths of photoionized lines in the optical (we have used the work of Shields & Kennicutt (1995), which includes the effects of dust in metal-rich HII regions). We assume a stellar temperature of 38,000 K (the lowest for which Shields & Kennicutt give calculations) and solar metallicity. We also use the OI/H α ratio for the Orion nebula to represent a typical HII region. The results of these predictions are summarized in Table 3.7.

The agreement between predicted and observed line ratios is well within the uncertainties. About 85% of the OI and half of the [OIII] are excited in the supernovae remnants, whereas most of the [NII], [SII], and H recombination are excited by photoionization. Although the photoionized portion of the [OIII] will decrease rapidly with decreasing stellar temperature, the large portion of shock-excited [OIII] will maintain good agreement with the observations. Recall also that the intrinsic OI/[Fe II] ratio in supernovae is uncertain; if the correct value is a factor of 1.5 higher than we have used (which is within our guess of the errors), the agreement between predictions and observations is improved and the [OIII]/H β ratio becomes almost independent of a decreased stellar temperature.

Thus, a combination of a metal-rich HII region photoionization model with the shocked optical line strengths predicted by assuming the [Fe II] is produced by supernovae provides a satisfactory fit to all the LINER characteristics of the NGC 253. This fit involves no free parameters, other than those determined independently of the LINER characteristics. The Filippenko & Terlevich (1992) hot star photoionization model would predict that LINERs appear as a very early stage in a starburst. Instead, we suggest that the LINER characteristics emerge

after the stars emitting most vigorously in the UV have died, so the HII region characteristics will fade sufficiently to reveal the supernova shock excitation.

The decay time for ionizing flux in a starburst is only a few million years, whereas the supernova rate is maintained for about 30 million years. Therefore, if the star-forming episodes in starbursts are typically short in duration, of order 10 million years, then there should be a significant population of objects in the transitional stage that produces LINER characteristics. In agreement with this conclusion, we show in §3.7.2 that starburst models with these characteristics give the best overall fit to the properties of NGC 253.

3.5. Morphology

3.5.1. Continuum morphology

In Figure 3.1 we have presented J, H, and K-band images of NGC 253. The most striking feature of the images, aside from the very bright nucleus, is the bright, elongated feature centered on the nucleus and oriented roughly east-west. This feature is $\sim 230''$ long as projected on the sky and was first noted by Scoville et al. (1985), who describe it as a bar; Pompea & Rieke (1990) noted that it curves as it approaches the nucleus and suggested it might instead be inner spiral arms. Our deep infrared images presented here indicate that this apparent curvature arises from a zone of strong extinction. Our dereddened K-band image presented in Figure 3.3 leaves little doubt the feature is a bar.

Also evident is a ring with a diameter of $\sim 350''$ (~ 4 kpc) along the major axis of the galaxy. This ring is very nearly circular, as can be seen in our deprojected image of the galaxy in Figure 3.3. The prominence of the bar is reduced in the

deprojected image. This behavior is expected if the bar is thick perpendicular to the plane of the galaxy; then, the deprojection incorrectly stretches the bar. Figure 3.3 suggests a bar thickness of the order of 200 pc. This image also shows that the bar has a length of $\sim 350''$. The ring is also apparent in the deep H-band image from Forbes & DePoy (1992), although they do not discuss this feature.

Canzian, Mundy, & Scoville (1988) show a bar in CO emission that is about $30''$ long and oriented along the stellar bar discussed above. Thus, the configuration of molecular gas in the nucleus of NGC 253 approximates the theoretical predictions that mutual torques between stellar and gas bars will allow the gas to lose angular momentum and sink into the nucleus, where it concentrates until instabilities set in that trigger a starburst.

The images in Figure 3.1 clearly show the effects of dust extinction. A progression in amount of small-scale structure can be seen from the short-wavelength J-band image to the longer-wavelength K-band image, with the K-band image being visibly smoother. A prominent dust lane which extends into the nucleus from the west is readily apparent in the J-band image and is much less so in the K-band image.

3.5.2. Emission-line morphology

In Figure 3.11 we present position-velocity diagrams of seven strong emission lines in NGC 253 along the major axis and two of these lines along the minor axis as well. These images show that the starburst is not distributed symmetrically about the major axis but instead is concentrated in a region north-east of the nucleus. They also show that the H_2 emission is significantly more extended than the other lines shown here.

3.6. Other Parameters of the NGC 253 Starburst

We now consider the starburst properties of NGC 253 in detail. Our discussion will parallel those in Rieke et al. (1993 – hereafter RLRT93) and ERRL96.

Typical estimates of the distance to NGC 253 found in the literature range from 2.5 to 3.5 Mpc. We will adopt a distance of 2.5 Mpc (de Vaucouleurs 1978); as discussed in ERRL96, choosing a distance at the low end of the range places the most conservative constraints on our starburst models.

The reference aperture we will use is $7''.5$ in radius. We chose this radius because most of the $\text{Br}\gamma$ and H_2 flux (as measured in our narrow-band images) and the radio flux (as measured in the continuum observations of Antonucci & Ulvestad (1988) or Turner & Ho (1983)) arises from within this radius. The 10, 20 and $30\mu\text{m}$ maps of NGC 253 from Telesco, Dressel, & Wolstencroft (1993) as well as the far-infrared measurements by Smith & Harvey (1996) also show that most of the mid- and far-infrared flux is produced in this region.

3.6.1. Mass

Rotation

An abundance of kinematic data exists for the nuclear region of NGC 253. Several rotation curves exist in the literature that have been obtained at radio wavelengths, in molecular emission lines such as CO (e.g., Mauersberger et al. 1996, Canzian et al. 1988) or CS (Peng et al. 1996) or in hydrogen recombination lines (Anantharamaiah & Goss 1996). While most of these observations have high spectral resolution, they typically have poor spatial resolution and are not always useful for probing the dynamics very close to the nucleus. The data of

Anantharamaiah & Goss are an exception to this—their data have a spatial scale similar to ours and indicate a mass of $3 \times 10^8 M_{\odot}$ inside a radius of $5''$, comparable to the mass we derive in the next section.

Optical rotation curves of the nuclear region also exist (e.g., Muñoz-Tuñón, Vilchez, & Castañeda 1993 and Arnaboldi et al. 1995). The observations by Muñoz-Tuñón et al. are likely affected by dust extinction in the sense that they indicate a rotation curve that is too shallow (as demonstrated by Prada et al. 1996) and would therefore imply a mass which is too small for the nuclear region. The measurements by Arnaboldi et al. were obtained at higher spatial resolution and indicate a slope for the rotation curve that is somewhat higher than indicated by our data (see below).

Puxley & Brand (1995) and Prada et al. (1996) have presented rotation curves obtained with near-infrared spectral lines, and these studies show that the near-infrared data agree with the radio data at large radii while providing a higher spatial resolution than much of the radio data in the inner regions. In Figure 3.12, we present rotation curves at a higher spatial resolution ($1''.2$ per pixel) than these authors and velocity resolution intermediate between the Puxley & Brand spectra and those of Prada et al. We also present position-velocity plots of many of the strong emission lines along both the major and minor axes of NGC 253 in Figure 3.11.

The large spectral coverage at high resolution we have obtained also allows us to present a rotation curve in a *stellar* feature, the (2,0) rovibrational band of CO at $2.3\mu\text{m}$. The stellar feature has the advantage that it traces a component of the galaxy nucleus which is not affected by non-gravitational processes such as shocks, winds, or magnetic fields, all of which are likely to be strong in a highly disturbed

galaxy nucleus such as that found in NGC 253. The stellar feature also traces a component of the population which is smoothly distributed throughout the region of interest, as indicated by our K-band image. The CO maps of Mauersberger et al. (1996) show that the molecular gas does *not* follow the smooth stellar distribution but instead is concentrated in lobes on either side of the nucleus. Tracers such as Br γ and H $_2$ are likely concentrated in discrete HII regions and the surfaces of molecular clouds, although we note that the rotation curves derived from both the gaseous and stellar features match quite well in the central region.

The velocity gradients across the nucleus along the major axis are tabulated for our three chosen near-infrared features in Table 3.8. They overlap within the uncertainties, and the combined average is $7.5 \pm 0.3 \text{ km s}^{-1}/''$. This number is not corrected for inclination. Our infrared emission lines probably trace a compact nuclear disk of gas, however, and there is no way to be certain from our data that the inclination of the nuclear region follows that of the rest of the galaxy. The only correction we can reasonably make is to correct for the inclination of the galaxy as a whole, which is 78° (Pence 1981); this correction gives us a value of $7.7 \pm 0.3 \text{ km s}^{-1}/''$. This value is similar to that from Puxley & Brand but somewhat lower than we find from the data of Prada et al., from which we calculate 7.8 ± 0.4 and 9.8 ± 0.2 , respectively, if we eliminate points that are obviously not on a linearly-rising rotation curve. The rotation curve indicated by all the near-infrared measurements is quite shallow, however, and indicates a mass of $1.7 \times 10^8 M_\odot$ within a $10''$ radius (the radius at which the rotation curve turns over) if we assume the mass is distributed spherically. Given the presence of the strong bar in NGC 253, it is possible that the rotational motions have been modified by radial motions along the bar and that the velocity curve does not give an accurate estimate of the nuclear mass.

We have also obtained a rotation curve for the well-studied galaxy NGC 3115 as an evaluation of our technique for measuring the stellar rotation, which relies on a cross-correlation routine developed by L. Shier (private communication) and modified by us. We obtained the spectrum with the same instrumentation and techniques discussed here at the Steward Observatory 1.55m telescope on the night of 10 May 1996. In Figure 3.12, we compare our results with the optical data of Kormendy & Richstone (1992). The rotation curves compare quite well, although the Kormendy & Richstone rotation curve rises more steeply in the center, most likely due to better seeing and their smaller pixel size ($0''.435$) as compared with our $1''.8$ pixels at the 1.55m telescope. This comparison gives us confidence that we are correctly measuring the stellar rotation curve, despite the fact that the CO band is a broad and one-sided feature.

Dispersion

A more robust way to determine the mass in the nuclear region is to measure the velocity dispersion of the stars and compute the mass by assuming a model for the stellar distribution, as in Shier et al. (1994). Using the cross-correlation routines described in Shier et al. we measure a stellar velocity dispersion in the CO(2,0) feature of $87 \pm 10 \text{ km s}^{-1}$ in the $12''$ aperture we used to extract the spectra, where the error bars include both the statistical uncertainty as measured by a Monte Carlo simulation and an estimate of the systematic uncertainty as determined by experiments with fitting standard stars. The template star for this calculation was HR 7475.

The observed velocity dispersion is the sum of the dispersions in each extracted pixel, weighted by the luminosity profile of the galaxy. We fit a profile to the $2.3\mu\text{m}$

region of our spectrum of NGC 253, modeling the light distribution using the η models presented by Tremaine et al. (1994). The model that best fit the luminosity profile has a scale radius of $6''$, or about 73 pc at the distance of NGC 253, and $\eta = 3$. Using this galaxy profile, we measure a mass of $3.9 \times 10^8 M_{\odot}$ within a $7''.5$ radius. The uncertainties in the mass determination are dominated by uncertainties in the velocity dispersion, as the derived mass depends on the square of the velocity. Even though the galaxy profile was fit by eye via a comparison of the models with the observed profile, we believe the scale radius is easily determined to within an arcsecond. An error of an arcsecond in the scale radius leads to an error in the derived mass of only 5%.

The derived mass is much larger than that derived from our rotation curve, but quite similar to the mass derived by Mauersberger et al. (1996) within a similar radius, using a rotation curve derived from radio CO measurements. This discrepancy between our rotation curve and the stellar dispersion could be explained if the nucleus of NGC 253 has a small net rotation and the dynamics are instead dominated by the dispersion or if radial motions along the bar are occurring. We will use the mass derived in this section to constrain our starburst models, allocating $3.9 \pm 0.9 \times 10^8 M_{\odot}$ for the dynamical mass within a $7''.5$ radius of the nucleus, where the error bars are due to the uncertainty in the velocity dispersion. We will take the 2σ upper limit of $5.8 \times 10^8 M_{\odot}$ as a conservative upper limit on the dynamical mass in the nuclear region.

Mass Budget

To determine the mass we may allocate to star formation in a recent starburst, we must subtract from the dynamical mass the mass already present in NGC 253 as

a preexisting nucleus. Rieke et al. (1993) assumed that the preexisting nucleus in M 82 would account for at least 50% of the dynamical mass in the nuclear region, which may have been an overly conservative estimate. Recent hydrodynamical simulations (Bekki 1995) suggest that a gas inflow amounting to no more than 20% of the nuclear dynamical mass would be sufficient to trigger a starburst in a highly perturbed system such as a pair of merging galaxies, while other simulations (Wada & Habe 1992) suggest that this number may be as small as 10% in isolated systems. We will follow ERRL96 and take the conservative estimate that 80% of the dynamical mass in the nucleus must be in the form of an old stellar population not participating in the most recent starburst.

Of the remaining $1.2 \times 10^8 M_{\odot}$ some remains in the form of molecular gas out of which stars are being formed. The standard method by which one estimates the mass of molecular gas in an external galaxy is to measure the intensity of CO rotational transitions and convert that measurement to a mass of H_2 using a conversion factor based on observations of molecular clouds in our own galaxy. There has been much discussion (e.g., Maloney & Black 1988; Shier et al. 1994; Mauersberger et al. 1996) about problems with this approach when applied to starburst galaxy nuclei. In any case, the H_2 mass in the central $15''$ of NGC 253 as measured by the standard method is $1.4 \times 10^8 M_{\odot}$ (Mauersberger et al. 1996), which is larger than the total mass we have allocated for gas plus stars in the starburst. In the spirit of placing the most conservative constraints possible on the starburst models, We will follow Mauersberger et al., who present two alternate estimates of the molecular mass which are in rough agreement with each other, although they do not agree with the standard method. We take the average of their results and allocate $3 \times 10^7 M_{\odot}$ to molecular mass in the nucleus, leaving $9 \times 10^7 M_{\odot}$ as the maximum for the recently formed stars.

3.6.2. Luminosity

The bolometric luminosity of a starburst galaxy is typically dominated by the far-infrared (see, for example, the review by Telesco 1988). In a dusty region full of young stars (such as a nuclear starburst) much of the stellar radiation is reprocessed by dust into far-infrared photons. The dust absorption is especially efficient at short wavelengths where much of the luminosity of a young stellar population is emitted. The far-infrared luminosity thus serves as a reliable estimate of the integrated luminosity of the stellar population at short wavelengths. Some of the stellar radiation at longer wavelengths does escape to be directly observed, for example, in the near-infrared, but as we show below this is a small fraction of the bolometric luminosity.

We have used data from the literature to estimate the bolometric luminosity of the starburst in NGC 253. To do this, we have made use of measurements from 1.3mm (Krügel et al. 1990), the submillimeter (Gear et al. 1986), the far-infrared (Smith & Harvey 1996, plus IRAS measurements from Rice et al. 1988), and the mid-infrared (Rieke & Low 1975). The near-infrared and optical portions of the spectrum supply little of the integrated luminosity from the nuclear region—we ignore this small contribution. The small-beam measurements by Smith & Harvey proved particularly useful in determining the fraction of luminosity actually arising from the starburst, as the scans of Rice et al. show that a non-negligible fraction of the far-infrared luminosity in NGC 253 is due to a cool extended component. We integrated the flux and determined a bolometric luminosity of the starburst in NGC 253 of $1.1 \times 10^{10} L_{\odot}$. This should be considered a lower limit since a significant fraction of the luminosity may be escaping perpendicular to the galaxy.

We can compute the luminosity of the underlying stellar component, the

mass of which we estimated in §3.6.1. Assuming the same conversion from mass to K-band luminosity determined by ERRL96, the preexisting stellar population (which should have a mass no larger than $4.6 \times 10^8 M_{\odot}$) has an absolute K magnitude of -18.6. We will correct the observed K-band flux in NGC 253 for this small contribution.

Using $BC_K = 2.7$ and $M_{\text{Bol}}(\odot) = 4.75$, we compute that the bolometric luminosity of the underlying population is less than $2 \times 10^8 L_{\odot}$, or less than 2% of the observed value, so we will ignore this small contribution to the total.

3.6.3. Ionizing Flux

An estimate of $Q(\text{H})$ (number of hydrogen ionizations per second) can be obtained from the data presented here. We can correct the longest-wavelength (i.e., the line least affected by extinction) hydrogen recombination line flux we observe ($\text{Br}\gamma$) for extinction and convert it to $Q(\text{H})$ using the ratio $I(\text{H}\beta)/I(\text{Br}\gamma) = 30.3$ (from Hummer & Storey 1987) and $\alpha_{\text{B}}/\alpha_{\text{H}\beta}^{\text{eff}} = 8.40$.

From our narrow-band images, we determine the $\text{Br}\gamma$ flux in a $15''$ aperture to be $9.16 \times 10^{-13} \text{ erg/s/cm}^2$. We correct this flux to $2.14 \times 10^{-12} \text{ erg/s/cm}^2$ using $A_K = 0.9$ from §3.3.1. The value of $Q(\text{H})$ implied by this $\text{Br}\gamma$ flux is $1.0 \times 10^{53} \text{ s}^{-1}$. This number would be approximately equal to the total number of ionizing photons per second, N_{LyC} , were it not for the presence of significant amounts of dust in the starburst region, which can compete effectively with hydrogen atoms in absorbing ionizing photons, possibly absorbing most of those photons before they have a chance to ionize a hydrogen atom (e.g., Aannestad 1989). As such, we can take $Q(\text{H})$ to be a lower limit on N_{LyC} .

We obtain a similar value from our $[\text{Ne II}]$ measurement. The dereddened

($A_V=14$ mag) [Ne II] flux is $(6.6 \pm 0.2) \times 10^{-11}$ erg/s/cm². Combined with the formula of Roche et al. (1991) and a distance of 2.5 Mpc, this gives $N_{\text{LyC}}=1.3 \times 10^{53}$ photons s⁻¹.

We obtain a very similar rate from the thermal radio flux measured by Turner & Ho (1983), using their equation for converting the thermal component of the 6cm radio flux to $Q(\text{H})$. They estimate that 125mJy, or less than 10% of the total flux at 6cm, is due to thermal emission, implying $Q(\text{H}) \sim 8 \times 10^{52}$ s⁻¹.

We will take the lower limit on N_{LyC} from our data, so that $\log(N_{\text{LyC}}) \gtrsim 53$.

3.6.4. Absorption Features

CO index

Using the definition of the CO index by Kleinmann & Hall (1986), who compare the flux in a “band” region from 4351 to 4361 cm⁻¹ to the flux in a “continuum” region from 4362 to 4372 cm⁻¹, our spectroscopic CO index is 0.31, which corresponds to a photometric index of 0.18, and where we have redshifted the wavelengths by 245 km s⁻¹. If we deredden the spectra using the extinction described in §3.3.1, our spectroscopic index is 0.32, for a photometric index of 0.19.

We obtain a similar number using the Doyon, Joseph, & Wright (1994a) definition, which specifies the CO index as

$$-2.5 \log \langle R_{2.36} \rangle, \quad (3.2)$$

where $\langle R_{2.36} \rangle$ is the average of the “rectified” spectrum (i.e., the spectrum has been divided by a power-law fit to featureless regions of the spectrum between 2 and 2.29 μm) between 2.31 and 2.40 μm in the galaxy’s rest frame; we measure $CO_{sp} = 0.29$. Doyon et al. use the following formula to convert between CO_{sp} and

CO_{ph} :

$$CO_{sp} = 1.46CO_{ph} - 0.02, \quad (3.3)$$

which gives us $CO_{ph} = 0.21$.

The Doyon et al. formulae are more appropriate for data of lower resolution than ours: we will therefore use the Kleinmann and Hall definition. We will correct our measured value for dilution by an underlying population by assuming that the old stellar population contributes 20% of the K-band light (see §3.6.2) and that the old population has a CO index of 0.15 (Frogel et al. 1978), giving us an intrinsic CO index of 0.20 for the starburst population.

Other absorption lines

The high-sensitivity near-infrared spectra presented here reveal a profusion of stellar absorption features. We have tabulated equivalent widths of these features in Table 3.9. The K-band wavelengths are taken from Kleinmann & Hall (1986), while the H-band wavelengths of the atomic lines are taken from Livingston & Wallace (1991) and the wavelengths of the second-overtone CO transitions were computed using a program by N. Gaffney (private communication).

The continuum structure provides important qualitative constraints on the conditions in the galaxy. For example, our models would predict that the near-infrared stellar continuum should be dominated by cool supergiants—the continuum of NGC 253 is consistent with being dominated by these kinds of stars, as confirmed by comparisons with our stellar library or the compilations of stellar spectra by Origlia, Moorwood, & Oliva (1993). We have also made the assumption that the near-infrared continuum is produced purely by starlight, both in making

our extinction correction and in deriving the K-band luminosity of the galaxy. The strength of the stellar absorptions listed in Table 3.9 are consistent with a pure stellar spectrum and show no sign of veiling by a smooth continuum from sources such as hot dust or synchrotron emission associated with an active nucleus. In the future, we may be able to make use of high-quality infrared spectra such as those presented here and those contained in our stellar library to compute the spectrum of the starburst population directly and provide a more rigorous comparison with the observations.

3.7. Starburst models

3.7.1. Description of Models

RLRT93 modeled the starburst in M 82 using the models of Rieke et al. 1980 with updated stellar tracks and atmospheric parameters. The starburst model uses the grid of stellar evolution tracks of Maeder (1992), which have been assigned observational parameters based on a combination of atmosphere models and empirical calibration. The starburst models use the evolutionary tracks over a range of stellar masses up to $80M_{\odot}$ and interpolate between the tracks to reduce oscillations caused by discreteness in the stellar masses. The models presented here form stars over a short Gaussian burst (FWHM of 5 million years), with the number of stars in each bin determined by the IMF. The observational parameters are predicted as the stars evolve along theoretical tracks. Further details can be found in RLRT93.

3.7.2. NGC 253 models

For NGC 253, the model values of N_{LyC} , L_{Bol} , CO index, K-band flux and ν_{SN} (supernova rate) are displayed as a function of time for two different IMF's in Figure 3.13. Each point along the curves presented has been divided by the observed values for NGC 253 in Table 3.10, so the target value for each quantity is 1. A fit can be considered good when all curves meet the target value simultaneously. In practice, since some of the observational parameters are uncertain or are merely lower limits, we choose the point on the plot where the curves can simultaneously meet the target values within the specified range of uncertainty.

The various input parameters constrain the starburst model in different ways, depending on how each is determined. The value we derived in §3.6.3 for N_{LyC} must be considered a lower limit—while there are observational uncertainties in the measurement of the $\text{Br}\gamma$ flux and further uncertainties in converting that measurement to N_{LyC} , the largest unknown is the number of ionizing photons that are absorbed by dust grains and reemitted as far-infrared photons without getting an opportunity to ionize a hydrogen atom. The derivation of the L_{Bol} suffers from uncertainty in the observations, especially in the far-IR, where most of the luminosity is emitted. It is also possible that our procedure for estimating L_{Bol} from observations made with a range of instruments and aperture sizes has underestimated that number, so we require our models to match the observed L_{Bol} to within 50%. The formal uncertainties in our determination of the CO index and K-band flux are small, but due to uncertainties about continuum placement and corrections for extinction and in the spirit of placing the smallest demands on the models as reasonable, we conservatively assign uncertainties to these quantities of 20%. As discussed in §3.3.2, the supernova rate as determined from

our observations and those of Ulvestad & Antonucci (1991) is probably no more certain than a factor of two—we require a successful model to be within this limit. However, since our estimate is generally on the low side compared with those derived by other means, and this discrepancy cannot be removed in the starburst models by changing the distance to the galaxy (since the supernova rate and other luminosity-derived parameters will scale together), we prefer models that do not fall significantly below the estimated rate.

We first attempted to fit the observations with a simple, single-burst model. with the star formation rate a Gaussian in time with a FWHM of 5 million years. The model begins 5 million years before the peak of the star formation. This short Gaussian burst of star formation has the dual advantages of being more realistic than a delta function burst as well as being very efficient in converting stellar mass to luminous output—an important consideration given our tight mass limit and the large luminosity of NGC 253.

We have also made use of the temperature constraint derived in §3.3.4. In the figure, we plot a curve labeled $T(\text{UV})_{40}$, which is the ratio of the total ionizing flux to the ionizing flux produced by stars hotter than 40,000 K. The starburst model is required to age sufficiently that no more than a small percentage of the ionizing flux comes from stars hotter than 40,000 K.

Our first model, using a solar-neighborhood IMF (RLRT93's IMF3), does a poor job of fitting the observations. Using the maximum mass allowed by our nominal upper limit derived in §3.6.1 ($9 \times 10^7 M_{\odot}$), we can only just attain the values indicated by the observations at a time of 5.5 million years after the peak of the star formation. At this point, The CO index, the ionizing flux, and K-band luminosity are very close to the observed values, while the bolometric luminosity

is a factor of 30% higher than observed and the supernova rate is a factor of 2 too low. This model only barely meets the observational constraints, however, and since we have been fairly conservative in choosing most of them we expect a successful model to meet the constraints with ease. This model also makes the uncomfortable prediction that the star formation efficiency is 75%, assuming the mass not used to make stars is still in the form of molecular gas. The implied star formation efficiency is even higher if there has been significant gas inflow into the nucleus over the ~ 10 million years since the start of the burst.

We also attempted to model the starburst using an IMF biased towards the formation of massive stars. Such a model produces much more luminosity for a given mass and should do a better job of fitting the observations of NGC 253 while remaining within the mass constraint. We used the IMF found by RLRT93 to fit the M82 observations best (their IMF 8). This model does as good a job of fitting the observations as the solar-neighborhood IMF, and in fact looks very similar to that model. The main advantage of this model is that it only uses $3.5 \times 10^7 M_{\odot}$, well within the mass limit determined in §3.6.1. As a result, this model implies a star formation efficiency of just over 50%.

To illustrate how the uncertainties in the various parameters affect the determination of the mass and age of the starburst, in Figure 3.14 we have plotted the range of allowed values for each quantity constraining the starburst for the biased IMF model we have just discussed. For example, the two dot-dashed lines in the plot indicate a range of 20% around the nominal K-band luminosity. Quantities such as the CO index and $T(\text{UV})_{40}$ do not scale with mass and so serve primarily as age constraints, showing up as vertical lines on this plot. The hatched region indicates the space in the (mass, age) plane that can be occupied by the model

while still matching the observations. In this case, the primary constraints are the lower limits on the supernova rate and the UV flux and the upper limits on the K-band luminosity and the bolometric luminosity. This figure shows that the age and mass of the starburst (given an IMF and a star formation history) are tightly constrained to 6 million years after the peak of star formation (which occurs at 5 million years in our models) and $3.9 \times 10^7 M_{\odot}$, respectively.

We next explored the effect of varying the star formation history by adding a second burst. We have parameterized this second burst by a time delay (Δt) after the initial burst and a fraction (f) of the mass consumed by both bursts that goes into the second burst, so that $f = 0.5$ implies identical masses for both bursts. In Figure 3.13 we display a model with two bursts of equal strength, separated by 25 million years. Since we have diluted the mass available by putting it into two widely-separated bursts, this model requires a total mass of $6 \times 10^7 M_{\odot}$. This model achieves a good fit at a time of 34.5 million years. The two main advantages of this double-burst model are that the bolometric luminosity is now only about 20% from the target value and the supernova rate is much higher, in reasonable agreement with the target value, because the massive stars left over from the previous burst are still producing supernovae.

It should be noted that these three models only meet the temperature constraint with difficulty - if we reduce the allowed fraction of ionizing photons emitting by stars hotter than 40000 K to less than 10%, significantly more mass is required so that the model can meet the luminosity constraints at the later time required to meet the temperature constraint. The temperature constraint is satisfied trivially if we arbitrarily impose an upper-mass cutoff on the models. This model simply eliminates the most massive, hottest stars from the beginning,

allowing the UV output of the model to be dominated by cooler stars. This scenario is unlikely, however, since observations of very young star formation regions always indicate that very massive stars are formed. Extending the duration of the burst of star formation, as in the model we present in the last panel, only aggravates the temperature problem, as a larger fraction of the ionizing flux is produced by recently-formed massive stars.

In addition to providing the best fit to the data, the model with the widely spaced bursts is in accord with the suggestion in Section 4 that HII/weak-OI LINERs are a late-starburst stage of starburst evolution. Although for convenience in modeling, we have used two separated bursts in this model, similar results would be obtained with other time dependencies for the star formation rate, so long as: 1.) a substantial portion of stars formed about 30 million years ago, so they can produce supernovae without ionizing flux; and 2.) the star formation rate has decayed rapidly for the last roughly 5 million years, so the correct ionizing flux can be produced without an excess of very hot stars.

3.8. Conclusion

We have presented high-quality spectra of the nuclear region of NGC 253 in the J, H, and K bands. We have synthesized a stellar spectrum and subtracted it from that of NGC 253 to allow us to obtain accurate measurements of faint emission lines free from the spectral structure due to stellar absorptions. We have also presented J, H, and K-band images, narrow-band images in the lines of Br γ and the (1,0)S(1) line of H₂, and high-resolution spectra at 10.5 μ m. We have used these data and data from the literature to perform a detailed study of the interstellar medium and nuclear starburst in NGC 253. We find:

- 1.) The density in the [FeII]-emitting region is $\sim 5 \times 10^3 \text{ cm}^{-3}$, similar to that observed for [FeII] emitting regions in supernova remnants. The strength of the [FeII] emission is consistent with the supernova rate estimated from radio observations and predicted by starburst models. Together, these results demonstrate that the [FeII] is produced predominantly in the supernovae in the starburst.
- 2.) Although the H_2 line ratios suggest that the emission is thermally excited, we show that roughly two thirds of the infrared H_2 luminosity is due to UV fluorescence. It is likely that significant fluorescent- excited components of H_2 emission in other starburst galaxies have been missed because the distribution of emission over many relatively faint lines makes detection difficult in spectra of modest resolution and signal to noise.
- 3.) From the mid-infrared fine structure lines of [Ne II] and [S IV], we estimate the temperature of the stars photoionizing the gas in NGC 253 to be $35,500 \pm 1000\text{K}$. We also use an upper limit to $\text{HeI}(1.7)/\text{Br}10$ to place an upper limit on the stellar temperature of $\sim 37,000\text{K}$. These values are consistent with the temperature determination of $34,500 \pm 1,000\text{K}$ derived from far infrared fine structure lines by Carral et al. (1994).
- 4.) The optical line ratios in NGC 253 indicate it is a weak-[OI] LINER and they are fitted well by the hot-star ($T \sim 45,000\text{K}$) photoionization models proposed for this type of active galaxy by Filippenko & Terlevich (1992). However, the three independent stellar temperature determinations from our work and that of Carral et al. (1994) are inconsistent with the hot star model.
- 5.) The line ratios can also be fitted by a combination of two components that are consistent with our data. The first, which accounts for the H recombination lines

and most of the forbidden optical lines, is a photoionization model for metal rich HII regions, assuming solar metallicity and an effective stellar temperature of $\sim 38,000\text{K}$ (Shields & Kennicutt 1995). The second, which accounts for the [OI] and [FeII] emission, is shocks in supernovae occurring at the rate required from our starburst models for NGC 253. These components fit NGC 253 with virtually no adjustment of free parameters. We suggest that many weak-[OI] LINERs can be explained in the same manner, rather than by the presence of a mini-AGN or by hot stars.

6.) We have used the infrared data to derive extinction-independent estimates of the primary boundary conditions for starburst models of NGC 253: mass, N_{LyC} , maximum stellar temperature, bolometric luminosity, and CO absorption depth.

7.) We find that a variety of starburst models can fit these constraints roughly. The model using a solar-neighborhood IMF requires $9 \times 10^7 M_{\odot}$ and an age near the minimum of the permitted range. It implies a star formation efficiency of 75%. Models using an IMF biased towards massive stars (and identical to the IMF fitted to the starburst in M82) require as little as $3.5 \times 10^7 M_{\odot}$ and are compatible with a larger range of starburst ages. They can have star formation efficiencies of near 50%. We tend to favor the latter class of model because its fits are more robust and because we have selected the least demanding set of observational constraints on the models (e.g., we have assumed a minimum distance to the galaxy and have assumed a lower limit to the ionizing flux).

8.) The model giving the best fit assumes that the star formation is extended over 20 to 30 million years. A portion of the supernovae are associated with stars formed near the beginning of the burst, while the ionizing flux arises from the most recently formed stars. The rate of star formation must have declined rapidly during

the last roughly 5 million years, to account for the absence of very hot stars. This model is in agreement with our suggestion that a HII/weak-OI LINER can arise from a late phase of a starburst.

Table 3.1. NGC 253 Aperture Photometry

aperture(")	m_J	m_H	m_K	$J - H$	$H - K$
3	11.55	10.41	9.51	1.14	0.90
6	10.36	9.19	8.44	1.17	0.74
12	9.34	8.25	7.56	1.09	0.69
15	9.05	7.96	7.30	1.09	0.66
2.4×12	10.41	9.21	8.45	1.20	0.76

Note. — Aperture sizes are diameters of circular apertures except for the $2.4 \times 12''$ aperture which was used to calibrate the spectra as described in the text. Typical statistical uncertainties are 2% - 5%, as determined from multiple observations of the standard star at different airmasses.

Table 3.2. Hydrogen Recombination Line Measurements

Line	$\lambda_{vac}(\mu\text{m})$	Ratio to Br γ	
		Observed	Case B
Pa β	1.2822	1.66 ± 0.10	5.58
Br13	1.6114	0.10 ± 0.03	0.14
Br12	1.6412	...	0.18
Br11	1.6811	0.12 ± 0.03	0.24
Br10	1.7367	0.26 ± 0.05	0.32
Br δ	1.9451	0.61 ± 0.04	0.65
Br γ	2.1661	1.00	1.00

Note. — No corrections for extinction have been made. The flux in Br γ is $2.59 \pm 0.10 \times 10^{-13}$ erg/s/cm² in a $2''.4 \times 12''$ aperture. The Case B values were derived from Hummer & Storey (1987), for $n = 10^2$ cm⁻³, $T = 5000$ K.

Table 3.3. He Lines

Transition	$\lambda(\mu\text{m})$	$10^{-14} \text{ erg/s/cm}^2$
$3P - 4D$	1.7007	< 1.0
$2S - 2P$	2.0586	9.38 ± 1.1

Note. — These values are uncorrected for extinction.

Table 3.4. [Fe II] Lines

Transition	$\lambda_{air}(\mu\text{m})$	Ratio to $\lambda 1.644\mu\text{m}$
$a^6D_{9/2} - a^4D_{7/2}$	1.257	0.68 ± 0.04
$a^6D_{3/2} - a^4D_{3/2}$	1.279	0.04 ± 0.01
$a^6D_{5/2} - a^4D_{5/2}$	1.294	0.13 ± 0.03
$a^6D_{7/2} - a^4D_{7/2}$	1.321	0.18 ± 0.02
$a^4F_{9/2} - a^4D_{5/2}$	1.533	0.13 ± 0.03
$a^4F_{9/2} - a^4D_{7/2}$	1.644	1.00
$a^4F_{7/2} - a^4D_{5/2}$	1.677	0.06 ± 0.02

Note. — No correction has been made for extinction. The flux in the $\lambda 1.644\mu\text{m}$ line in a $2'.4 \times 12''$ aperture is $3.56 \pm 0.18 \times 10^{-13}$ erg/s/cm².

Table 3.5. H₂ Line Fluxes

Transition	$\lambda_{vac}(\mu\text{m})$	Ratio to (1,0)S(1)				
		Obs.	Dered.	Fluor.	Therm.	Mix
(5,3)Q(1)	1.4929	< 0.1	< 0.18	0.43	1.0×10^{-4}	0.11
(4,2)O(3)	1.5099	< 0.1	< 0.18	0.42	7×10^{-4}	0.11
(6,4)Q(1)	1.6015	< 0.15	< 0.24	0.33	1.3×10^{-4}	0.08
(5,3)O(3)	1.6135	< 0.15	< 0.23	0.38	9×10^{-5}	0.10
(6,4)O(3)	1.7326	< 0.15	< 0.20	0.31	1×10^{-5}	0.08
(1,0)S(3)	1.9576	0.89 ± 0.08	0.99 ± 0.09	0.67	1.02	0.93
(2,1)S(4)	2.0041	0.18 ± 0.02	0.19 ± 0.02	0.12	0.02	0.05
(1,0)S(2)	2.0338	0.36 ± 0.05	0.38 ± 0.05	0.50	0.38	0.41
(2,1)S(3)	2.0735	0.26 ± 0.06	0.27 ± 0.06	0.35	0.08	0.15
(1,0)S(1)	2.1218	1.00	1.00	1.00	1.00	1.00
(2,1)S(2)	2.1542	0.20 ± 0.04	0.20 ± 0.04	0.28	0.04	0.09
(1,0)S(0)	2.2233	0.30 ± 0.03	0.28 ± 0.03	0.46	0.21	0.27
(2,1)S(1)	2.2477	0.21 ± 0.02	0.20 ± 0.02	0.56	0.08	0.21
(2,1)S(0)	2.3556	< 0.1	< 0.09	0.26	0.02	0.08
(3,2)S(1)	2.3865	< 0.1	< 0.09	0.29	5.8×10^{-3}	0.08
(1,0)Q(1)	2.4066	0.79 ± 0.16	0.68 ± 0.14	0.99	0.70	0.77
(1,0)Q(2)	2.4134	0.34 ± 0.07	0.29 ± 0.06	0.51	0.23	0.31
(1,0)Q(3)	2.4237	0.75 ± 0.15	0.64 ± 0.13	0.70	0.70	0.70
(1,0)Q(4)	2.4375	0.20 ± 0.04	0.17 ± 0.03	0.28	0.21	0.23

Note. — The flux in the (1,0)S(1) line is $1.21 \pm 0.07 \times 10^{-13}$ erg/s/cm² (uncorrected for extinction) in a $2''.4 \times 12''$ aperture.

Table 3.6. H₂ rotational excitation temperatures

Vibrational Level	Rotational Levels	Rotational Excitation Temperature (K)
1	0,2	1350 ± 229
	1,3	1921 ± 175
2	1,3	3528 ± 860

Table 3.7. Predicted optical line ratios

ratio	predicted	observed	ref.
OI/H α	0.026	0.044	1
[NII]/H α	0.78	0.78	1
[SII]/H α	0.45	0.40	1
[OIII]/H β	0.49	0.47	2

Note. — (1) Armus, Heckman, & Miley 1989; (2) Tadhunter et al. 1993.

Table 3.8. Velocity gradients of spectral features

Feature	gradient ($\text{km s}^{-1}/''$)
Br γ	7.4 ± 0.4
H ₂	7.7 ± 0.4
CO(2,1)	7.5 ± 0.9

Note. — These numbers are not corrected for inclination.

Table 3.9. Absorption features

Species	$\lambda_{vac}(\mu\text{m})$	$W_\lambda(\text{\AA})$
MgI	1.4882	1.6
MgI	1.5048	5.5
$^{12}\text{CO}(3,0)$	1.5582	4.0
MgI	1.5770	1.1
$^{12}\text{CO}(4,1)$	1.5780	5.6
FeI	1.5823	3.4
SiI	1.5893	4.6
SiI	1.5964	3.3
$^{12}\text{CO}(5,2)$	1.5982	3.6
$^{12}\text{CO}(6,3)$	1.6189	7.0
$^{12}\text{CO}(8,5)$	1.6618	2.2
AlI	1.6755	3.1
$^{12}\text{CO}(9,6)$	1.6840	4.3
$^{12}\text{CO}(10,7)$	1.7067	2.5
MgI	1.7146	2.3
FeI	1.7307	1.6
SiI	1.7332	3.0
FeI	2.0704	1.0
MgI	2.1066	1.2
AlI	2.1170	1.4
SiI	2.1360	1.4
NaI	2.207	3.2
FeI	2.2263	2.0
CaI	2.2631	3.3
CaI	2.2657	1.8
MgI	2.2814	1.1
$^{12}\text{CO}(2,0)$	2.2935	13.1
$^{12}\text{CO}(3,1)$	2.3227	16.4
$^{13}\text{CO}(2,0)$	2.3448	10.8
$^{12}\text{CO}(4,2)$	2.3525	16.4
$^{13}\text{CO}(3,1)$	2.3739	13.0
$^{12}\text{CO}(5,3)$	2.3830	17.1

Table 3.10. Summary of Starburst Parameters

Parameter	Value
Mass	$< 9 \times 10^7 M_{\odot}$
L_{Bol}	$1.1 \times 10^{10} L_{\odot}$
M_K	-20.4
$\log N_{\text{LyC}}$	> 53.0
SNR	0.03 yr^{-1}
CO	0.20

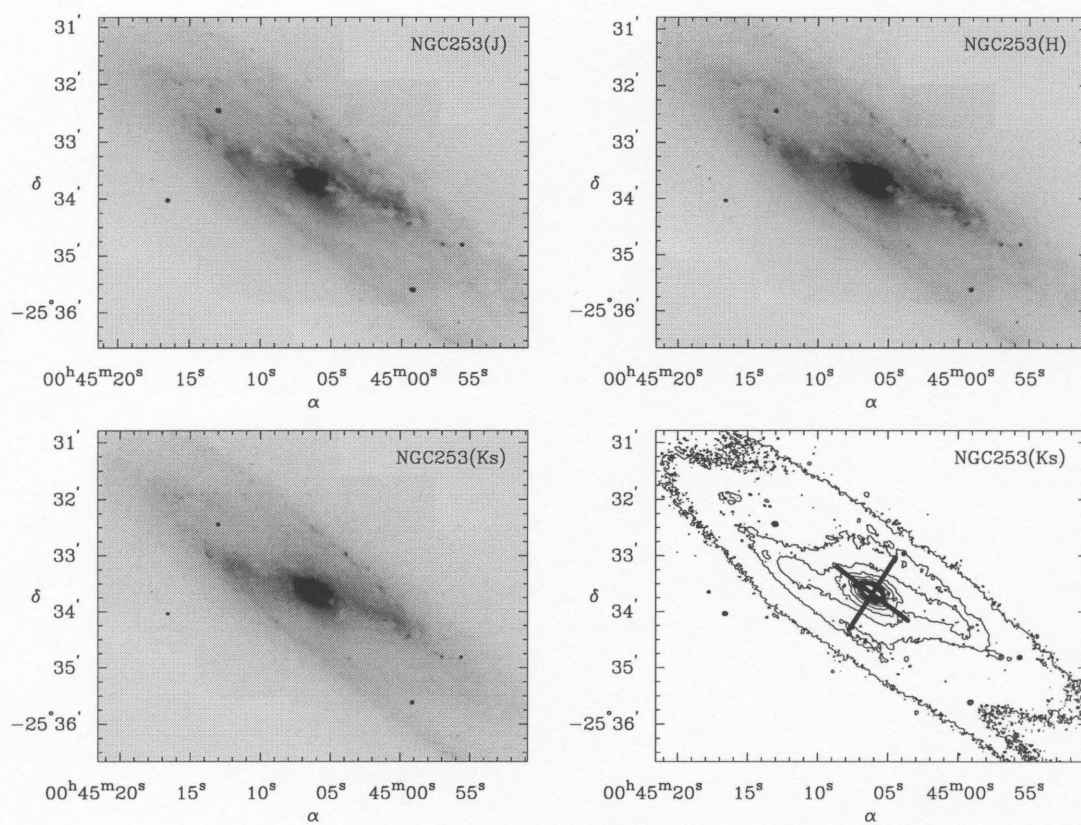


Figure 3.1 Greyscale images of NGC 253 in J, H, and Ks bands, plus a contour map at Ks overlaid with the slit positions.

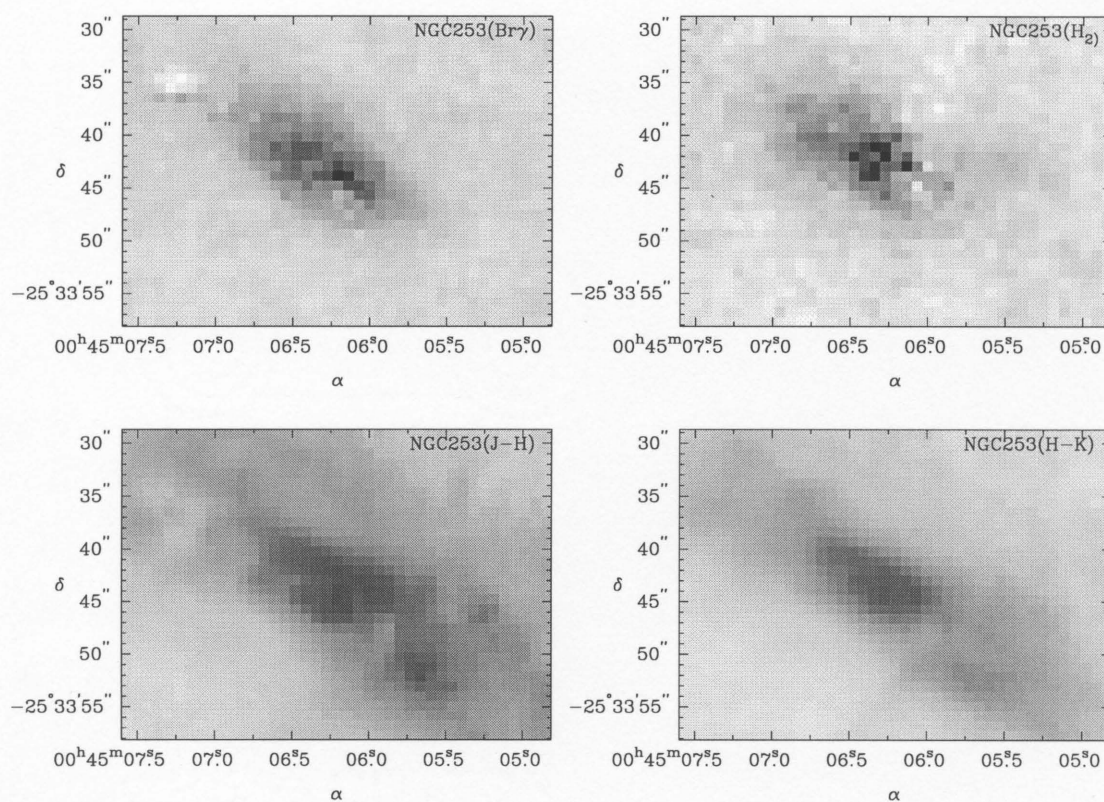


Figure 3.2 Greyscale images of the nuclear region of NGC 253 in narrow, continuum-subtracted bands centered at the lines of H $_2$ (1,0)S(1) and Br γ , plus $J-H$ and $H-K$ color maps of the same region. The display range is 0.6 to 1.5 magnitudes for the $J-H$ image and 0.1 to 1.2 magnitudes for the $H-K$ image.

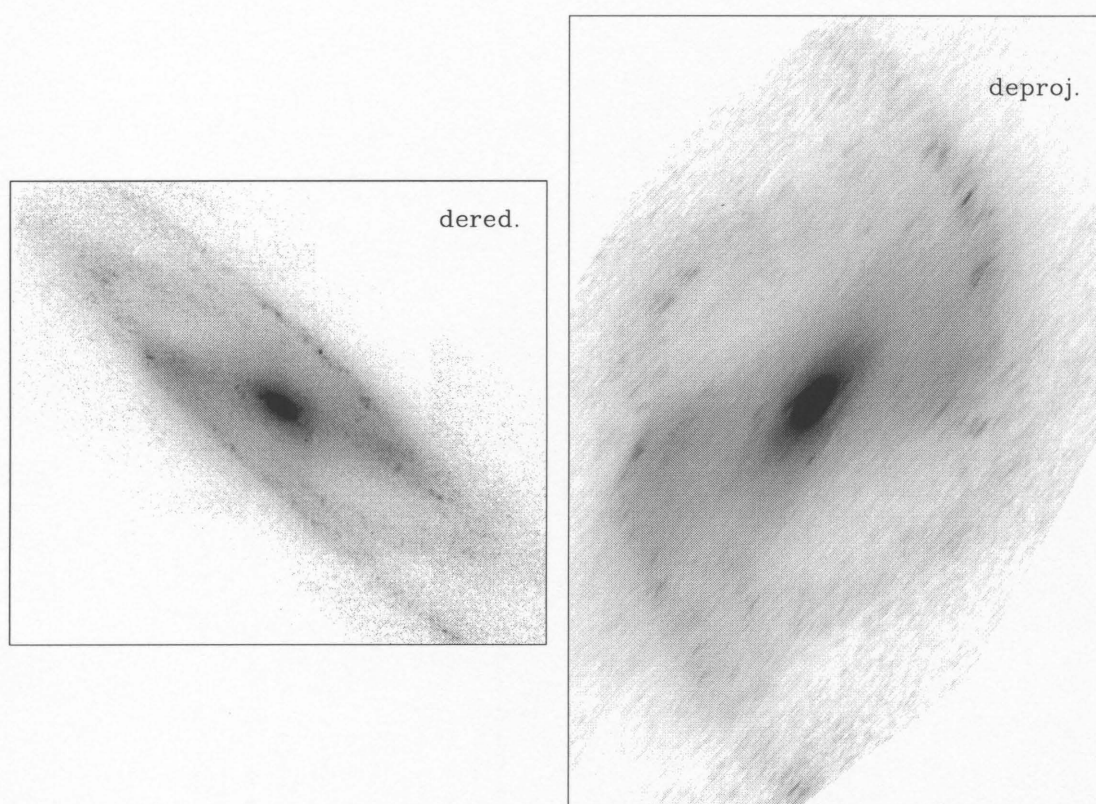


Figure 3.3 K-band image of NGC 253 dereddened as described in the text, then deprojected along the minor axis to determine how the galaxy would appear if viewed face on. The images are presented on a logarithmic intensity scale.

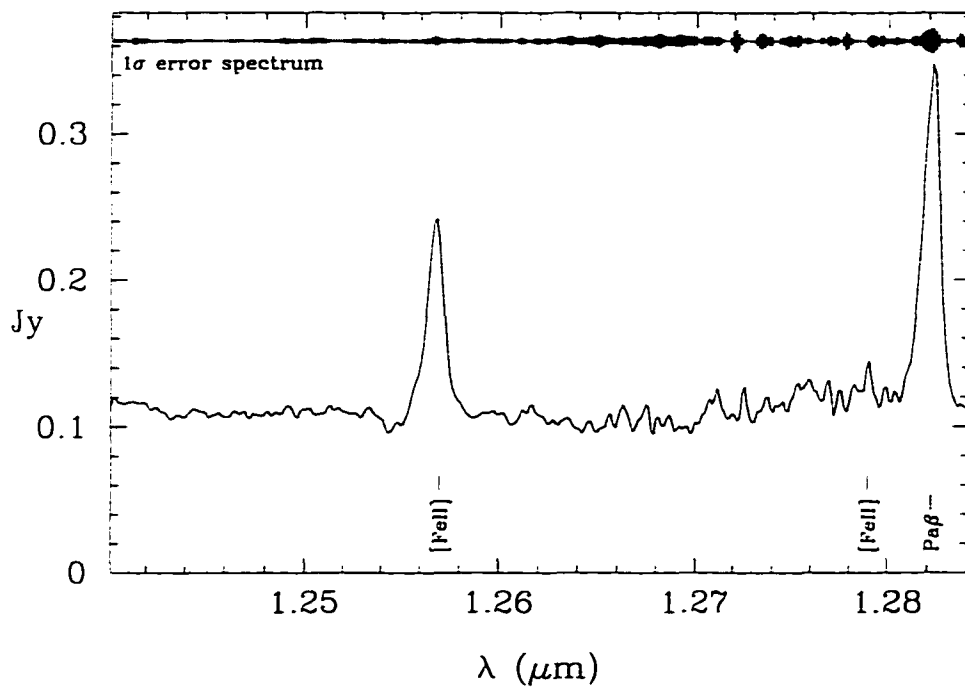


Figure 3.4 High-resolution J-band spectrum of NGC 253. The slit was oriented along the plane of the galaxy and was $2''.4$ wide. The spectrum shown here is the sum of the central $12''$. The spectrum was flux-calibrated as described in the text and has been shifted to zero velocity. Above the flux spectrum is plotted the 1-sigma error spectrum, simply determined from the dispersion in the measurements at each point in the spectrum.

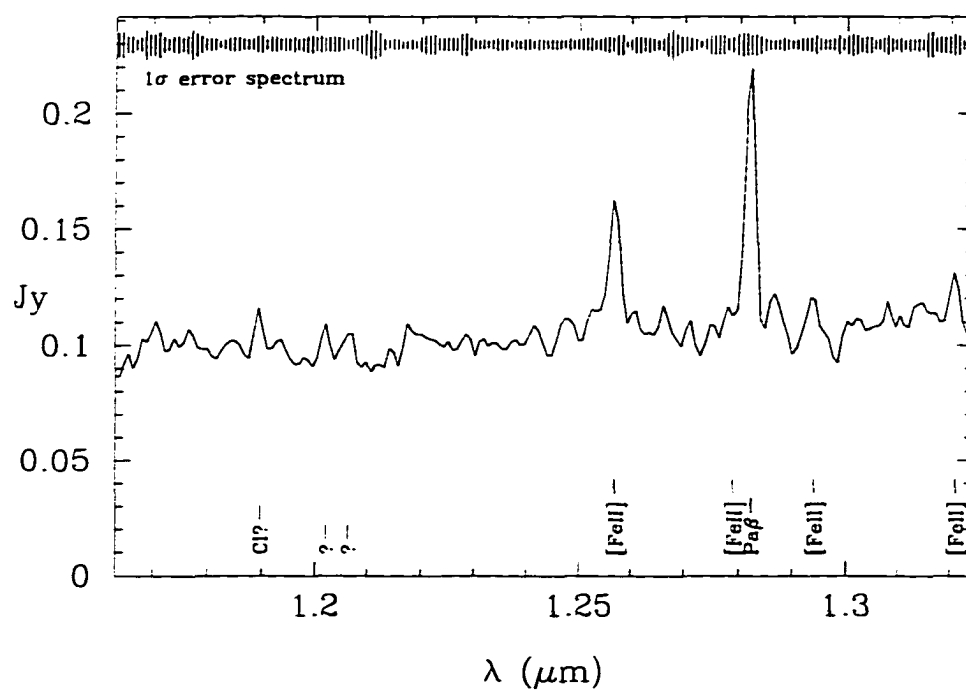


Figure 3.5 Low-resolution J-band spectrum of NGC 253. Details as for high-resolution spectrum.

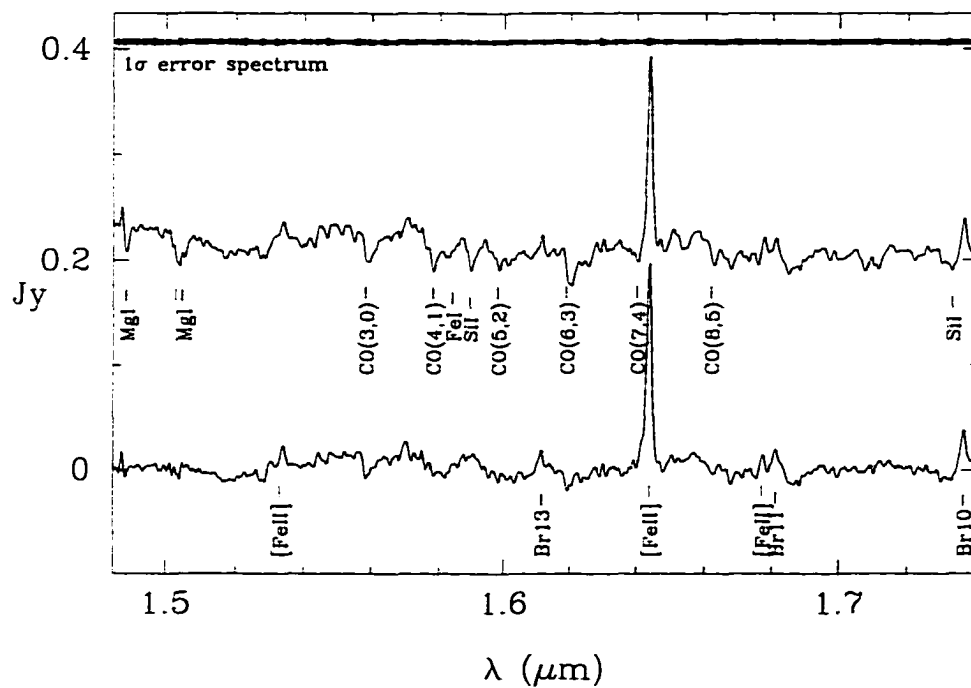


Figure 3.6 High-resolution H-band spectrum of NGC 253. Details as for J-band spectrum. The lower spectrum is the result of subtracting a stellar continuum spectrum (produced by combining several late-type stellar spectra as described in the text) from the galaxy spectrum. The positions of several interesting spectra features are marked.

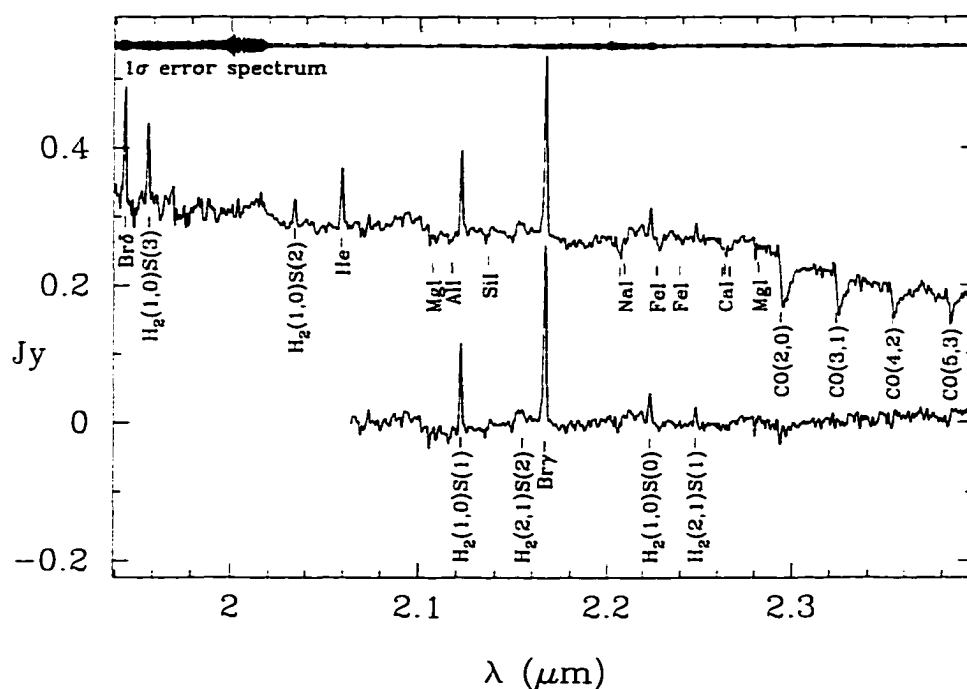


Figure 3.7 High-resolution K-band spectrum of NGC 253. Details as for J-band spectrum, and a stellar continuum subtraction has been performed as for the H-band spectrum. The region shortward of $2.06\mu\text{m}$ contains few significant stellar absorptions and so many of our stellar spectra do not cover this region. Note that the error spectrum indicates the spectrum is significantly noisier shortward of $2.02\mu\text{m}$, where the atmospheric transmission becomes poor.

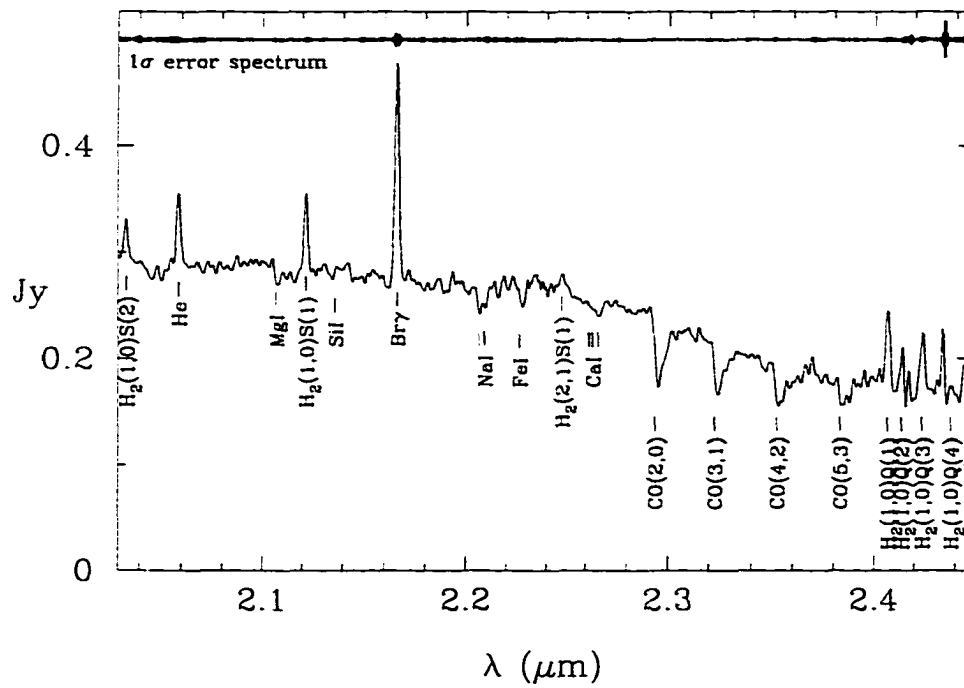


Figure 3.8 Low-resolution K-band spectrum of NGC 253. Details as for J-band spectrum. The apparent emission features beyond $2.4\mu\text{m}$ that are not labeled as H_2 lines correspond to regions of poor atmospheric transmission, as indicated by the spikes in the error spectrum at those points.

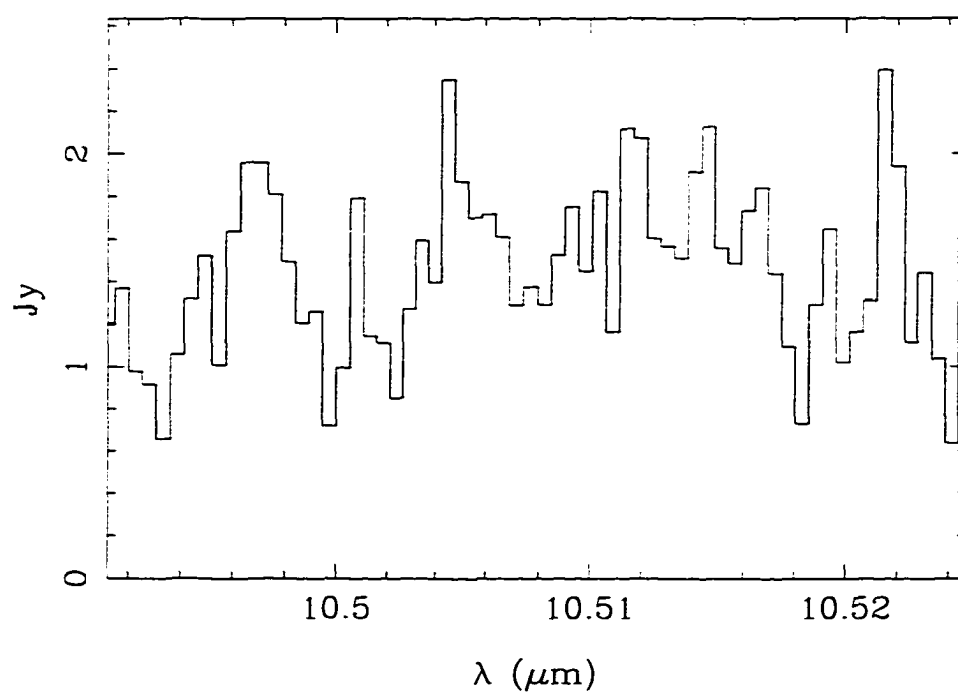


Figure 3.9 Spectrum of [S IV] emission from central region of NGC 253. See details in Section 3.2.3.

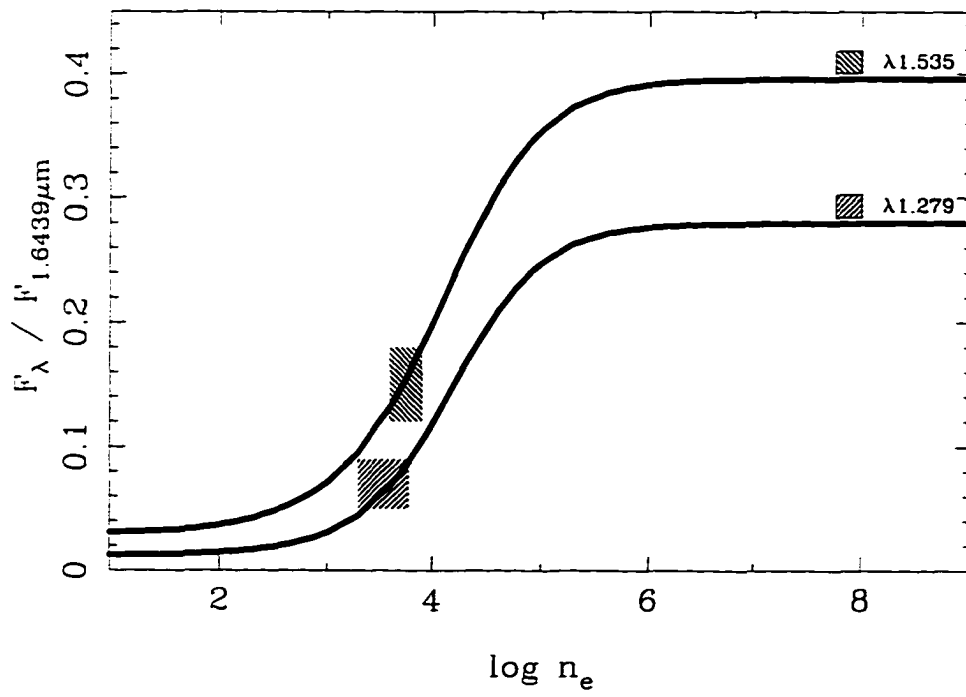


Figure 3.10 Plot of [Fe II] line ratios as a function of density. The range of the observations is indicated by the shaded region. The diagnostic lines we have used here indicate that $\log(n_e)$ in the [Fe II] -emitting region is 3.7 ± 0.13 .

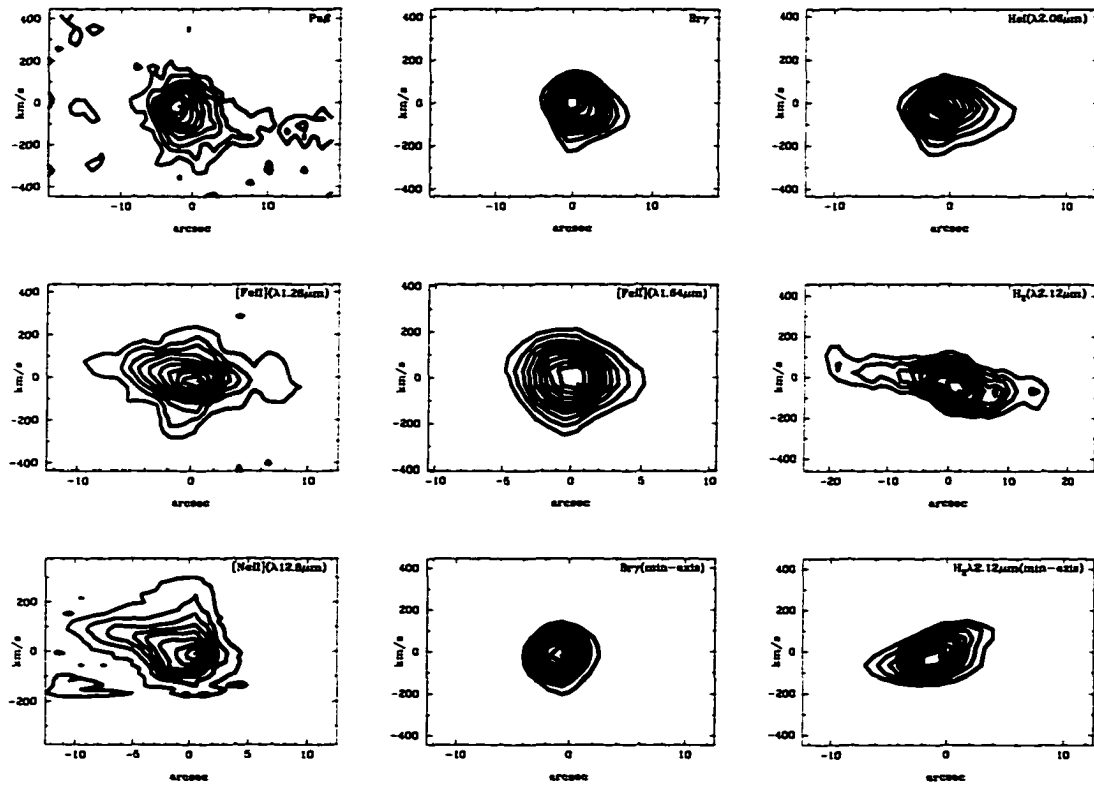


Figure 3.11 Position-velocity plots along the major axis for several strong lines. Also included are plots along the minor axis for Br γ and H $_2$ (1,0)S(1). In each case, the upper 80% of the contours are plotted. Note that the spatial axis of the major-axis H $_2$ plot is larger to cover the extent of the emission.

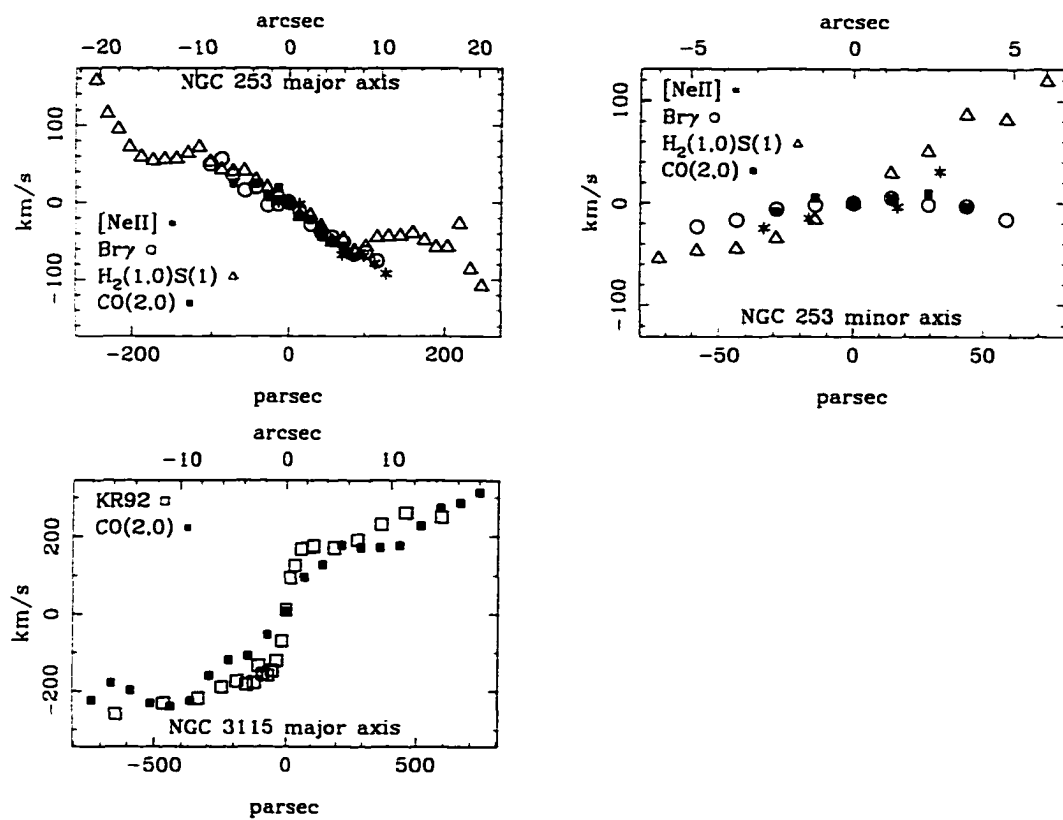


Figure 3.12 Rotation curves for NGC 253 and NGC 3115. The linear dimensions have been determined by assuming distances of 2.5 Mpc and 8.4 Mpc, respectively, for NGC 253 and NGC 3115.

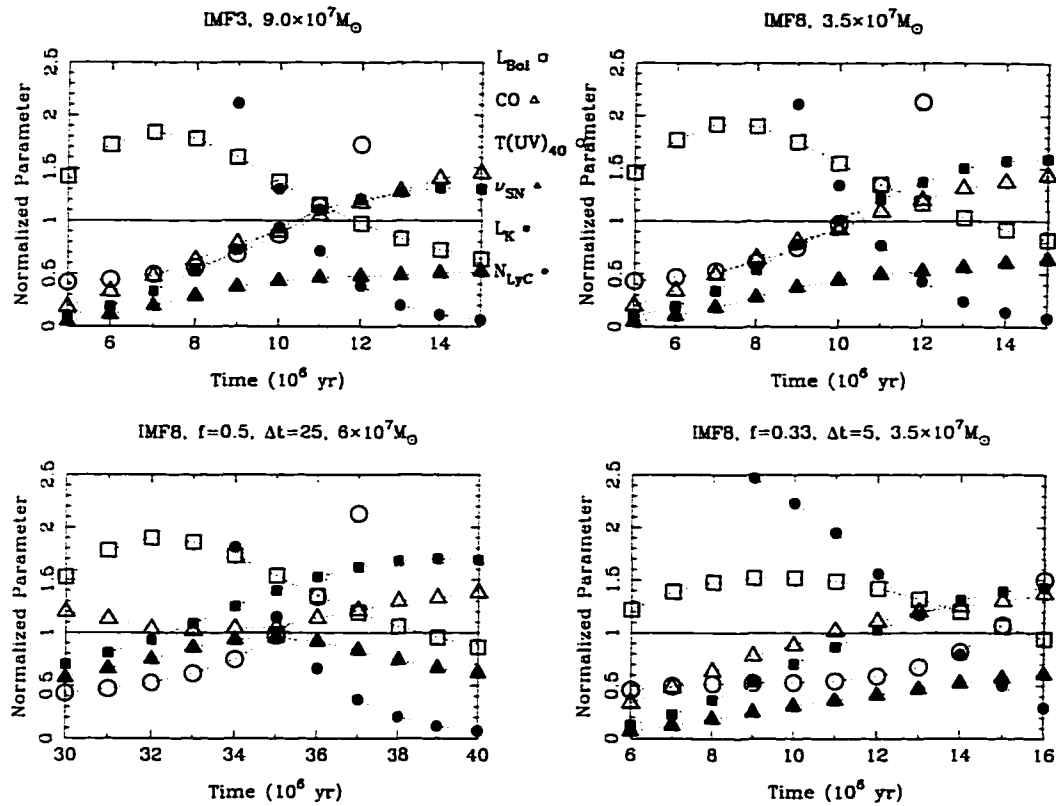


Figure 3.13 Starburst models of NGC 253 using a solar-neighborhood IMF (RLRT93's IMF 3) and an IMF biased towards massive-star formation (RLRT93's IMF 8). The points represent output from our starburst model as a function of time, where each curve has been ratioed to the corresponding observational parameter listed in Table 3.10. A reasonable fit is indicated where all the curves come within the range of uncertainties to match the target value (ideally at 1). The IMF used and the mass required to match the observations is indicated for each panel. For the bottom panels, double-burst models with a delay Δt (in millions of years) between bursts and the fraction f of the mass that was contained in the second burst are presented.

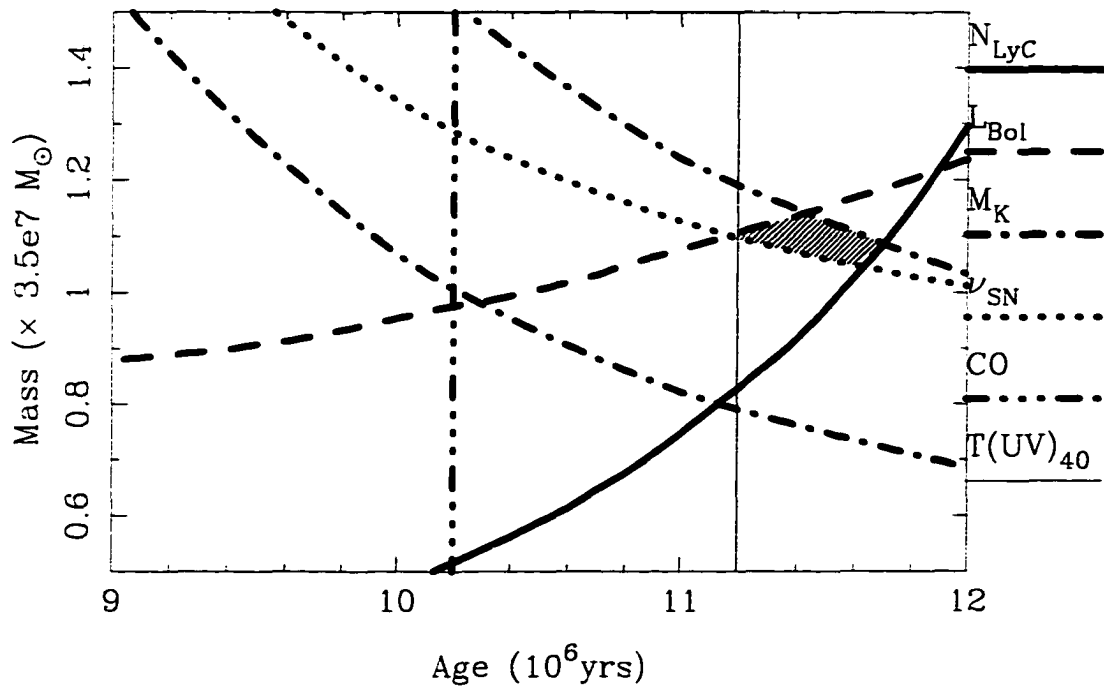


Figure 3.14 Allowed values in the (mass, age) plane for a single-burst starburst model using IMF 8 of RLTLT93. The hatched region is constrained by the model values from Figure 3.13 with uncertainty ranges as described in the text. The CO index and $T(\text{UV})_{40}$ parameters do not scale with mass and therefore serve primarily as age constraints.

CHAPTER 4

EXPLORING THE RANGE OF STARBURST PROPERTIES

We present high-resolution ($R \sim 3000$), long-slit spectroscopic observations of the galaxies IC 342, NGC 2146, NGC 3079, and NGC 7714 in the H and K bands, plus J-band spectra at high resolution for IC 342 and at a resolution of 800 for the other three galaxies. We have obtained broadband imaging of these galaxies in the J, H, and Ks bands, plus narrowband imaging in Br γ and the (1,0)S(1) line of H $_2$ for NGC 2146. We use these data and data from the literature to constrain models of the nuclear starbursts in these galaxies. The high sensitivity and resolution of the spectra plus the use of a long slit allows us to derive kinematic properties of the nuclear region in addition to other constraints on the starburst population, such as ionizing flux and CO index.

We use the models to derive the intensity and age of the starburst in each galaxy. We find that the starbursts in these four galaxies display a large range in age and strength, with NGC 7714 being the youngest and NGC 3079 the oldest.

Our model fits indicate that the starburst in IC 342 is the least massive, with at least $1.0 \times 10^7 M_{\odot}$ required to fit the observations, and the starburst in NGC 2146 the largest, requiring at least $3.3 \times 10^8 M_{\odot}$. As the starburst in a galaxy ages and decreases in luminosity, it becomes more difficult to disentangle the burst from the underlying stellar population. For the younger starbursts, however, in which the observed emission is dominated by the starburst, we find strong evidence for a starburst IMF that is biased towards massive stars.

4.1. Introduction

In this paper, we describe observations and modeling of four starburst galaxies. We list some properties of these four galaxies in Table 4.1. The prodigious star formation in these galaxies has been studied in detail by other authors. For example, Becklin et al. (1980) present infrared and radio observations of IC 342 and interpret the large luminosity of the nuclear region as due to enhanced star formation there. Smith, Harvey, & Lester (1995) present high-resolution FIR imaging of NGC 2146 and show that the bulk of this radiation is attributable to heating by young stars. Hutchings et al. (1990) present extensive optical and NIR data (both imaging and spectroscopy) of NGC 2146 and demonstrate that star formation is sufficient to account for their observations. NGC 3079 has undergone a powerful starburst and has developed a dramatic galactic superwind (Armus, Heckman, & Miley 1989; Veilleux, Cecil, & Bland-Hawthorn 1995; Filippenko & Sargent 1992) which has impacted the nearby galaxy NGC 3073 and may even have triggered a starburst there (Irwin et al. 1987).

NGC 7714 is an especially interesting case because the starburst is so young and intense there. Weedman et al. (1981) present an early study of NGC 7714

in which they account for observations over a broad range of wavelengths with a simple model of nuclear star formation. Bernlöhner (1993) discusses sophisticated starburst modeling of a sample of interacting galaxies and includes a detailed discussion of NGC 7714, reaching similar conclusions to us regarding the form of the IMF in that galaxy. Calzetti (1997) concludes that *no* modification to a solar-neighborhood IMF is required to fit the observations of NGC 7714, although the observations upon which this conclusion are based were obtained in an aperture much larger than the starburst covers (see §4.4.1), raising the observed M/L via dilution from an older disk population and therefore easing the constraints on the models considerably. Recently, González-Delgado et al. (1995) detected Wolf-Rayet features in the spectrum of NGC 7714, indicating that this galaxy has undergone a strong and very recent burst of star formation.

Most of these galaxies (except for IC 342) show obvious signs of gravitational interactions. It seems likely that the starbursts in these galaxies have been triggered by the interaction. The companion galaxy has not yet been identified in the case of NGC 2146, but Hutchings et al. (1990) argue that a smaller companion may have been completely disrupted by its encounter with NGC 2146. NGC 3073 is a nearby companion of NGC 3079 and, as discussed above, shows obvious signs of a physical interaction with NGC 3079. NGC 7714 is connected to the nearby spiral NGC 7715 by a bridge of emission (e.g., González-Delgado et al. (1995)) and may even have triggered a recent starburst in that galaxy (Bernlöhner 1993). Although IC 342 has no obvious, close companion, it does reside in a well-populated group and is separated from the dwarf galaxy UGC A86 by only $1''.6$, which implies a physical separation of 100 kpc if UGC A86 lies at the same distance (3.6 Mpc) as IC 342. This dwarf galaxy is also undergoing a period of higher-than-average star formation (Hodge & Miller 1995).

4.2. Observations and Data Reduction

4.2.1. Images

J , H , and K -band images of the galaxies were obtained at the Steward Observatory (SO) 1.55m and 2.3 telescopes on three different observing runs using the NICMOS3-based SO infrared camera. We also obtained narrowband images of NGC 2146 in $\text{Br}\gamma$ and the $(1,0)\text{S}(1)$ line of H_2 on 7 November 1995, using a tilting interference filter (described in Latter et al. 1993) in the infrared camera. A summary of the observations is presented in Table 4.2. This table also lists the standard stars used, which include stars from Courteau (1994) and Elias et al. (1982). Tables 4.4 through 4.7 list photometric measurements for each galaxy in multiple apertures to facilitate comparison with measurements by other workers. We note in passing that the NGC 7714 photometry may have been slightly affected by smoke from a forest fire burning a mile away from the observatory during the observing run, although our photometry compares well to results in the literature.

Data reduction procedures are as described in ERRL96. The plate scale was 0.92 "/pixel at the 1.55m telescope and 0.65 "/pixel at the 2.3m telescope. The broad-band images are presented as contour plots in Figures 4.1 through 4.4. Each image is presented with north at the top and east to the left. The coordinate scale is plotted assuming that the K -band peak corresponds to the coordinates quoted for that galaxy in the NASA Extragalactic Database (NED).

$J - H$ and $H - K$ color images of the galaxies are presented in Figures 4.5 through 4.7. The color images of NGC 7714 showed only that the colors become slightly redder towards the nucleus as already indicated by Table 4.7, so we have not displayed them here. Narrowband H_2 and $\text{Br}\gamma$ images of NGC 2146 are

presented in Figure 4.6.

We applied additional processing to our images of NGC 2146 and NGC 3079. These galaxies cover a large angular area in our images and display an irregular structure, most likely due to patchy dust extinction. We have produced dereddened images of these galaxies by using our $H - K$ color images as an indicator of the amount of dust extinction, under the assumption of a foreground screen geometry for the dust. As shown in ERRKA97, this assumption predicts a K-band extinction which is similar to that obtained using more complex dust geometries, although the extinction at shorter wavelengths will not, in general, be correctly predicted by this procedure. We have assumed an intrinsic $H - K$ color of 0.2 for the stellar population and used the extinction law of Rieke & Lebofsky (1985) to compute A_K from $E(H - K)$, then corrected the K-band images of NGC 2146 and NGC 3079 for the predicted amount of extinction. The dereddened image of NGC 2146 is presented in Figure 4.2.

The dereddened image of NGC 3079 made evident spiral arms which can be traced all the way into the nucleus of this nearly edge-on galaxy. To bring out this faint structure in our images, we smoothed the dereddened image of NGC 3079 with a boxcar filter and subtracted this from the unsmoothed image. The residual is presented in Figure 4.7. We discuss the morphology in more detail in §4.3.1.

4.2.2. Near-IR spectra

We obtained J, H and K-band spectra at the Steward Observatory 2.3m telescope during several observing runs from 1994 to 1996. The instrument used was FSpec, which is described in Williams et al. (1993). The scale along the spatial axis was 1.2 "/pixel and the spectral resolution was ~ 3500 , ~ 2000 , and ~ 3000 in the J,

H, and K bands, respectively, in the high-resolution mode and ~ 800 in the J-band low-resolution mode. The slit was two pixels wide. A summary of the observations is presented in Table 4.3. Data reduction procedures are as described in ERRL96 and ERRKA97.

The spectrometer slit was generally oriented East/West, although we repositioned the slit for those galaxies which were extended enough to obtain a significant rotation curve (i.e., NGC 2146 and NGC 3079) or to explore the extent of the emission associated with the starburst. Positioning of the slit and guiding during the observations was facilitated by a slit-viewing infrared camera (using a NICMOS2 array), allowing us to position the slit precisely on the nuclei of the galaxies, especially those for which heavy dust obscuration hides the nucleus at optical wavelengths. The slit positions used for each galaxy are represented graphically in Figures 4.1 through 4.4.

4.3. Discussion

4.3.1. Continuum morphology

IC 342 is a nearby galaxy at a low galactic latitude of $10^\circ 6'$ and as a result many foreground stars are apparent in the images presented here. It has a very bright, compact nucleus and an outer disk of fairly low surface brightness, low enough that the spiral arms are not apparent in our images. Close to the nucleus, however, spiral-like structures appear in our $H - K$ color map and faintly in our $J - H$ color map (see Figure 4.5). The spiral structure seen in the color maps has a very similar morphology to the CO emission observed by Ishizuki et al. (1990). We attribute this structure to reddening due to dust associated with the concentrations of molecular gas in this region. The red structures we observe in the near-infrared

correspond to dark dust lanes observed, for example, in (unpublished) WFPC2 images of this galaxy.

The most striking feature of NGC 2146 is the prominent dust lane across the galaxy. The structure of the dust lane is most easily discerned in our color maps (Figure 4.6, or in CCD images such as those of Hutchings et al. (1990). NGC 2146 also displays a highly disturbed morphology, probably due to an interaction with an as-yet unidentified galaxy. Some of the asymmetric structure of NGC 2146 can be attributed to patchy dust extinction—our dereddened image of the galaxy (in Figure 4.2) shows much more regular contours than even the K-band image, which is subject to only 10% of the attenuation due to dust that affects visible light. The ridge of emission on the southeast side of the galaxy noted by Hutchings et al. (1990) is most clearly seen in our dereddened image and is probably a continuation of the structure seen at larger scales in, e.g., Benvenuti, Cappaccioli, & D’Odorico (1975) or Young et al. (1988). Whether this structure is a spiral arm or some sort of tidal feature is unclear.

NGC 3079 is a large spiral galaxy viewed nearly edge-on. This galaxy shows signs of having undergone a gravitational interaction, possibly with the nearby galaxy NGC 3073. The faintest contours of our infrared images show a distinctive warping, and it is also interesting to note that the K-band isophotes twist by $\sim 3^\circ$ as they approach the nucleus. The filtered image displayed in Figure 4.7 clearly shows the spiral arms winding into the strong peak at the nucleus of the galaxy, and it is also clear from this image that the bright nuclear region has a different position angle from the rest of the galaxy. Several knots of emission are apparent in this image, which we interpret as local regions of active or recent star formation in the disk of the galaxy. A comparison of this image with the $H\alpha$ image presented

by Veilleux, Cecil & Bland-Hawthorn (1995) shows that these knots coincide, as expected, with regions of strong $H\alpha$ emission.

NGC 7714 has a highly asymmetric appearance and is probably interacting with the nearby galaxy NGC 7715. At the faintest flux levels in our images, we can trace the bridge of emission between these two galaxies observed by Gonz  les-Delgado et al. (1995). Like most of the other galaxies here (except for NGC 2146), the starburst region is quite compact and appears to be confined to the nucleus. The northern spiral arm wraps around to the east and nearly forms a semicircle, while the southern spiral arm is probably warped into the plane of the sky so that we can't observe it. The nucleus is very bright compared to the disk of the galaxy, as can be seen from the broadband images.

4.3.2. Emission-line morphology

We can use the position-velocity maps presented in Figures 4.20 through 4.22 to trace the emission-line morphology along the slit. This provides us with information on the spatial extent of the starburst in each galaxy. To create the position-velocity maps, the continuum around each line was fitted with a second-order polynomial at each image column and subtracted from the two-dimensional spectrum. The image was then trimmed to the region around the spectral line to produce the plots shown here. For each spectral line we have presented in this manner, we have centered the plot on the peak of the continuum emission near the spectral line. Since the galaxy nuclei we are studying here are fairly dusty, there is some concern that strongly asymmetric extinction might cause the continuum peak to shift systematically with wavelength, as the effect of attenuation by dust decreases with wavelength. If this were occurring, the position-velocity plots of short wavelength lines would not be aligned with lines at long wavelengths. The color images of each galaxy

and the position-velocity diagrams discussed here, though, demonstrate that this is probably not a strong effect in these galaxies. For the one galaxy discussed in this paper that has a very extended starburst, we have obtained narrow-band images (Figure 4.6) and multiple slit positions to constrain better the extent of the line emission.

Figure 4.5 shows position-velocity diagrams of strong lines of ionized hydrogen, molecular hydrogen, helium, and forbidden lines from singly-ionized iron in the nuclear region of IC 342. The line emission shows that we detect no significant velocity gradients at a slit position of 90° , which is not surprising since the nucleus is so compact and the inclination of this galaxy so low. Interestingly, this figure shows that the starburst in this galaxy is *not* centered on the nucleus, but instead peaks about $4''$ on either side of the nucleus. With only one slit position, we cannot tell if the star formation occurs mainly in the two regions we observe or is distributed in a ring around the nucleus. The lines from $\text{Br}\gamma$, He, and $[\text{Fe II}](1.644\mu\text{m})$ are stronger in the eastern region, probably indicating that the star formation event there consumed more mass than its counterpart in the west, occurred more recently, or both. The contrast between the eastern and western star formation regions is not as strong in our J-band spectra, specifically in the lines of $\text{Pa}\beta$ and $[\text{Fe II}](1.257\mu\text{m})$. This suggests that the extinction in the eastern lobe may be higher, causing this region to be attenuated more than the western lobe at short wavelengths. The asymmetric dust extinction suggested by the spectra is not reflected in our $J - H$ and $H - K$ color images, where if anything the western region shows redder colors indicative of heavier extinction.

We detect strong line emission across a significant fraction of the disk of NGC 2146, as shown in Figures 4.6 and 4.21. Except for the $[\text{Fe II}]$ line, the

emission is stronger in the southeastern half of the galaxy. The emission, especially in molecular hydrogen, is quite extended—the (1,0)S(1) line of H_2 is significantly detected over nearly an arcminute centered on the nucleus, which corresponds to 4 kpc at the distance of NGC 2146. The color maps (Figure 4.6) show that the reddening is not significantly greater northwest of the nucleus as compared to southeast, so the starburst must be intrinsically stronger or younger to the southeast. We detect strong velocity gradients in this galaxy, as discussed in §4.4.5. We have also presented plots of spectral lines along the minor axis of this galaxy, which show that strong line emission extends well over the central kiloparsec along the minor axis.

We detect only weak recombination-line emission from NGC 3079 while lines from singly-ionized iron and molecular hydrogen are quite strong. Most of our spectra of this galaxy were obtained with the slit oriented along the minor axis, and we detect no significant extension of spectral features along that axis. We also obtained major-axis spectra near the (1,0)S(1) line of H_2 at $2.12\mu\text{m}$. The position-velocity diagram of this line (Figure 4.22) shows a large velocity gradient through the nuclear region and also shows that the H_2 emission is extended over more than 1 kpc at the center of this galaxy.

The emission we detect in NGC 7714 is quite compact, being largely confined to the nucleus. There is some hint that in this galaxy, as in the others studied here, the H_2 emission tends to be more extended than the other spectral lines.

4.3.3. Spectral features

Infrared spectra of these galaxies are presented in Figures 4.8 through 4.19. The spectra are characterized by strong hydrogen recombination lines, most prominently

$\text{Br}\gamma$ and $\text{Pa}\beta$, but higher-order Brackett lines ($\text{Br}10 - \text{Br}13$) are also observed in most of the galaxies. The fluxes of the strongest recombination lines we have observed are listed in Table 4.8. Most of the galaxies display a helium line at $2.058\mu\text{m}$. All of the galaxies display strong H_2 emission, especially NGC 2146 and NGC 3079, which have a luminosity in the (1,0)S(1) line that is nearly two orders of magnitude larger than in IC 342, which has the weakest H_2 emission of the galaxies studied here. All these galaxies also display strong [Fe II] lines. The measurements of strong emission lines other than $\text{Pa}\beta$ and $\text{Br}\gamma$ are listed in Table 4.9.

These galaxies also display prominent absorption lines, most significantly from first and second overtone CO transitions in the K and H bands, respectively. Many atomic lines are present, too, with the strongest lines due to Na, Ca, Mg, Si, Fe, and Ti. The continuum spectra closely resemble cool supergiants.

4.4. Model constraints

We now derive specific constraints on our starburst models for each galaxy.

4.4.1. Size of starburst region

The size of the starburst region can be defined as the region containing significant numbers of massive stars, indicative of recent, prodigious star formation. We thus require a tracer which can be uniquely identified with massive stars and for which data can be obtained at high spatial resolution and which is not strongly affected by extinction. Several types of observations are appropriate: a hydrogen recombination line such as $\text{Br}\gamma$, broad-band MIR flux from hot dust associated with massive stars, or radio continuum emission (both thermal emission from HII regions and nonthermal from SNR's). Since much of the luminosity of a starburst is

emitted at FIR wavelengths, such long wavelength observations can be quite useful for constraining the extent of the starburst, but the available spatial resolution of such observations is often too low to be indicative of the size of the (often compact) starburst regions.

IC 342: $10.8\mu\text{m}$ and $19.2\mu\text{m}$ measurements by Telesco, Dressel, & Wolstencroft (1993) indicate the size of the emitting region at those wavelengths is $4''.6 \times 8''.0$, oriented east-west. Our spectra indicate the east-west extent of the line emission is about $8''$, so we have assigned an $8''$ aperture to the starburst in this galaxy.

NGC 2146: Our measurements of strong spectral lines indicate the starburst covers the central $20''$. Measurements at 50 and $100\mu\text{m}$ by Smith, Harvey, & Lester (1995) indicate the far infrared luminosity arises from a region $21'' \times 16''$ (FWHM), elongated along the major axis of the galaxy. We therefore take the fiducial starburst aperture in this galaxy to be $20''$.

NGC 3079: The $10\mu\text{m}$ observations by Devereux (1987) show that the emission in this galaxy is quite extended: a $5''.5$ aperture accounts for only 4% of the color-corrected $12\mu\text{m}$ flux measured by IRAS. There's relatively little (in a starburst context) star formation going on in this galaxy now, so the starburst region is difficult to define. At low levels, the H_2 flux extends over the central $16''$, but most of it seems confined to the inner $8''$. The broadband images in Figure 4.3 show that the central $8''$ region is significantly brighter than the surrounding galaxy, so an $8''$ aperture seems appropriate to define as the starburst region, in the sense that strong star formation occurred there in the recent past.

NGC 7714: $10\mu\text{m}$ observations by Devereux (1987) show that a $5''.5$ aperture contains essentially all the IRAS $12\mu\text{m}$ flux, color-corrected to $10\mu\text{m}$, so the starburst region must be quite compact. Our P-V diagrams of the strong emission

lines indicate a $6''$ aperture contains most of the emission-line flux. This estimate is confirmed by the $\text{Br}\gamma$ measurements of Calzetti, Kinney, & Storchi-Bergman (1996)—our measurements contain 70% of the flux in their $6'' \times 9''$ aperture. We assign a diameter of $6''$ to the starburst region in this galaxy.

4.4.2. Extinction

Broad-band colors

We assume an intrinsic color for the stellar population and further assume that colors redder than the assumed intrinsic color are purely due to reddening by dust. This correction is adequate if the only contribution to the NIR bands is stellar light and not some extra component such as hot dust, nebular emission, or synchrotron emission associated with an active nucleus. We find no need to invoke such extra sources of emission for these galaxies, though, both because the colors can be adequately accounted for by a population of dust-enshrouded stars and because the spectra we have obtained show no signs of veiling due to a featureless continuum.

At optical wavelengths, the the amount of obscuration due to dust depends critically on the location of the dust relative to the emitting sources (foreground screen, uniformly mixed, etc.). As shown in ERRL96 and ERRKA97, however, the extinction correction at *infrared* wavelengths derived from the $H - K$ color is relatively insensitive to changes in dust geometry, so we can use a simple foreground screen approximation to correct our broadband measurements. Using the $H - K$ colors listed in Tables 4.4 through 4.7, the apertures listed in Table 4.11, an intrinsic $H - K$ color of 0.2, and the Rieke & Lebofsky (1985) extinction law, we derive values for A_K of 0.64, 0.68, 0.78, and 0.46 magnitudes for IC 342,

NGC 2146, NGC 3079, and NGC 7714, respectively. These values are summarized in Table 4.10.

Extinction estimates from the spectra

Since we have observed at least two hydrogen recombination lines in the NIR region for each galaxy, we are able to estimate the extinction to the ionized gas by assuming the intrinsic line ratios are predicted by case-B recombination theory. This avoids potential problems with comparing recombination line measurements made by different workers, with different instrumentation, or at very different wavelengths. In particular, through the use of infrared recombination lines, we greatly lessen the possibility that we are sampling only a foreground region of these dusty galaxies, as would be the case if dust were mixed with the emitting regions and we used optical recombination lines.

The observed $\text{Pa}\beta$ to $\text{Br}\gamma$ line ratios for each galaxy are summarized in Table 4.8. We compared the observed ratios to the case B predictions of Hummer & Storey (1987), for a density of 10^2 cm^{-3} and a temperature of 5000 K, for a nominal $\text{Pa}\beta$ to $\text{Br}\gamma$ ratio of 5.58. Under the assumption of a foreground screen geometry, we then derive A_V . The results are summarized in Table 4.10.

Since we have observed two [Fe II] transitions that have the same upper level, their relative intensities can be predicted using the A-values of Nussbaumer & Storey (1988). To proceed, we make use of the [Fe II] fluxes listed in Table 4.9 and a nominal [Fe II]($\lambda 1.257\mu\text{m}$) to [Fe II]($\lambda 1.644\mu\text{m}$) ratio of 1.35. The extinction predicted by this line ratio is also listed in Table 4.10.

We note that extinction values derived from the $H - K$ color and from the

line ratios discussed here are generally consistent within the uncertainties.

4.4.3. UV flux

Br γ flux

We can directly measure the Br γ flux in our 20" aperture on NGC 2146 using our narrowband Br γ image. For the rest of the galaxies we will correct the Br γ flux as observed in the spectrometer aperture to our fiducial starburst aperture by using the ratio of the K-band fluxes in those apertures—in effect, we are assuming that the equivalent width of Br γ is approximately the same throughout the starburst aperture. This is unlikely to be true on small scales because the starburst region is probably a composite of clusters of star formation of various ages and the Br γ equivalent width of a coeval stellar population is a strong function of age. Averaged over larger diameters, however, we can hope that the mix of small stellar populations of different ages is roughly similar throughout the region, resulting in a Br γ equivalent width which does not vary strongly when integrated over large regions in the starburst. In cases where we have narrowband images and can check the conversion (e.g. NGC 6946 (ERRL96) and NGC 253 (ERRKA97)), the Br γ flux extrapolated from the spectra is generally very similar to that directly measured from the narrowband images. Even for the big aperture we have used for NGC 2146, extrapolating from the spectra predicts a flux that is within 40% of that measured from the narrowband image. In any event, the fiducial apertures we have used for the other galaxies are not much larger than the slit size, so the corrections are small.

We will also assume the extinction correction derived for the stars will be about the same for the gas—Table 4.10 shows this to be approximately true, and

the difference between using this extinction and using one derived directly from the $\text{Br}\gamma/\text{Pa}\beta$ ratio is small.

The adjusted $\text{Br}\gamma$ fluxes we compute for the four galaxies are $8.0 \pm 0.1 \times 10^{-14} \text{ erg/s/cm}^2$ (IC 342), $1.6 \pm 0.1 \times 10^{-13} \text{ erg/s/cm}^2$ (NGC 2146), $3.4 \pm 1.8 \times 10^{-15} \text{ erg/s/cm}^2$ (NGC 3079), and $3.4 \pm 0.2 \times 10^{-14} \text{ erg/s/cm}^2$ (NGC 7714). The $\text{Br}\gamma$ flux for NGC 7714 compares well with previous work (Puxley & Brand 1994, and references therein). We compute a UV flux using the models of Hummer & Storey (1987) for a density of 10^2 cm^{-3} and a temperature of 5000 K. The UV fluxes we compute this way are listed in Table 4.11.

[Ne II] flux

As an independent check on the calculation of the ionizing flux, the $[\text{Ne II}]$ line at $12.8\mu\text{m}$ can be used to calculate the number of ionizing photons per second. We have used the measurements from Roche et al. (1991). Two galaxies in this paper overlap with the Roche et al. sample. UV fluxes derived from $[\text{Ne II}]$ measurements of those galaxies are $N_{\text{LyC}} = 3 \times 10^{52} \text{ s}^{-1}$ (IC 342) and $N_{\text{LyC}} = 3 \times 10^{53} \text{ s}^{-1}$ (NGC 7714), where we have corrected for distances used. The apertures used to measure the $[\text{Ne II}]$ flux are quite similar to the sizes of the starburst regions ($7''.6$ for IC 342 and $5''.9$ for NGC 7714), so we make no aperture-size corrections to the flux.

4.4.4. Luminosity

The luminosity of a young starburst is dominated by massive, short-lived stars which emit most of their luminosity in the UV. In the dusty galaxy nuclei studied here, most of this radiation is absorbed by dust and reemitted in the FIR. We

can therefore use the FIR luminosity as an estimate of the total luminosity. The extensive IRAS database provides large-beam FIR measurements of all these systems, while measurements in a smaller beam are available for NGC 2146. Where available, we also add in the flux contribution from MIR and NIR wavelengths, although these typically make only a small contribution to the total.

Becklin et al. (1980) determine L_{Bol} to be $2.6 \times 10^9 L_{\odot}$ (corrected to a distance of 3.6 Mpc) in the central $30''$. Since the maps by Telesco et al. (1993) show most of the emission to be coming from the central $8''$, we'll assume the derived luminosity applies to our smaller aperture.

Using small-beam FIR measurements of NGC 2146, Smith & Harvey (1996) determine the bolometric luminosity to be $4.4 \times 10^{10} L_{\odot}$ in that galaxy. They don't try to include flux outside their observed bands, so this estimate might be a little low. If instead we assume that the SED is about the same as in NGC 253 and just scale the bolometric luminosity determined in ERRKA97 by the $100\mu\text{m}$ flux tabulated by Smith & Harvey, we derive $5.9 \times 10^{10} L_{\odot}$.

Spinoglio et al. (1995) determine the global bolometric luminosity of NGC 3079 to be $4.1 \times 10^{10} L_{\odot}$. Devereux (1987) using small-beam ($5''.5$) measurements at $10\mu\text{m}$ to show that this small aperture contains approximately 4% of the flux in the large IRAS beam. To correct Devereux's measurement to our $8''$ starburst aperture, we use the N-band measurements by Edelson, Malkan, & Rieke (1987) in an $8''.5$ aperture. Their data indicate a $10\mu\text{m}$ flux which is larger by factor which is very close to the change in aperture size. We therefore scale the 4% estimate by Devereux to our $8''$ aperture size by the change in aperture size, or by a factor of 2.1 to 8%. We therefore assign a luminosity of $3.3 \times 10^9 L_{\odot}$ to the nucleus of NGC 3079.

For NGC 7714, we use the estimate of L_{TOT} from Spinoglio et al. (1995) without correction. Although they have extrapolated the NIR fluxes to large aperture to estimate a total luminosity, the correction to our smaller aperture is only a few percent. Similarly, the results of Devereux (1987) show that small-aperture ($5''.5$) $10\mu\text{m}$ measurements of NGC 7714 contain essentially all the flux in the much larger IRAS beam, so we can assume that the L_{Bol} of $9.5 \times 10^{10} L_{\odot}$ Spinoglio et al. derive for the whole galaxy is a good estimate of the nuclear luminosity.

4.4.5. Mass

Rotation

IC 342 doesn't have any measurable rotation in our spectra, mostly likely due to a combination of its low inclination and its intrinsically low nuclear mass (see next section).

NGC 2146 has a well-determined rotation curve. We have measured velocity gradients for all strong emission lines in NGC 2146 and for the strong absorption lines of CO. To summarize these measurements, we present the best velocity curves from both the emission (in the form of H_2) and absorption (in the form of CO) lines in Figure 4.24, although all the lines give a similar answer. The rotation curve flattens out at a radius of about $5''$. To determine the velocity at the $10''$ radius appropriate to our starburst aperture, we have averaged the velocities on both sides of the nucleus at a radius of $10''$ for the lines of H_2 , $[\text{Fe II}]$, He, and $\text{Br}\gamma$. In this way, we measure a velocity of about 176 km s^{-1} (corrected for inclination). Inside our starburst aperture of $10''$ radius, this implies an enclosed mass of $4.9 \times 10^9 M_{\odot}$.

NGC 3079 has a steeply-rising rotation curve in the center. It flattens out at a

velocity of about 196 km s^{-1} at a radius of $2''.5$. Inside our starburst aperture of $4''$ radius, this implies a mass of $2.7 \times 10^9 M_{\odot}$.

We don't detect significant rotation in our spectrum of NGC 7714, but our spectral lines aren't measurable very far out from the nucleus, and our slit position did not match the major axis of the galaxy, anyway. See González-Delgado et al. (1995) for an optical rotation curve. Their rotation curve flattens out at a radius of $10''$, which is much farther out than the nominal $3''$ radius of the starburst. We could put an upper limit on the mass in our $6''$ aperture by assuming that the velocity at the $3''$ radius can be no higher than the velocity at which their rotation curve flattens out, or 130 km s^{-1} at a radius of 570 pc . This implies a mass of no more than $2.2 \times 10^9 M_{\odot}$, although the true dynamical mass is likely to be much less than this.

Dispersion

We can use the velocity dispersion of the strong CO absorption as an estimate of the velocity dispersion of the stars in the nuclei of these galaxies. To compute masses from the velocity dispersion, we make use of the models of Tremaine et al. (1994), as described in ERRL96.

We measure a scale radius for an $\eta = 3$ model for IC 342 of $2''.2$. The velocity dispersion is too small to be measured with our spectra; we assign it an upper limit of about 40 km s^{-1} , which is about as small as we can reliably measure the dispersion. This implies a mass contained within a $4''$ radius of $6.9 \pm 3.9 \times 10^7 M_{\odot}$, or a 2σ upper limit of $1.5 \times 10^8 M_{\odot}$, where the error bar is dominated by an uncertainty in the velocity dispersion of about 10 km s^{-1} .

We measure a scale radius of $7''.5$ for an $\eta = 3$ model for NGC 2146, plus a velocity dispersion of $72 \pm 11 \text{ km s}^{-1}$. At a radius of $10''$, this implies an enclosed mass of $2.1 \pm 0.7 \times 10^9 M_{\odot}$, or a 2σ upper limit of $3.5 \times 10^9 M_{\odot}$.

We get scale radius of $2''.5$ for NGC 3079, and again the $\eta = 3$ model seems a plausible fit to the light profile. We measure a velocity dispersion for this galaxy of $102 \pm 15 \text{ km s}^{-1}$. Inside a radius of $4''$, this implies a mass of $1.9 \pm 0.6 \times 10^9 M_{\odot}$, or a 2σ upper limit of $3.1 \times 10^9 M_{\odot}$.

An $\eta = 3$ model with a scale radius of $2''.5$ seems to do the best job of fitting NGC 7714, although it is not as good a fit as for the other galaxies. As in IC 342, the velocity dispersion is too small for us to measure reliably, so again we'll assume it's no higher than $40 \pm 10 \text{ km s}^{-1}$ (i.e., no greater than 50 km s^{-1}). This implies a mass of $5.1 \pm 2.9 \times 10^8 M_{\odot}$, or a 2σ upper limit of $1.1 \times 10^9 M_{\odot}$, within a radius of $3''$.

Mass Budget

Now that we have a limit on the dynamical mass, we have to decide how much gets allocated to make stars in the starburst. As described in ERRL96, we assume 80% of the mass must be in the form of an underlying nuclear population. From what's left we'll have to subtract some for molecular gas still present in the nucleus (and presumably the fuel for the current burst). What's left over indicates how much mass got turned into stars in the last burst.

4.4.6. CO index

We can measure the CO index directly from our spectra. We use the definition given by Kleinmann & Hall (1985). The results are tabulated in Table 4.11.

4.4.7. Supernova rate

For each galaxy, we estimate the current supernova rate using the $[\text{Fe II}](1.644\mu\text{m})$ flux and the formula of Vanzi & Rieke (1997). To compute the correct $[\text{Fe II}]$ flux for our chosen apertures, we scale the flux observed in the spectrometer slit by the ratio of the H-band fluxes in the two apertures, similar to what we did with the $\text{Br}\gamma$ flux in §4.4.3. This correction probably overestimates the $[\text{Fe II}]$ flux for the large aperture on NGC 2146, so we correct the $[\text{Fe II}]$ flux by the same factor that the $\text{Br}\gamma$ flux estimated from the spectra and from the narrow-band images differed. We also correct for extinction. In this way, we derive $[\text{Fe II}]$ luminosities of 3.4×10^{38} , 8.8×10^{39} , 2.8×10^{39} , and 1.2×10^{40} erg s $^{-1}$ for IC 342, NGC 2146, NGC 3079, and NGC 7714, respectively. These luminosities imply supernova rates of 0.004, 0.11, 0.035, and 0.15 yr $^{-1}$.

We can also use the nonthermal radio flux and equation 8 of Condon & Yin (1990). From Turner & Ho (1983), the nonthermal radio flux at 5 GHz is 40 mJy in IC 342, corresponding to a luminosity of 6.22×10^{19} W Hz $^{-1}$ and a supernova rate of about 0.002 yr $^{-1}$, about a factor of two lower than that derived from the $[\text{Fe II}]$ flux.

4.5. Starburst models

4.5.1. Description of Models

Rieke et al. 1993 (RLRT93 hereafter) modeled the starburst in M 82 using the models of Rieke et al. 1980 with updated stellar tracks and atmospheric parameters. The starburst model uses the grid of stellar evolution tracks of Maeder (1992), which have been assigned observational parameters based on a combination of atmosphere models and empirical calibration. The starburst models use the evolutionary tracks over a range of stellar masses up to $80M_{\odot}$ and interpolate between the tracks to reduce oscillations caused by discreteness in the stellar masses. The models form stars over a short gaussian burst (FWHM of 5 million years), with the number of stars in each bin determined by the IMF. The observational parameters are predicted as the stars evolve along theoretical tracks. Further details can be found in RLRT93.

4.5.2. Individual galaxy models

The models for IC 342 and NGC 7714 provide spectacular fits to the derived starburst properties. The model for NGC 2146 also does a good job fitting the constraints except that the model predicts more luminosity than is observed. This may not be a problem, though, since this system is edge on and much of the luminosity could be escaping perpendicular to the plane like it does in M82. The luminosity is also a problem with NGC 3079—where the best fit occurs, the model predicts a bolometric luminosity that is a factor of 7.5 too high. Since NGC 3079 is almost perfectly edge-on, this could also be a problem with luminosity escaping perpendicular to the plane. It could also be partly due to the way we determined the bolometric luminosity. The compactness argument indicates that only a small

fraction of the luminosity comes from the nucleus of this galaxy. This picture doesn't seem to apply to the other starbursts we have observed, in which the emission is dominated by the nuclear region. It is possible we have underestimated the nuclear luminosity in NGC 3079, as well.

Several observations indicate that the starburst in NGC 3079 is fairly old, at least several times 10^7 years. For example, the optical spectrum of this galaxy nucleus (Filippenko & Sargent (1992) shows a moderately strong $H\beta$ absorption, indicating that a population of B or A stars (rather than younger O stars) dominates the optical continuum. Also, as Filippenko & Sargent estimate, the superwind from the nucleus of NGC 3079 required roughly 3×10^7 years to reach NGC 3073. Our spectra are consistent with the picture of an intermediate-age population dominating the continuum emission. For example, the CO index in NGC 3079 is somewhat weaker than the rest of the galaxies in this sample, which would easily occur if most of the massive, cool supergiants that dominate younger starbursts have already evolved. Also, the ^{13}CO bands in NGC 3079 are fairly strong, indicating that perhaps intermediate-age AGB stars rather than young, massive supergiants dominate the K-band spectrum. The deficiencies in our model of NGC 3079 could likely be overcome by combining an early, very strong burst of star formation with a more recent minor burst or a low level of continuous star formation. The initial burst would drive the outflow, and would dominate both the continuum emission and the current rate of supernova. Recent star formation (either in a small burst or a low level of continuous star formation) would provide the hydrogen recombination line emission currently observed.

4.6. Conclusion

We use new, high-quality infrared imaging and spectroscopy of four starburst galaxies at various evolutionary stages to derive properties of the starbursts in the nuclei of these galaxies and to constrain starburst models. The imaging provides us not only with detailed morphological information but colors, luminosities, and a flux calibration for the spectra. The spectra provide information on several different populations of objects in the starburst: the stellar continuum arises largely from cool, evolved stars; several emission lines (e.g., atomic hydrogen, helium) arise from regions photoionized by very young stars; [Fe II] lines mostly trace supernova remnants; and H₂ lines are probably produced in a combination of HII regions, supernova remnants, and bulk motions of molecular clouds. Both emission and absorption lines provide us with kinematic information which allows us to constrain the dynamical mass in the nuclear region, a critical step in constraining the low-mass end of the IMF.

We derive a range of ages and masses for the starbursts discussed here, with NGC 7714 being the youngest at 5 million years and NGC 3079 being the oldest at several times 10^7 years. Our models indicate ages of 6-7 million years for IC 342 and NGC 2146. The young age for NGC 7714 is consistent with the presence of Wolf-Rayet features in its spectrum. The old age for NGC 3079 is consistent with the well-developed superwind this galaxy is famous for. Using the IMF found by RLRL93 to best fit M82, the mass required to have been consumed in the recent starbursts in these galaxies range over nearly two orders of magnitude, from $1.0 \times 10^7 M_{\odot}$ in IC 342 to $3.3 \times 10^8 M_{\odot}$ in NGC 2146. The mass consumed by the starbursts range from a small fraction of the dynamical mass, from about 5% for NGC 3079, to over 20% in the case of NGC 7714. The total mass in stars required

to fit the observations goes up by about a factor of three if an IMF similar to that derived for the solar neighborhood is used, i.e., to an improbable 65% in the case of NGC 7714, compelling evidence that, for this galaxy at least, an IMF that is biased against low-mass star formation is indicated. Since the low-mass stars in these young, dramatic star-formation events contribute very little to the luminosity at any wavelength, their only measurable impact is through the gravitational influence of their mass. As a result, it is only in a massive, young starburst (such as the one in NGC 7714), where the burst completely dominates the observed emission, where we can claim that the IMF *must* be biased towards massive stars to fit the observations.

We find that most of these galaxies show some sign of interaction which may have triggered the starbursts. NGC 7714 and NGC 3079 have nearby companions with which they are obviously interacting. NGC 2146 has a highly disturbed morphology and may have completely engulfed a small companion. IC 342, while not obviously disturbed, resides in a well-populated group with other starbursting galaxies (e.g., Maffei 2 and NGC 1569) and in projection has a nearby dwarf companion which is also undergoing significant star formation.

Table 4.1. Galaxy Data

Parameter	IC 342	NGC 2146	NGC 3079	NGC 7714
$\alpha(1950)$	03 ^h 41 ^m 58 ^s .6	06 ^h 10 ^m 40 ^s .1	09 ^h 58 ^m 35 ^s .0	23 ^h 33 ^m 40 ^s .6
$\delta(1950)$	+67°56'26"	+78°22'23"	+55°55'15"	+01°52'42"
D(Mpc)	3.6	14	15.6	39
P.A.	40°	128°	165°	155°
inclination	25°	51°	80°	45°
references	1,2	3,4	5,6	7

Note. — Sources for the distances, position angles, and inclinations: (1) Rogstad & Shostak 1972; (2) Krismer, Tully, & Gioia 1995; (3) Smith, Harvey, & Lester 1995; (4) Young et al. 1988; (5) Sofue & Irwin 1992; (6) Frei et al. 1996; (7) Demoulin, Burbage, & Burbage 1968.

Table 4.2. Imaging Observation Log

Galaxy	Date	Telescope	int. time (sec.) per passband					Flux Standard
			<i>J</i>	<i>H</i>	<i>Ks</i>	<i>Br</i> γ	<i>H</i> ₂	
IC 342	11/6/95	2.3 <i>m</i>	200	200	200
NGC 2146	11/7/95	2.3 <i>m</i>	400	200	200	600	600	HD44612
NGC 3079	3/30/96	1.55 <i>m</i>	1125	900	900	HD84800
NGC 7714	10/24/96	1.55 <i>m</i>	450	450	450	FS30

Note. — The images were obtained with the Steward Observatory (SO) NICMOS3-based camera at the SO 2.3m on Kitt Peak and at the SO 1.55m on Mt. Bigelow outside of Tucson, AZ.

Table 4.3. Spectroscopy Observation Log

Galaxy	Dates Observed	Itime/Setting	Extracted Aperture (")
IC 342	12/8/94	800s	2.4×6
NGC 2146	12/13 – 14/94, 2/11/95, 11/19/96	1000s	2.4×18
NGC 3079	12/12/94, 2/11/95, 11/19/96	700s	2.4×6
NGC 7714	12/15 – 16/94, 11/19/96	800s	2.4×6

Note. — We have indicated a typical integration time per grating setting. We generally obtained 1 grating setting at J, 3 at H, and 6 at K. Since NGC 2146 occupied a significant fraction of the slit, we had to move the telescope off the galaxy periodically to measure the sky background and so the total observing time per grating setting was approximately twice the time indicated in the table. The spectra were all obtained at $R \sim 3000$ except for the J-band spectra of NGC 2146, NGC 3079, and NGC 7714, which were obtained at $R \sim 800$.

Table 4.4. IC 342 Photometry

aperture(")	m_J	m_H	m_K	$J - H$	$H - K$
3	11.34	10.45	9.98	0.89	0.47
6	10.56	9.75	9.21	0.81	0.54
8	10.30	9.50	8.94	0.80	0.56
12	10.00	9.20	8.65	0.80	0.55
16	9.77	8.98	8.43	0.79	0.55
20	9.60	8.80	8.25	0.80	0.55
2.4×6	11.13	10.23	9.71	0.90	0.52

Note. — Since we were unable to obtain photometry for this galaxy, the images have been scaled to match the photometry from Becklin et al. (1980), in a $3''.8$ aperture.

Table 4.5. NGC 2146 Photometry

aperture('')	m_J	m_H	m_K	$J - H$	$H - K$
3	12.41	11.41	10.84	1.00	0.57
6	11.37	10.34	9.73	1.03	0.61
12	10.51	9.47	8.87	1.04	0.60
20	9.94	8.93	8.35	1.01	0.58
41	9.23	8.29	7.79	0.94	0.50
2.4×18	11.34	10.24	9.64	1.10	0.60

Table 4.6. NGC 3079 Photometry

aperture(")	m_J	m_H	m_K	$J - H$	$H - K$
3	12.88	11.51	10.76	1.37	0.75
6	11.80	10.51	9.79	1.29	0.72
8	11.51	10.30	9.66	1.21	0.64
12	10.95	9.80	9.22	1.15	0.58
20	10.41	9.32	8.83	1.09	0.49
41	9.69	8.71	8.32	0.98	0.39
2.4×6	12.71	11.40	10.71	1.31	0.69

Table 4.7. NGC 7714 Photometry

aperture('')	m_J	m_H	m_K	$J - H$	$H - K$
3	13.00	12.10	11.67	0.90	0.43
6	12.16	11.48	11.02	0.68	0.46
8.5	11.92	11.25	10.80	0.67	0.45
12	11.68	11.04	10.59	0.64	0.45
15	11.55	10.91	10.46	0.64	0.45
2.4×6	12.62	11.88	11.41	0.74	0.47

Table 4.8. Hydrogen Recombination Lines

Galaxy	$\text{Br}\gamma$	$\text{Pa}\beta$	$\text{Pa}\beta/\text{Br}\gamma$
IC 342	3.94 ± 0.20	8.29 ± 0.41	2.10 ± 0.15
NGC 2146	6.77 ± 0.34	14.3 ± 0.75	2.11 ± 0.15
NGC 3079	0.13 ± 0.07	0.14 ± 0.07	1.08 ± 0.79
NGC 7714	2.35 ± 0.12	7.56 ± 0.38	3.22 ± 0.23

Note. — $\text{Br}\gamma$ and $\text{Pa}\beta$ fluxes are in units of $10^{-14}\text{erg/s/cm}^2$ and have been measured in the apertures listed in Table 4.3. The quoted errors are a combination of the uncertainty in the flux calibration and an estimate of the uncertainty in the continuum placement.

Table 4.9. Other Emission Lines

λ_{vac}	species	IC 342	NGC 2146	NGC 3079	NGC 7714
1.2571	[Fe II]	3.55 ± 0.18	4.41 ± 0.22	0.86 ± 0.17	1.92 ± 0.10
1.6441	[Fe II]	4.83 ± 0.24	5.46 ± 0.27	1.00 ± 0.20	2.26 ± 0.11
2.0338	H ₂	< 0.3	2.12 ± 0.21	0.61 ± 0.06	0.14 ± 0.03
2.0586	HeI	1.15 ± 0.06	4.37 ± 0.25	< 0.06	1.74 ± 0.09
2.7035	H ₂	< 0.3	0.68 ± 0.07	0.10 ± 0.05	< 0.07
2.1218	H ₂	0.64 ± 0.06	2.46 ± 0.12	1.79 ± 0.10	0.49 ± 0.05
2.2233	H ₂	< 0.3	0.91 ± 0.14	0.54 ± 0.05	0.07 ± 0.04
2.2477	H ₂	< 0.3	0.67 ± 0.13	0.11 ± 0.02	< 0.07

Note. — All lines are measured in units of 10^{-14} erg/s/cm².

Table 4.10. A_V Estimated From Colors and Line Ratios

Galaxy	Method Used			
	$\text{Pa}\beta/\text{Br}\gamma$	$[\text{Fe II}]_{\frac{1.257\mu\text{m}}{1.644\mu\text{m}}}$	$J - H$	$H - K$
IC 342	7.50	7.64	2.18	5.11
NGC 2146	7.46	6.36	4.36	6.39
NGC 3079	12.64	5.63	6.66	7.83
NGC 7714	4.22	5.77	0.44	4.31

Note. — Typical errors are 1 magnitude except for A_V determined from line ratios in NGC 3079, due to the weakness of the lines. The uncertainty in A_V from the $\text{Br}\gamma/\text{Pa}\beta$ ratio and from the $[\text{Fe II}]$ lines is 5.6 magnitudes and 3.4 magnitudes, respectively, in that galaxy.

Table 4.11. Starburst parameters

Parameter	IC 342	NGC 2146	NGC 3079	NGC 7714
size	8''	20''	8''	6''
Mass ($10^8 M_{\odot}$)	0.3	10	6	2
M_K	-19.26	-23.06	-22.12	-22.39
L_{Bol} ($10^9 L_{\odot}$)	2.6	59	3.3	95
$\log (N_{\text{LyC}}) \text{ (s}^{-1}\text{)}$	52.1	53.7	52.1	53.8
CO_{ind}	0.22	0.17	0.17	0.19
$\nu_{\text{SN}} \text{ (yr}^{-1}\text{)}$	0.004	0.11	0.035	0.15

Note. — The size of the starburst region indicates the diameter of a circular aperture which contains most of the flux from the starburst region, as defined in the text. It is within this region that the other parameters are derived. The K-band magnitude has been adjusted for the presence of a preexisting old population, as described in ERRL96. The CO index has also been adjusted for dilution by an old population, as described in the text.

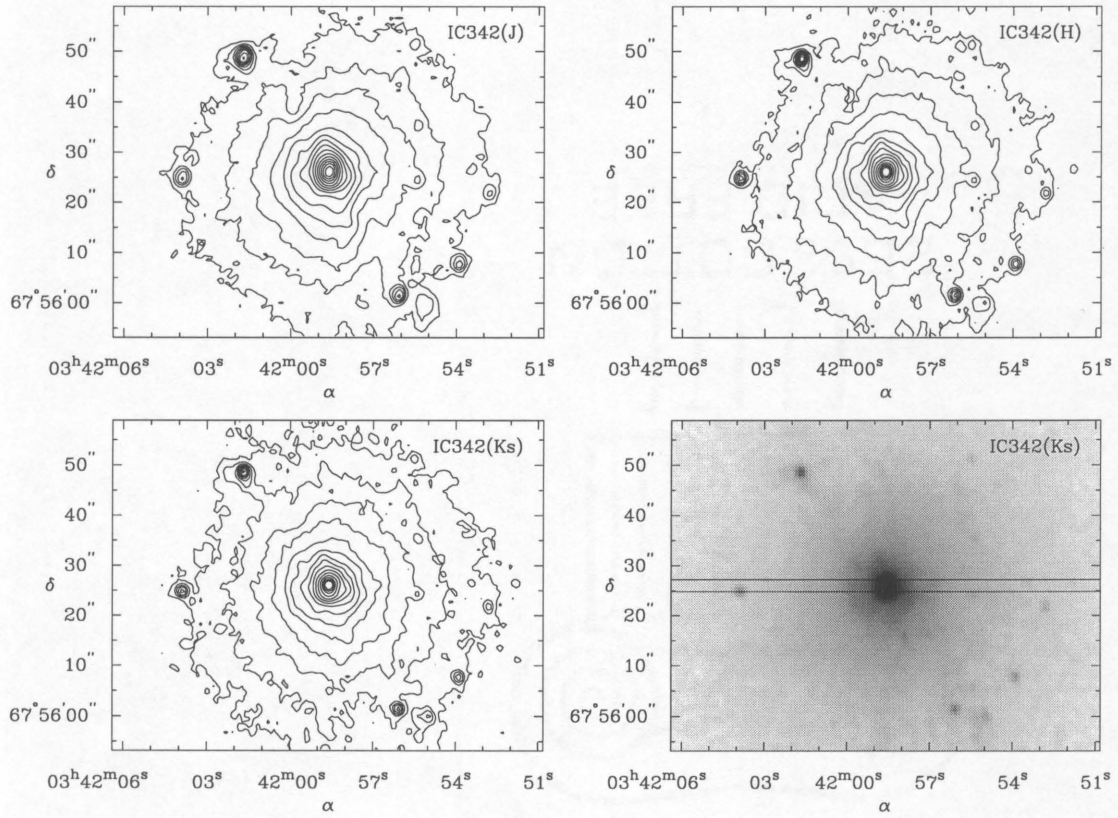


Figure 4.1 J, H, and Ks-band images of IC 342 plotted as contours, plus a grayscale image in the Ks band. The lines in the lower right-hand panel indicates the size and position of our spectrometer slit. The display levels are 13.5 to 18.5, 12.5 to 17.7, and 12 to 17.4 magnitudes per square arcsecond in the J, H, and Ks-band images, respectively.

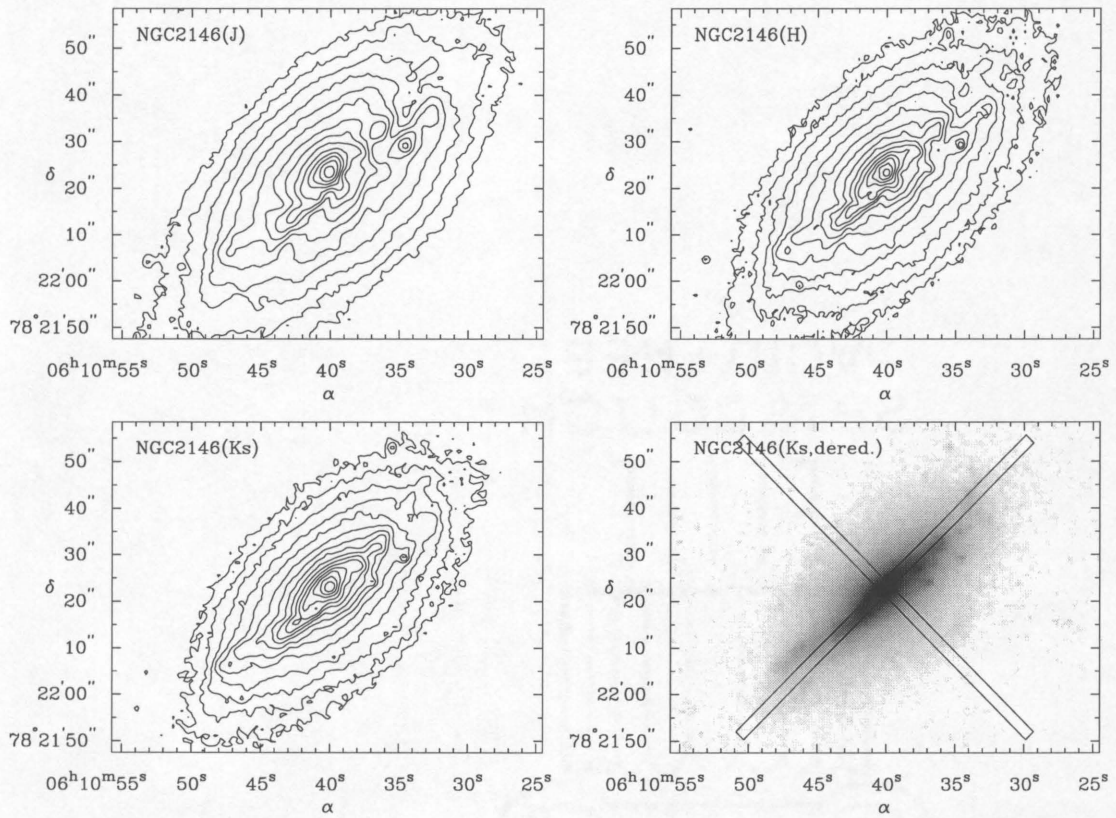


Figure 4.2 J, H, and Ks-band images of NGC 2146 plotted as contours, plus a version of the Ks-band image that has been dereddened as described in the text. Two slit positions are marked on the dereddened image. The contour levels are 14.4 to 19.4, 13.5 to 18.5, 13 to 18, and 12.5 to 17.5 magnitudes per square arcsecond in the J, H, Ks, and dereddened images, respectively.

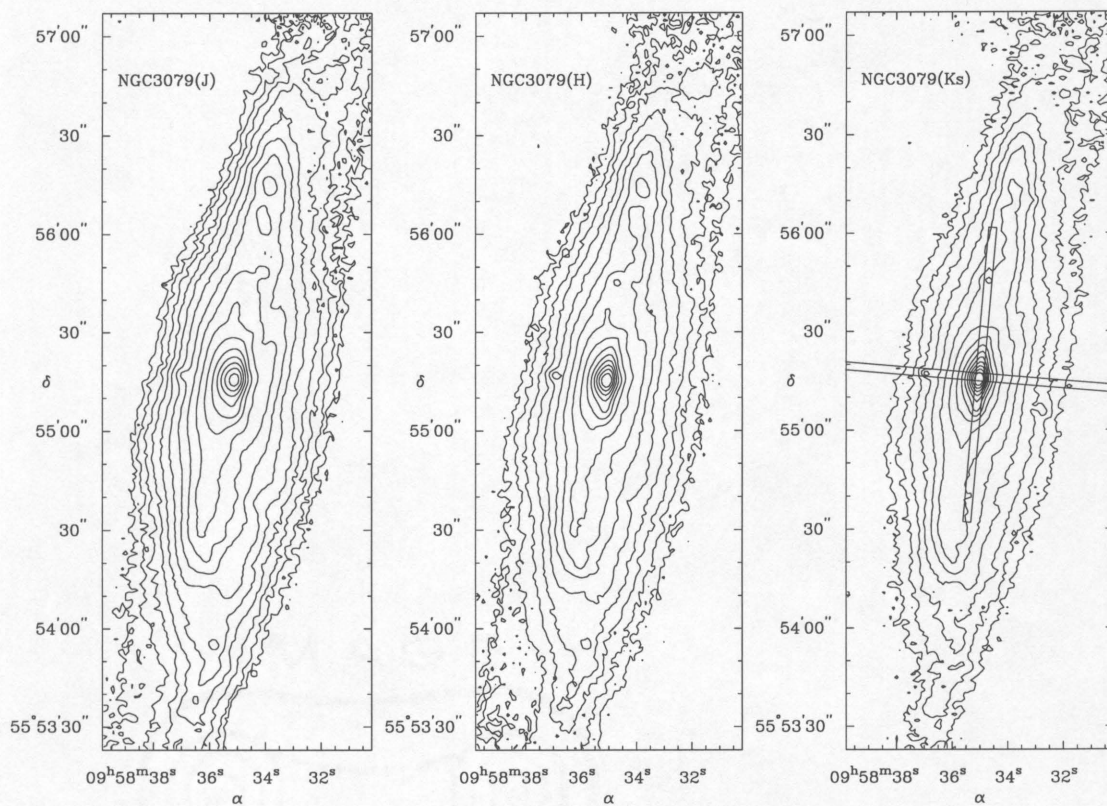


Figure 4.3 J, H, and Ks-band images of NGC 3079 plotted as contours. Two slit positions are marked on the Ks-band image. The contour levels are 15.5 to 21, 14.2 to 19.7, and 13.4 to 18.9 magnitudes per square arcsecond in the J, H, and Ks-band images, respectively.

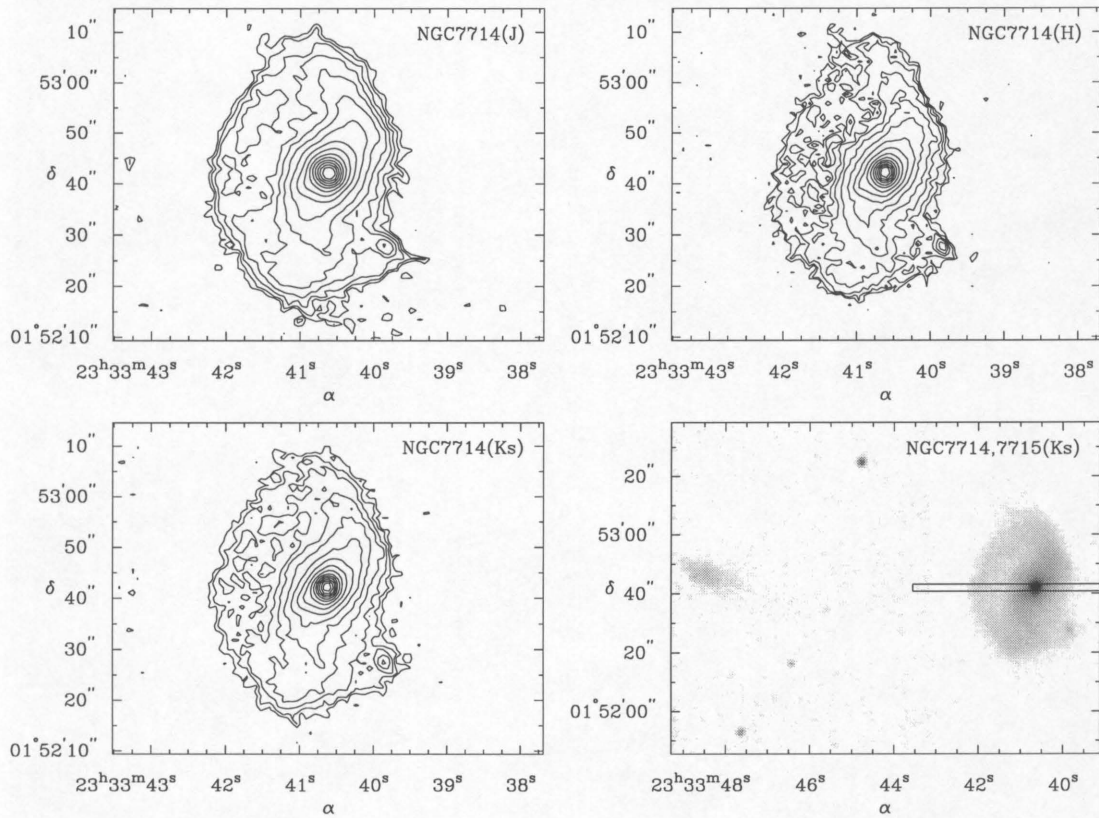


Figure 4.4 J, H, and Ks-band images of NGC 7714 plotted as contours, plus a Ks-band image plotted in a larger field-of-view to show the position of NGC 7715 relative to NGC 7714. The slit position is marked in the lower-right-hand panel. The contour levels are 15.3 to 21.3, 14.3 to 20.3, and 13.7 to 19.7 magnitudes per square arcsecond in the J, H, and Ks-band images, respectively.

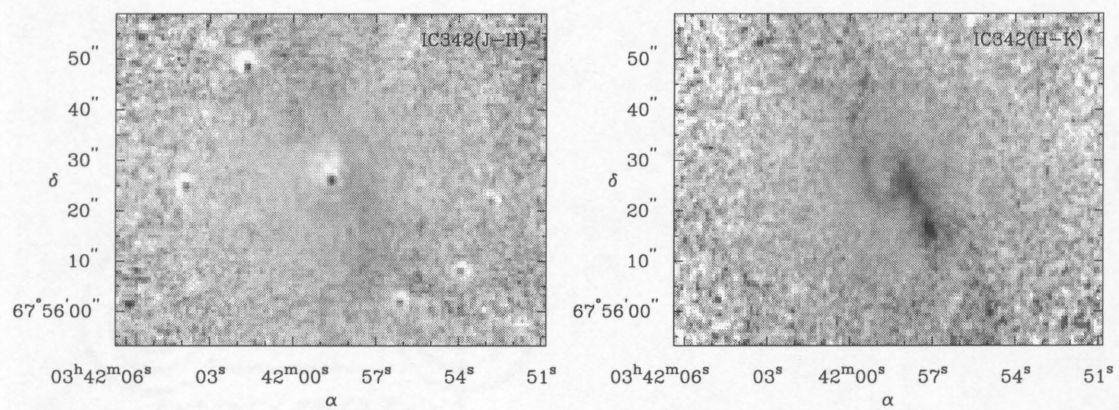


Figure 4.5 $J - H$ and $H - K$ color images of the nuclear region of IC342. The grayscale display range is 0.5 to 1.5 magnitudes for the $J - H$ image and 0.1 to 1 magnitudes for the $H - K$ image.

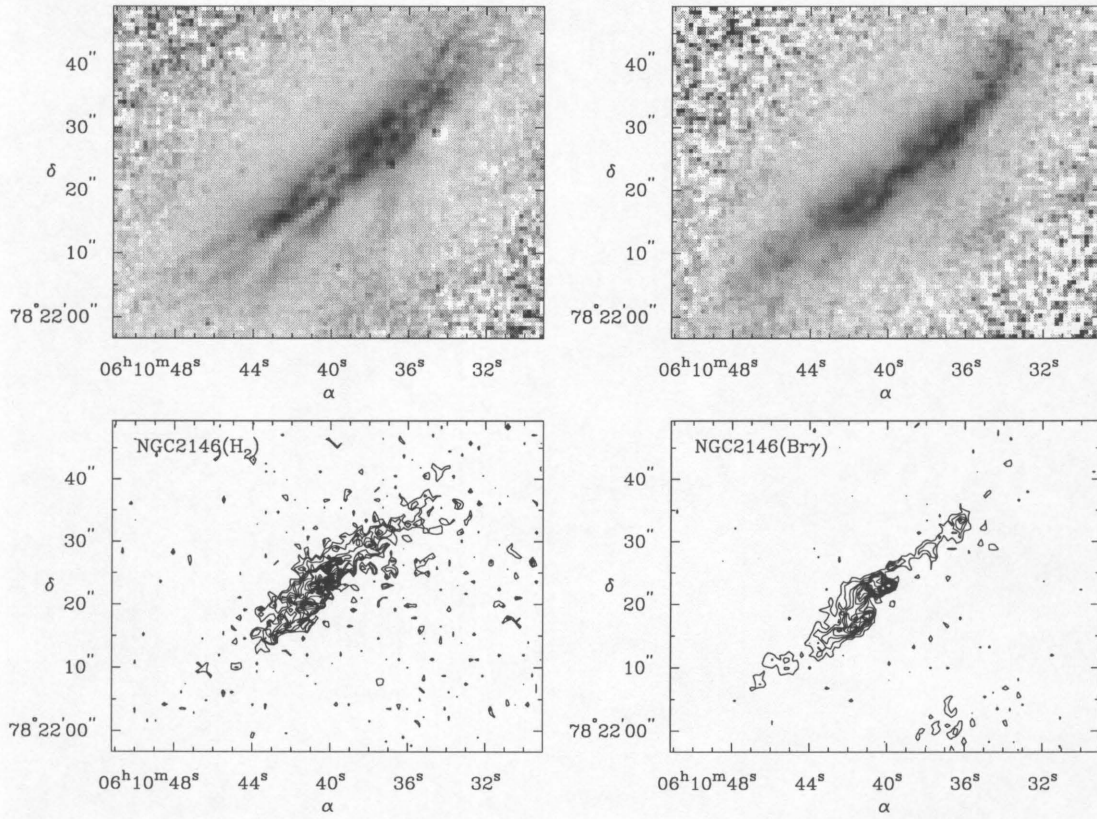


Figure 4.6 In the upper-left-hand panel we have plotted the $J - H$ color image of the nuclear region of NGC 2146 in greyscale, while the $H - K$ color image is plotted in the upper right. The grayscale range is 0.5 to 1.5 magnitudes for the $J - H$ image and 0.1 to 1 magnitude for the $H - K$ image. We have also plotted H₂ and Brγ contour maps of the same region, in a linear scale from a minimum value of 3×10^{-16} erg/s/cm² in both images to a maximum value of 2×10^{-15} erg/s/cm² for the H₂ image and 4×10^{-15} erg/s/cm² for the Brγ image.

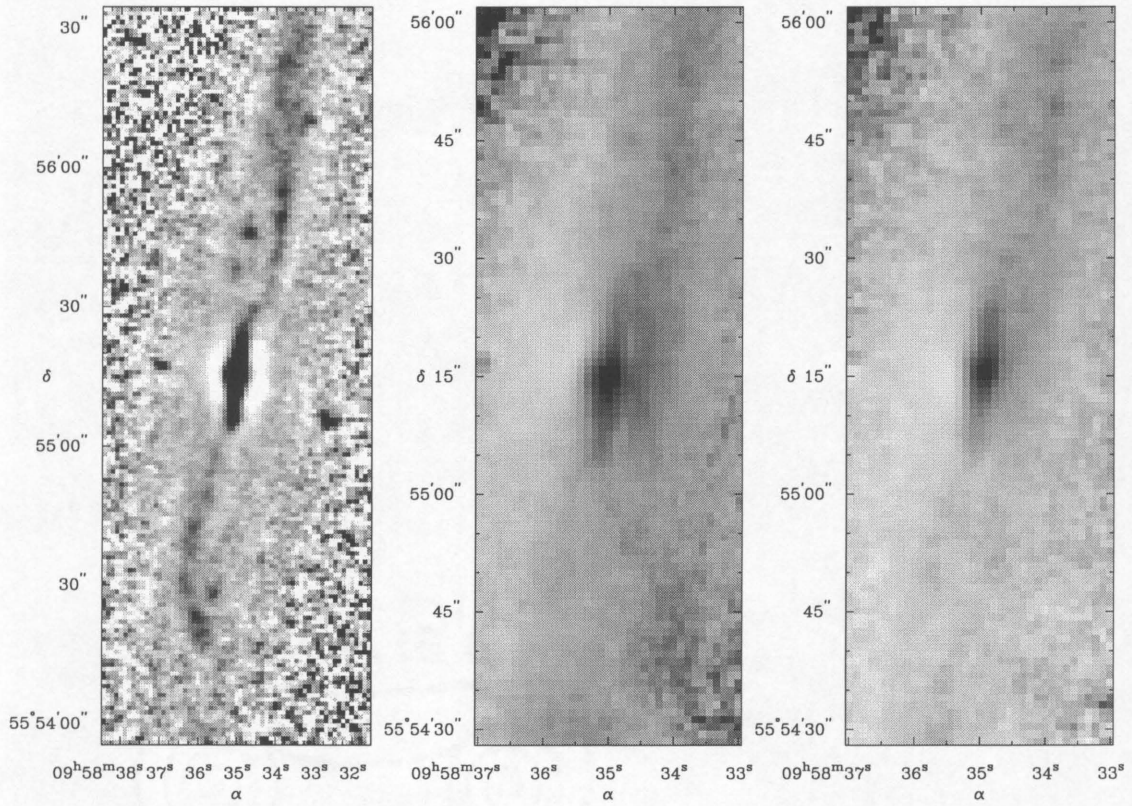


Figure 4.7 A Ks-band image of NGC 3079 that has been dereddened and filtered as described in the text is shown in the left-hand panel. We also present $J - H$ (display range 0.5 to 1.5 magnitudes; center panel) and $H - K$ (display range 0 to 1 magnitude; right-hand panel) color images of a somewhat smaller region around the nucleus.

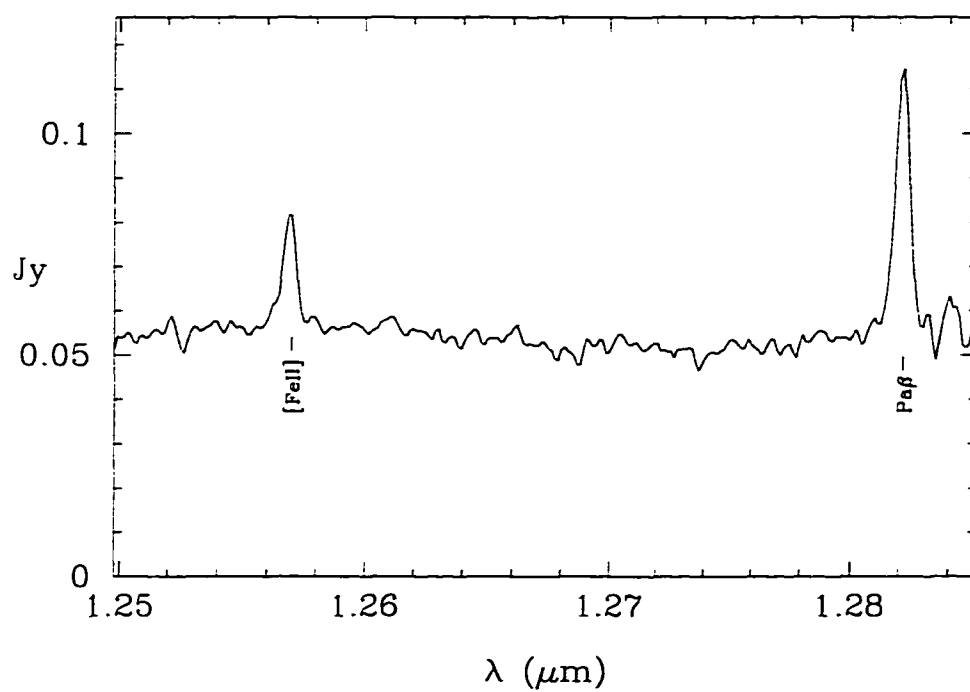


Figure 4.8 J-band spectrum of IC342. The spectrum is the sum over a $6''$ region of the $2''.4$ -wide slit, as summarized in Table 4.3. The spectrum was flux-calibrated using the calibrated broad-band images.

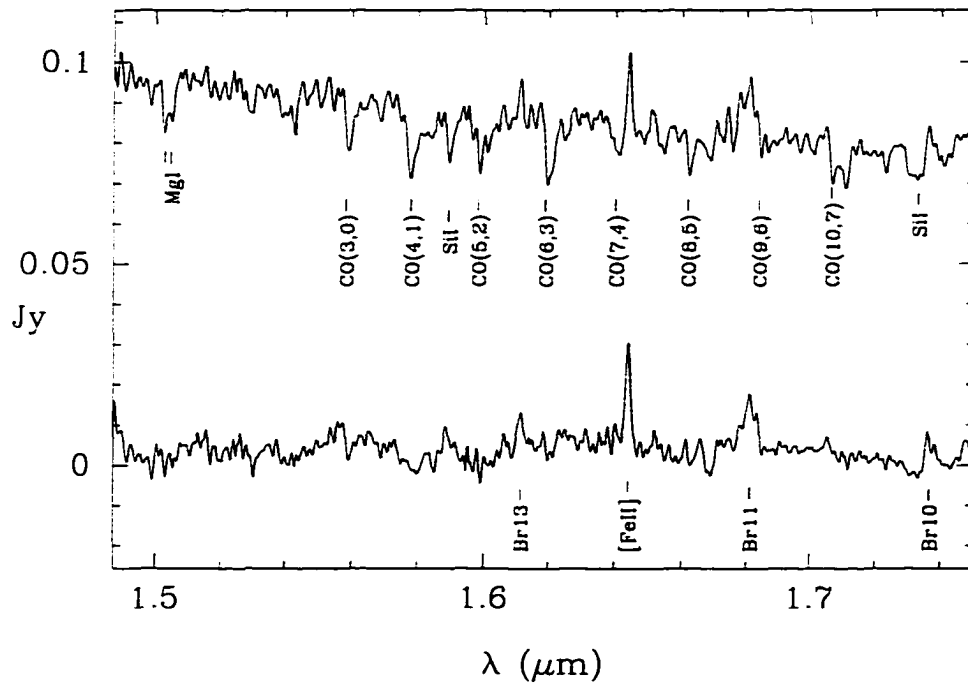


Figure 4.9 H-band spectrum of IC342. Details as for J-band spectrum.

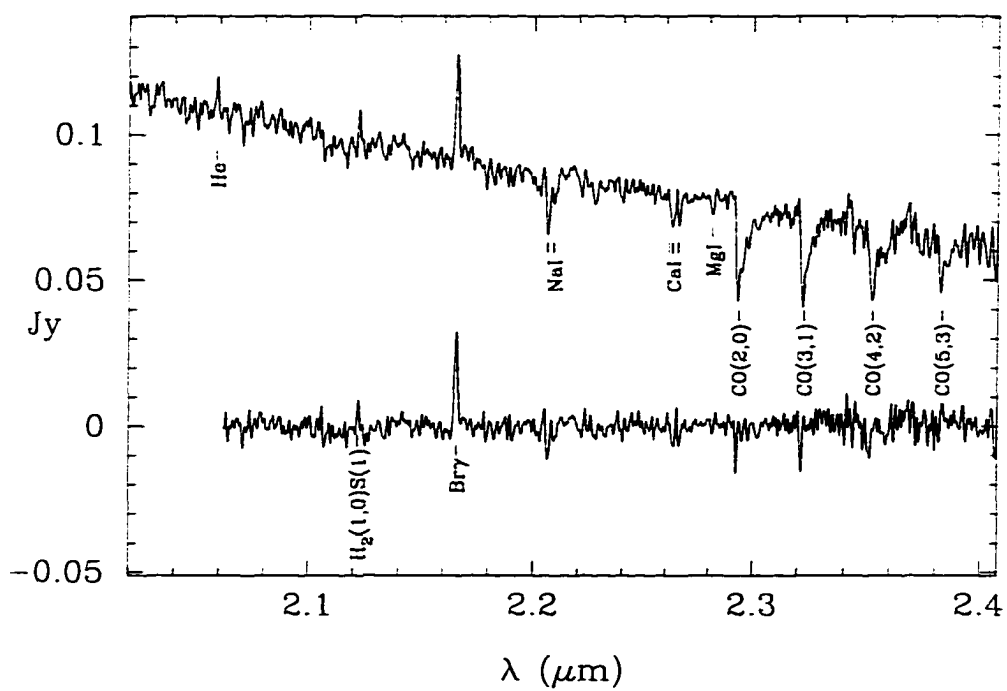


Figure 4.10 K-band spectrum of IC342. Details as for J-band spectrum.

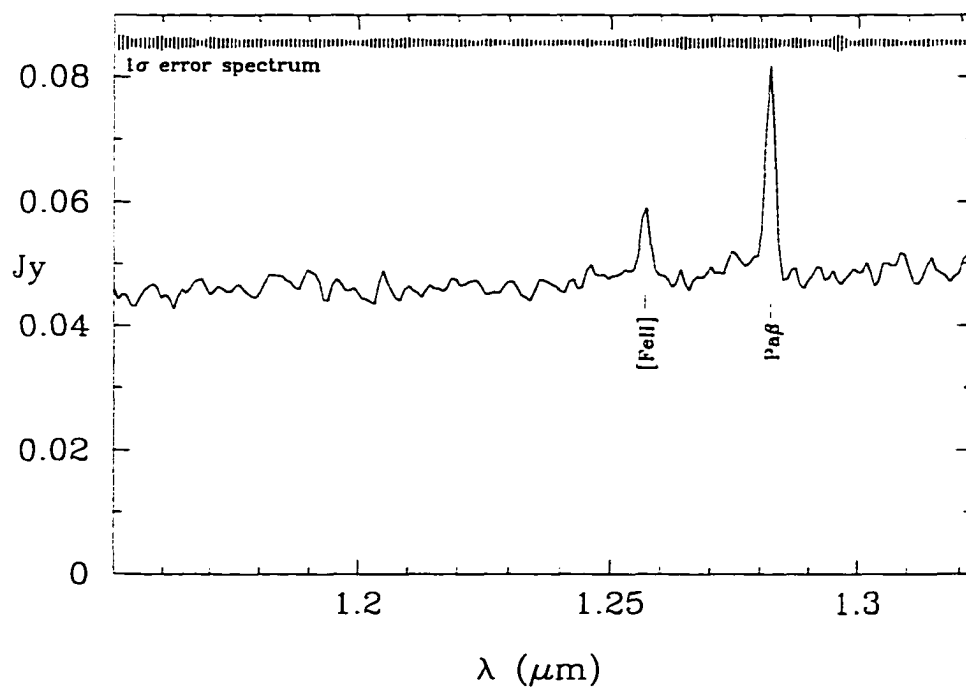


Figure 4.11 J-band spectrum of NGC2146.

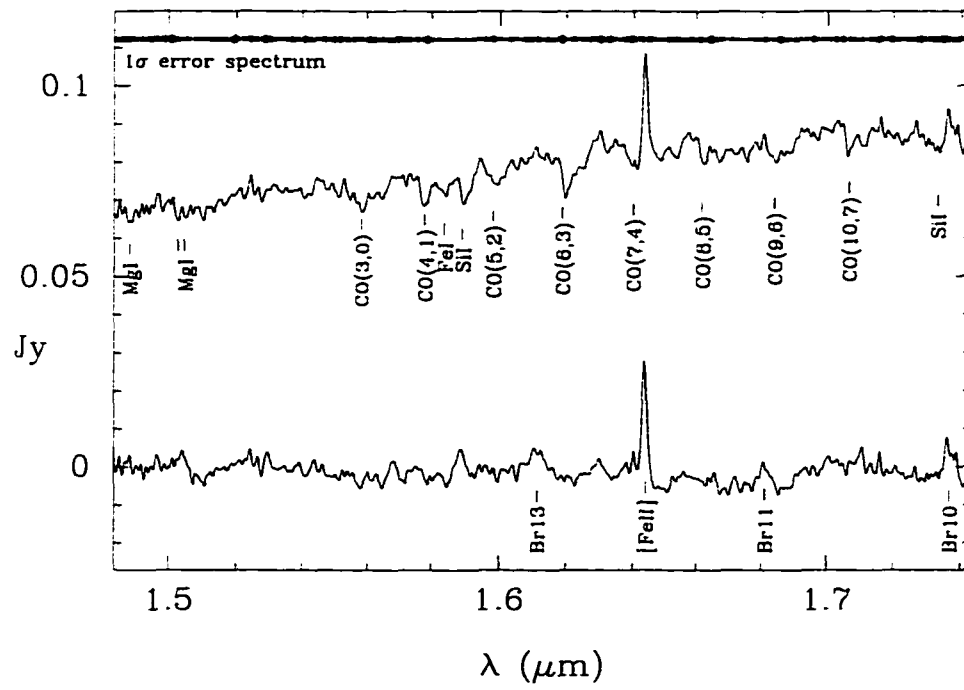


Figure 4.12 H-band spectrum of NGC2146.

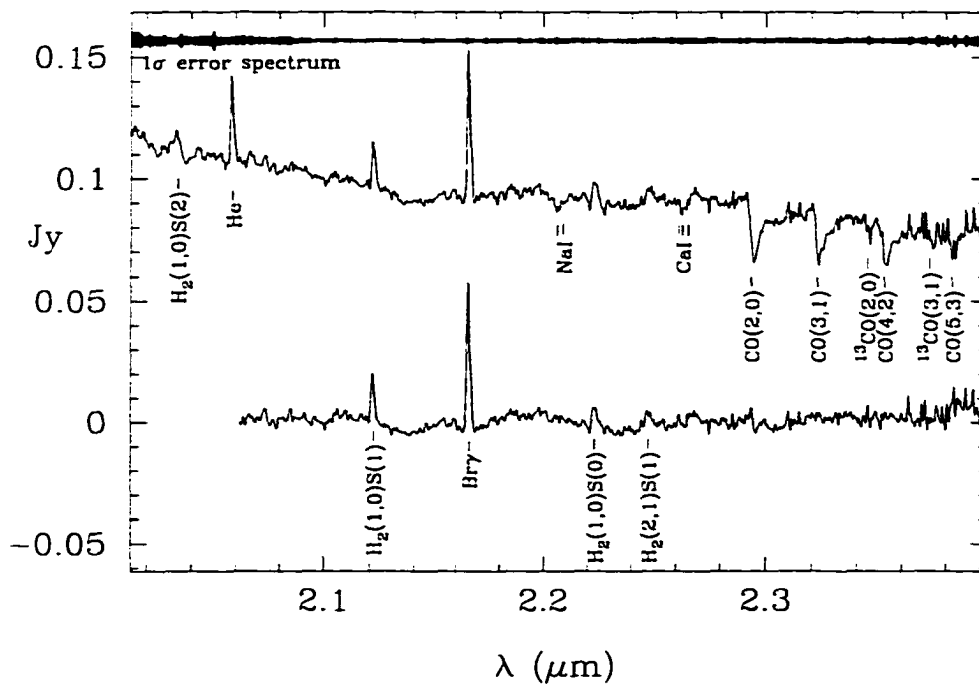


Figure 4.13 K-band spectrum of NGC2146.

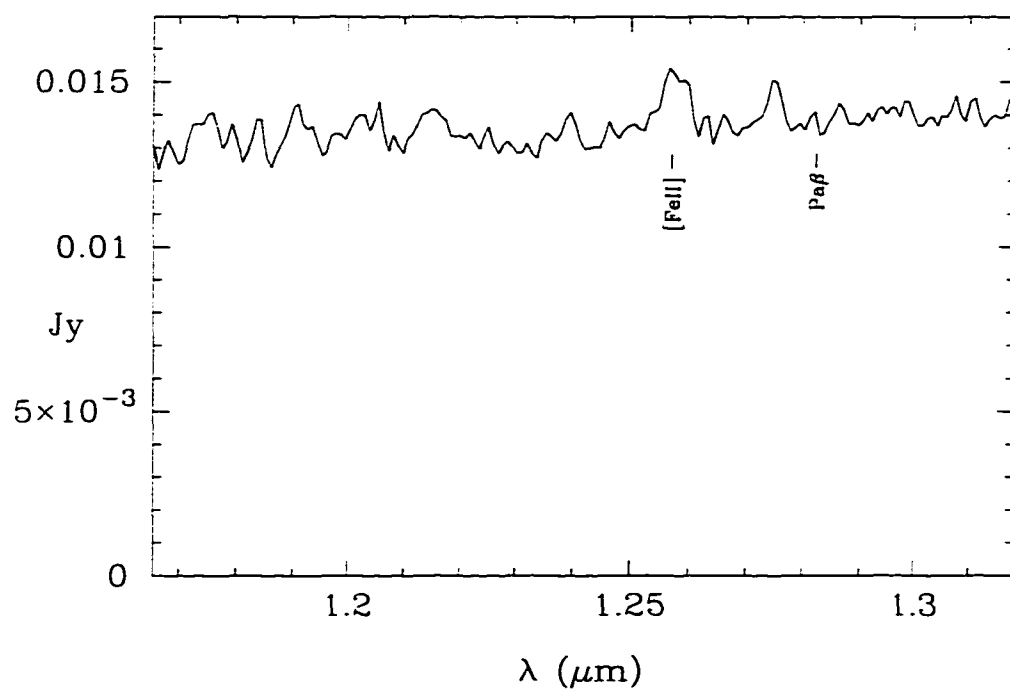


Figure 4.14 J-band spectrum of NGC3079.

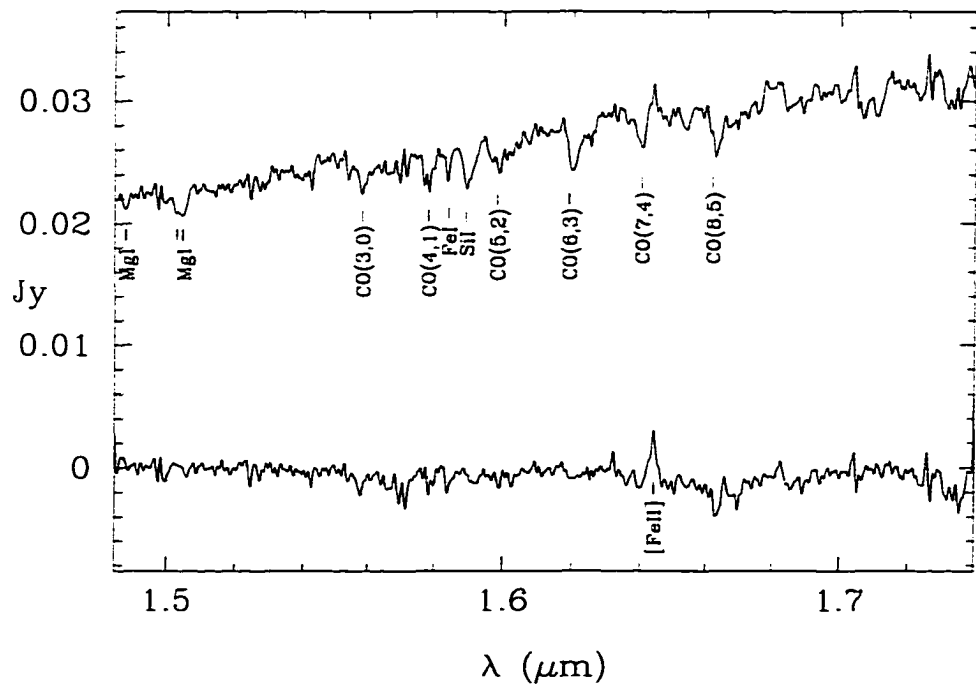


Figure 4.15 H-band spectrum of NGC3079.

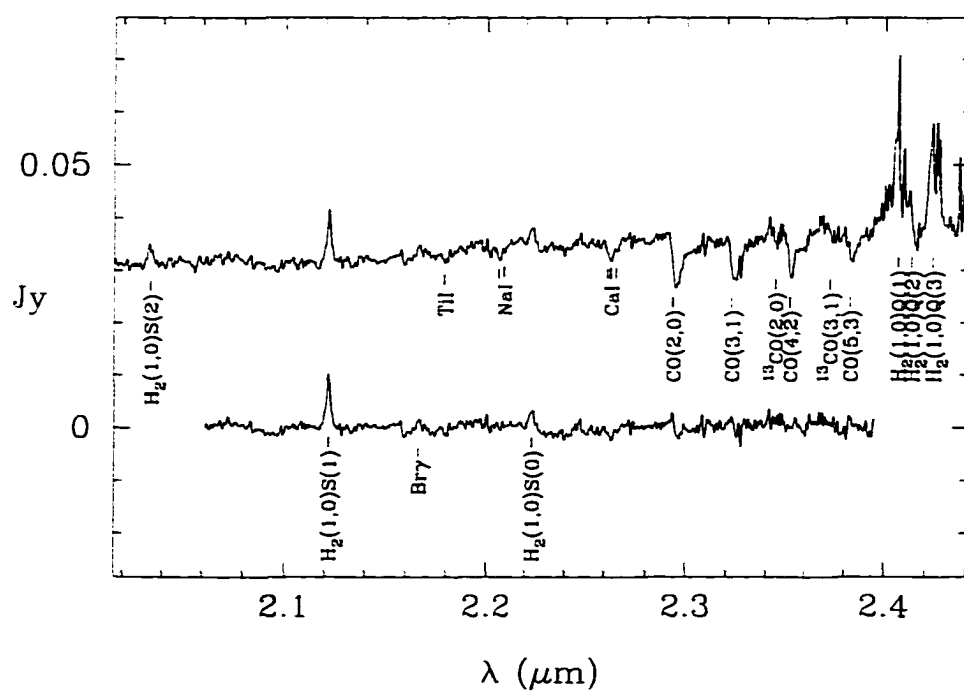


Figure 4.16 K-band spectrum of NGC3079.

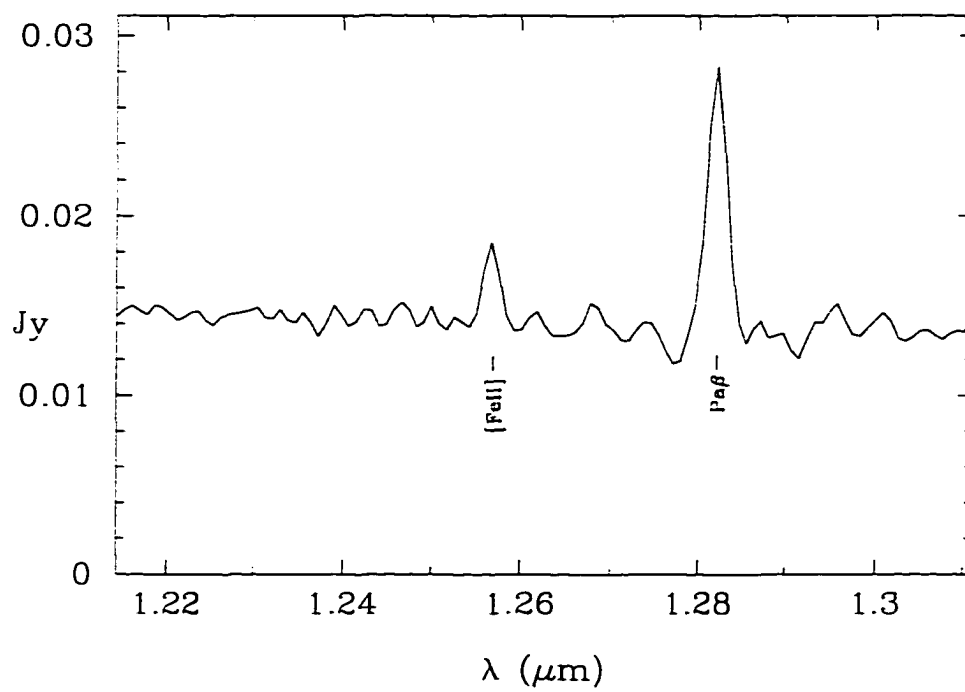


Figure 4.17 J-band spectrum of NGC7714.

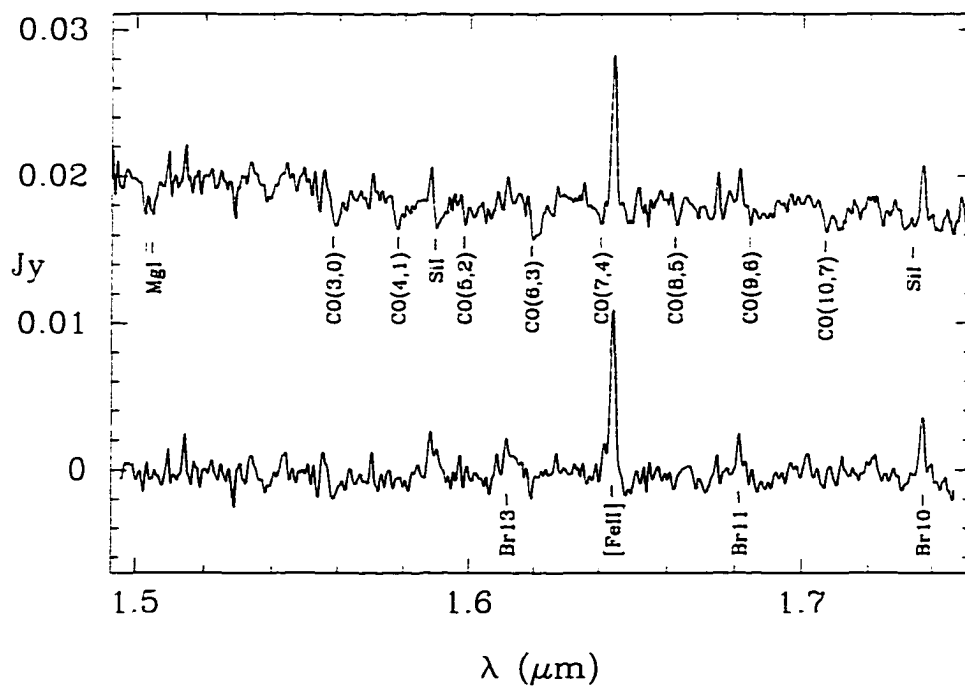


Figure 4.18 H-band spectrum of NGC7714.

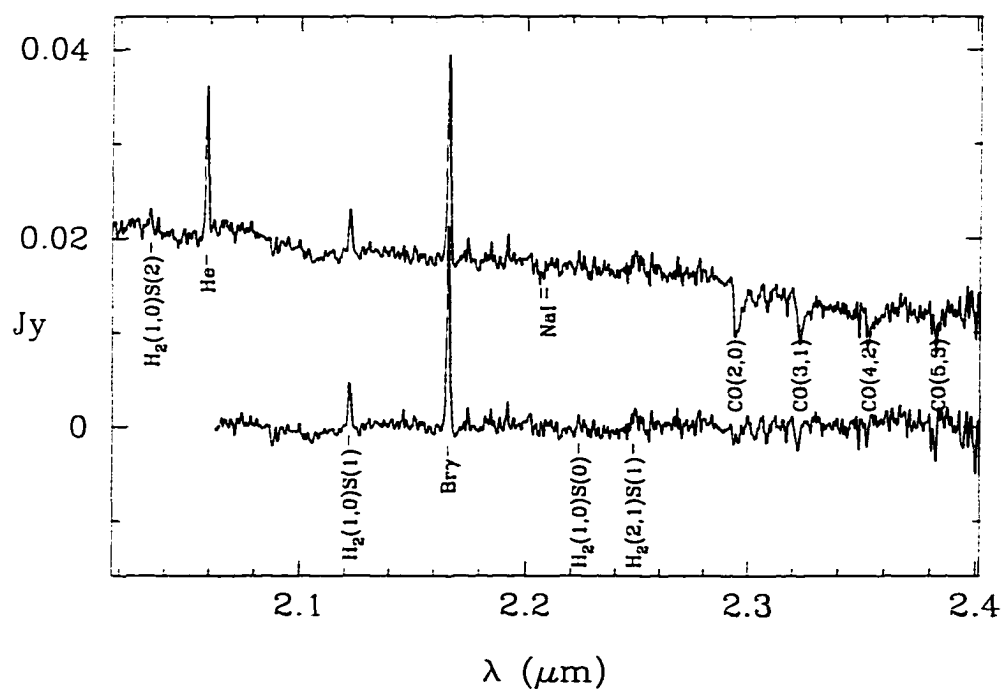


Figure 4.19 K-band spectrum of NGC7714.

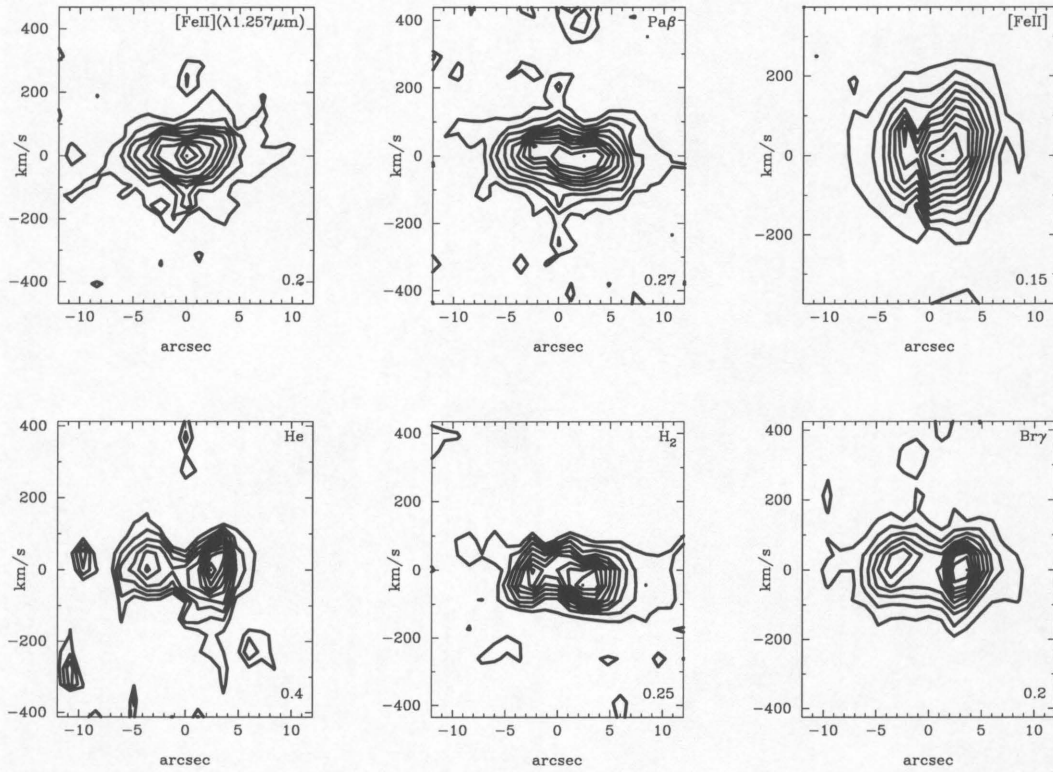


Figure 4.20 Position-velocity diagrams for strong emission lines in IC 342, obtained with the slit oriented at a P.A. of 90° . East is to the right and west is to the left. For each spectral line, the lowest contour (as a fraction of the peak) is indicated in the lower-right-hand corner. The line identification is printed in the upper-right-hand corner. Unless otherwise indicated, [Fe II] is the $1.644\mu\text{m}$ feature, He is the $2.058\mu\text{m}$ feature, and H_2 is the $2.121\mu\text{m}$ feature.

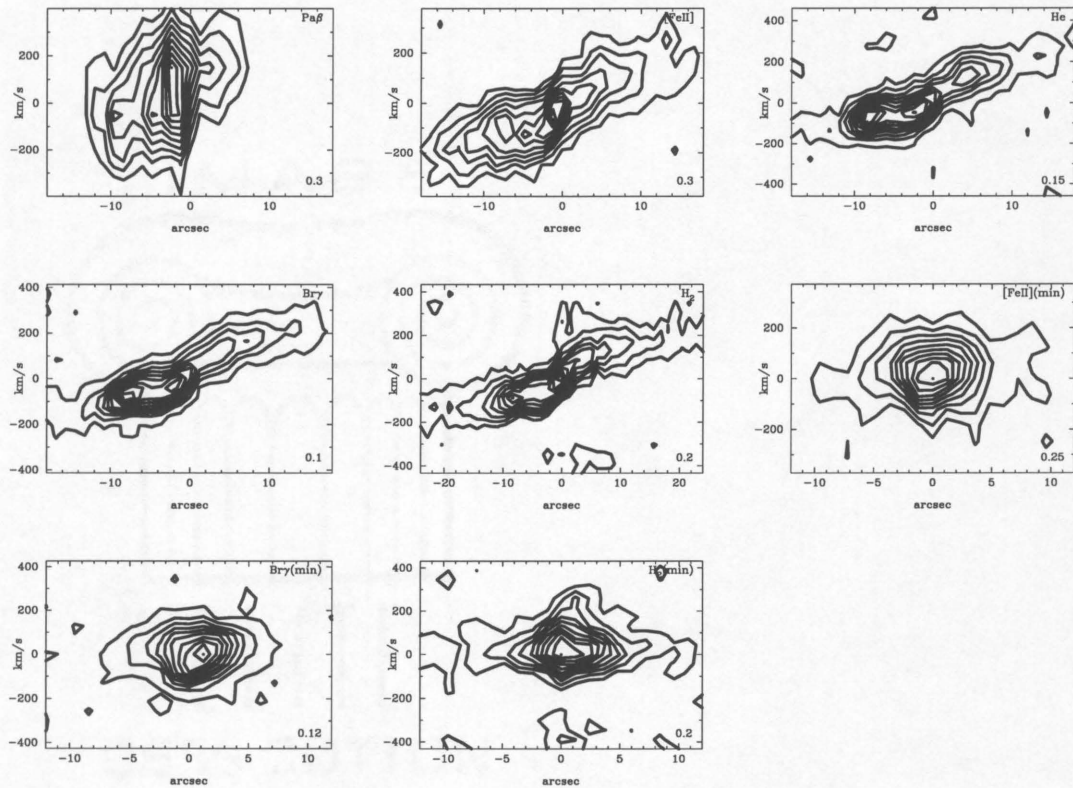


Figure 4.21 Position-velocity diagrams of five strong emission lines along the major axis of NGC 2146. Southeast is to the left and northwest is to the right. $\text{Pa}\beta$ appears broader than the other lines because that spectrum was obtained at lower resolution. Contours plotted as in Figure 4.20. Note that the spatial axis on the H_2 plot extends twice as far as the other plots. Also plotted are three emission lines along the minor axis (labeled with a “min”), where southwest is to the left and northeast to the right.

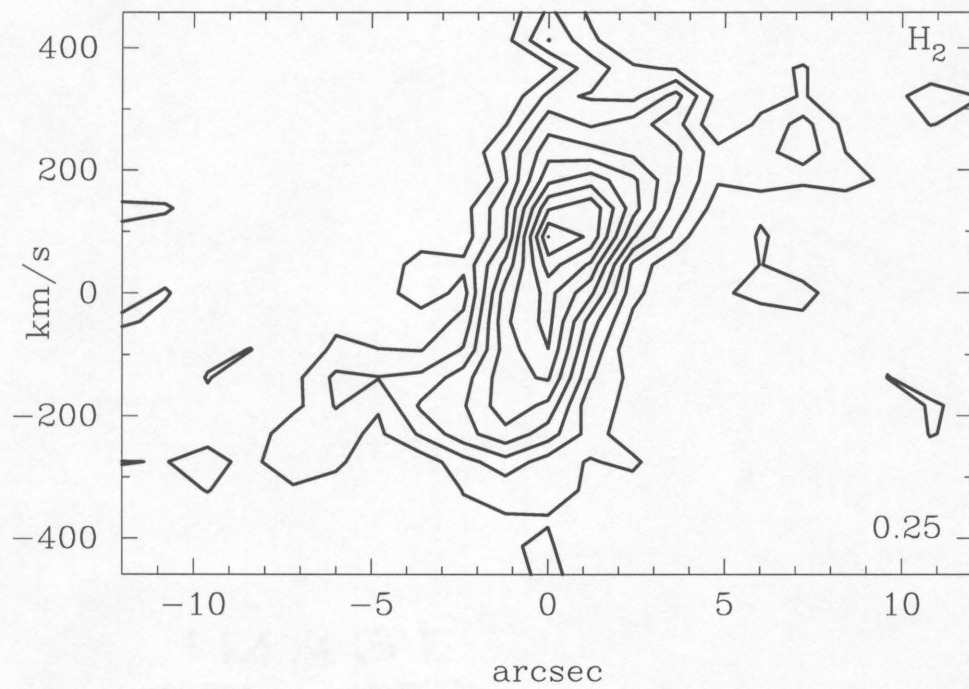


Figure 4.22 Position-velocity diagram for H_2 (1,0)S(1) along the major axis of NGC 3079. Details as in Figure 4.20.

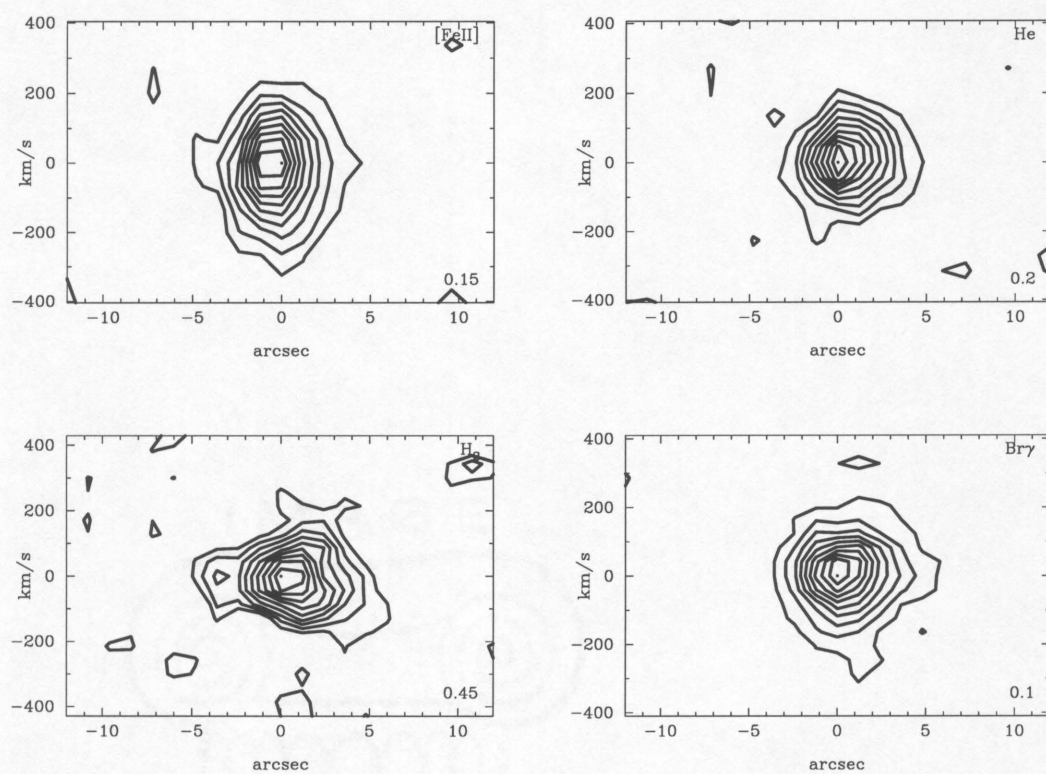


Figure 4.23 Position-velocity diagrams of four strong emission lines in NGC 7714, observed with the slit oriented at a P.A. of 90° . Details as in Figure 4.20.

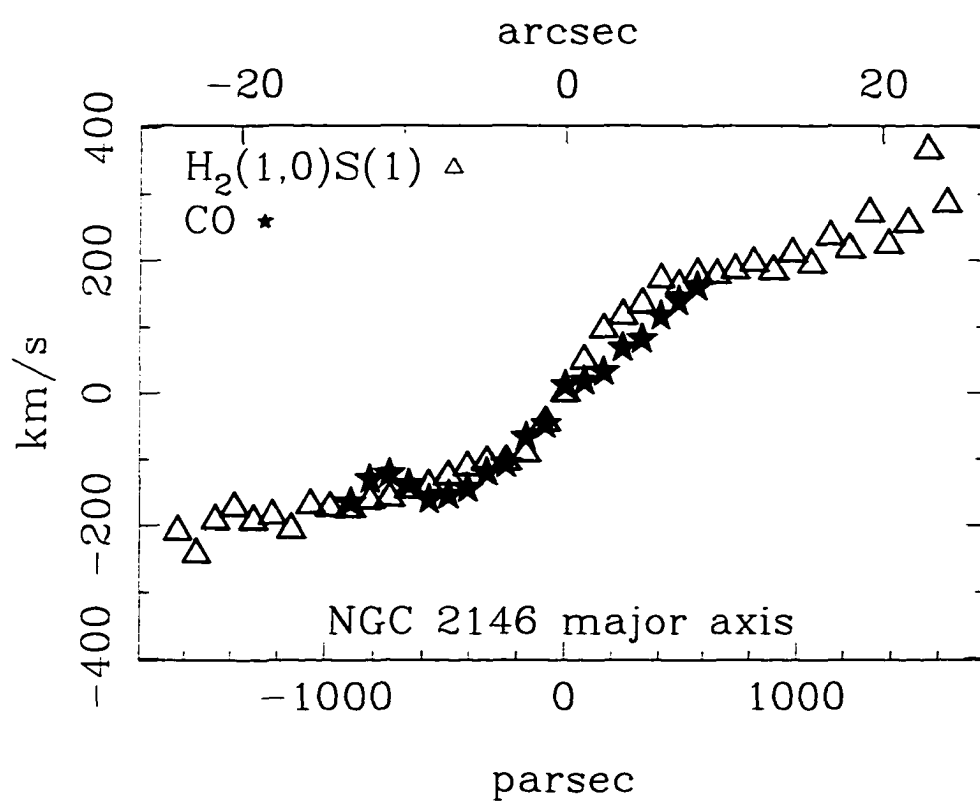


Figure 4.24 Velocity gradients of H_2 and the stellar CO absorption along the major axis of NGC 2146. The points have been corrected for an inclination of 51° .

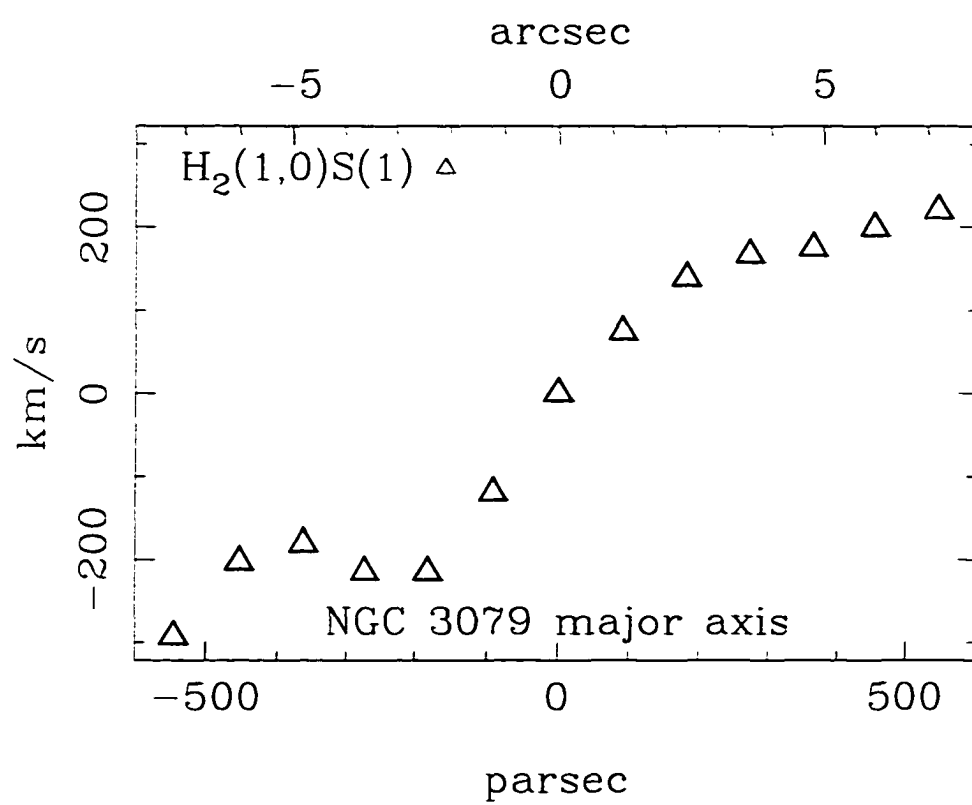


Figure 4.25 Velocity gradient of H_2 along the major axis of NGC 3079. The points have been corrected for an inclination of 80° .

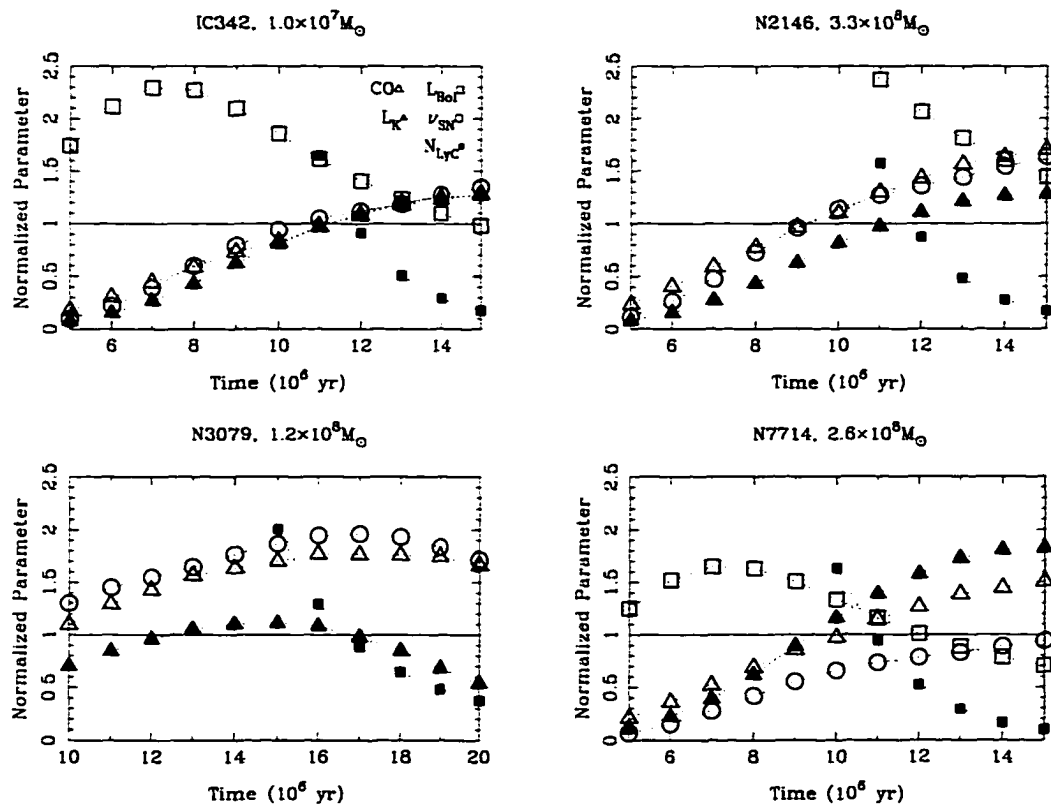


Figure 4.26 Starburst models using RLRT93's IMF 8.

CHAPTER 5

FILLING IN THE GAPS—A SEQUENCE OF STARBURST EVOLUTION

We present high-resolution ($R \sim 3000$), long-slit spectroscopic observations of 12 starburst galaxies in the H and K bands, plus J-band spectra at a resolution of 800. We also present broadband images of these galaxies in the J, H, and Ks bands. For comparison to a typical, “old” population, we have obtained similar data for four early-type galaxies. We use these data and data from the literature to constrain models of the nuclear starbursts for several of these galaxies. The high sensitivity and resolution of the spectra plus the use of a long slit allows us to derive kinematic properties of the nuclear region in addition to other constraints on the starburst population, such as ionizing flux and CO index.

We combine these results with analyses of a larger sample of galaxies to explore the range of properties and evolutionary status of 18 starburst galaxies. We find that a burst of star formation can easily account for the galaxy properties and that the range of properties observed is the result of a range of burst ages and strengths.

We find for several of the galaxies, in which the starburst is young enough and powerful enough to dominate the luminosity of the galaxy, that an IMF biased against the formation of low-mass stars is required to fit the observations.

Our large collection of high-quality spectra also allows us to produce a highly-detailed composite starburst spectrum which is the combination of approximately 15 starburst galaxy spectra and which displays typical starburst spectral features in very clear fashion.

5.1. Introduction

We present observations and modeling of a disparate sample of starburst galaxies. We have chosen galaxies classified as starbursts in the sample of mid-infrared spectra by Roche et al. (1991) (which gives us an additional constraint on the ionizing flux for some galaxies, based on the [Ne II] emission), and to this sample we have added several well-known starbursts. Much of the sample was selected on the basis of high $10\mu\text{m}$ flux and so the systems display a large range of properties in the near-infrared. As a result, the systems at larger distances tend to be biased towards the most spectacular examples of starburst activity, as only these galaxies will be bright enough to stand out in surveys. Based on our detailed studies of the nearby members of the sample, however, we can extend our conclusions to the distant members of the sample—many of the distant starbursts remain similar in character to the nearby starbursts, albeit with star formation at a much larger scale.

The large number of starbursts for which we have obtained detailed observations allow us to explore the range of starburst evolution discussed in the previous chapter more thoroughly. Our sample contains very young starbursts that

likely represent the first strong burst of star formation in those systems as well as more evolved starbursts which may be the product of multiple bursts of star formation.

5.2. Observations and Data Reduction

5.2.1. Images

J, H, and Ks-band images of the galaxies were obtained at the Steward Observatory (SO) 1.55m and 2.29 telescopes on several different observing runs using the NICMOS3-based SO infrared camera. A summary of the observations is presented in Table 5.2. This table also lists the standard stars used, which include stars from Courteau (1994) and Elias et al. (1982). Table 5.4 lists photometric measurements for each galaxy in different apertures to facilitate comparisons with other measurements and to provide a flux calibration for the spectra. With the exception of NGC 4194 (which was calibrated by averaging the results of Balzano (1983) and Spinoglio et al. (1995)), the data were obtained in photometric conditions and typical statistical uncertainties in the photometry are 2% to 3%, as determined from the scatter in multiple standard-star measurements. In some cases we were able to bracket the galaxy observations with observations of the same standard star at multiple airmasses, and the dispersion in these measurements is consistent with the level of uncertainty implied from the internal scatter of a single set of standard-star observations. In all cases we have used the Ks-band observations to compute K-band magnitudes for the galaxies—tests show that the deviation from a true K-band magnitude depends on color and is only a few percent for the galaxies observed here, so we have made no correction for this effect.

Infrared observations of many of these galaxies exist in the literature.

Comparison with these data indicate that systematic differences in the photometry are typical small (a few percent), but zero-point offsets are as high as 15% or 20% in a few cases. These differences are probably due to the different photometric systems used and to differences in the observing and data-reduction procedures.

Data reduction procedures are as described in ERRL96. The plate scale was typically 0.92 "/pixel at the 1.55m telescope and 0.65 "/pixel at the 2.29m telescope. We observed a few of the galaxies at the 1.55m telescope with a finer pixel scale of 0.32 "/pixel. The galaxies observed in this higher-resolution mode are NGC 4102, NGC 4194, NGC 5590, and NGC 6240. In particular, since the seeing was relatively good the night we observed NGC 6240, we took advantage of the fact that we had obtained many individual exposures with the galaxy on different parts of the array to subsample the image by a factor of two to obtain an image at a scale of 0.16 "/pixel (it should be noted, however, that the spatial resolution of this image is limited by the seeing, which was about 1").

The J, H, and K-band images are all flux-calibrated and are presented as contour plots in Figures 5.1 through 5.16, in units of magnitudes per square arcsecond. Each image is presented with north at the top and east to the left. The coordinate scale is plotted assuming that the K-band peak corresponds to the coordinates quoted for that galaxy in the NASA Extragalactic Database (NED). The fourth panel of each figure is used to display the galaxy in slightly different fashion, often in a grayscale rendering of the K-band image that in some cases has been dereddened as described below. In the case of NGC 6240, the fourth panel of the figure shows a zoomed-in view of the nuclear region to display more clearly the separation between the two nuclei, while for MKN 331 we display an expanded view of the field to show that galaxy's nearby companions.

We have produced $J - H$ and $H - K$ color images of the galaxies which have a large angular extent or which display an unusual morphology (which turns out to be a large fraction of the starburst galaxies). These images are presented in Figures 5.17 through 5.22, along with a K-band image of the same region for comparison. For some galaxies, we have used the $H - K$ image to generate a dereddening map. We assume an intrinsic $H - K$ color of 0.2 and compute a foreground screen extinction based on the color excess and the extinction law of Rieke & Lebofsky (1985). As discussed in ERRL96 and ERRKA97, the NIR extinction derived in this manner is relatively insensitive to dust geometry. We compute A_K from the dereddening map and subtract this image from the K-band image to produce a dereddened image of the galaxy.

5.2.2. Near-IR spectra

We obtained J, H and K-band spectra at the Steward Observatory 2.29m telescope during several observing runs from 1994 to 1996. The instrument used was FSpec, which is described in Williams et al. (1993). The scale along the spatial axis was 1.2 "/pixel (resulting in a slit length of $\sim 90''$ and the 2.29m telescope) and the spectral resolution depended on the grating used. For most of the H and K-band observations, we used the 600 l/mm grating, which corresponded to resolutions of ~ 2000 and ~ 3000 in the H and K bands, respectively. For a few of the galaxies, we obtained spectra with a 300 l/mm grating, which provided a resolution of ~ 800 , ~ 1000 , and ~ 1200 in the J, H, and K bands, respectively. For one galaxy, we obtained spectra with a 75 l/mm grating which supplied a resolution of ~ 800 in each band. The slit was two pixels wide. A summary of the observations is presented in Table 5.3. Data reduction procedures are as described in ERRL96 and ERRKA97.

The spectrometer slit was generally oriented East/West, although we repositioned the slit for those galaxies which were extended enough to obtain a significant rotation curve (e.g., NGC 3628 and NGC 660) or to explore the extent of the emission associated with the starburst. Positioning of the slit and guiding during the observations was facilitated by a slit-viewing infrared camera (using a NICMOS2 array), allowing us to position the slit precisely on the nuclei of the galaxies, especially those for which heavy dust obscuration hides the nucleus at optical wavelengths. This guider camera also allowed us to obtain images of the galaxies obtained simultaneously with the spectral observations.

We present the starburst spectra in Figures 5.23 through 5.25, where we have normalized each spectrum to fit them all on the plots. Each spectrum has also been shifted to zero redshift.

Noting that many of the starburst galaxy spectra are similar, we have used the large sample of galaxies we have obtained (including those in ERRL96, ERRKA97, and Paper I) to produce a “composite” starburst galaxy spectrum to explore the weaker features of the spectra with high sensitivity. We have excluded galaxies from this composite that have lines which are obviously broader than the rest of the sample (i.e., NGC 520, NGC 3079, and NGC 6240) or for which the H and K-band spectra were obtained at low resolution (i.e., NGC 5990 and NGC 6000). We have produced a similar composite spectrum for the control galaxies (NGC 3115, NGC 3379, NGC 4339, and NGC 5590), which we use to represent an old stellar population. These composite spectra are presented in Figures 5.26 through 5.28, where they are labeled as “SB” and “old”, respectively. Since the lines in the control sample galaxies were intrinsically broad, (i.e., the high-resolution and low-resolution spectra looked similar), we have combined data at different

resolutions to form the composite spectrum of the “old” stellar population.

We have produced position-velocity plots of strong spectral lines for many of the galaxies. These plots are displayed in Figures 5.29 through 5.37. These plots were derived from two-dimensional wavelength-calibrated spectra by fitting a continuum to the region around the spectral line and subtracting it from the image. The lines we present in this manner are typically [Fe II](1.644 μ m), He(2.058 μ m), H₂(2.122 μ m), and Br γ (2.166 μ m).

5.3. Model constraints

We now derive a series of observational constraints on the properties of the starbursts in our sample of galaxies. The main constraints on the youngest stars are the ionizing flux and the bolometric luminosity. The evolved stars dominate the near-infrared continuum and are thus mainly constrained by the K-band luminosity and by the spectral features in the near-infrared, such as the strong CO absorptions in the H and K bands. Slightly older populations give rise to supernovae and can thus be constrained by the supernova rate and sometimes by spectra if AGB stars dominate in the near-infrared or if the extinction is low enough for optical spectra to show strong Balmer absorptions.

The observations just listed constrain only the massive star population. Since the luminosity of the starburst is so thoroughly dominated by these stars, it is difficult to place constraints on the lower-mass component of the starburst. The approach we have taken is to constrain the dynamical mass of the starburst region, placing limits on the amount of mass that could be contained in stars in the burst and allowing the models to determine what fraction of that mass is in the form of low-mass stars. In the case of a young, powerful starburst, the mass constraint

is tight enough that a modification of the IMF is typically required if the large luminosity of the starburst is to be produced entirely by stars.

Since the nuclear regions of these galaxies are typically quite dusty, we must make a correction for the amount of light extinguished by dust to derive the true luminosity of the starburst. We first calculate the extinction for each galaxy. We then apply an extinction correction to the fluxes derived from our near-infrared data to determine extinction-free values of the starburst parameters which form the constraints on our models.

5.3.1. Extinction

The starburst galaxies in this sample are clearly affected by strong dust extinction towards their nuclei, as shown by the obvious dust lanes in many of the edge-on galaxies and the very red colors of much of the sample. This is to be expected, since large concentrations of gas and dust must exist in the nucleus to fuel the starburst. To place accurate constraints on the stellar populations in the starburst, however, we must correct for the attenuating effects of dust towards the emission regions. Since the amount of *attenuation* by dust is unknown a priori, we must estimate it from the amount of *reddening* caused by the wavelength dependence of dust absorption. The reddening is straightforward to measure in principle, if intrinsic colors or line ratios are known. The uncertainty in calculating the unextinguished flux derives from the mapping between the amount of reddening and the level of attenuation, which is dependent on the location of the dust relative to the emitting sources. As shown by the models of Witt, Thronson, & Capuano (1992), several different dust distributions can produce identical levels of reddening while absorbing very different amounts of light. Thus, at short wavelengths at least, the dust geometry has a strong effect on the derived attenuation factor. As shown in

ERRL96 and ERRKA97, however, the amount of absorption in the near-infrared bands is relatively insensitive to dust geometry if the extinction is determined using indicators in the near-infrared. We can therefore use a simple dust geometry like a foreground screen to correct the near-infrared fluxes, although this approach will almost certainly underestimate the amount of attenuation at shorter wavelengths.

Broad-band colors

A straightforward estimate of the reddening can be made from the $H - K$ color excess, $E(H - K)$, provided we know the intrinsic color of the stellar population. As in the previous papers of this series, we assume that the stellar population has an intrinsic $H - K$ color of 0.2 and that colors redder than that are entirely due to reddening by dust. This assumption breaks down if a significant fraction of the broadband flux is due to some source other than stars, such as emission from hot dust. Our spectra show, however, that the continuum light is dominated by stars and is not diluted by a featureless continuum source.

Once we determine $E(H - K)$, we use an analytical fit to the extinction law of Rieke & Lebofsky (1985) to determine A_λ . For reference, we list the A_V determined via this method for each galaxy in Table 5.6. Since we intend to compare these results with extinction determinations from the spectra, we have used photometry in an aperture carefully matched to the spectrometer slit, as listed in Table 5.4. We caution the reader that the values of A_V determined this way are almost certainly an underestimate. The values we actually use to correct our data for extinction are the corresponding A_J , A_H , and A_K , which are only weakly dependent on the assumed dust geometry.

Line ratios

We can use line ratios from the spectra we have presented here to constrain the reddening. There are two pairs of lines for which we know the intrinsic ratio— $\text{Pa}\beta/\text{Br}\gamma$ and the $[\text{Fe II}]$ transitions at $1.257\mu\text{m}$ and $1.644\mu\text{m}$, which come from the same upper level. The intrinsic $\text{Pa}\beta$ to $\text{Br}\gamma$ ratio we assume to be 5.58, using the results of Hummer & Storey (1987) for a temperature of 5000 K and a density of 100 cm^{-2} . We use the A-values of Nussbaumer & Storey (1988) to derive an intrinsic ratio of the $[\text{Fe II}]$ lines of 1.36. We then use the observed ratios to determine the amount of reddening, using the Rieke & Lebofsky extinction law as described above. The calculated values of A_V are listed in Table 5.6, and the caveats discussed in the previous section apply.

Comparison

It can be seen from the table that the line ratios give results that are similar to the broadband results. This suggests both that the K-band continuum is not affected by emission sources besides stars, and that the young stars (traced by the hydrogen recombination lines) and the old stars (traced by the K-band light and the $[\text{Fe II}]$ flux from supernova remnants) are affected by the same level of extinction. We illustrate this in Figure 5.42, where we plot the extinction determined from the broad-band measurements vs. the extinction determined via line ratios. We have included data from ERRL96, ERRKA97, and Paper I.

5.3.2. Luminosity and spectral index constraints

The main constraints on the starburst models are described in detail in the previous papers in this series. In summary, we make use of the K-band and bolometric

luminosity, the number of ionizing photons per second (N_{LyC}), the CO index, the supernova rate, and the dynamical mass. The K-band luminosity is derived from our images and corrected for dust attenuation using the extinction derived in §5.3.1. We take L_{Bol} from the results of Spinoglio et al. (1995), who derive total luminosities from the near-infrared to the far-infrared. Although the luminosity of galaxies with a young and powerful starburst is very much dominated by the starburst nucleus, the total luminosity is probably an overestimate of the nuclear luminosity for those older systems which have a significant contribution from the older population in the rest of the galaxy. The number of ionizing photons per unit time is derived both from our data (using the $\text{Br}\gamma$ flux and assuming case B recombination) and from the $[\text{Ne II}]$ line at $12.8\mu\text{m}$, using the results of Roche et al. (1991). We estimate the supernova rate using the flux in the $[\text{Fe II}]$ line at $1.644\mu\text{m}$ and the relation derived by Vanzi & Rieke (1997). The CO index is measured directly from our spectra.

5.3.3. Dynamical mass

Rotation

The dynamical masses of the nuclear regions of the galaxies can be obtained from the rotation curves of those few systems which are viewed at moderate to high inclination angle and which display strong enough spectral features to measure a velocity offset along the slit. We present rotation curves measured in $\text{Br}\gamma$ and the (1,0)S(1) line of H_2 for four of the starbursts discussed here in Figures 5.38 through 5.41. The galaxies NGC 660 and NGC 3628 are nearly edge-on and our slit orientation lay along the major axis of the galaxy, so we have made no correction to the observed velocity offsets along the slit. We measure circular velocities of 140 km s^{-1} and 120 km s^{-1} at the radius of our slit extraction (indicated in

Table 5.3) in these two galaxies, implying masses of $10^9 M_\odot$ and $5 \times 10^8 M_\odot$, respectively. The galaxies NGC 2782 and NGC 4102 displayed large velocity gradients across the slit but are only moderately-inclined to our line of sight, so a correction for inclination was required. We used the ellipse-fitting routines in the STSDAS (Space Telescope Science Data Analysis System) package in IRAF to determine the ellipticity and position angles of these two galaxies in our K-band images. We find values of (0.25, 75°) and (0.35, 45°) for (ellipticity, position angle) in NGC 2782 and NGC 4102, respectively. We correct our observed velocity gradients across the slit for the implied inclination (40° and 50°) as well as for the difference in position angle between our slit and the galaxy. The implied masses are $4 \times 10^9 M_\odot$ and $8 \times 10^8 M_\odot$ in NGC 2782 and NGC 4102.

Velocity dispersion

As discussed in the previous chapters, our spectra are of sufficient resolution and signal-to-noise to determine reliably the velocity dispersion of the stellar population. This is useful as a check on the mass determined via rotation in those systems which have both a well-measured rotation curve and a significant spheroidal component which allows us to model the velocity dispersion in straightforward fashion. We have performed this comparison in NGC 2782 and obtain results very similar to those obtained from the rotation curve (the dispersion measurement indicates a mass of $\sim 3 \times 10^9 M_\odot$). The velocity dispersion is also the only constraint on the mass that we have for face-on systems or galaxies for which we are unable to measure a rotation curve for other reasons.

As discussed in ERRL96, we measure the velocity dispersion using the (2,0) CO band head at $2.3\mu\text{m}$, with a cool giant or supergiant as a template. The

stellar spectrum is cross-correlated with the galaxy spectrum and the width of the cross-correlation peak is used to determine the velocity dispersion. In practice, we compare the galaxy spectrum to several stars from our stellar library (described in Chapter 3), which allows us to estimate the uncertainty in the velocity dispersion, which is typically $\sim 20\%$.

We assume a spheroidal stellar distribution and further assume that the scale radius is comparable to the size of the slit aperture. This assumption is approximately true for the galaxies for which we have measured the scale radius; in any case, the derived mass is not very sensitive to the scale radius. The uncertainty in the mass determination is dominated by the velocity dispersion, since the mass scales as the square of the dispersion. To place a conservative constraint on the dynamical mass, we have set the mass equal to the 2σ upper limit for each galaxy. The results are listed in Table 5.7. The masses for NGC 1614 and NGC 6240 are obtained from Shier et al. (1996). We have not listed a mass for NGC 5990 and NGC 6000 because our spectra of these galaxies are of insufficient resolution. No mass is listed for NGC 520 because we have no observation of the CO bands in this galaxy. The emission lines in this galaxy are of sufficient strength to trace out a velocity curve, but the disturbed morphology of this strongly-interacting system precludes us from determining the geometry of the nuclear region or even from assuming that a disk in keplerian rotation is an appropriate model for the gas distribution.

5.3.4. Summary

We have summarized the derived constraints in Table 5.7. With the exception of Maffei 2 (which is by far the closest galaxy in the sample and has a starburst region much larger than our slit width), the luminosities of the small regions

covered by our spectra are quite large. The K-band magnitudes of the starbursts range from -20 to brighter than -25, while our comparison galaxies range from -20 to -21 in the same aperture. The most luminous galaxy in our fixed aperture is (not surprisingly) the most distant, so if we restrict our comparison to galaxies within the range of distance covered by the control sample, the starbursts are only moderately brighter, ranging up to $M_K \sim -22$.

The ionizing fluxes are quite large even in our small aperture, with a typical value $\sim 10^{53} \text{ s}^{-1}$. That the estimates of N_{LyC} made using the [Ne II] flux are systematically larger than those made with our Br γ measurements probably indicates that the extent of the starburst in most of the galaxies is significantly larger than our spectrometer aperture (since the [Ne II] measurements were made in circular apertures larger than the regions from which we have extracted spectra).

The supernova rates implied by the [Fe II] flux typically range from 1 to 10 per century, with the exception of the very strong starburst in NGC 1614 (which is over 50 per 100 years) and the merger system NGC 6240 (which is an order of magnitude larger than NGC 1614—see also van der Werf et al. (1993)).

With the exception of a couple of systems, the CO index of the starbursts is much larger than is typical for evolved populations, indicating that the K-band spectra are dominated by supergiants or perhaps AGB stars in some of the older systems.

5.4. Models

To estimate the relative strength of the starbursts studied here, we have made use of the models of Rieke et al. (1993). As a first comparison, we have produced

starburst models for each galaxy using a single burst of star formation that is gaussian in time with a FWHM of 5 million years. The models use IMF 8 of Rieke et al., which is the IMF those authors found to best fit the starburst in M 82. The IMF is similar to that of the solar neighborhood at the high-mass end but has a much shallower slope at the low-mass end and is therefore biased against the formation of low-mass stars. In the short timespans we are considering here, the low-mass stars contribute nothing to the luminosity, so the only effect of the altered IMF is to change the total mass in stars required to meet a given luminosity constraint. In the discussion that follows, the reader should note that qualitatively similar results can be obtained with a solar-neighborhood IMF, but that roughly 3 times as much mass is required as compared to IMF 8 of Rieke et al..

This simple, single-burst approximation ignores the evidence for a complex star-formation history in many of these systems, a point we discuss further in §5.5. Nevertheless, this approach will give us a qualitative idea of the relative burst strengths and ages in these galaxies. For each galaxy, we employ the simple procedure of varying the mass until the luminosity constraints can all be met at some time. For a single burst, the age is usually tightly constrained because as the massive stars evolve, the ionizing flux drops quickly at the same time that the K-band luminosity and CO index are increasing. Matching these quantities simultaneously requires that the starburst has aged slightly, so that the most massive stars have already exploded as supernova, somewhat less massive stars are now old supergiants, and somewhat lower-mass stars are still on the main sequence providing ionizing flux. The results for each galaxy are listed in Table 5.8.

For each galaxy, we have also listed the fraction of the dynamical mass that is required for the starburst model to match the observations. These numbers are

very much lower limits for several reasons. For example, we have only required the models to produce the luminosity observed in the spectrometer aperture. For the most distant galaxies in the sample, the spectrometer slit probably contains most of the starburst flux, but this is clearly not true for the nearby systems. In some cases, the luminosity of the starburst in the region for which we have derived the mass may be at least a factor of 2 or 3 higher than listed in Table 5.7, with a corresponding larger mass required to meet the observational target. Also, as discussed above, the IMF used in these computations is biased against the formation of low-mass stars in the sense that the slope of the IMF is nearly flat below $3 M_{\odot}$. An IMF more nearly like recently-determined forms for the solar neighborhood requires roughly 3 times as much mass in this context to match the observations. For some of the galaxies in this sample (particularly NGC 1614 and NGC 4194), the fraction of the dynamical mass required in the starburst is uncomfortably high, 60% - 70%, if a solar-neighborhood IMF is used. We have also not discussed the issue of fueling the starburst. Molecular gas observations (mostly in CO) exist for many of these galaxies, and they indicate that large concentrations of molecular gas lie in the nuclei of these galaxies. This is not surprising, since we know that this gas is required to fuel the starburst. As discussed in the previous chapters, mass estimates of the molecular gas are difficult to obtain, since there is evidence that the standard $I(\text{CO})$ to M_{H_2} conversion can drastically overestimate the gas mass. Nevertheless, we would expect the molecular gas mass to be at least comparable to, or much greater than, the mass of stars formed in the burst, since star formation efficiencies approaching 100% must be difficult if not impossible to obtain. From the arguments outlined above and with support from hydrodynamical simulations it seems unlikely that significantly more than 20% of the dynamical mass could be turned into stars in a burst and that an old stellar population must

dominate the nuclear mass. As we can see from Table 5.8, however, several of the galaxies are quite close to this limit, even using the biased IMF derived by Rieke et al. (1993) for M 82.

5.5. Discussion of individual galaxies

NGC 520—This galaxy is clearly in the process of colliding with a smaller companion. The main nucleus is heavily obscured, and is nearly invisible at short wavelengths, even in the J band. The spectrum of this galaxy displays strong and broad line emission indicative of a fairly young starburst. This contrasts with evidence from optical spectra of this galaxy (Bernlöhr 1993; Liu & Kennicutt 1995), which show strong Balmer absorptions indicative of a large population of stars of order 10^8 years old. It seems likely that the collision of these two galaxies has triggered multiple episodes of star formation, with the intermediate-age population dominating outside the nucleus and a young starburst dominating in the nucleus behind too much extinction to be observed in the optical. The intense interaction and strong dust lane makes the orientation of the component galaxies difficult to discern.

NGC 660—NGC 660 is a well-known polar-ring galaxy and shows a moderately-disturbed morphology in the NIR. It has a strong bar which is most evident in the dereddened K-band image.

Maffei 2—This galaxy is a member of the nearby IC 342 group and is a fairly close companion of the large elliptical Maffei 1. The projected separation between these two galaxies is only 40 kpc if the distance to this galaxy is similar to other galaxies in this group (3.6 Mpc, Krismer, Tully, & Gioia 1995). Maffei 2 has a strong bar and a fairly disturbed morphology (for example, spiral-arm-like

structures project in both directions from the eastern end of the bar!) It has been suggested (Hurt et al. 1996) that Maffei 2 is in the process of devouring a small companion galaxy which may have triggered the starburst activity.

Although this galaxy is one of the nearest large starbursts, it has not been well studied because it is heavily obscured by the plane of our galaxy, as can be seen by the high density of foreground stars in the images. Our spectra of this galaxy indicate that it hosts a relatively old starburst, as the emission lines are quite weak but the CO bands are very strong, indicating that the K-band spectrum is either dominated by supergiants which must have formed recently or perhaps by a population of AGB stars which could give rise to the strong ^{13}CO bands observed in this galaxy.

NGC 1614—NGC 1614 is a nearly face-on galaxy with a well-defined spiral pattern. The nucleus is extremely bright; the galaxy is similar to NGC 7714 in this respect. The outer isophotes of this galaxy suggest tidal tails, possibly from an encounter with some nearby galaxy. The equivalent widths of the emission lines in the galaxy are quite high and the optical spectrum shows Wolf-Rayet features, suggesting that this galaxy hosts a very young starburst, again similar to NGC 7714.

NGC 2782—NGC 2782 is a nearly face-on galaxy with a poorly-defined spiral pattern. A hint of a spiral arm is evident in the western half of this galaxy, and the knotted structure there corresponds to a string of HII regions apparent in $\text{H}\alpha$ images of this galaxy (S. Jogee, private communication). The galaxy clearly shows tidal structures in the western part of the galaxy, although the identification of a companion galaxy that might be the cause of these structures is unclear. This galaxy also appears to have a bar in the center which may play a role in fueling the

starburst.

NGC 3628—This galaxy is a prominent member of the Leo I triplet and has probably undergone some sort of interaction with the other members of that group. It is an edge-on spiral with a strong dust lane that nearly completely obscures the nucleus at short wavelengths. The dereddened image is dominated by the nucleus and a very bright, thin disk. The color images of this galaxy indicate that the reddening is stronger in the southern half of the galaxy, suggesting that this galaxy is slightly inclined with the northern half being the near side.

NGC 4102—Little is known about this galaxy. The isophotes in the central region seem to be oriented at a different position angle than the rest of the galaxy, suggesting that we might be looking at a moderately-inclined spiral galaxy with a bar or oval distortion.

NGC 4194—This galaxy is also known as MKN 201, and clearly is undergoing some sort of interaction. Our images display a double nucleus and strong tidal tails to the north and south in the fainter isophotes. The galaxy is host to a very strong burst of star formation, as is evident from the strengths of the emission lines in the spectra.

NGC 5990—Very little is known about this galaxy. As far as we know, the images presented here are the only infrared images in the literature. The starburst in this galaxy appears fairly weak and is probably old, since the emission lines have a low equivalent width and the continuum spectrum indicates that it probably arises from a mixture of giants and supergiants.

NGC 6000—Very little is known about this galaxy, as well. It is a moderately-inclined spiral. This galaxy appears to host a fairly young and powerful starburst.

We are unaware of any other infrared images of this galaxy in the literature.

NGC 6240—This is perhaps the most unusual galaxy in the sample. The object appears to be the result of a collision between two large galaxies, and we can just barely resolve the two nuclei in the images here. The outer isophotes indicate a highly disturbed and asymmetric morphology. The color images of this galaxy indicate that the brighter of the two nuclei is also the most heavily obscured. It is one of the most luminous objects known in the (1,0)S(1) line of H_2 and shows very strong and broad [Fe II] emission as well, while the hydrogen recombination line flux is quite weak.

MKN 331—This system is composed of three galaxies, the brightest one of which is the object of study here. This galaxy appears to be a spiral galaxy viewed at a low inclination angle. It has an edge-on spiral and an irregular galaxy as companions.

5.6. Conclusion

We have presented imaging and spectroscopy in the near-infrared for a large sample of starburst galaxies. We use these data and data from the literature to derive a series of constraints on the stellar populations in these galaxies. We use the high resolution and sensitivity of our spectra to derive mass constraints on the nuclear regions of the galaxies. Given these mass limits, at least the young and powerful starbursts must form stars with an IMF that is biased against the formation of low-mass stars relative to the solar neighborhood.

We find a large range of starburst age and strength throughout our sample. While some of the galaxies are dominated by a single, young burst, many of the

galaxies display evidence of a mixture of young and intermediate-age populations that indicates a complex star formation history. A picture of starburst evolution in which the starburst region is made up of smaller units with a range of ages would seem to be indicated.

Table 5.1. Galaxy Data

Galaxy	$\alpha(1950)$	$\delta(1950)$	D(Mpc)
NGC 520	01 ^h 22 ^m 00 ^s .0	+03°31'52"	30
NGC 660	01 ^h 40 ^m 20 ^s .7	+13°23'32"	11
Maffei 2	02 ^h 38 ^m 08 ^s .2	+59°23'27"	3.6
NGC 1614	04 ^h 31 ^m 35 ^s .5	-08°40'42"	64
NGC 2782	09 ^h 10 ^m 53 ^s .8	+40°19'17"	34
NGC 3115	10 ^h 02 ^m 44 ^s .4	-07°28'32"	9
NGC 3379	10 ^h 45 ^m 11 ^s .0	+12°50'48"	12
NGC 3628	11 ^h 17 ^m 39 ^s .6	+13°51'48"	11
NGC 4102	12 ^h 03 ^m 51 ^s .6	+52°59'23"	11
NGC 4194	12 ^h 11 ^m 41 ^s .7	+54°48'21"	33
NGC 4339	12 ^h 21 ^m 01 ^s .3	+06°21'32"	17
NGC 5590	14 ^h 19 ^m 32 ^s .0	+35°25'57"	43
NGC 5990	15 ^h 43 ^m 44 ^s .8	+02°34'11"	51
NGC 6000	15 ^h 46 ^m 44 ^s .3	-29°14'06"	28
NGC 6240	16 ^h 50 ^m 27 ^s .8	+02°29'03"	98
MKN 331	23 ^h 48 ^m 53 ^s .5	+20°18'27"	74

Note. — All distances were determined assuming $H_0 = 75 \text{ km s}^{-1} \text{ Mpc}^{-1}$ except for the distance to Maffei 2, which was taken from Krismer, Tully, & Gioia 1995.

Table 5.2. Imaging Observing Log

Galaxy	Date	Telescope	itime (sec)			Standard
			<i>J</i>	<i>H</i>	<i>Ks</i>	
NGC 520	10/24/96	1.5 <i>m</i>	400	400	400	FS4
NGC 660	10/24/95	1.5 <i>m</i>	400	200	220	FS3
Maffei 2	10/24/96	1.5 <i>m</i>	300	300	300	FS4
NGC 1614	10/13/95	1.5 <i>m</i>	540	300	300	HD22686
NGC 2782	12/19/96	2.3 <i>m</i>	700	800	800	HD84800
NGC 3115	3/31/96	1.5 <i>m</i>	200	200	200	HD84800
NGC 3379	3/31/96	1.5 <i>m</i>	200	200	200	HD105601
NGC 3628	3/31/96	1.5 <i>m</i>	1800	1800	1800	HD105601
NGC 4102	3/31/96	1.5 <i>m</i>	270	270	270	HD129653
NGC 4194	3/30/96	1.5 <i>m</i>	540	540	1080	HD129653
NGC 4339	12/19/96	2.3 <i>m</i>	320	320	320	HD106965
NGC 5590	3/31/96	1.5 <i>m</i>	1260	1350	1350	HD129653
NGC 5990	4/29/97	2.3 <i>m</i>	240	240	240	HD129655
NGC 6000	4/29/97	2.3 <i>m</i>	240	240	240	S-R 3
NGC 6240	3/30/96	1.5 <i>m</i>	1080	1080	1080	HD161903
MKN 331	10/24/96	1.5 <i>m</i>	480	480	480	FS30

Note. — The data were obtained either at the 2.29m telescope on Kitt Peak or at the 1.55m telescope on Mt. Bigelow outside of Tucson, AZ. The images were obtained at a platescale of 0.92"/pixel at the 1.55m telescope and 0.65"/pixel at the 2.29m telescope, with the exception of NGC 4102, NGC 4194, NGC 5590, and NGC 6240, which were taken at a spatial scale of 0.32"/pixel.

Table 5.3. Spectroscopy Observing Log

Galaxy	Dates	Itime (min.)	Extracted Aperture(")	slit P.A.(°)
NGC 520	12/14/94	48	2.4×9.6	140
NGC 660	12/12, 12/15/94, 11/19/96	16	2.4×9.6	40
Maffei 2	12/15, 12/16/94, 11/20/96	15	2.4×6	90
NGC 1614	12/13, 12/16/94, 11/20/96	18	2.4×6	90
NGC 2782	12/15/94, 11/20/96	22	2.4×6	90
NGC 3115	12/9, 12/13/94	8	2.4×14.4	90
NGC 3379	12/14/94	6	2.4×14.4	90
NGC 3628	1/21, 1/22/95, 2/20/97	19	2.4×6	120
NGC 4102	1/22, 5/19, 6/12, 6/24/95	10	2.4×6	90
NGC 4194	1/22, 5/19, 6/12, 6/24/95	14	2.4×6	90
NGC 4339	6/27/96	16	2.4×6	90
NGC 5590	2/11/95	12	2.4×6	90
NGC 5990	6/23, 6/26/96	44	2.4×6	90
NGC 6000	6/24, 6/26/96	20	2.4×6	90
NGC 6240	2/11, 6/14, 6/15/95, (6/28/96)	19(4)	2.4×6	90
MKN 331	12/13/94, (11/19/96)	18(23)	2.4×6	90

Note. — All spectra presented here were obtained at the 2.29m Bok telescope on Kitt Peak. We present both high (600 l/mm grating) and moderate (300 l/mm grating) resolution spectra for NGC 6240 and MKN 331—the numbers in parentheses refer to the intermediate-resolution observations. Integration times are average values per grating setting.

Table 5.4. Aperture Photometry

Galaxy	12'' circular aperture			slit aperture ^a		
	<i>J</i>	<i>H</i>	<i>K</i>	<i>J</i>	<i>H</i>	<i>K</i>
NGC 520	12.13	11.07	10.33	13.83	12.52	11.55
NGC 660	10.49	9.45	8.87	11.64	10.56	9.96
Maffei 2	10.79	9.42	8.75	12.36	10.93	10.20
NGC 1614	11.31	10.60	10.17	12.28	11.48	11.06
NGC 2782	11.30	10.45	10.14	12.48	11.58	11.20
NGC 3115	8.78	8.11	7.85	9.82	9.16	8.93
NGC 3379	9.28	8.58	8.36	10.35	9.66	9.44
NGC 3628	11.46	10.32	9.74	13.53	12.15	11.34
NGC 4102	10.05	9.22	8.75	11.20	10.27	9.71
NGC 4194	11.27	10.47	10.12	12.38	11.49	11.07
NGC 4339	11.15	10.40	10.17	12.57	11.74	11.47
NGC 5590	11.68	11.01	10.71	13.09	12.37	12.04
NGC 5990	11.37	10.53	10.06	12.46	11.64	10.96
NGC 6000	10.60	9.84	9.41	11.81	11.15	10.63
NGC 6240	11.73	10.70	10.01	12.82	11.64	10.82
MKN 331	11.55	10.76	10.28	12.50	11.62	11.12

^aSee Table 5.3 for aperture size.

Note. — The statistical uncertainties in the photometric measurements are small, typically 2%-3%.

Table 5.5. Strong Emission Line Fluxes

Galaxy	Transition ($\lambda(\mu\text{m})$)					
	[Fe II] (1.257)	Pa β (1.282)	[Fe II] (1.644)	HeI (2.059)	H ₂ (2.122)	Br γ (2.166)
NGC 520	1.24	0.36	0.89	0.99
NGC 660	3.85	7.11	4.35	0.51	2.37	3.13
Maffei 2	0.93	1.39	1.40	0.22	0.70	0.85
NGC 1614	3.74	11.6	4.20	1.92	0.70	3.20
NGC 2782	2.49	4.20	2.67	0.52	0.62	0.92
NGC 3628	0.45	0.79	1.16	< 0.16	0.80	1.49
NGC 4102	3.70	5.06	4.72	0.55	2.12	2.78
NGC 4194	3.46	8.14	3.63	1.10	0.65	2.48
NGC 5990	0.37	0.59	0.53	< 0.14	0.60	0.27
NGC 6000	2.82	3.98	2.16	0.42	0.98	1.78
NGC 6240	5.35	1.37	6.97	< 0.14	15.1	0.69
MKN 331	2.22	2.39	1.73	0.22	1.21	0.95

Note. — Line fluxes are in units of 10^{-14} erg/s/cm². Typical uncertainties are 10% to 15%.

Table 5.6. Visual extinction from colors and line ratios

Galaxy	technique		
	$(H - K)$	$(\text{Pa}\beta/\text{Br}\gamma)$	$([\text{Fe II}]_{\frac{1.257\mu\text{m}}{1.644\mu\text{m}}})$
NGC 520	12.3
NGC 660	6.4	6.9	5.3
Maffei 2	8.5	9.4	8.8
NGC 1614	3.5	3.3	5.2
NGC 2782	2.9	1.5	4.6
NGC 3628	9.7	18.1	15.4
NGC 4102	5.7	8.6	6.8
NGC 4194	3.5	4.1	4.4
NGC 5990	7.7	7.2	8.2
NGC 6000	5.1	7.0	0.5
NGC 6240	9.9	7.9	7.0
MKN 331	4.8	6.1	0.7

Note. — Extinctions are measured in magnitudes. Errors are computed assuming average uncertainties of 5%, 14%, and 21% for the broad-band magnitudes, hydrogen recombination lines, and $[\text{Fe II}]$ lines, respectively, and so are roughly 1, 2, and 4 magnitudes for the broad-band measurements, the hydrogen lines, and the $[\text{Fe II}]$ lines, respectively.

Table 5.7. Starburst model constraints

Galaxy	M_K	N_{LyC}^a	N_{LyC}^b	$\nu_{SN}(\text{yr}^{-1})$	L_{Bol}^c	CO	Mass ^d
NGC 520	-22.2	53.4	...	0.1	11.1
NGC 660	-21.0	52.7	53.1	0.02	11.1	0.17	10
Maffei 2	-18.5	51.3	...	0.001	...	0.21	1.5
NGC 1614	-23.4	54.2	54.5	0.5	11.7	0.23	30 ^e
NGC 2782	-21.8	53.0	...	0.07	10.8	0.14	40
NGC 3628	-20.0	52.6	...	0.01	9.6	0.18	5
NGC 4102	-21.1	52.7	53.4	0.02	10.5	0.17	8
NGC 4194	-21.9	53.5	...	0.1	11.0	0.15	13
NGC 5990	-23.4	53.1	...	0.07	11.2	0.14	...
NGC 6000	-22.2	53.3	54.0	0.06	...	0.21	...
NGC 6240	-25.2	54.2	54.6	5	12.0	0.22	550 ^e
MKN 331	-23.8	53.8	54.3	0.3	11.6	0.16	90

^aLogarithm of number of ionizing photons per second, calculated from the Br γ measurements reported in this paper.

^bLogarithm of number of ionizing photons per second, calculated from the [Ne II] flux reported in Roche et al. 1991 after corrected for the different distances adopted in this paper.

^cLogarithm of L_{Bol} , in units of L_{\odot} .

^dDynamical mass within the spectrometer aperture in units of $10^8 M_{\odot}$.

^e 2σ upper limit from Shier et al. 1996.

Note. — M_K , $N_{LyC}(\text{Br}\gamma)$, SNR, and CO index refer to the slit apertures listed in Table 5.3. L_{Bol} is taken from Spinoglio et al. (1995).

Table 5.8. Starburst modeling results

Galaxy	Mass ($10^8 M_{\odot}$)	% of M_{dyn}	Age (10^6 yrs)
NGC 520	1.5	...	12.5
NGC 660	0.7	7	11.5
Maffei 2	0.05	3	14.5
NGC 1614	7	23	10.5
NGC 2782	1	3	13
NGC 3628	0.25	5	12
NGC 4102	0.5	6	13
NGC 4194	1.5	12	11.5
NGC 5990	4	...	15
NGC 6000	1.7	...	12
NGC 6240	20	4	13.5
MKN 331	6	7	13

Note. — Masses and ages are derived assuming a single burst of star formation, using IMF 8 of Rieke et al. 1993, and only requiring the model to match the luminosity in the spectrometer aperture. Thus, as discussed in §5.4, the masses are lower limits only, and the ages are not representative of those systems which have had a complex star formation history.

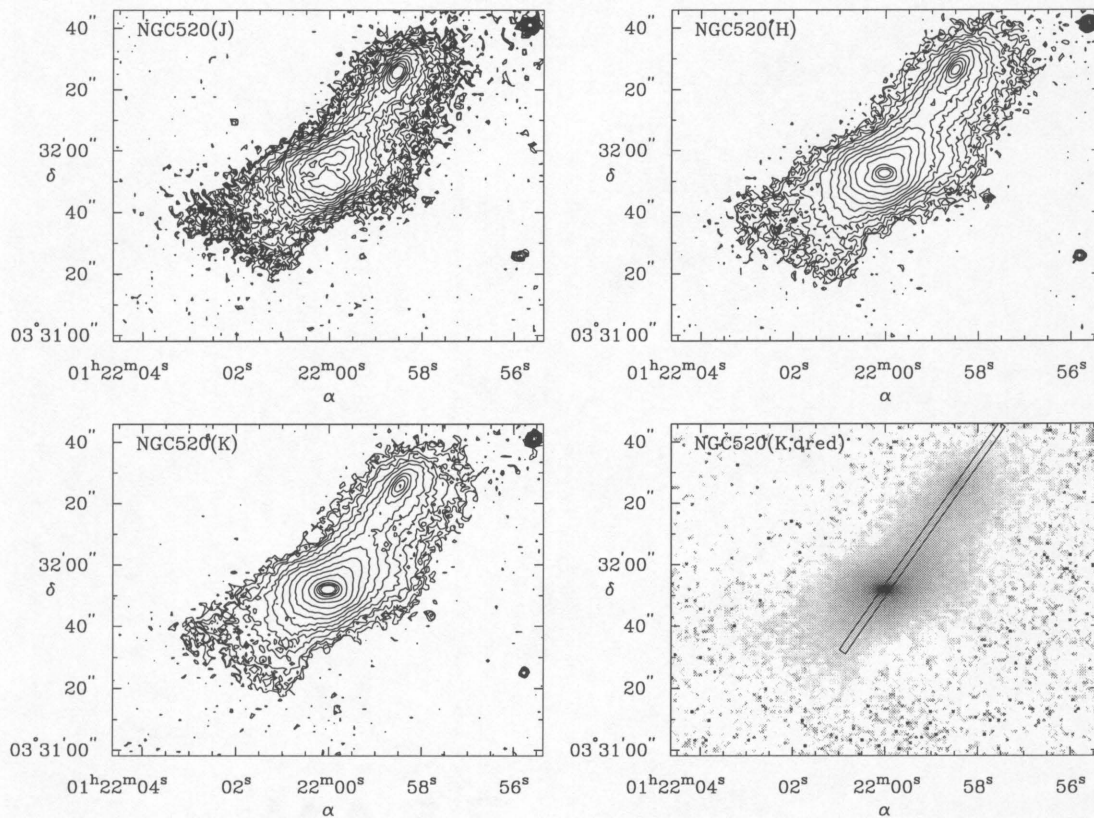


Figure 5.1 J, H, and K-band images of NGC 520, plus a grayscale display of the K band image that has been dereddened as described in the text. The display range covers 20 to 17.3, 19.5 to 15.7, 19.3 to 14.7, and 19.3 to 12 magnitudes per square arcsecond in the J, H, K, and dereddened K bands, respectively. The grayscale image shows the size and position of the spectrometer slit.

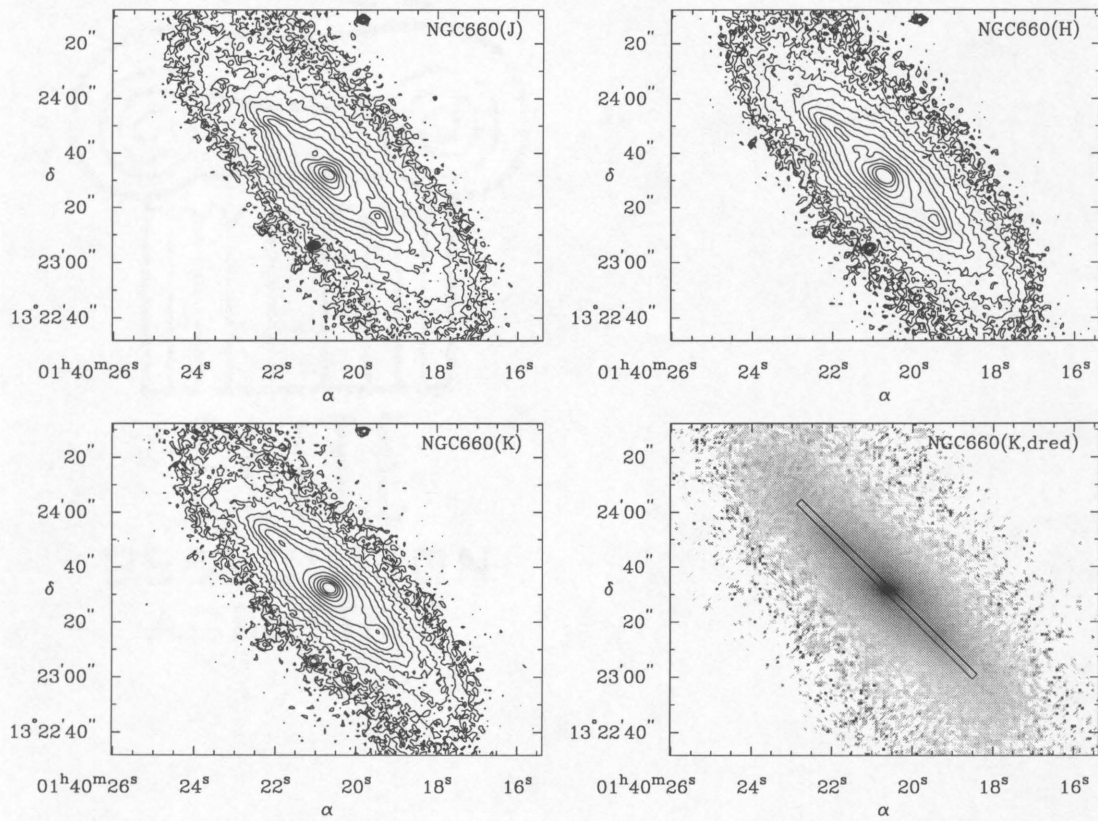


Figure 5.2 J, H, K, and dereddened K-band images of NGC 660. The display range covers 21 to 15, 20.3 to 14.3, 19.3 to 13.3, and 19.3 to 11.5 magnitudes per square arcsecond in the J, H, K and dereddened K bands, respectively.

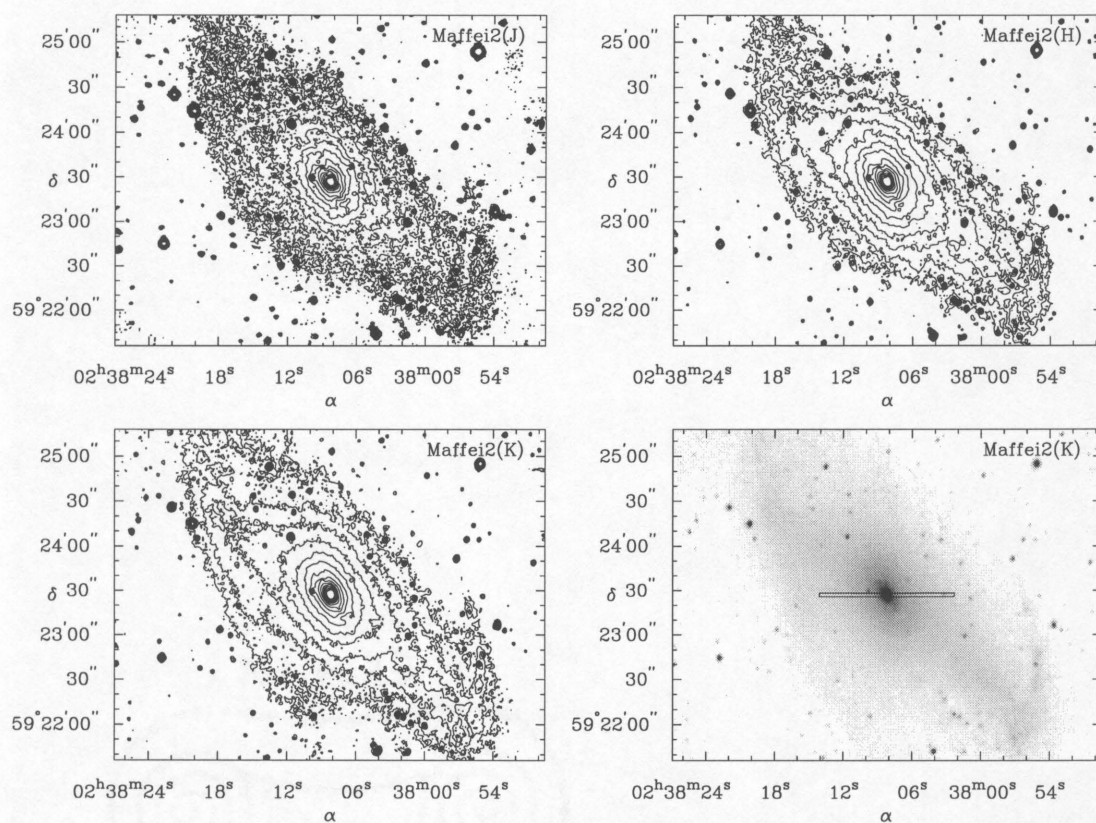


Figure 5.3 J, H, and K-band images of Maffei 2. The display range covers 19.5 to 15.5, 18.3 to 14.3, and 17.5 to 13.5 magnitudes per square arcsecond in the J, H, and K bands, respectively.

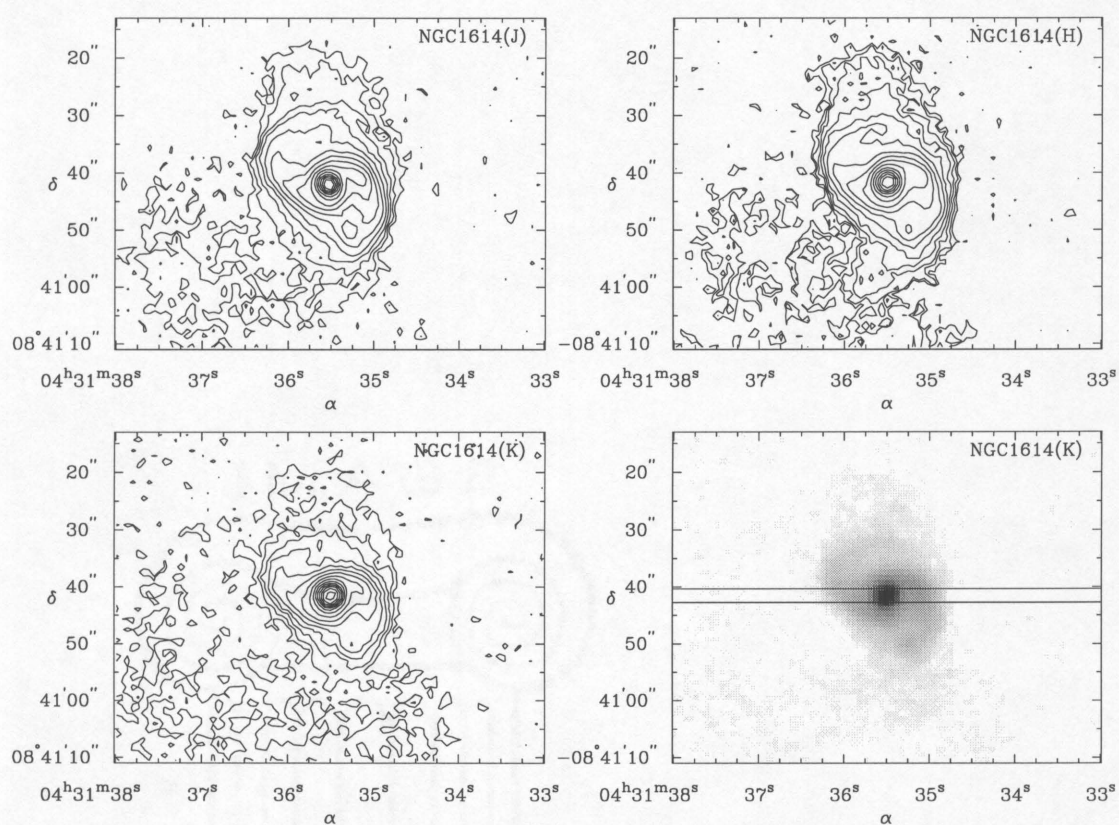


Figure 5.4 J, H, and K-band images of NGC 1614. The display range covers 20.4 to 13.9, 20.3 to 13.3, and 18.7 to 12.7 magnitudes per square arcsecond in the J, H, and K bands, respectively.

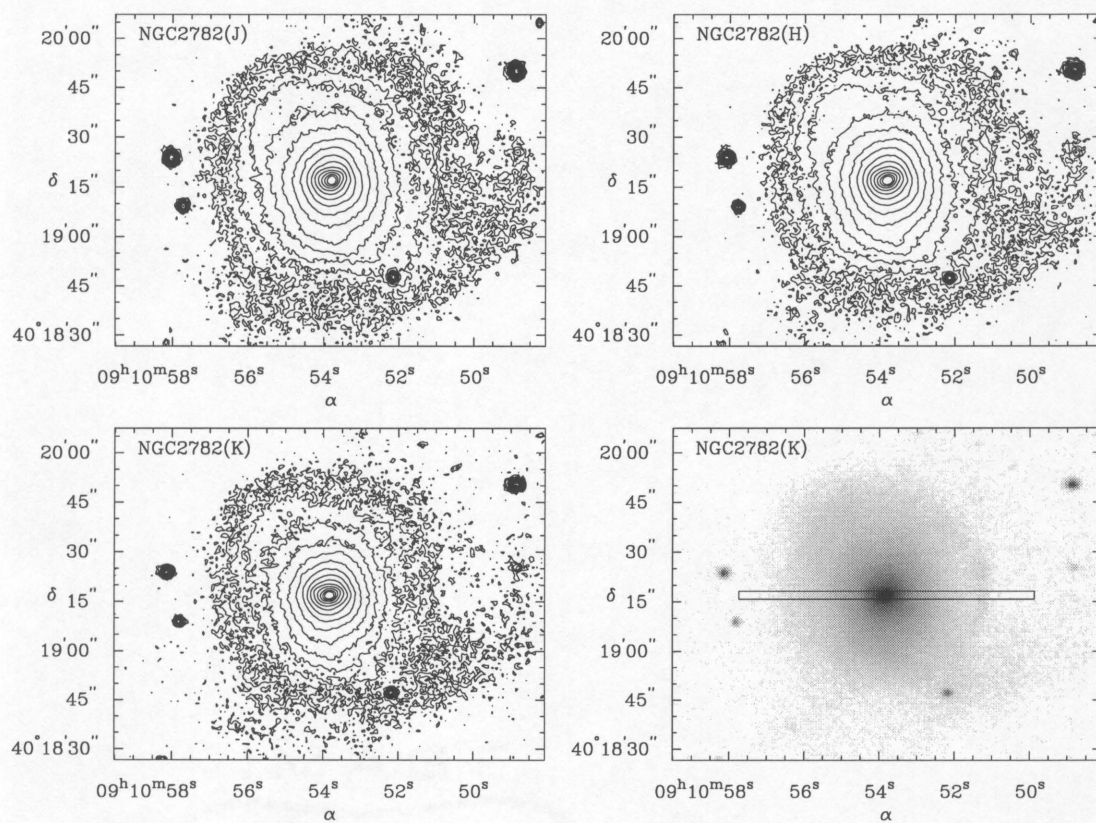


Figure 5.5 J, H, and K-band images of NGC 2782. The display range covers 21.2 to 15.3, 20.5 to 14.5, and 20 to 14 magnitudes per square arcsecond in the J, H, and K bands, respectively.

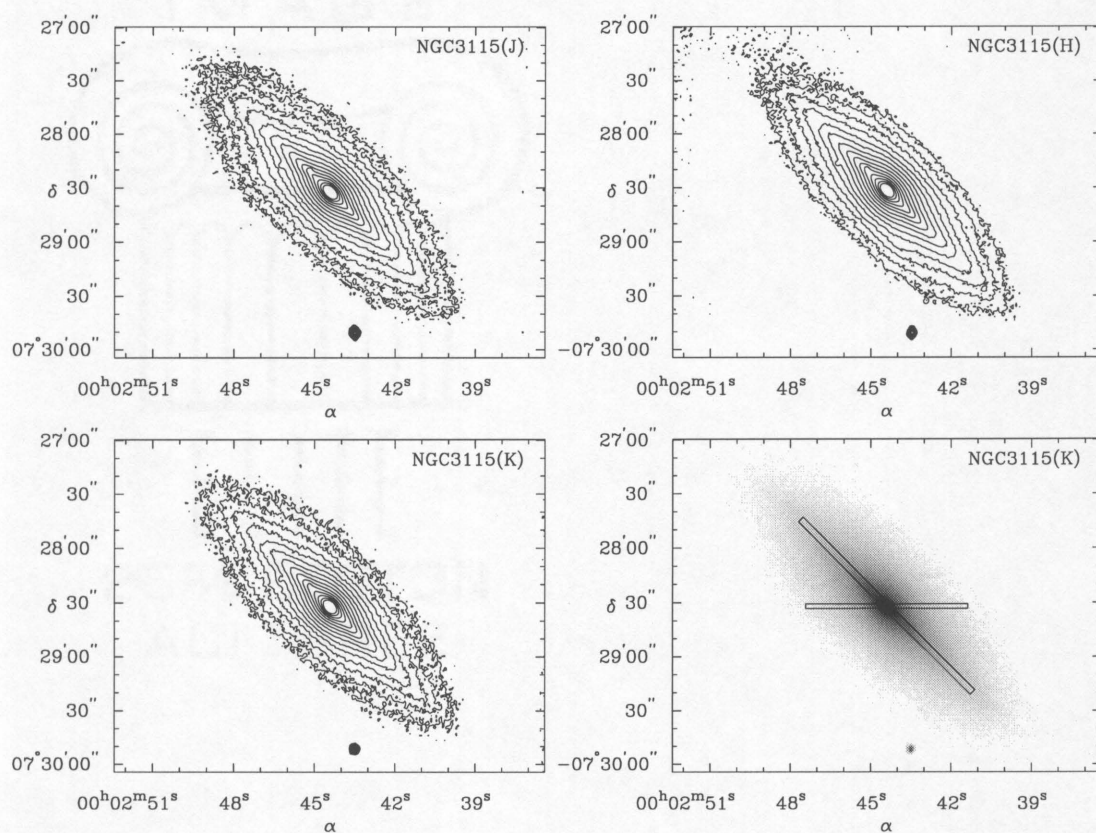


Figure 5.6 J, H, and K-band images of NGC 3115. The display range covers 19 to 14, 18.3 to 13.3, and 18 to 13 magnitudes per square arcsecond in the J, H, and K bands, respectively.

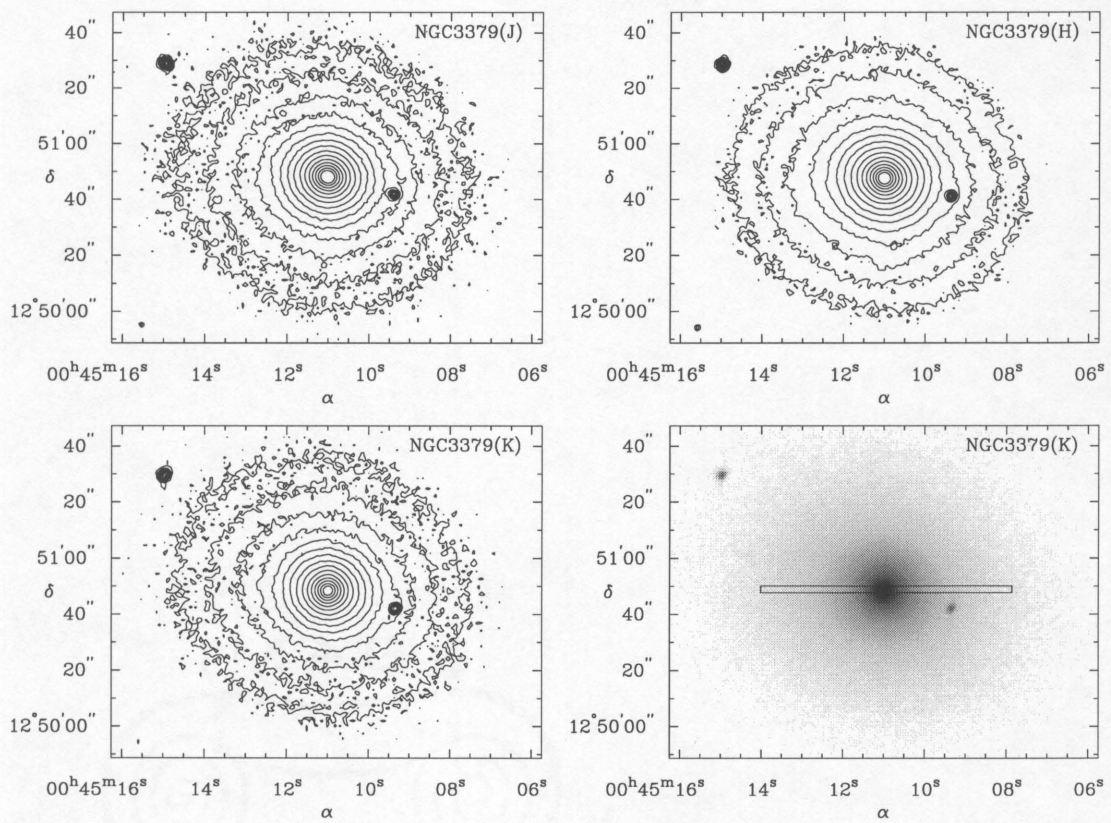


Figure 5.7 J, H, and K-band images of NGC 3379. The display range covers 18.6 to 14, 18 to 13.2, and 17.8 to 12.8 magnitudes per square arcsecond in the J, H, and K bands, respectively.

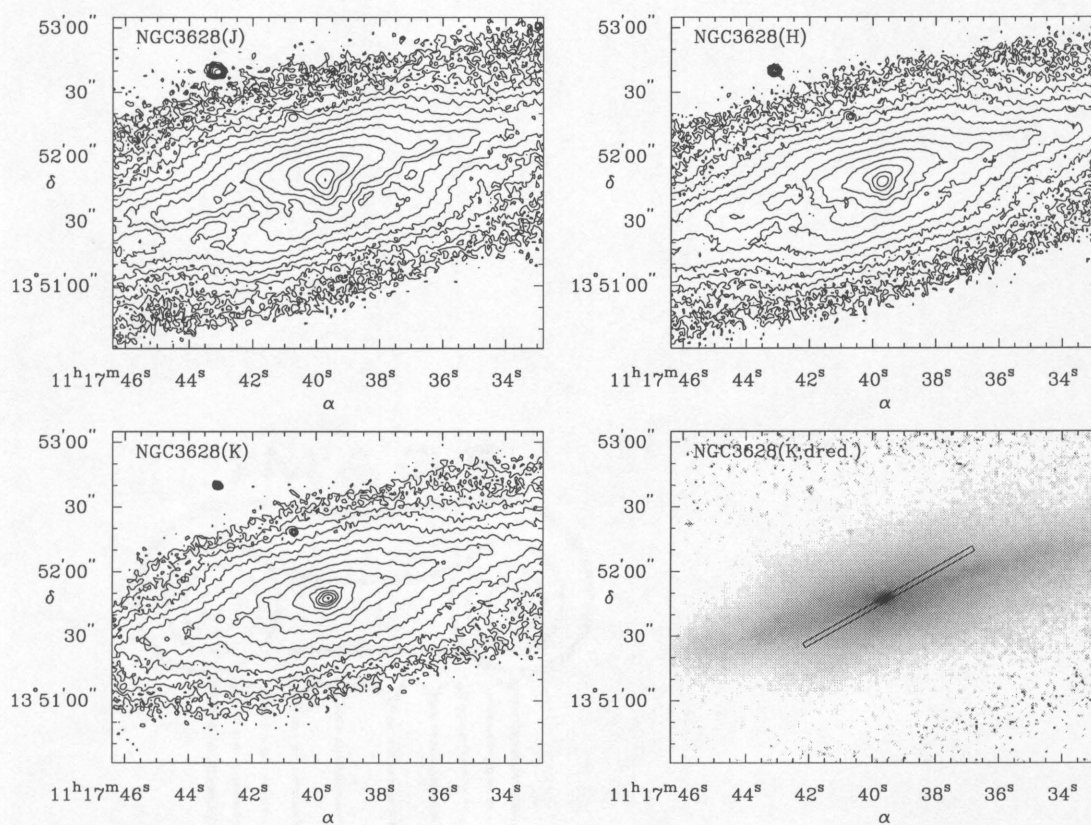


Figure 5.8 J, H, K, and dereddened K-band images of NGC 3628. The display range covers 20.5 to 16.3, 20 to 14.8, 19.5 to 14.0, and 19 to 12.6 magnitudes per square arcsecond in the J, H, K, and dereddened K bands, respectively.

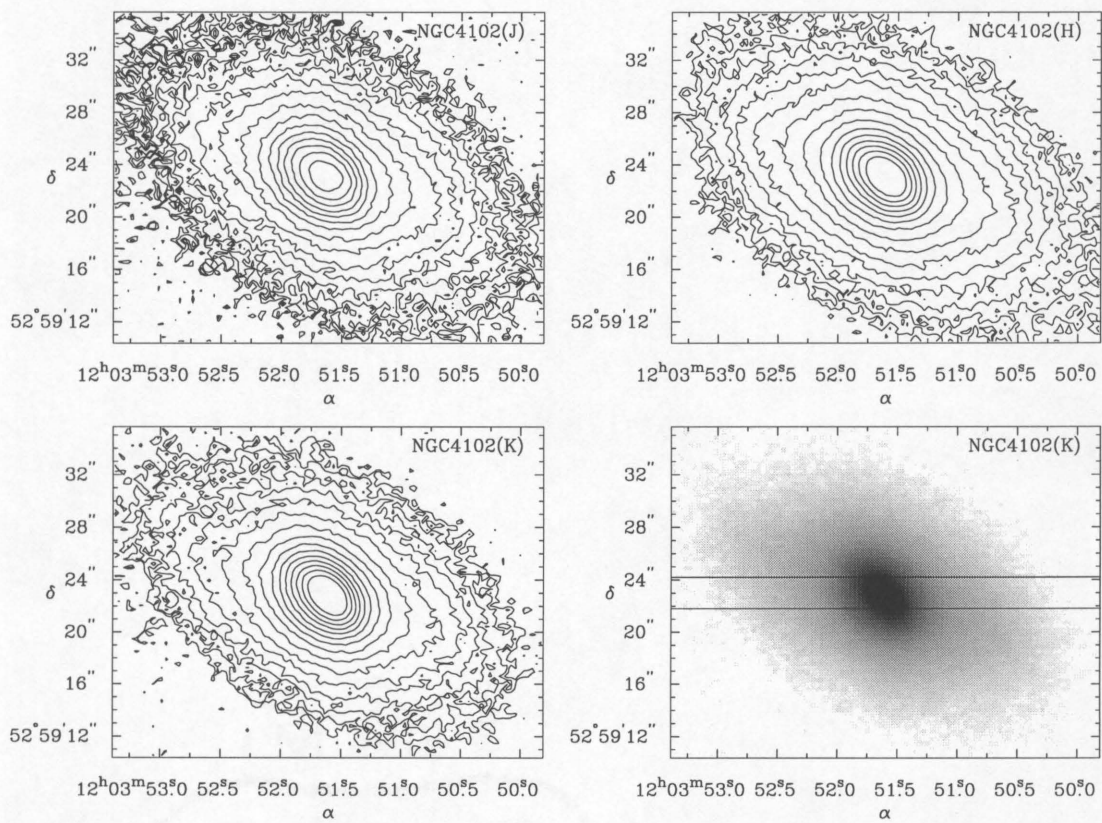


Figure 5.9 J, H, and K-band images of NGC 4102. The display range covers 28.5 to 13.5, 17.7 to 12.7, and 17.1 to 12.1 magnitudes per square arcsecond in the J, H, and K bands, respectively.

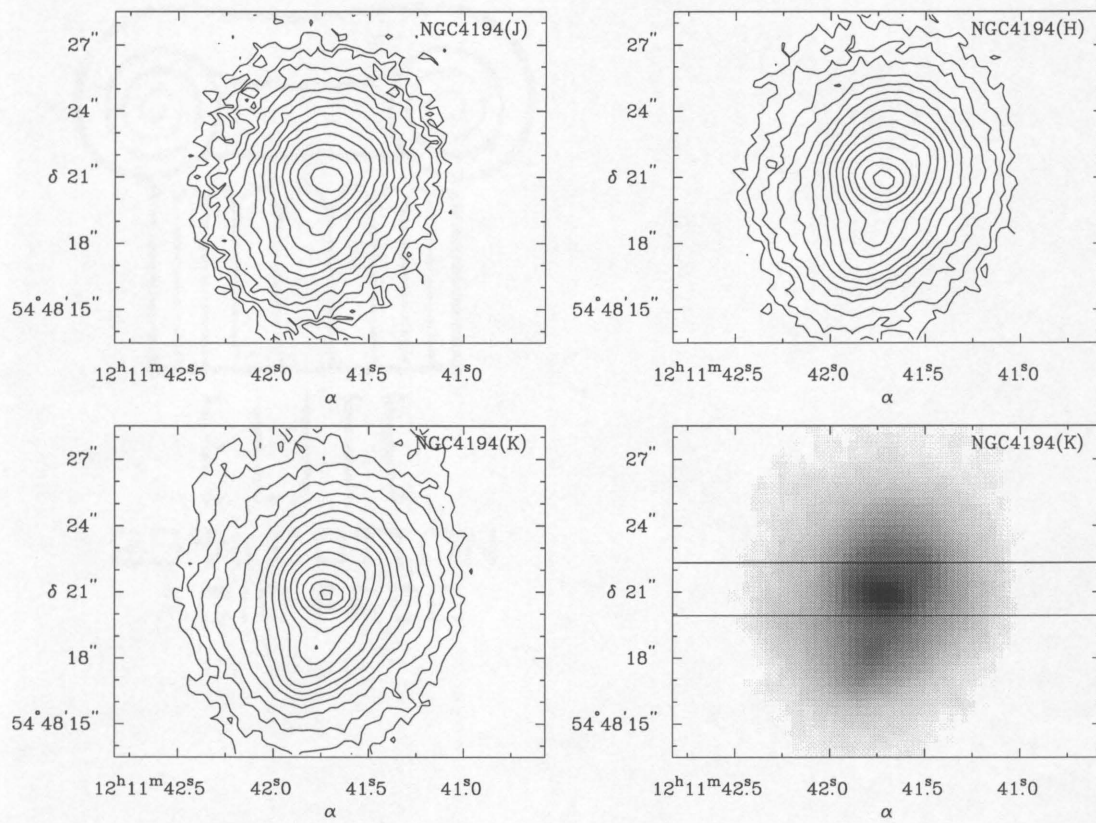


Figure 5.10 J, H, and K-band images of NGC 4194. The display range covers 18 to 13.9, 17.5 to 12.9, and 17.5 to 12.5 magnitudes per square arcsecond in the J, H, and K bands, respectively.

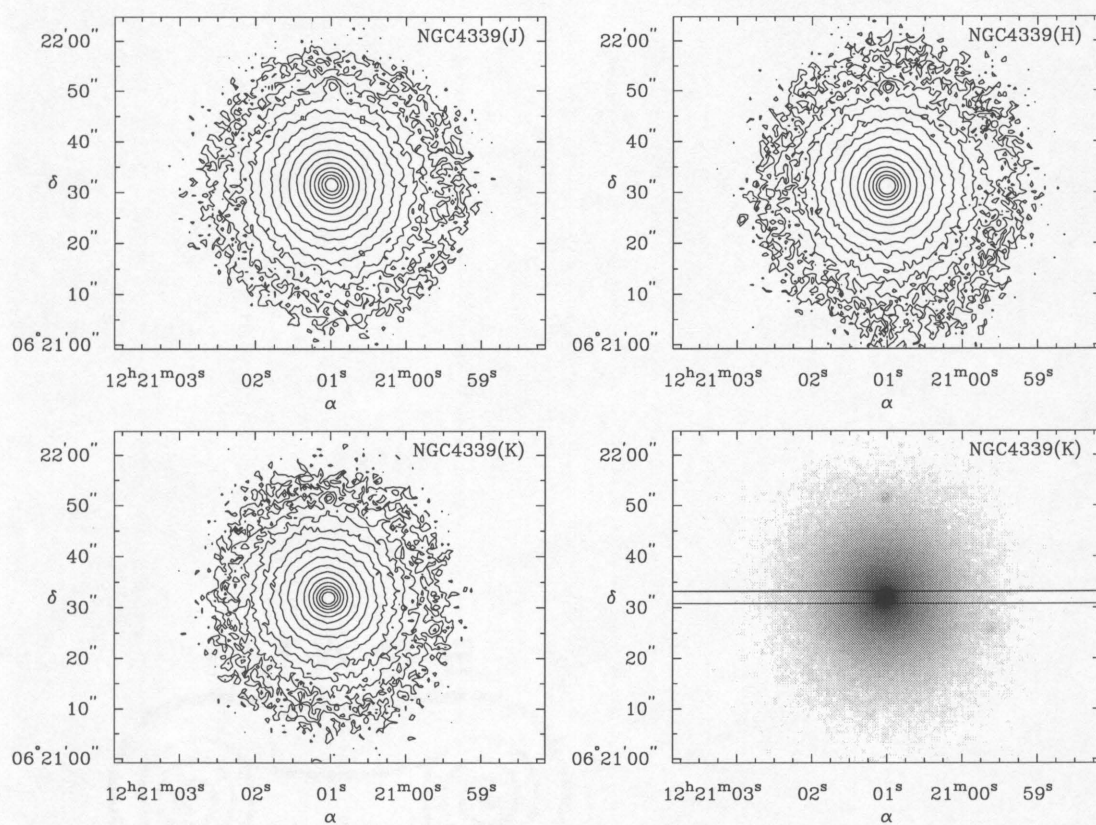


Figure 5.11 J, H, and K-band images of NGC 4339. The display range covers 20.3 to 15.3, 19.7 to 14.7, and 19.2 to 14.2 magnitudes per square arcsecond in the J, H, and K bands, respectively.

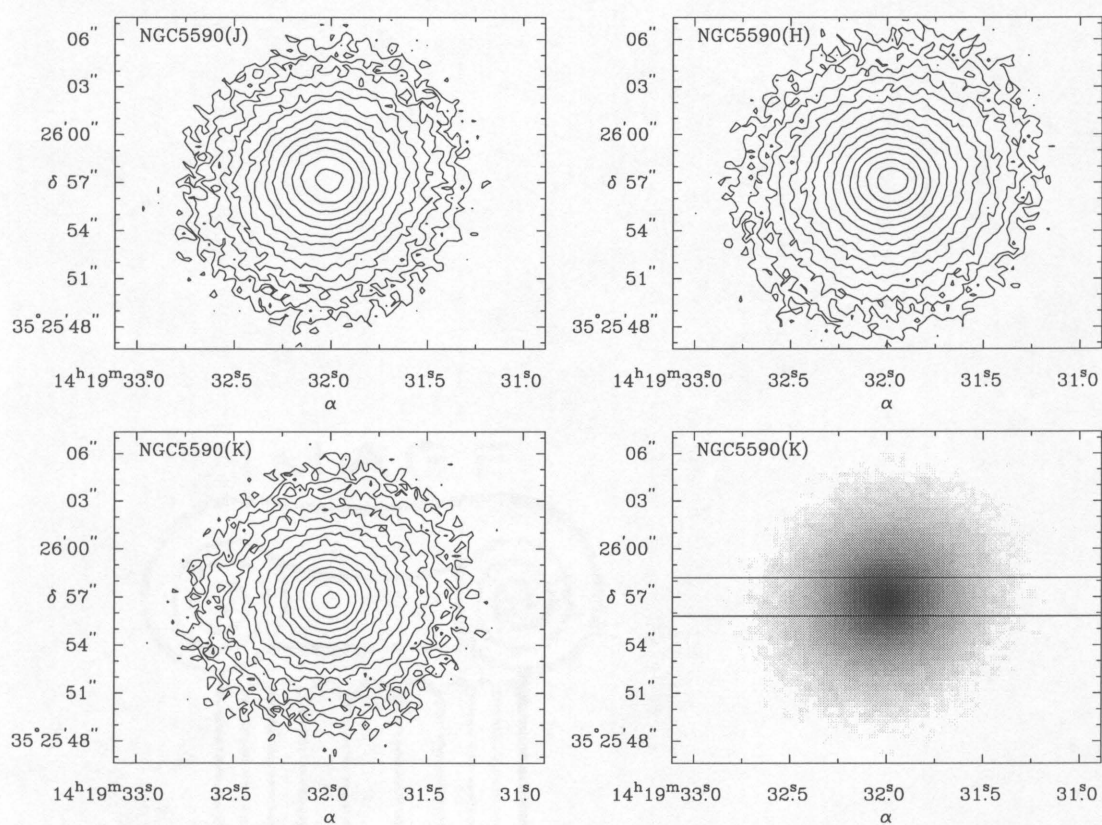


Figure 5.12 J, H, and K-band images of NGC 5590. The display range covers 18.5 to 15, 18 to 14.5, and 17.5 to 14 magnitudes per square arcsecond in the J, H, and K bands, respectively.

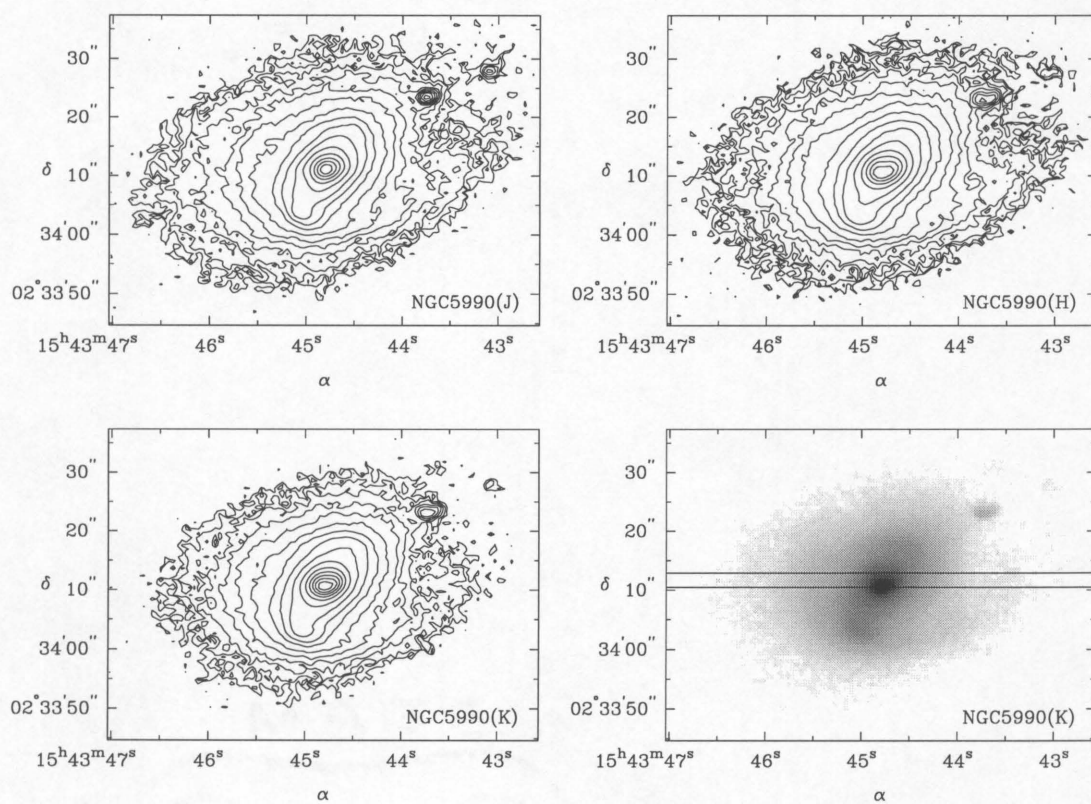


Figure 5.13 J, H, and K-band images of NGC 5990. The display range covers 21 to 14.5, 20.5 to 14, and 19.5 to 13 magnitudes per square arcsecond in the J, H, and K bands, respectively.

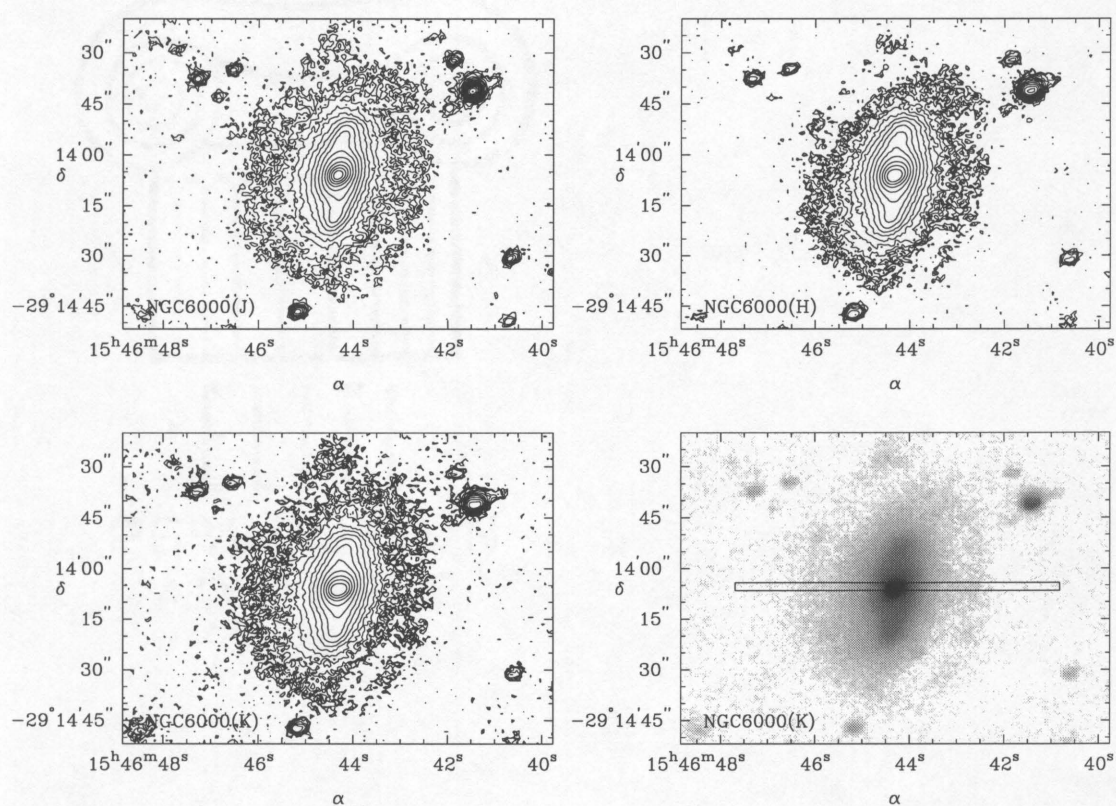


Figure 5.14 J, H, and K-band images of NGC 6000. The display range covers 20 to 14.2, 20 to 13.8, 20 to 13.3, and 21 to 13.3 magnitudes per square arcsecond in the J, H, K, and greyscale K bands, respectively.

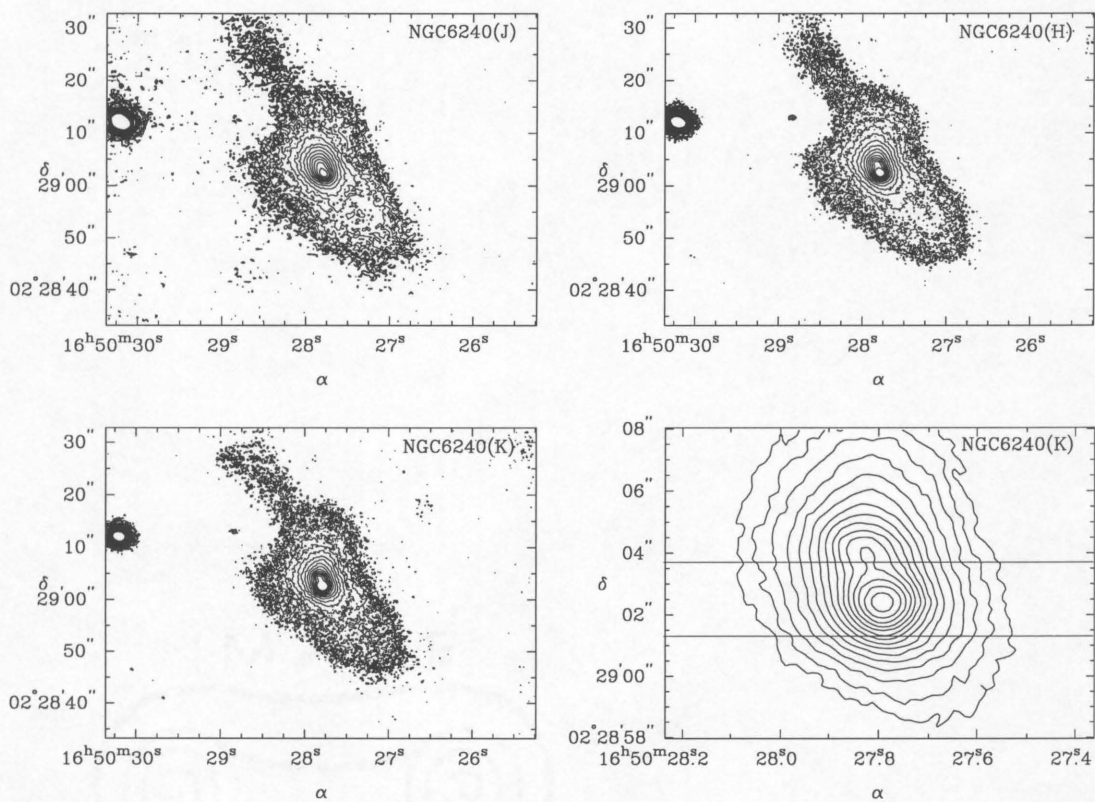


Figure 5.15 J, H, and K-band images of NGC 6240. The display range covers 20 to 15, 18.8 to 13.8, 18.2 to 13.2, and 16.5 to 12.2 magnitudes per square arcsecond in the large-scale J, H, and K-band contour plots and the fine-scale contour plot, respectively.

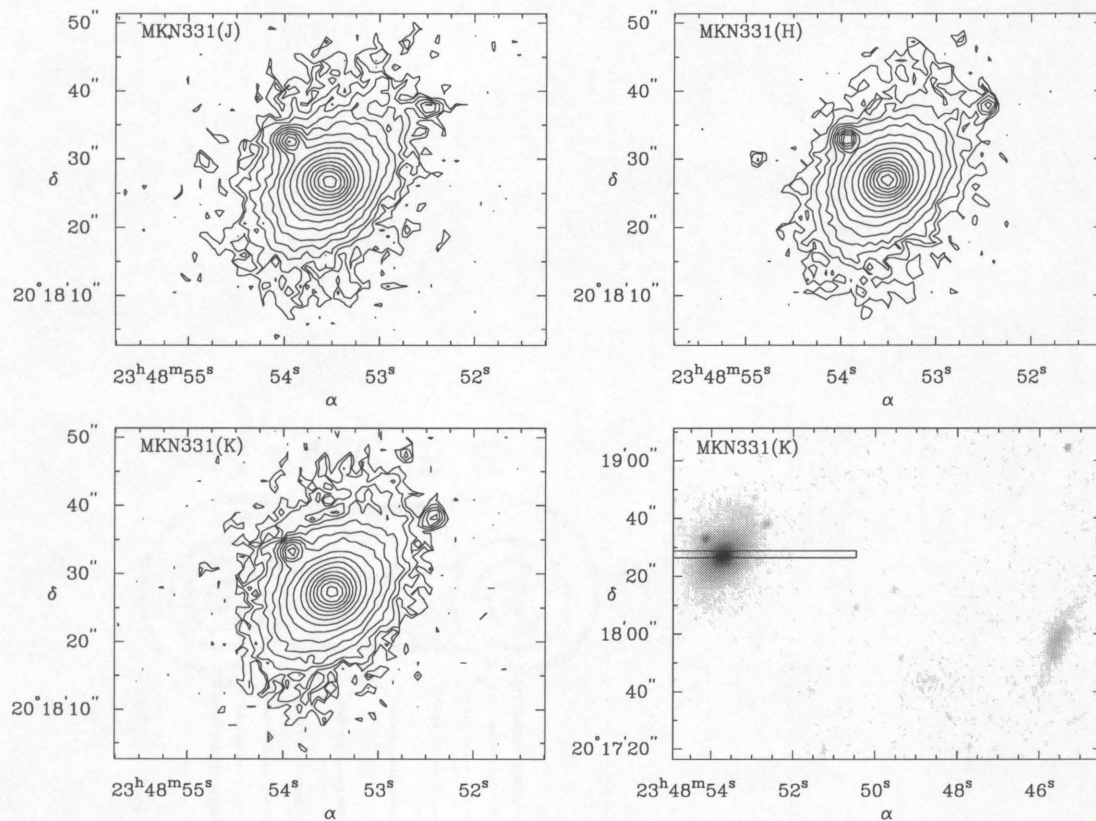


Figure 5.16 J, H, and K-band images of MKN 331. The display range covers 21.2 to 15, 20.5 to 14, and 20.8 to 13.5 magnitudes per square arcsecond in the J, H, and K bands, respectively. The final panel displays an expanded view of the MKN 331 system so that the two companion galaxies are visible.

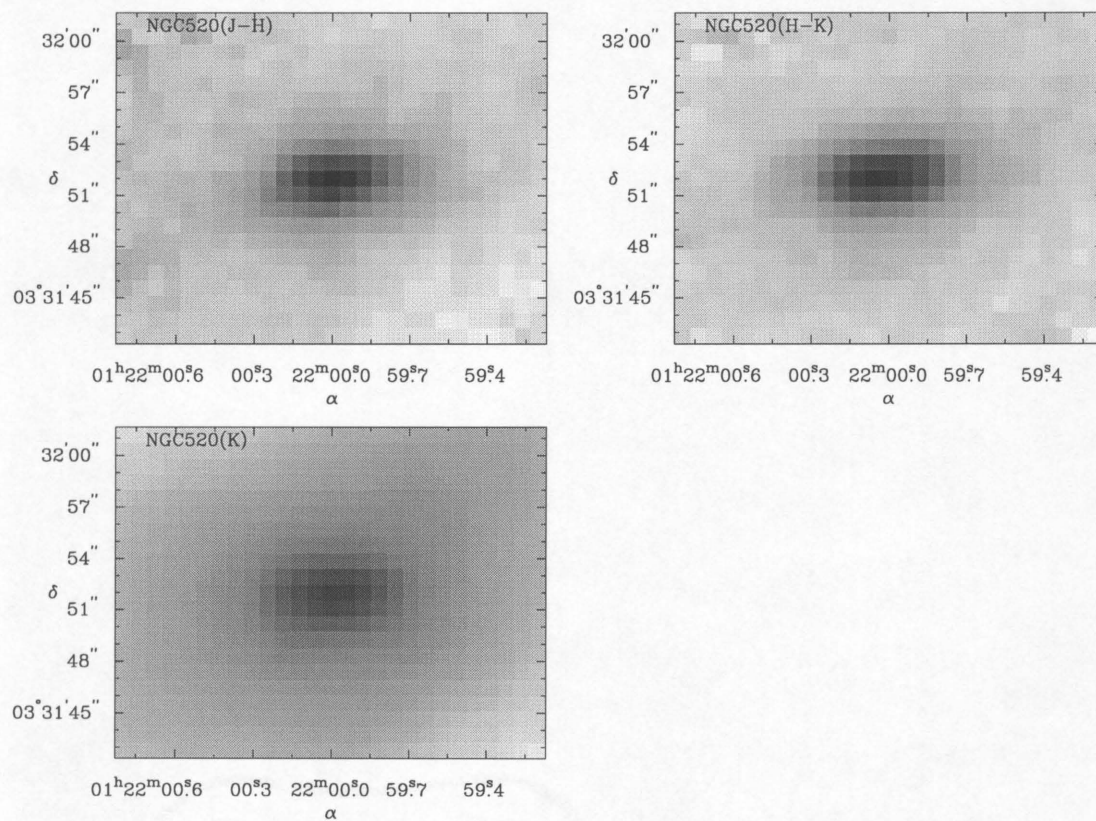


Figure 5.17 $J - H$ and $H - K$ color images of NGC 520, along with a K-band image of the same region. The display levels are 0.4 to 2 magnitudes ($J - H$), 0 to 1.5 magnitudes ($H - K$), and 19 to 13 magnitudes per square arcsecond (K-band image).

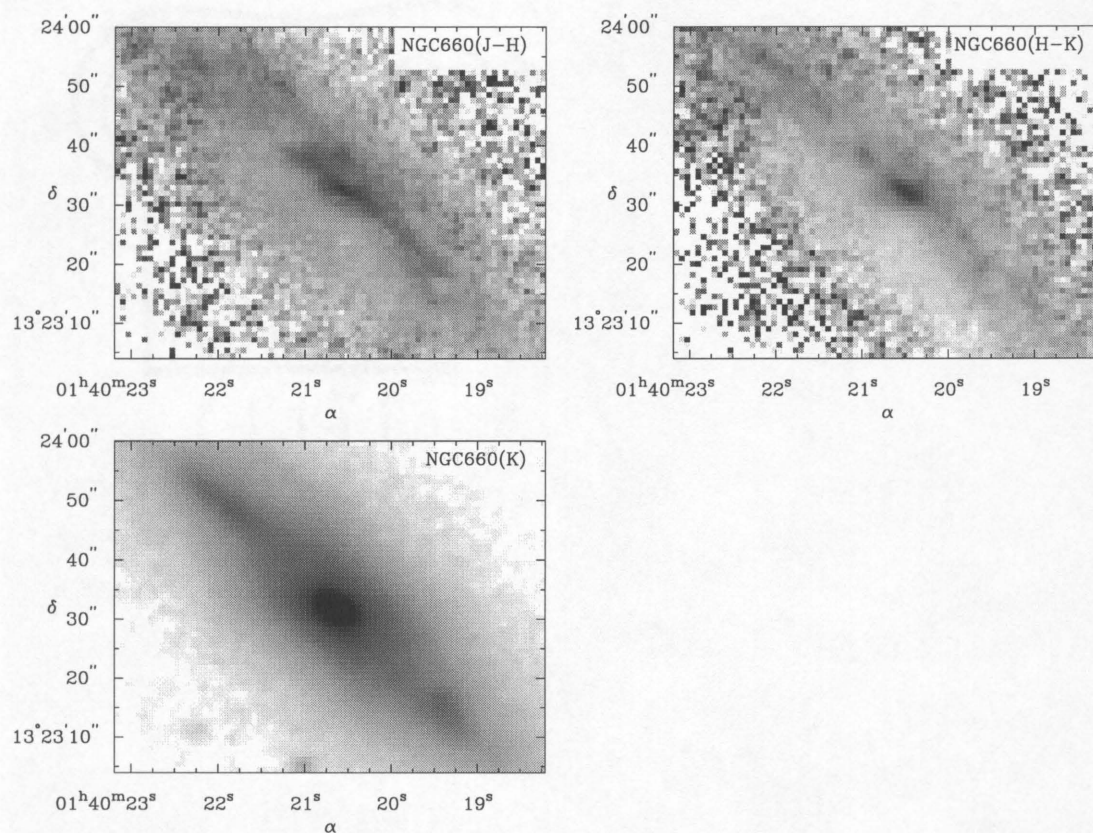


Figure 5.18 $J-H$ and $H-K$ color images of NGC 660, along with a K-band image of the same region. The display levels are 0.4 to 1.5 magnitudes ($J-H$), 0.1 to 1 magnitudes ($H-K$), and 19.3 to 13.3 magnitudes per square arcsecond (K-band image).

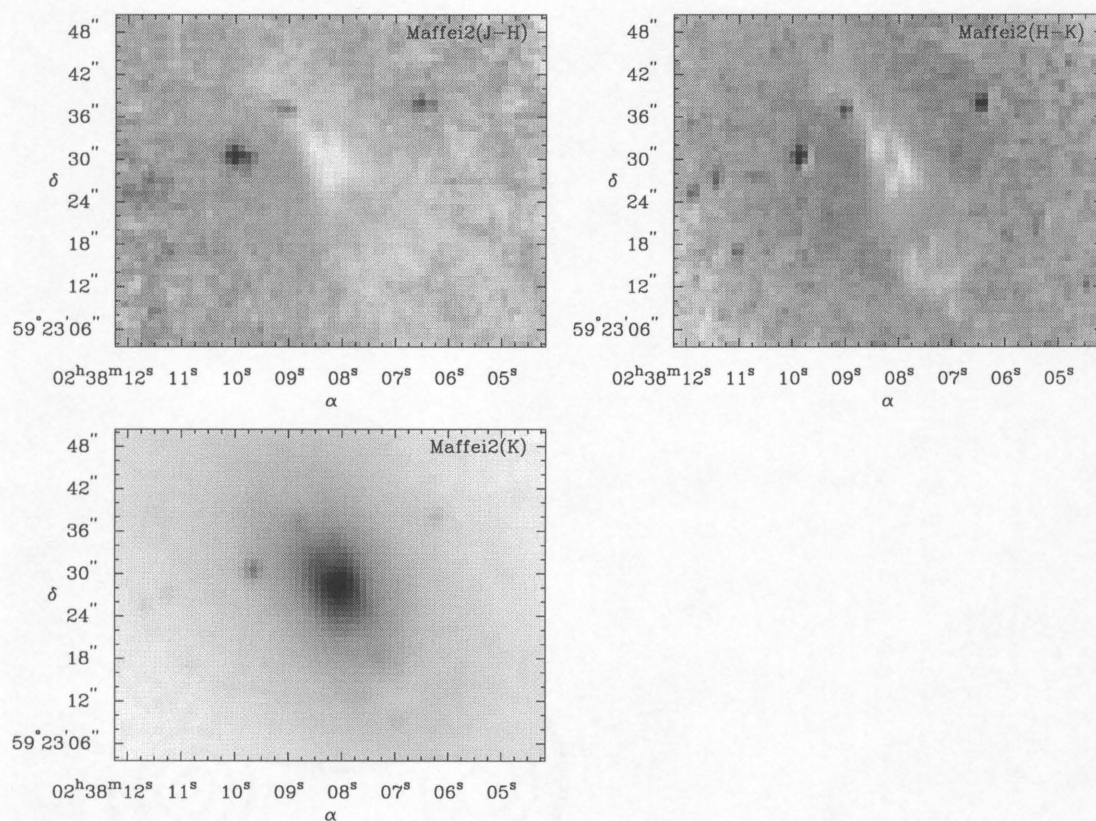


Figure 5.19 $J - H$ and $H - K$ color images of Maffei 2, along with a K-band image of the same region. The display levels are 0.5 to 1.6 magnitudes ($J - H$), 0.1 to 1 magnitudes ($H - K$), and 17 to 12.6 magnitudes per square arcsecond (K-band image).

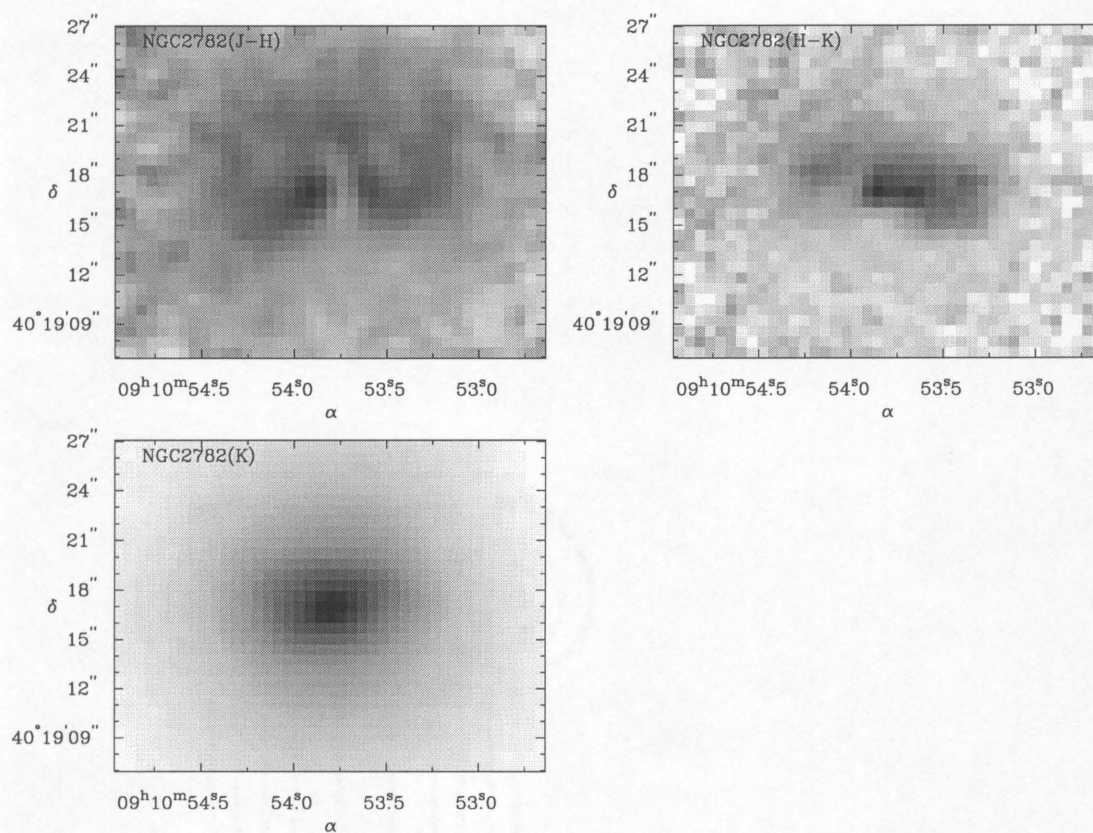


Figure 5.20 $J - H$ and $H - K$ color images of NGC 2782, along with a K-band image of the same region. The display levels are 0.65 to 1 magnitudes ($J - H$), 0.1 to 0.5 magnitudes ($H - K$), and 19 to 14 magnitudes per square arcsecond (K-band image).

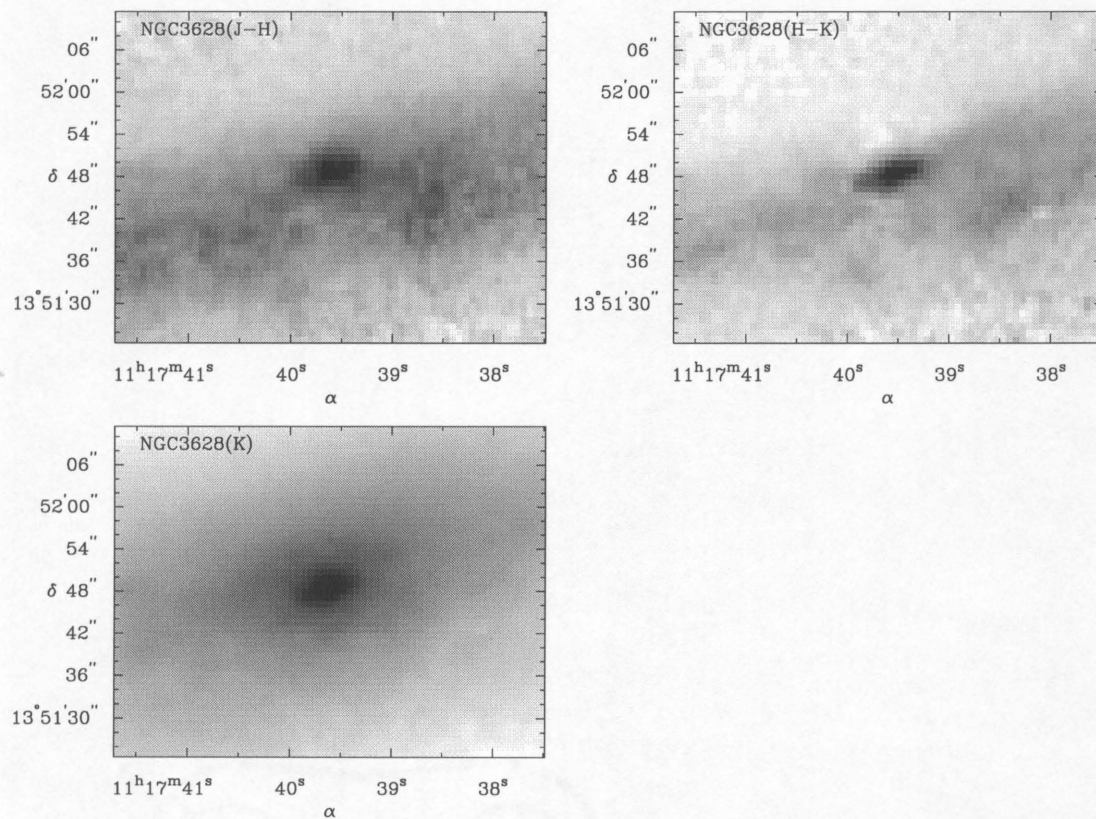


Figure 5.21 $J - H$ and $H - K$ color images of NGC 3628, along with a K-band image of the same region. The display levels are 0.5 to 1.6 magnitudes ($J - H$), 0 to 1 magnitudes ($H - K$), and 18 to 14 magnitudes per square arcsecond (K-band image).

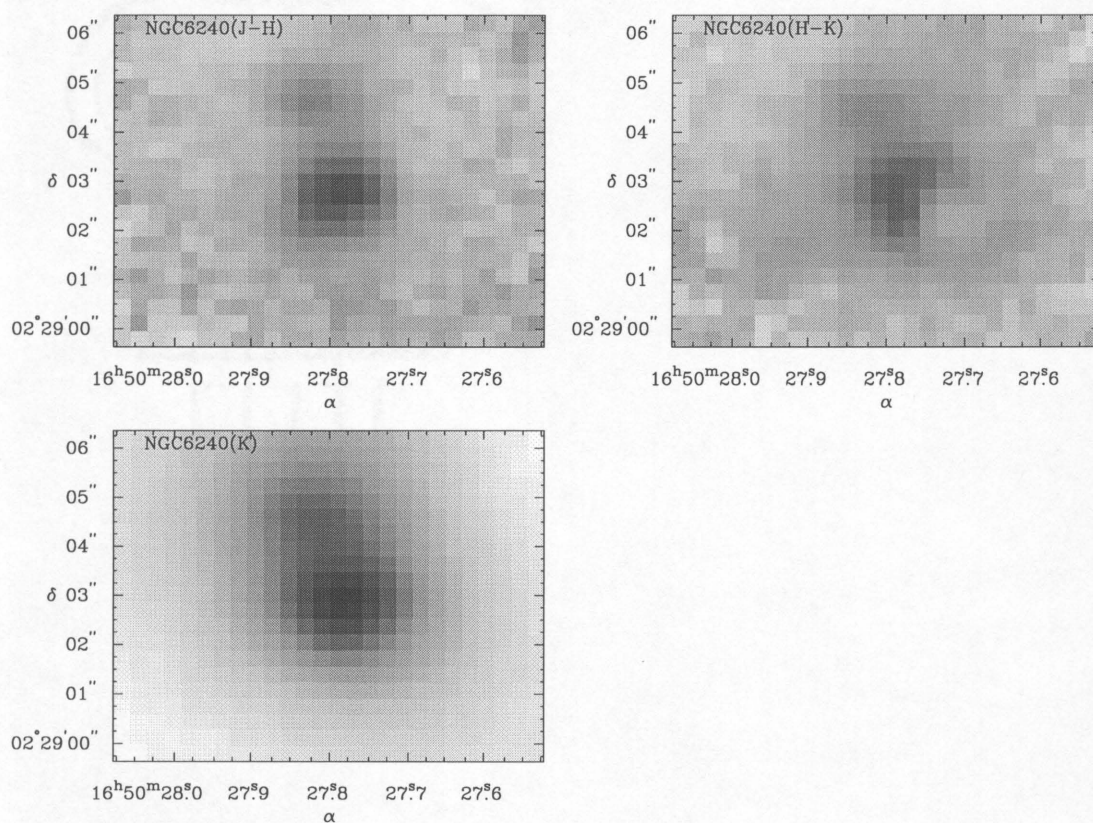


Figure 5.22 $J - H$ and $H - K$ color images of NGC 6240, along with a K-band image of the same region. The display levels are 0.4 to 2 magnitudes ($J - H$), 0.1 to 1.5 magnitudes ($H - K$), and 17 to 11 magnitudes per square arcsecond (K-band image).

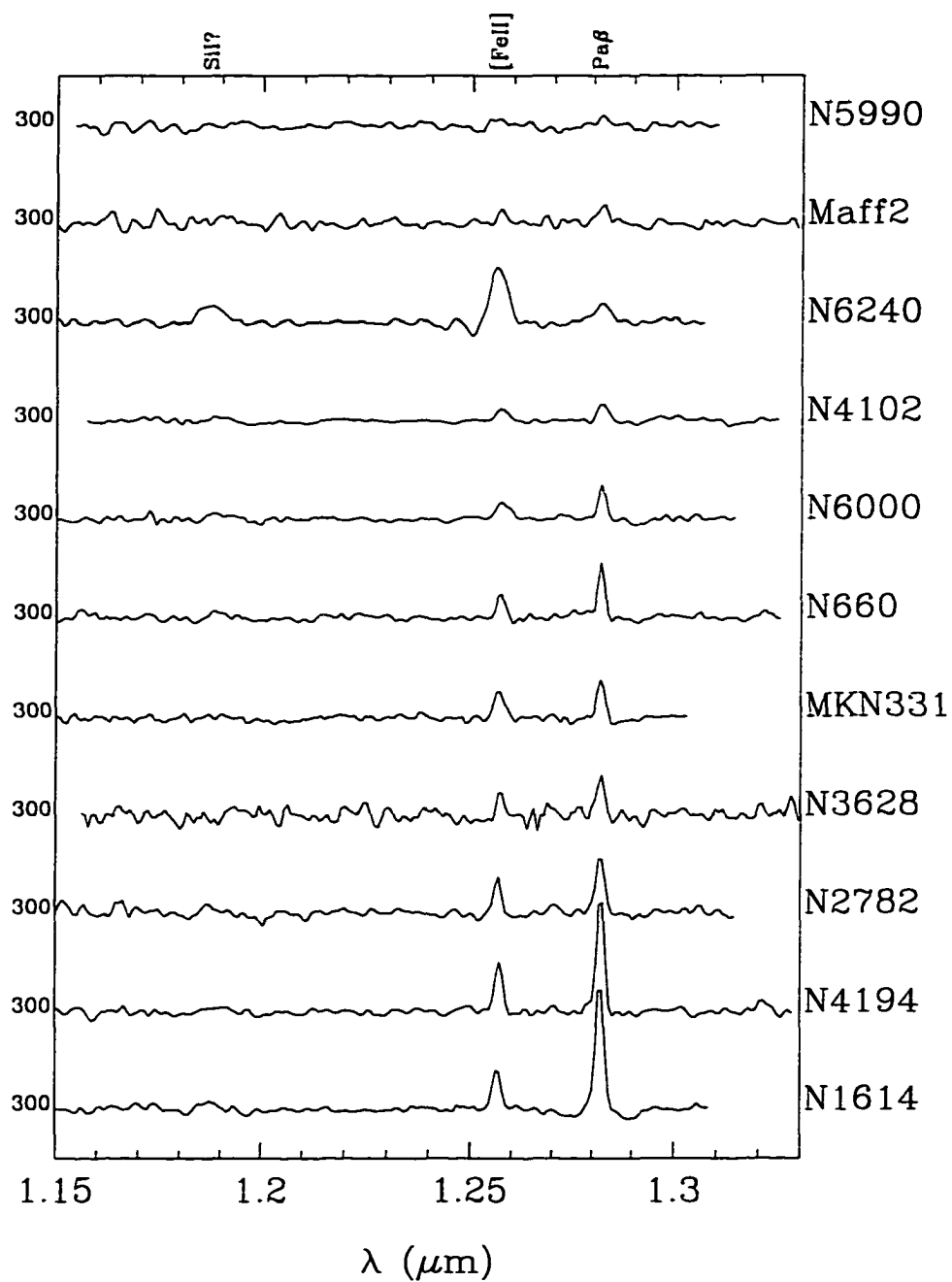


Figure 5.23 J-band spectra of starburst galaxies. These data were all obtained with the 300 l/mm grating ($R \sim 800$), as indicated by the labels on the left-hand side of the plot. The spectra have all been normalized for display purposes.

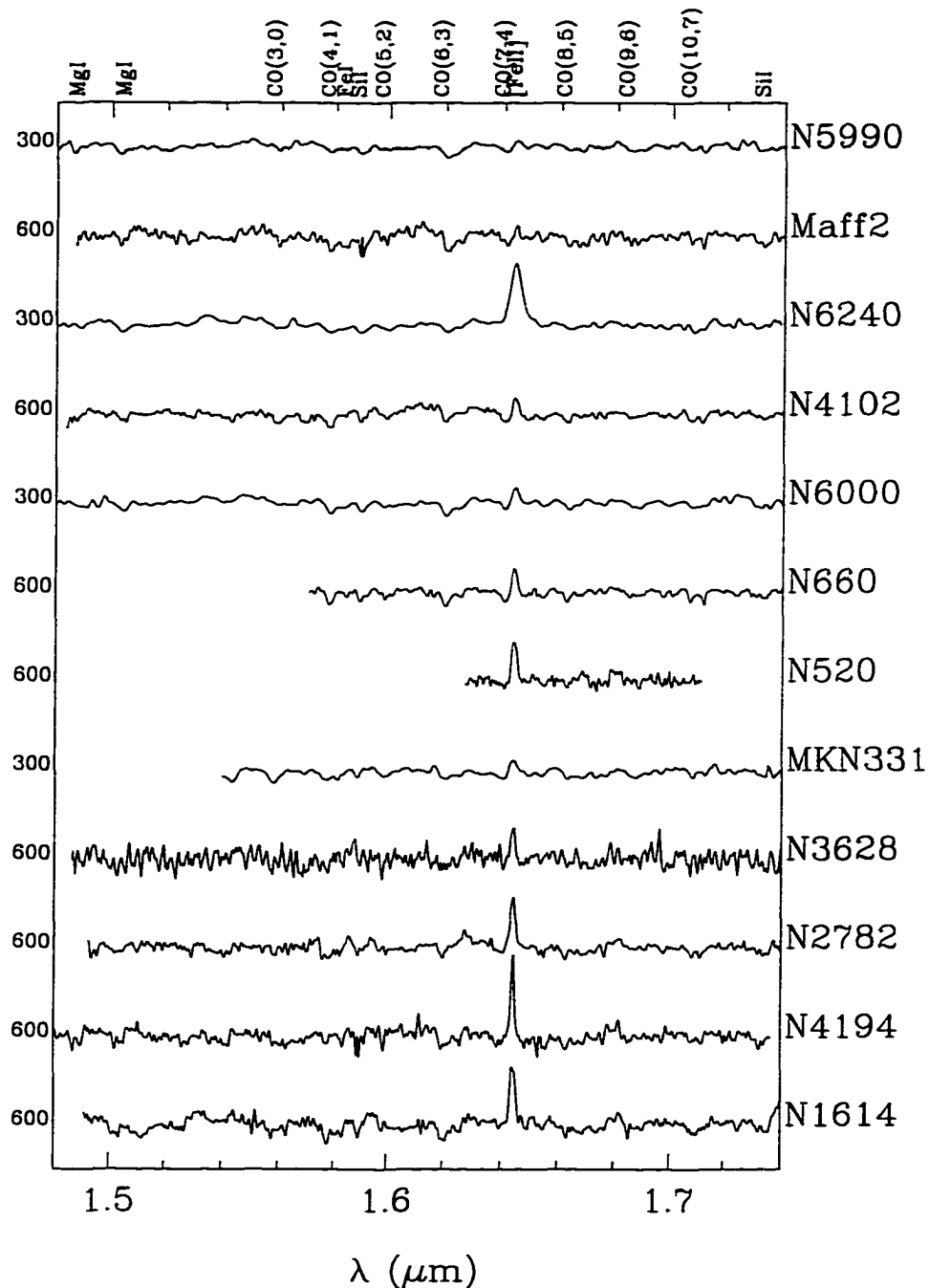


Figure 5.24 H-band spectra of starburst galaxies. These data were obtained with both the 300 l/mm ($R \sim 1000$) and 600 l/mm ($R \sim 2000$) gratings, as indicated by the labels on the left-hand side of the plot. The spectra have all been normalized for display purposes.

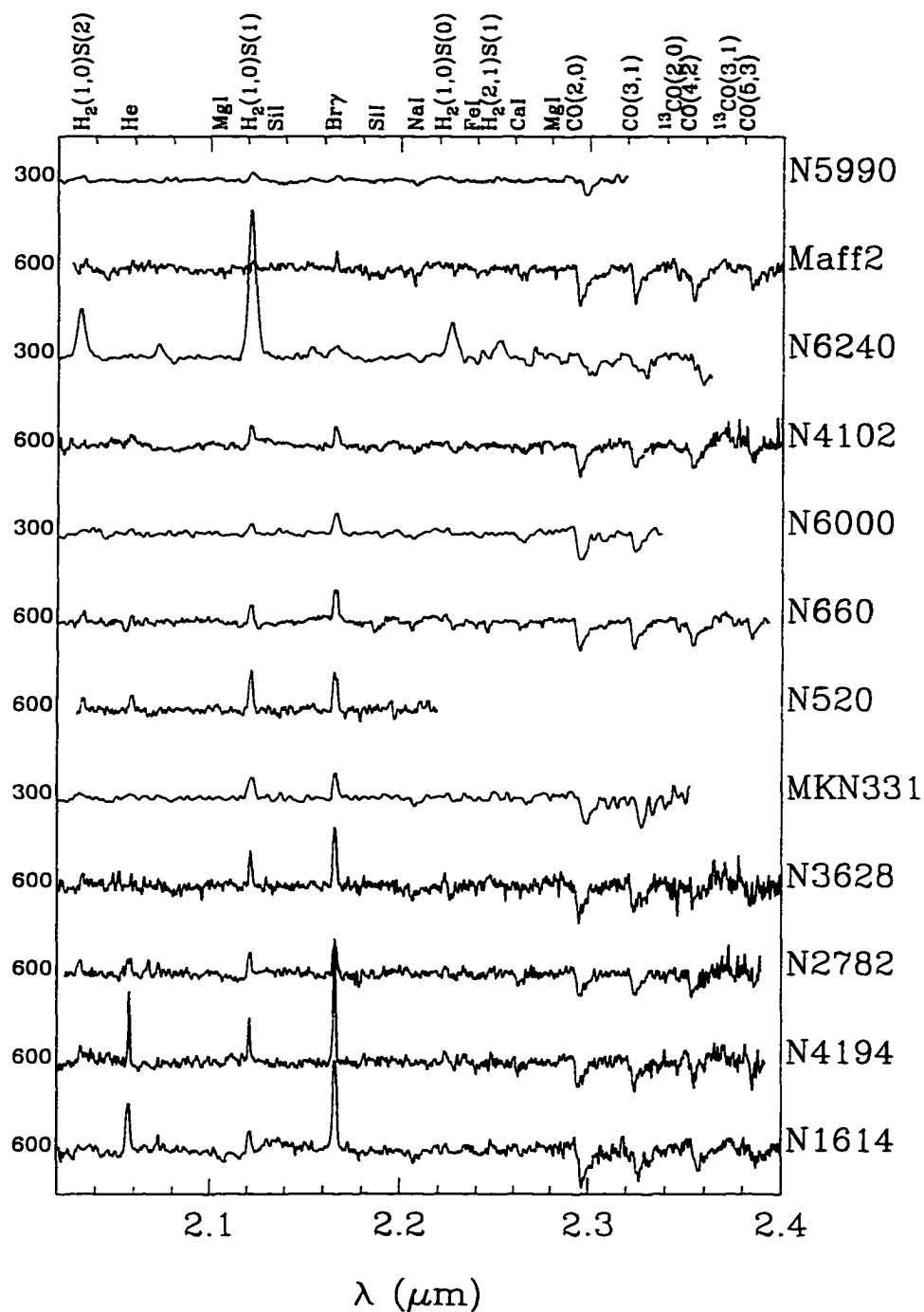


Figure 5.25 K-band spectra of starburst galaxies. These data were obtained with both the 300 l/mm ($R \sim 1200$) and 600 l/mm ($R \sim 3000$) gratings, as indicated by the labels on the left-hand side of the plot. The spectra have all been normalized for display purposes.

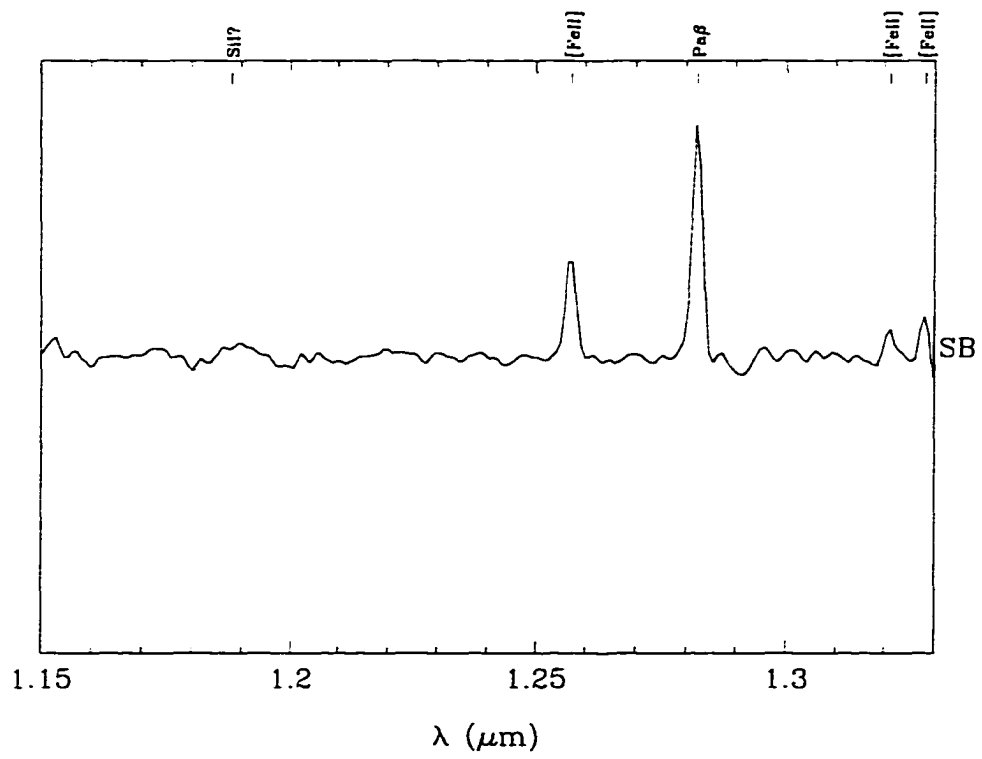


Figure 5.26 This J-band spectrum is the composite of 13 starburst galaxies with similar spectra, as discussed in §5.2.2.

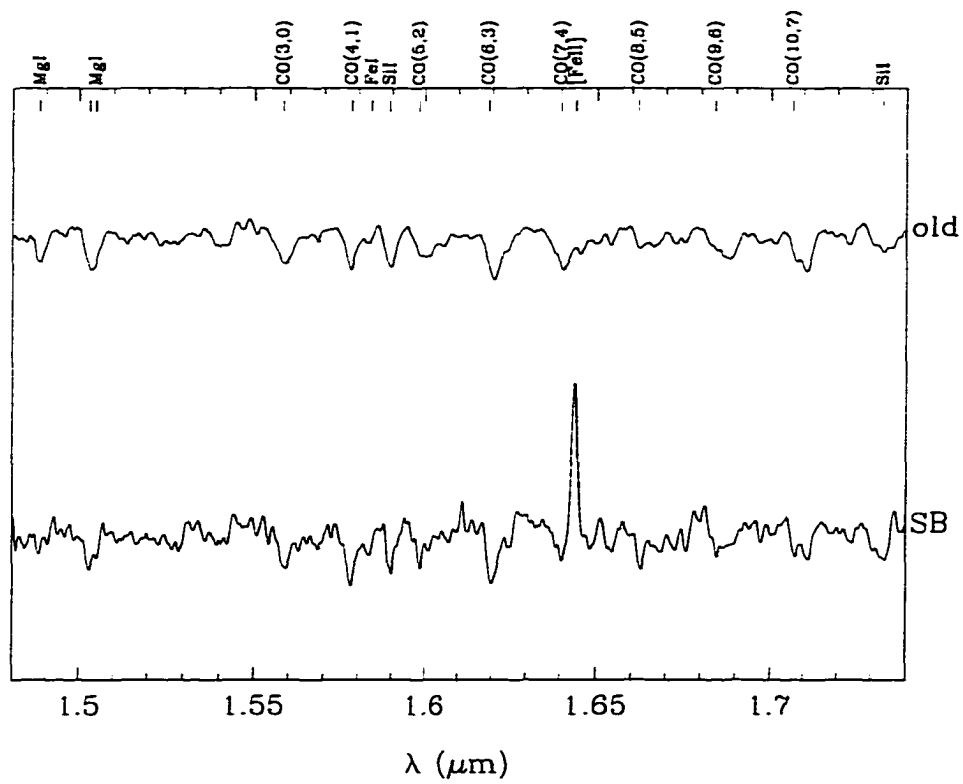


Figure 5.27 This figure displays an H-band composite spectrum of the same starburst galaxies as in Figure 5.26, plus a composite spectrum of our four control galaxies, as discussed in §5.2.2.

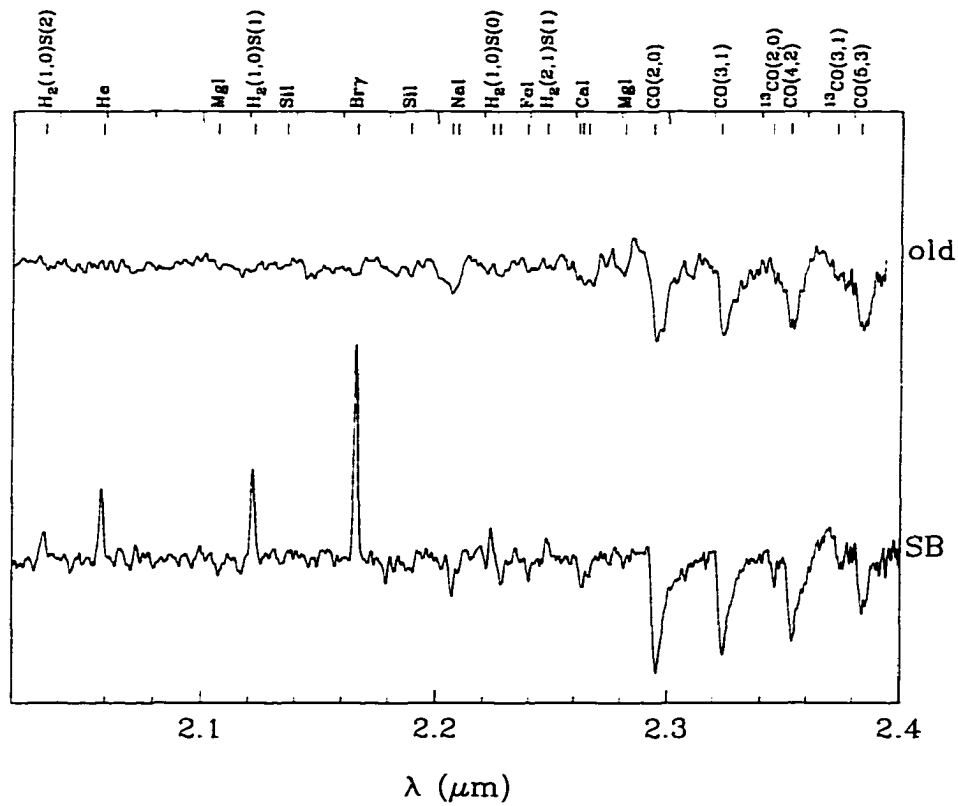


Figure 5.28 This figure displays a K-band composite spectrum of the same starburst galaxies as in Figure 5.26, plus a composite spectrum of our four control galaxies, as discussed in §5.2.2.

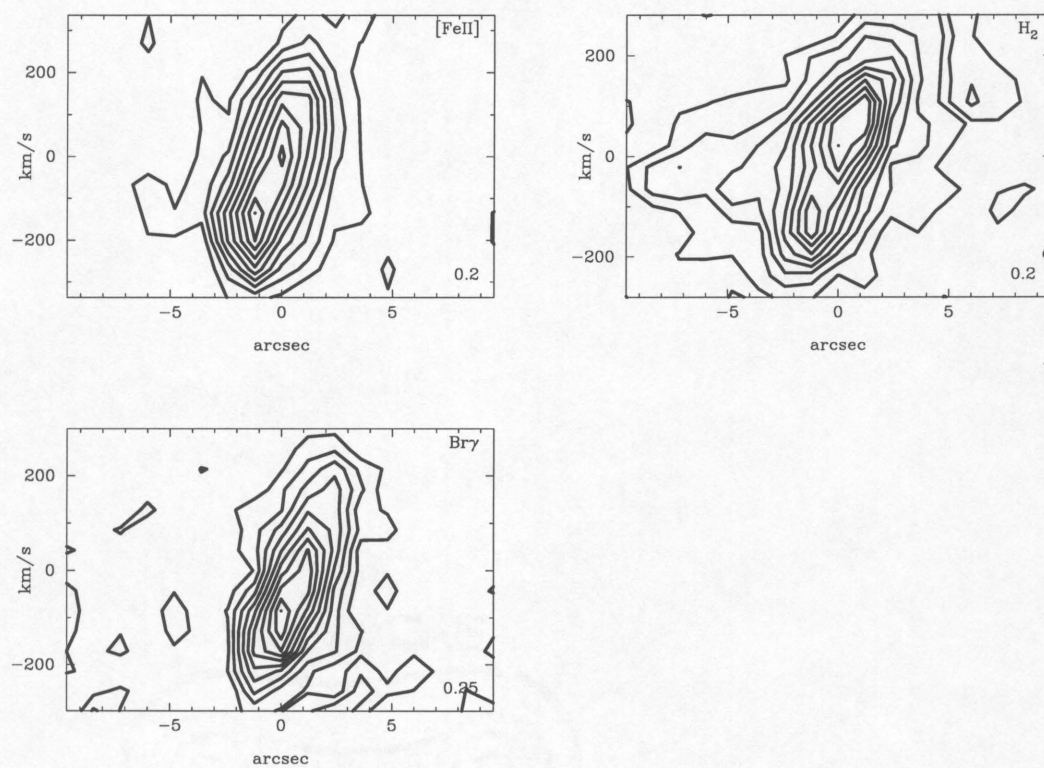


Figure 5.29 Position-velocity plots of strong spectral lines in NGC 520. The number in the lower-right-hand corner indicates the value of the lowest contour as a fraction of the maximum contour, which is set to the image maximum.

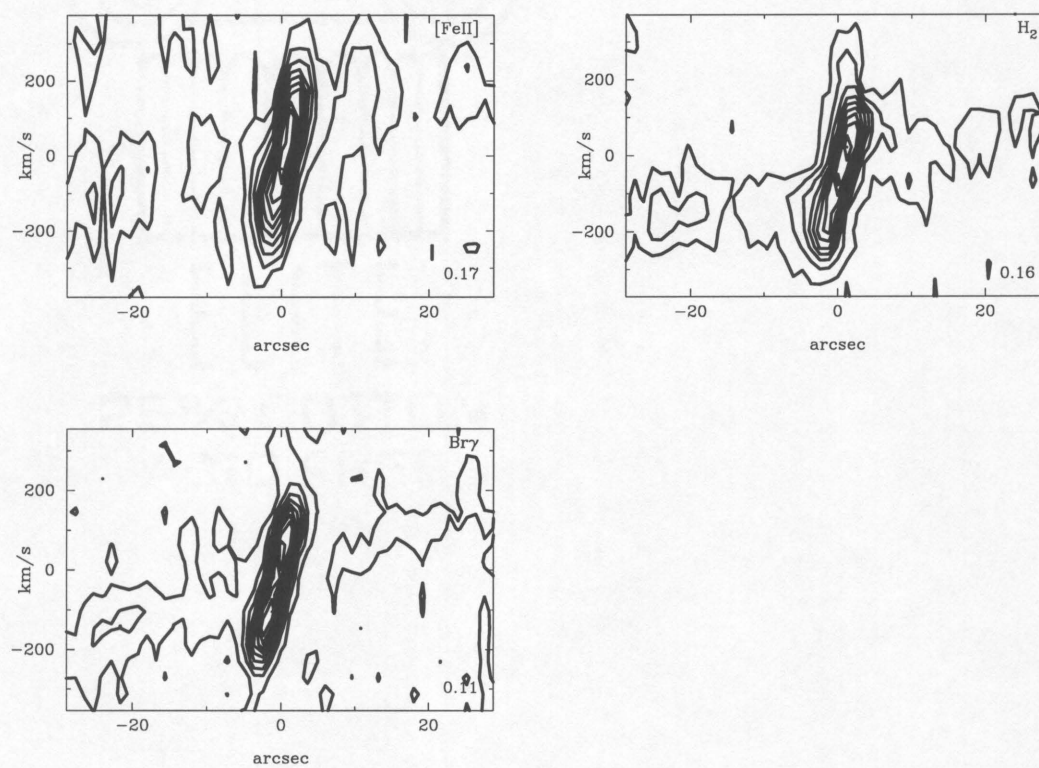


Figure 5.30 Position-velocity plots of strong spectral lines in NGC 660. Details as for Figure 5.29.

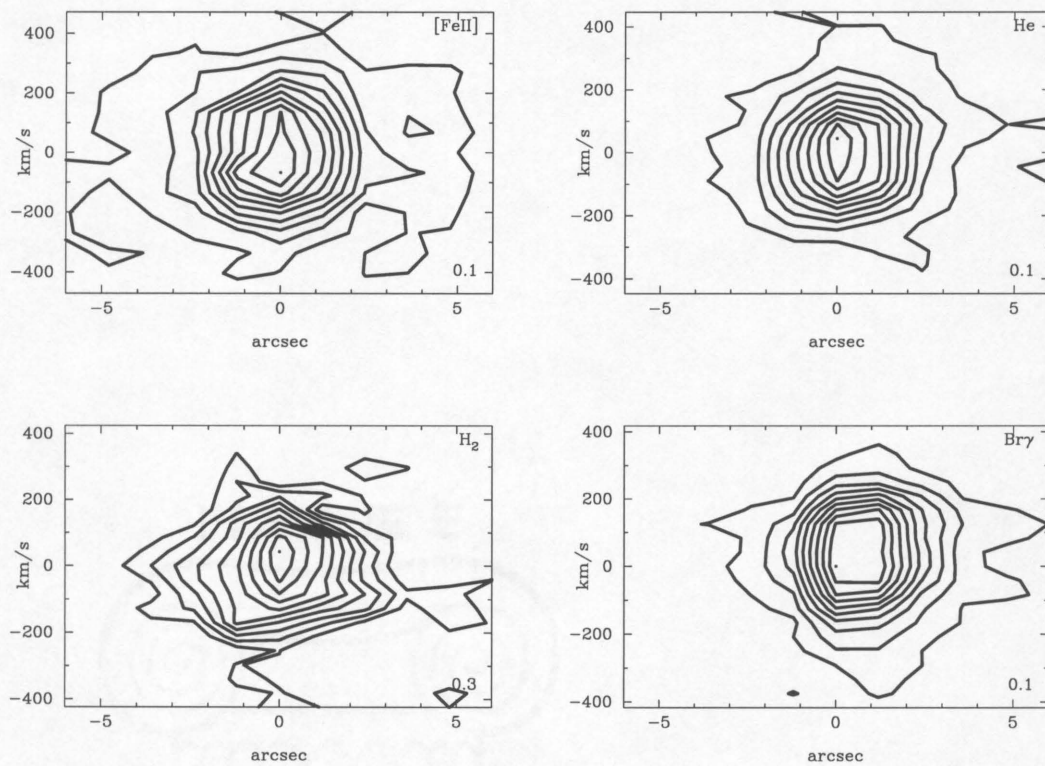


Figure 5.31 Position-velocity plots of strong spectral lines in NGC 1614. Details as for Figure 5.29.

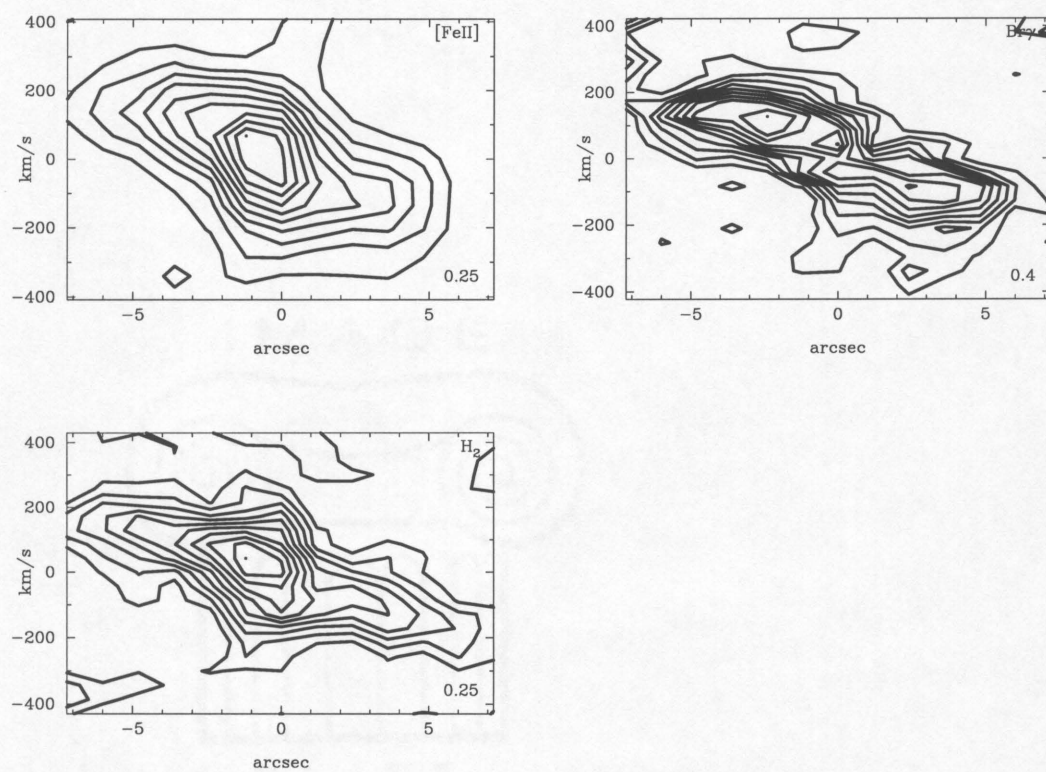


Figure 5.32 Position-velocity plots of strong spectral lines in NGC 2782. Details as for Figure 5.29.

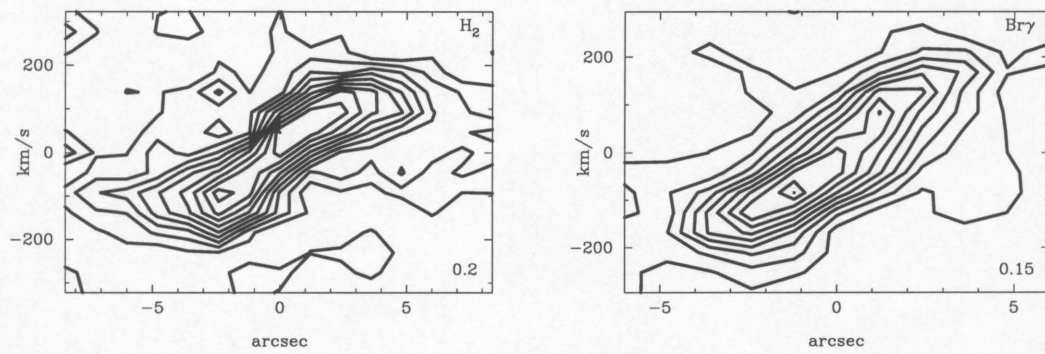


Figure 5.33 Position-velocity plots of strong spectral lines in NGC 3628. Details as for Figure 5.29.

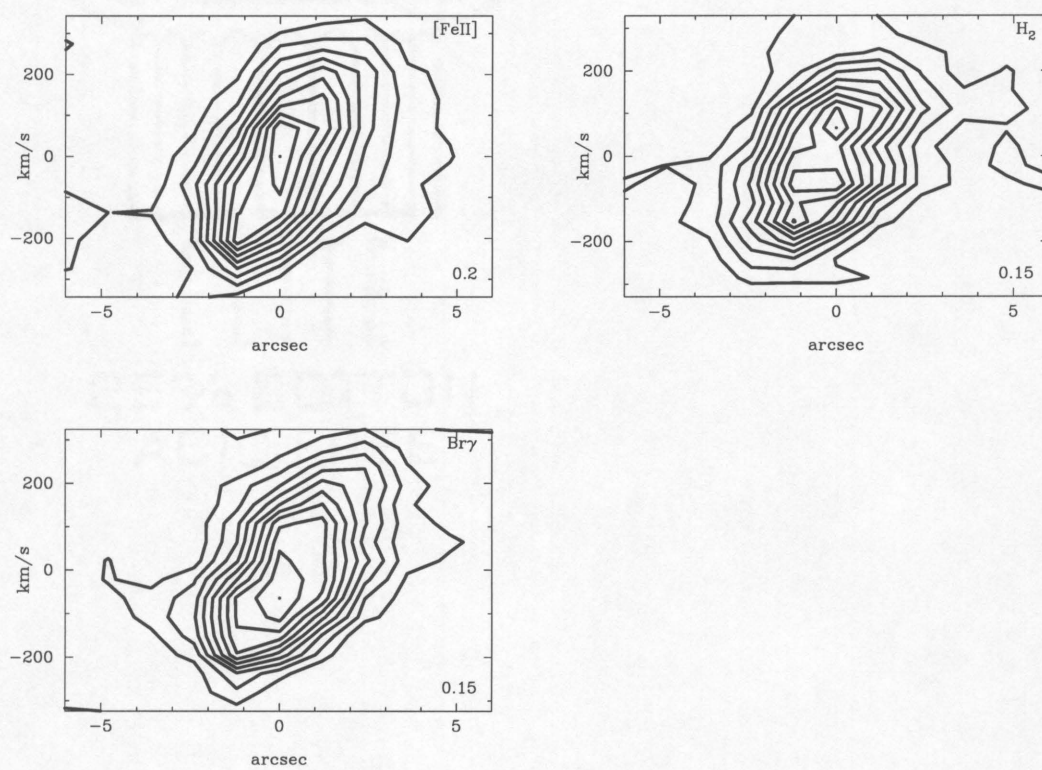


Figure 5.34 Position-velocity plots of strong spectral lines in NGC 4102. Details as for Figure 5.29.

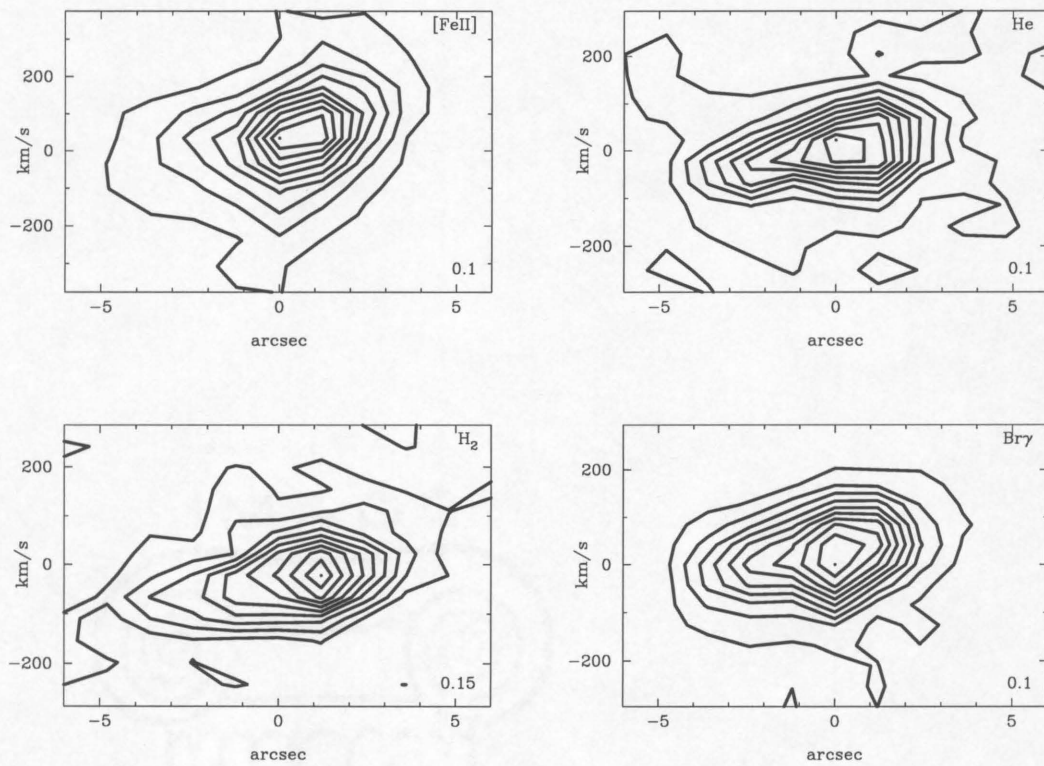


Figure 5.35 Position-velocity plots of strong spectral lines in NGC 4194. Details as for Figure 5.29.

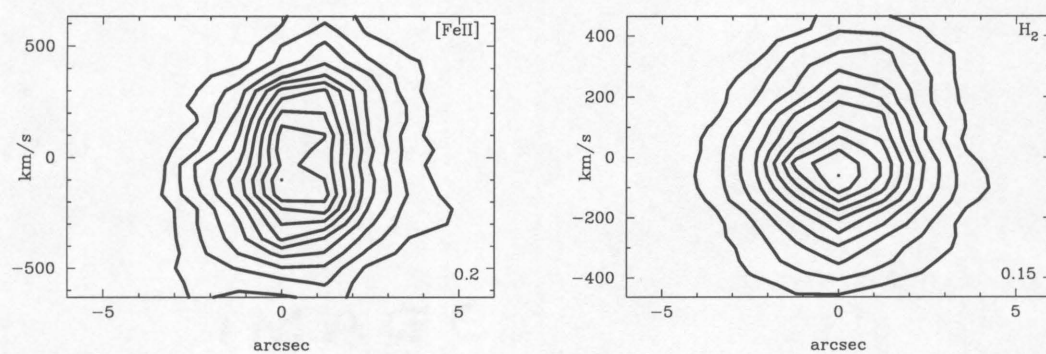


Figure 5.36 Position-velocity plots of strong spectral lines in NGC 6240. Details as for Figure 5.29.

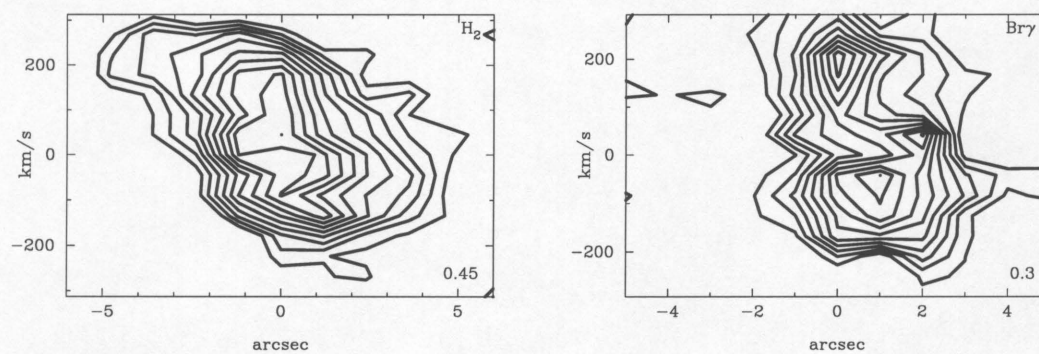


Figure 5.37 Position-velocity plots of strong spectral lines in MKN 331. Details as for Figure 5.29.

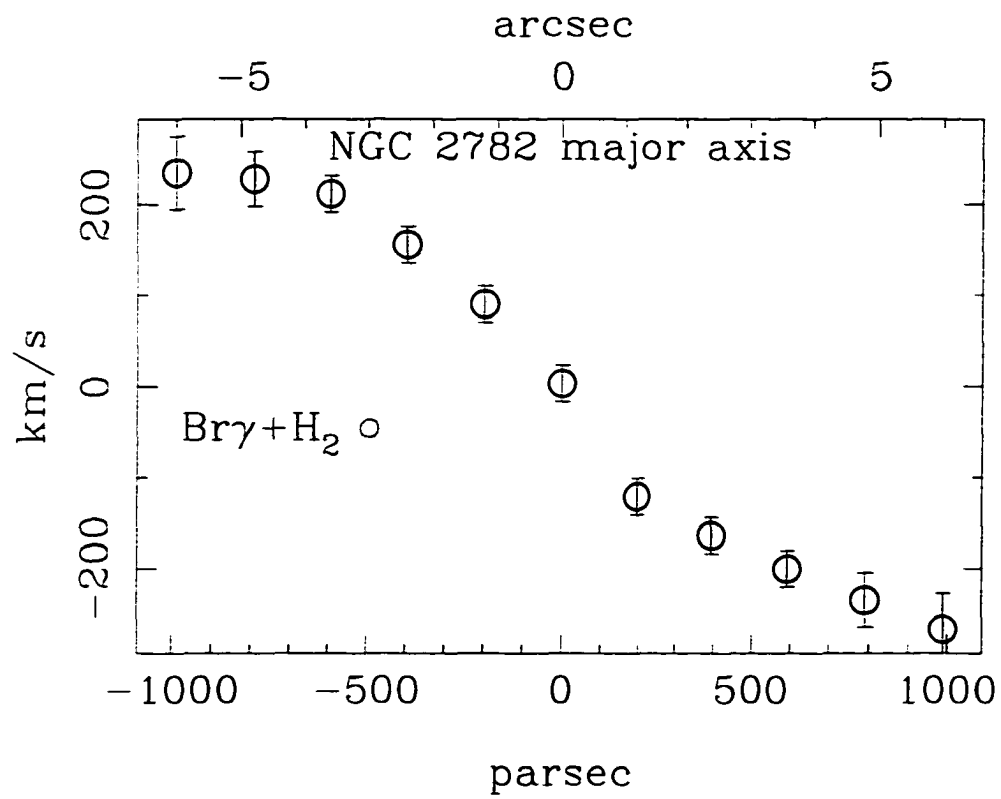


Figure 5.38 Averaged velocity curve of $\text{Br}\gamma$ and H_2 in NGC 2782. The points have been corrected for an inclination of 40° and a difference of 25° between the slit orientation and the galaxy position angle.

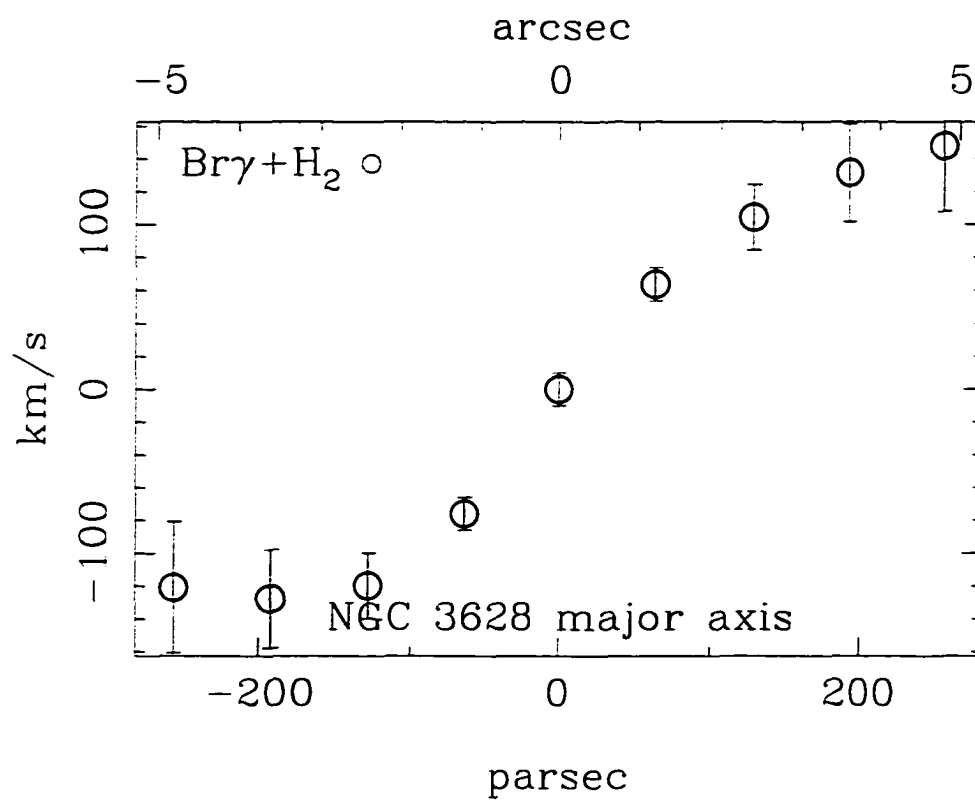


Figure 5.39 Averaged velocity curve of $\text{Br}\gamma$ and H_2 in NGC 3628. The galaxy is nearly edge-on and the slit orientation was close to the major axis of the galaxy, so no corrections to the observed velocities have been made.

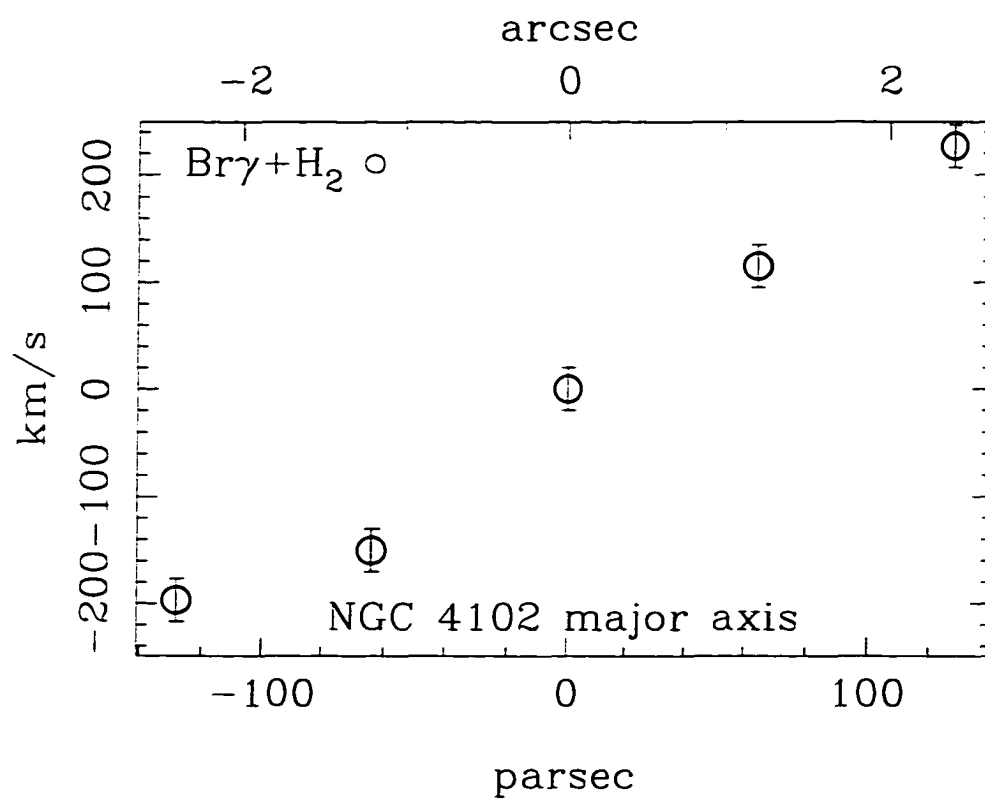


Figure 5.40 Averaged velocity curve of $\text{Br}\gamma$ and H_2 in NGC 4102. The points have been corrected for an inclination of 50° and a difference of 45° between the slit orientation and the galaxy position angle.

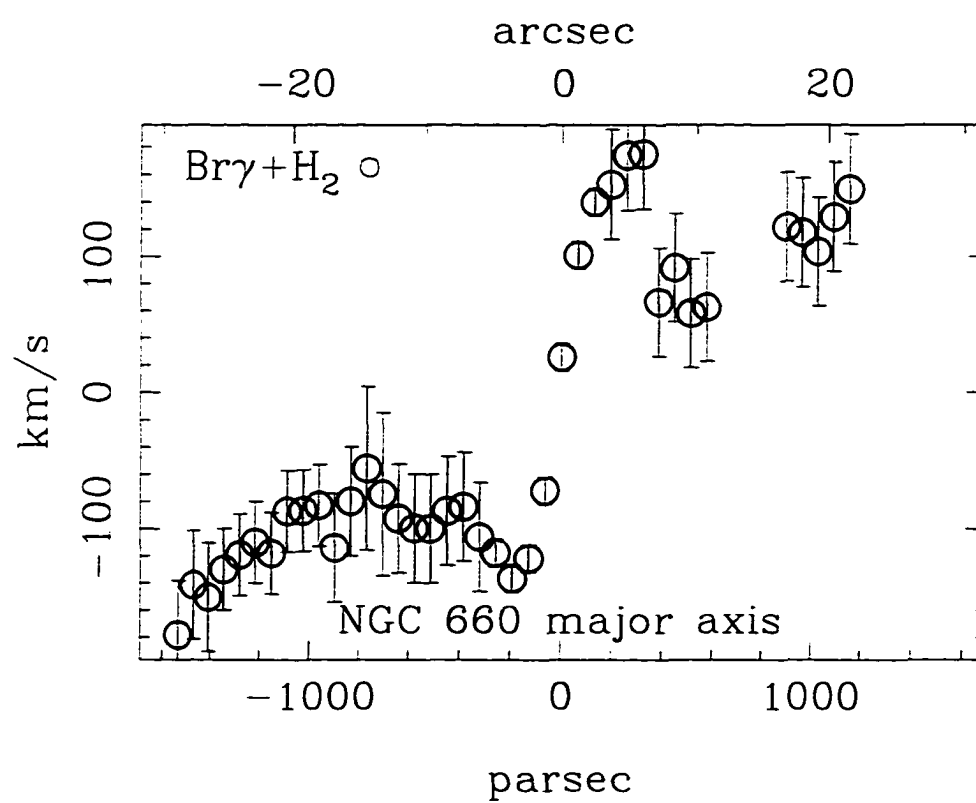


Figure 5.41 Averaged velocity curve of $\text{Br}\gamma$ and H_2 in NGC 660. The galaxy is nearly edge-on, so no inclination correction has been made.

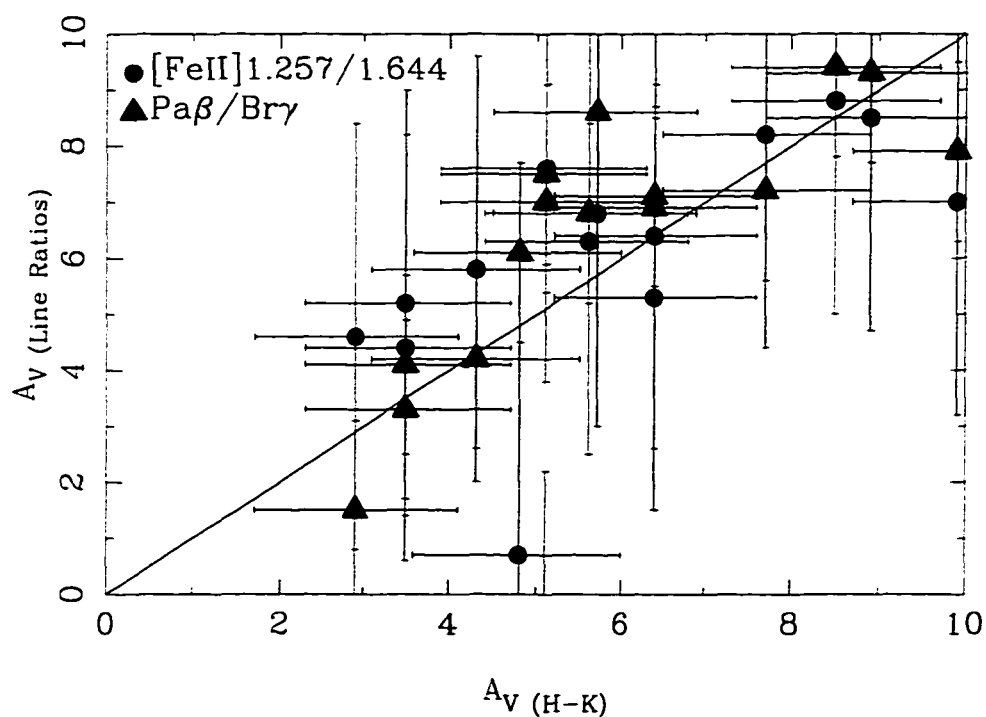


Figure 5.42 Visual extinction for the starburst galaxies in the sample as measured via three techniques (described in the text): (1) $H - K$ color excess, (2) $\text{Pa}\beta/\text{Br}\gamma$ line ratio, and (3) $[\text{Fe II}](1.257\mu\text{m})/(1.644\mu\text{m})$ line ratio. Data are taken from this paper, ERRL96, ERRKA97, and Paper I. The solid line indicates the locus of points where the extinction determined from line ratios and from broadband colors is the same.

CHAPTER 6

CONCLUDING REMARKS

6.1. Main results

We have used new infrared data and data from the literature to derive a number of properties of the nuclear starbursts in 18 galaxies. These include N_{LyC} , L_{Bol} , absolute magnitudes in the J, H and K bands, CO index, SNR, and the mass of stars formed in the starburst. The data were compared to starburst models to determine the age of the starbursts and to put constraints on the IMF. We have taken into account the properties of a preexisting nuclear population which must underly the starburst. In deriving the starburst parameters, we have tried to be conservative in such a way that it becomes easier for a given IMF to fit the data.

In addition to providing a consistent and detailed set of observations of a large sample of starburst galaxies in the form of flux-calibrated broadband imaging, narrowband imaging, and high-resolution spectroscopy, a significant advance of the current work is to provide constraints on the dynamical mass of the nuclear regions of these galaxies. Since the low-mass stars in a young starburst contribute very

little to the integrated luminosity, placing limits on the amount of mass contained in low-luminosity objects is one of the only ways to constrain this portion of the stellar population. The infrared observations of the galaxy kinematics are not strongly affected by extinction and therefore have a significant advantage over optical observations of these dusty systems.

One goal of this project was to explore the universality of the finding in M 82 that an IMF biased against the formation of low-mass stars is required to fit the observations (Rieke et al. 1980; Bernlöhr 1992; Rieke et al. 1993). Similar results have been found for the galaxies NGC 7714 (Bernlöhr 1993) and NGC 1614 (Shier et al. 1996). We find these galaxies to be strong cases for a biased IMF and add to the list the starburst in NGC 4194. It is interesting to note that these galaxies have in common moderate levels of interaction and that in each case the starburst dominates the total galaxy luminosity. Much of the rest of the sample tentatively requires a similar alteration to the IMF (particularly NGC 6946, NGC 253, NGC 660, NGC 4102, and MKN 331).

We find a range of ages in the starbursts discussed here. Galaxies such as NGC 7714, NGC 1614, and NGC 4194 host very young, compact, and powerful starbursts. These three galaxies also show strong tidal features indicative of gravitational interactions; it is likely that these interactions are what triggered the starbursts. We also observe evolved starbursts: the galaxy Maffei 2 appears to host a quietly fading burst while the galaxy NGC 3079 is currently driving a galactic superwind (presumably from a powerful burst several times 10^7 years ago) strong enough affect a neighboring galaxy. Again, these galaxies show evidence of gravitational interactions that likely triggered the starbursts. Some relatively isolated galaxies have features such as a strong bar which seem to be responsible

for driving gas to the center of the galaxy and fueling the starburst. However, not all starburst galaxies have an obvious triggering mechanism: the galaxies IC 342 and NGC 6946 have no known nearby companions or strong bars to drive gas into the nuclear region. We also see a dramatic range in the scale of the starbursts: IC 342 appears to host a small, centrally-concentrated burst while the burst in NGC 2146 is occurring on the scale of kiloparsecs.

Many of the starbursts show evidence for multiple bursts, either in the form of an intermediate-age population mixed with the current burst of star formation or simply because the models produce poor fits to single bursts—a second burst, or some other form of continuing star formation, is often required to produce the observed ionizing flux, supernova rate, or luminosity at late times that a single burst cannot produce.

We have introduced a technique of measuring weak emission lines whereby we subtract a composite stellar spectrum from the galactic spectrum to remove the effect of strong absorption lines in the spectrum. Applying this technique to NGC 253, we measure an unprecedented number of [Fe II] and H₂ lines in an extragalactic source. This allows us, for the first time, to estimate the density in [Fe II]-emitting region of this galaxy. The large number of H₂ lines observed allow us to determine the relative contributions of fluorescent and thermal processes to the emission.

6.2. Future work

The work we have done here suggests a number of directions for future studies. An obvious step would be to study more starbursts, building up the statistics. A more targeted approach can be made, however, since we have observed many stages of

evolution here and now have a better idea of what to look for. In principle, we can now study a wide range of starburst ages and measure the space density of these systems in detail, to build a consistent picture of starburst evolution and their relation to normal and active galaxies.

We can improve on the kinematic measurements, as well. We can perform more sophisticated modeling and make use of the extra information we have in our spectra, for example treating the velocity dispersion as a function of radius instead of an integrated value. A future upgrade planned for FSpec is a high-resolution ($R \sim 20000$), silicon-immersed grating that, coupled with the large telescopes available at Steward, will allow us to make detailed kinematic measurements of nearby galaxies.

Improved spatial resolution will allow us to constrain better the stellar population as a function of position in the galaxy, perhaps even allowing us to trace the propagation of the starburst throughout the galaxy. NICMOS will be central to this study, but exciting capabilities are being developed for ground-based observing as well, with the possibility of high spatial resolution imaging and spectroscopy in the near future.

An ambitious project we are in a unique position to undertake is to build a spectral synthesis program for starbursts. We have a well-developed evolutionary synthesis code, and have recently obtained (as discussed briefly in Chapter 2) a large (> 100 stars) library of infrared stellar spectra. We have already made some use of this library in this work, to disentangle weak emission lines from the strong stellar absorptions in the galaxy continuum or to create templates for velocity dispersion measurements. In principle, however, there is more information contained in the continuum absorptions than we are currently making use of. Our

main constraints on the evolved stellar population are the K-band luminosity and the CO index. Our high-quality spectra display a wealth of stellar features, however, which if modeled could serve as a further constraint on the stellar population. A self-consistent synthesized stellar continuum would improve the accuracy of our continuum subtractions, allowing us better access to weak emission features in the galaxy spectrum. A mix of appropriate stellar types should also serve as a better velocity dispersion template for a galaxy than the single stars we have been using. Finally, the large number of stars we have observed should enable us to discern some reliable metallicity indicators for the stellar population in the starburst.

REFERENCES

- Aannestand, P. 1989, *ApJ*, 338, 162
- Aaronson, M. 1977, Ph.D. thesis, Harvard Univ.
- Achtermann, J.M. 1994, PhD thesis, University of Texas
- Alonso-Herrero, A., Rieke, M. J., Rieke, G. H., Ruiz, M. 1997, *ApJ*, in press
- Anantharamaiah, K. R. & Goss, W. M. 1996, *ApJ*, 466, L13
- Antonucci, R. R. J. & Ulvestad, J. S. 1988, *ApJ*, 330, L97
- Armus, L., Heckman, T. M., & Miley, G. K. 1989, *ApJ*, 347, 727
- Arnaboldi, M., Capaccioli, M., Cappellaro, E., Held, E. V., & Koribalski, B. 1995, *AJ*, 110, 199
- Balzano, V. A. 1983, *ApJ*, 268, 602
- Bautista, M. A. & Pradhan, A. K. 1996, *A&AS*, 115, 551
- Beck, S. C. & Beckwith, S. V. 1984, *MNRAS*, 207, 671
- Becklin, E. E., Gatley, I., Matthews, K., Neugebauer, G., Sellgren, K., Werner, M. W., & Wynn-Williams, C. G. 1980, *ApJ*, 236, 441
- Bekki, K. 1995, *MNRAS*, 276, 9
- Benvenuti, P., Cappacioli, M., & D'Odorico, S. 1975, *A&A*, 41, 91
- Bernlöhr, K. 1992, *A&A*, 263, 54
- Bernlöhr, K. 1993, *A&A*, 268, 25
- Bernlöhr, K. 1993, *A&A*, 270, 20
- Black, J. H., & van Dishoeck, E. F. 1987, *ApJ*, 322, 412
- Blair, W. P. & Kirshner, R. P. 1985, *ApJ*, 289, 582
- Burton, M. G., Geballe, T. R., Brand, P. W. J. L., & Webster, A. S. 1988, *MNRAS*, 231, 617
- Calzetti, D., Kinney, A. L., & Storchi-Bergmann, T. *ApJ*, 458, 132
- Campins, H., Rieke, G. H., & Lebofsky, M. J. 1985, *AJ*, 90, 896
- Canzian, B., Mundy, L. G., & Scoville, N. Z. 1988, *ApJ*, 333, 157
- Carral, P., Hollenbach, D. J., Lord, S. D., Colgan, S. W. J., Haas, M. R., Rubin, R. H., & Erickson, E. F. 1994, *ApJ*, 423, 223
- Clegg, R. E. S. 1987, *MNRAS*, 229, 31p
- Colina, L. & Pérez-Olea, D. 1992, *MNRAS*, 259, 709
- Condon, J. J., & Yin, Q. F. 1990, *ApJ*, 357, 97

- Courteau, S. 1994, A Compilation of the Faint UKIRT Standards
- Danziger, I. J. & Leibowitz, E. M. 1985, MNRAS, 216, 365
- Danziger, I. J., Murdin, P. G., Clark, D. H., & D'Odorico, S. 1979, MNRAS, 186, 555
- Demoulin, M. H., Burbage, E. M., & Burbage, G. R. 1968, ApJ, 153, 31
- de Vaucouleurs, G. 1978, ApJ, 224, 710
- Devereux, N. A., Becklin, E. E., & Scoville, N. A. 1987, ApJ, 312, 529
- Devereux, N. ApJ, 323, 91
- Doyon, R., Joseph, R. D., & Wright, G. S. 1994, ApJ, 421, 101
- Draine, B. T., & Roberge, W. G., 1982, ApJ, 259, L91
- Edelson, R. A., Malkan, M. A., & Rieke, G. H. 1987, ApJ, 321, 233
- Elias, J. H., Frogel, J. A., Matthews, K., & Neugebauer, G. 1982, AJ, 87, 1029
- Elmegreen, B. V. G., Meloy Elmegreen, D., & Montenegro, L. ApJS, 79, 37
- Engargiola, G. 1991, ApJS, 76, 875
- Engelbracht, C. W., Rieke, M. J., Rieke, G. H., Kelly, D. M. & Achtermann, J. M. 1997, ApJ, submitted (ERRKA97)
- Engelbracht, C. W., Rieke, M. J., Rieke, G. H., & Latter, W. B. 1996, ApJ, 467, 227 (ERRL96)
- Engelbracht, C. W., Rieke, M. J., & Rieke, G. H. 1997, ApJ, submitted (Paper I)
- Fesen, R. A., Blair, W. P., & Kirshner, R. P. 1985, ApJ, 292, 29
- Filippenko, A. V. & Sargent, W. L. W. 1992 AJ, 103, 28
- Filippenko, A. V. & Terlevich, R. 1992, ApJ, 397, L79
- Forbes, D. A. & Depoy, D. L. 1992, A&A, 259, 97
- Forbes, D. A. & Ward, M. J. 1993, ApJ, 416, 150
- Forbes, D. A., Ward, M. J., DePoy, D. L., Boisson, C., & Smith, M. S. 1992, MNRAS, 254, 509
- Frei, Z., Guhathakurta, P., Gunn, J. E., & Tyson, J. A. 1996, AJ, 111, 174
- Frogel, J. A., Persson, S. E., Aaronson, M., & Mathews, K. 1978, ApJ, 220, 75
- Frogel, J. A., & Whitford, A. E. 1987, ApJ, 320, 199
- Gear, W. K., Gee, G., Robson, E. I., Ade, P. A. R., & Duncan, W. D. 1986, MNRAS, 219, 19p
- Goldader, J. D., Joseph, R. D., Doyon, R., & Sanders, D. B. 1995, ApJ, 444, 97
- Goldader, J. D., Joseph, R. D., Doyon, R., & Sanders, D. B. 1997, ApJS, in press

- González-Delgado, R. M., Pérez, E., Díaz, A. I., García-Vargas, M. L., Terlevich, E., & Vilchez, J. M. 1995, *ApJ*, 439, 604
- Graham, J. R., Wright, G. S., & Longmore, A. J., 1987, *ApJ*, 313, 847
- Greenhouse, M. A., Satyapal, S., Woodward, C. E., Fischer, J., Thompson, K. L., Forrest, W. J., Pipher, J. L., Raines, N., Smith, H. A., Watson, D. M., & Rudy, R. J. 1997, *ApJ*, 476, 105
- Greenhouse, M. A., Woodward, C. E., Thronson, H. A., Rudy, R. J., Rossano, G. S., Erwin, P., & Puetter, R. C. 1991, *ApJ*, 383, 164
- Heckman, T. M., 1980, *A&A*, 87, 152
- Heckman, T. M., Armus, L., & Miley, G. K. 1990, *ApJS*, 74, 833
- Ho, P. T. P., Beck, S. C., & Turner, J. L. 1990, *ApJ*, 349, 57
- Hodge, P. & Miller, B. W. 1995, *ApJ*, 451, 176
- Hollenbach, D. J., & Shull, J. M. 1977, *ApJ*, 216, 419
- Huang, Z. P., Thuan, T. X., Chevalier, R. A., Condon, J. J., & Yin, Q. F. 1994, *ApJ*, 424, 114
- Hudgins, D., Herter, T., & Joyce, R. J. 1990, *ApJ*, 354, 57
- Hummer, D. G. & Storey, P. J. 1987, *MNRAS*, 224, 801
- Hurt, R. L., Turner, J. L., & Ho, P. T. P. 1996, *ApJ*, 466, 135
- Hutchings, J. B., Neff, S. G., Stanford, S. A., Lo, E., & Unger, S. W. 1990, *AJ*, 100, 60
- Irwin, J. A., Seaquist, E. R., Taylor, A. R., & Duric, N. 1987, *ApJ*, 313, L91
- Ishizuki, S., Kawabe, R., Ishiguro, M., Okumura, S. K., Morita, K.-I., Chikada, Y., Kasuga, T., & Doi, M. 1990, *ApJ*, 355, 436
- Kelly, D. M., Lacy, J. H., van der Hulst, J. M., & Achtermann, J.M. 1997, in preparation
- Kleinmann, S. G. & Hall, D. N. B. 1985, *ApJS*, 62, 501
- Koornneef, J. & Israel, F. P. 1996, *New Astron.*, 1, 271
- Kormendy, J., & Richstone, D. 1992, *ApJ*, 393, 559
- Krügel, E., Chini, R., Klein, U., et al. 1990, *A&A*, 240, 232
- Krabbe, A., Sternberg, A., & Genzel, R. 1994, *ApJ*, 425, 72
- Krismer, M., Tully, R. B., & Gioia, I. M. 1995, *AJ*, 110, 1584
- Kulesa, C. A. & Black, J. H. 1997, submitted to *ApJ*
- Lacy, J.H., Achtermann, J.M., Bruce, D.E., Lester, D.F., Arens, J.F., Peck, M.C., & Gaalema, S.D. 1989, *PASP*, 101, 1166

- Lacy, J.H., & Achtermann, J.M. 1994, in *Infrared Astronomy with Arrays*, I. McLean (ed.), p.85
- Latter, W. B., Hora, J. L., Kelly, D. M., Deutsch, L. K., & Maloney, P. R. 1993, *AJ*, 106, 260
- Lebofsky, M. J. & Rieke, G. H. 1979, *ApJ*, 229, 111
- Lehnert, M. D. & Heckman, T. M. 1995, *ApJS*, 97, 89
- Liu, C. T. & Kennicutt, R. C. 1995, *ApJS*, 100, 325
- Livingston, W., & Wallace, L. 1991, *An Atlas of the Solar Spectrum in the Infrared from 1850 to 9000 cm⁻¹ (1.1 to 5.4 μ m)*, N.S.O. Technical Report # 91-001, National Solar Observatory, National Optical Astronomy Observatories, Tucson, AZ
- Luhman, M. L., Jaffe, D. T., Keller, L. D., & Pak, S. 1994, *ApJ*, 436, L185
- Maeder, A. 1992. Private communication
- Maiolino, R., Rieke, G. H., & Rieke, M. J. 1996, *AJ*, in press
- Maloney, P. R. & Black, J. H. 1988, *ApJ*, 325, 389
- Mauersberger, R., Henkel, C., Wielebinski, R., Wiklind, T., & Reuter, H.-P. 1996, *A&A*, 305, 421
- McLeod, K. K., Rieke, G. H., Rieke, M. J., & Kelly, D. M. 1993, *ApJ*, 412, 111
- Moorwood, A. F. M. & Oliva, E. 1988, *A&A*, 203, 278
- Muñoz-Tuñón, C., Vilchez, J. M., & Castañeda, H. O. 1993, *A&A*, 278, 364
- Nussbaumer, H. & Storey, P. J. 1988, *A&A*, 193, 327
- Oliva, E., Moorwood, A. F. M., & Danziger, I. J. 1989, *A&A*, 214, 307
- Oliva, E., Moorwood, A. F. M., & Danziger, I. J. 1990, *A&A*, 240, 453
- Oliva, E., & Origlia, L. 1992, *A&A*, 254, 466
- Origlia, L., Moorwood, A. F. M., & Oliva, E. 1993, *A&A*, 280, 536
- Pence, W. D. 1981, *ApJ*, 247, 473
- Peng, R., Zhou, S., Whiteoak, J. B., Lo, K. Y., & Sutton, E. C. 1996, *ApJ*, 470, 821
- Pompea, S. M. & Rieke, G. H. 1990, *ApJ*, 356, 416
- Prada, F., Manchado, A., Canzian, B., Peletier, R. F., McKeith, C. D., & Beckman, J. E. 1996, *ApJ*, 458, 537
- Pradhan, A. K., & Zhang, H. L. 1993, *ApJ*, 409, L77
- Puxley, P. J. & Brand, P. W. J. L. 1994, *MNRAS*, 266, 431

- Puxley, P. J., & Brand, P. W. J. L. 1995, MNRAS, 274, L77
- Ramsay, S. K., Chrysostomou, A., Geballe, T. R., Brand, P. W. J. L., & Mountain, M. 1993, MNRAS, 263, 695
- Rice, W., Lonsdale, C. J., Soifer, B. T., Neugebauer, G., Koplan, E. L., Lloyd, L. A., de Jong, T., & Habing, H. J. 1988, ApJS, 68, 91
- Rieke, G. H. 1976, ApJ, 206 L15
- Rieke, G. H. & Lebofsky, M. J. 1985, ApJ, 288, 618
- Rieke, G. H. & Low, F. J. 1975, ApJ, 197, 17
- Rieke, G. H., Lebofsky, M. J., Thompson, R. I., Low, F. J., & Tokunaga, A. T. 1980, ApJ, 238, 24
- Rieke, G. H., Lebofsky, M. J., & Walker, C. E. 1988, ApJ, 325, 679
- Rieke, G. H., Loken, K., Rieke, M. J., & Tamblyn, P. 1993, ApJ, 412, 99 (RLRT93)
- Rieke, G. H., & Lebofsky, M. J. 1978, ApJ, 220, L37
- Rieke, G. H., & Lebofsky, M. J. 1978, ARA&A, 1979, 17, 477
- Rix, H.-W., Carleton, N. P., Rieke, G. H., & Rieke, M. J. 1990, ApJ, 412, 99
- Roche, P. F., Aitken, D. K., Smith, C. H., & Ward, M. J. 1991, MNRAS, 248, 606
- Roche, P.F., & Aitken, D.K. 1985, MNRAS, 213, 789
- Rogstad, D. H. & Shostak, G. S. 1972, ApJ, 176, 315
- Sams, B. J., III, Genzel, R., Eckart, A., Tacconi-Garman, L., & Hofmann, R. 1994, ApJ, 430, L33
- Scoville, N. Z., Soifer, B. T., Neugebauer, G., Young, J. S., Matthews, K., & Yerka, J. 1985, ApJ, 289, 129
- Shields, J. C. 1993, ApJ, 419, 181
- Shields, J. C. & Kennicutt, R. C. 1995, ApJ, 454, 807
- Shier, L. M., Rieke, M. J., & Rieke, G. H. 1994, ApJ, 433, L9
- Shier, L. M., Rieke, M. J., & Rieke, G. H. 1996, ApJ, 470, 222
- Smith, B. J. & Harvey, P. M. 1996, ApJ, 468, 139
- Smith, B. J., Harvey, P. M., & Lester, D. F. 1995, ApJ, 442, 610
- Sofue, Y. & Irwin, J. A. 1992, PASJ, 44, 353
- Spinoglio, L., Malkan, M. A., Rush, B., Carrasco, L., & Recillas-Cruz, E. 1995, ApJ, 453, 616
- Sternberg, A., & Dalgarno, A. 1989, ApJ, 338, 197

- Tadhunter, C. N., Morganti, R., di Serego Alighieri, S., Fosbury, R. A. E., & Danziger, I. J. 1993, MNRAS, 259, 709
- Telesco, C. M. 1988, ARA&A, 26, 343
- Telesco, C. M., Dressel, L. L., & Wolstencroft, R. D. 1993, ApJ, 414, 120
- Tenjes, P., Haud, U., & Einasto, J. 1994, A&A, 286, 753
- Thronson, H. A., & Greenhouse, M. A. 1988, ApJ, 327, 671
- Tremaine, S., Richstone, D. O., Byun, Y., Dressler, A., Faber, S. M., Grillmair, C., Kormendy, J., & Lauer, T. R. 1994, AJ, 107, 634
- Tully, R. 1988, Nearby Galaxies Catalog (Cambridge: Cambridge Univ. Press)
- Turner, J. L. & Ho, P. T. P. 1983, ApJ, 268, L79
- Turner, J. L. & Ho, P. T. P. 1985, ApJ, 299, L77
- Ulvestad, J. S. & Antonucci, R. R. J. 1991, AJ, 102, 875
- Ulvestad, J. S. & Antonucci, R. R. J. 1994, ApJ, 424, L29
- Van Buren, D. & Greenhouse, M. A. 1994, ApJ, (431, 640)
- van der Werf, P. P., Genzel, R., Krabbe, A., Bietz, M., Lutz, D., & Drapatz, S. 1993, ApJ, 405, 522
- Vanzi, L. & Rieke, G. H. 1997, ApJ, 479, 694
- Vanzi, L., Rieke, G. H., Martin, C. L., & Shields, J. C. 1996, ApJ, 466, 150
- Vanzi, L., Rieke, G. H., Rieke, M. J., & Engelbracht, C. W. 1996, in preparation
- Veilleux, S., Cecil, G., & Bland-Hawthorn, J. 1995, ApJ, 445, 152
- Wada, K. & Habe, A. 1992, MNRAS, 258, 82
- Wade, K., & Habe, A. 1992, MNRAS, 258, 82
- Weedman, D. W., Feldman, F. R., Balzano, V. A., & Ramsey, L. W. 1981, ApJ, 248, 105
- Williams, D. M., Thompson, C. L., Rieke, G. H., & Montgomery, E. F. 1993, S. P. I. E., 1946, 482
- Witt, A. N., Thronson, H. A., & Capuano, J. M. 1992, ApJ, 393, 611
- Young, J. S., Claussen, M. J., Kleinmann, S. G., Rubin, V. C., & Scoville, N. Z. 1988, ApJ, 331, L81